

Interrogating K2P Pharmacology: development and characterization of  
small-molecule modulators of two-pore potassium channels

by  
Lianne Pope

DISSERTATION

Submitted in partial satisfaction of the requirements for degree of  
DOCTOR OF PHILOSOPHY

in

Chemistry and Chemical Biology

in the

GRADUATE DIVISION

of the

UNIVERSITY OF CALIFORNIA, SAN FRANCISCO

Approved:

DocuSigned by:

*Daniel Minor*

Daniel Minor

C039575D9EAB43B...

Chair

DocuSigned by:

*Adam Renslo*

Adam Renslo

DocuSigned by:

*Michelle Arkin*

Michelle Arkin

DocuSigned by:

*Lily Jan*

Lily Jan

394456D87457494...

Committee Members

Copyright 2019  
by  
Lianne Elizabeth Pope

*Dedicated to Justin Pope*

## ***Acknowledgements***

I would first like to thank my advisor, Daniel Minor, for his constant guidance, encouragement and determination in getting me to this point in my graduate study. From day one, I have admired his passion and high standard for science and truth, and I am extremely fortunate to have trained in the lab he has cultivated. I simply would not be here today without him and for that I am humbly grateful. I am also deeply appreciative to my thesis committee, Adam Renslo, Michelle Arkin and Lily Jan, for their thoughtful and critical feedback during my graduate study at UCSF.

Over the years, the mentorship and friendship from my generous labmates has meant the world to me and has undeniably aided my success – I would not have made it without you all. It has been amazing to work with such talented and thoughtful scientists and it has been incredibly fun and special to become friends with such a diverse group of people. Thank you for always lending an ear when science, lab and life were hard.

Finally, to my family and friends. None of this would have been possible without your love and support over the years, and I can only hope to be there for you in the same way you've all been there for me. For all of you, I am eternally grateful.

Parts of this thesis are reproductions of material previously published in:

**Pope, L., Arrigoni, C., Lou, H., Bryant, C., Gallardo-Godoy, A., Renslo, A. R., Minor, D. L. Jr. 2018.** Protein and chemical determinants of BL-1249 action and selectivity for  $K_{2P}$  channels. **ACS Chem Neurosci.** 9(12): 3153-3165. (doi: 10.1021/acscchemneuro.8b00337)

**Pope, L., Lolicato, M and Minor, D. L. 2019.** Polynuclear ruthenium amines inhibit  $K_{2P}$  channels via a 'finger in the dam' mechanism. Manuscript submitted. **Cell Chem Bio.** (pre-print on bioRxiv)

Findeisen, F., Campiglio, M., Jo, H., Abderemane-Ali, F., Rumpf, C. H., **Pope, L., Rossen, N. D., Flucher, B. E., DeGrado, W. F., and Minor, D. L. Jr. 2017.** Stapled voltage-gated calcium channel ( $Ca_v$ )  $\alpha$ -interaction domain (AID) peptides act as selective protein-protein interaction inhibitors of  $Ca_v$  function. **ACS Chem Neurosci.** 8(6): 1313-1326. (doi:10.1021/acscchemneuro.6b00454)

# Interrogating K<sub>2P</sub> Pharmacology: development and characterization of small-molecule modulators of two-pore potassium channels

by

Lianne Elizabeth Pope

## **Abstract:**

Two-pore potassium (K<sub>2P</sub>) channels are responsible for regulating the resting membrane potential of excitable cells. Though K<sub>2P</sub> channels are heavily implicated in disease, no approved therapies exist to specifically target K<sub>2P</sub> channels. Defined pharmacology for these channels has lagged, as K<sub>2P</sub>s differ from traditional potassium channels in a number of ways. By harnessing these differences, we aim to discover and characterize new K<sub>2P</sub> modulators to aid in the study of this unique channel class. Through the structural and functional characterization of small molecule K<sub>2P</sub> modulators, we will facilitate the understanding of how these channels contribute to physiology and disease.

The introduction of this thesis aims to define and describe the scope of K<sub>2P</sub> pharmacology, with a specific focus on TREK family modulation. High throughput methods for identifying new classes of TREK family modulators are reviewed, and a synthesis of the selectivity of small-molecule TREK family modulators has been compiled, with special attention to those compounds for which structural information has been elucidated. In chapter two, the action and selectivity of K<sub>2P</sub> activator BL-1249 is presented and, using a chimeric functional approach, subtle differences between K<sub>2P</sub>2.1 (TREK-1) and K<sub>2P</sub>4.1 (TRAAK) channels and their differential response to BL-1249 were pinpointed to specific areas involving M2 and M4 helices. This work highlights how channels within K<sub>2P</sub> families can differ from one another in their pharmacological profiles and how

selective molecules can help to tease apart these important differences. Chapter three presents structural and functional studies of polyruthenium amine inhibitors of  $K_{2P}$ s and creation of a ruthenium red super-binder with low nanomolar efficacy. Through our studies, we define the mechanism of polyruthenium amine inhibitors as an electrostatic block positioned above by coordinating acidic residues. Furthermore, we provide a template for future development of  $K_{2P}$  modulators which may target this novel binding site. From these and other recent studies, a multi-site model for  $K_{2P}$  pharmacological regulation has emerged and future work will require precise dissection to establish how each of these sites may preferentially affect gating in TREK, and more broadly, all  $K_{2P}$ s.

Finally, chapter four presents the synthetic modulation of a protein-protein interaction (PPI) using stapled peptides in a different context, departing from a focus on  $K_{2P}$  channels onto another voltage-gated ion channel (VGIC) family member, voltage-gated calcium channels ( $Ca_v$ ). Stapled peptide mimics of the  $\alpha$ -interacting domain (AID) were found to inhibit the high affinity interaction of the channel domain ( $Ca_v\alpha$ ) with its cytosolic subunit ( $Ca_v\beta$ ) to affect calcium channel properties. Establishing and improving the modulation of this type of PPI informs the future development of inhibitors of  $K_{2P}$  interactions with important cellular partners.

## **Table of Contents**

<b>Chapter 1 : Introduction</b> .....	<b>1</b>
<i>K<sub>2P</sub> channels: pharmacological relevance and therapeutic potential</i> .....	2
<i>The TREK family: a model K<sub>2P</sub> system</i> .....	3
<i>Discovering new chemical modulators of TREK channels</i> .....	5
<i>Pharmacological selectivity of TREK modulators, with structural perspectives</i> .....	8
<i>Modulation of protein-protein interactions – lessons from voltage-gated calcium channels (Ca<sub>v</sub>)</i> .....	12
<i>Emergence of a poly-site model for K<sub>2P</sub> modulation – future directions</i> .....	13
<i>References</i> .....	14
<b>Chapter 2 : Protein and chemical determinants of BL-1249 action and selectivity</b> .....	<b>30</b>
<i>Abstract</i> .....	31
<i>Introduction</i> .....	32
<i>Results</i> .....	34
<i>Discussion</i> .....	44
<i>Materials and Methods</i> .....	49
<i>References</i> .....	53
<b>Chapter 3 : Polynuclear ruthenium amines inhibit K<sub>2P</sub>s via a ‘finger in the dam’ mechanism</b> .....	<b>77</b>
<i>Abstract</i> .....	78
<i>Introduction</i> .....	79
<i>Results</i> .....	82
<i>Discussion</i> .....	91



*Materials and Methods* ..... 96  
*References* ..... 102

**Chapter 4 : Stapled voltage-gated calcium channel (Cav)  $\alpha$ -interaction domain (AID) peptides act as selective protein-protein interaction inhibitors of Cav**

**function** ..... 137  
*Abstract* ..... 138  
*Introduction* ..... 139  
*Results* ..... 142  
*Discussion* ..... 153  
*Materials and Methods* ..... 158  
*References* ..... 163

## **List of Figures**

### **Chapter 1**

Figure 1.1   A suite of ion channels controls the action potential .....	26
Figure 1.2   $K_{2P}$ channels are grouped according to structure and function.....	27
Figure 1.3   Selectivity profiles of small molecule modulators of TREK channels.....	28
Figure 1.4   Unified model for $K_{2P}$ poly-site pharmacology .....	29

### **Chapter 2**

Figure 2.1   External application of BL-1249 selectively activates mechanosensitive $K_{2PS}$ .....	63
Figure 2.2   BL-1249 activates the $K_{2P2.1}$ (TREK-1) C-type gate .....	64
Figure 2.3   $K_{2P2.1}$ (TREK 1) C-terminus affects BL-1249 response .....	65
Figure 2.4   BL-1249 responses of TREK-1/TRAAK chimeras .....	67
Figure 2.5   M2 residues contribute to BL-1249 selectivity between $K_{2P2.1}$ (TREK 1) and $K_{2P4.1}$ (TRAAK) .....	68
Figure 2.6   Structure activity relationships of BL-1249 analogues .....	70
Figure 2.7   Supplementary Figure 1 - Responses of TREK-1/TRAAK chimeras to ML355 and ML67-33 activators. ....	72
Figure 2.8   Supplementary Figure 2 - Exemplar responses of TREK-1/TRAAK chimeras to ML355 and ML67-33 activators.....	74

### **Chapter 3**

Figure 3.1   Functional and structural analysis of the $K_{2P2.1}$ I110D:RuR complex. ....	113
Figure 3.2   Functional and structural analysis of C-type gate activated $K_{2P2.1}$ I110D:RuR complexes. ....	115

Figure 3.3   Functional and structural analysis of $K_{2P}$ :Ru360: interactions. ....	117
Figure 3.4   Engineering $K_{2P}$ RuR super-responders .....	119
Figure 3.5   Mechanisms of small molecule $K_{2P}$ modulation .....	121
Figure 3.6   S1 - $K_{2P}$ CAP sequences and $K_{2P2.1}$ CAP mutant functional properties .....	122
Figure 3.7   S2 - $K_{2P2.1}$ I110D structures and structure comparisons .....	124
Figure 3.8   S3 - $K_{2P2.1}$ I110D ML335 response and structure of the $K_{2P2.1}$ I110D:RuR:ML335 complex.....	126
Figure 3.9   S4 - Ru360 inhibits $K_{2P}$ channels.....	127
Figure 3.10   S5 - $K_{2P}$ selectivity filter (SF) sequences and RuR responses of $K_{2P2.1}$ SF mutants.....	129
Figure 3.11   S6 - Double mutant cycle analysis.....	131

#### **Chapter 4**

Figure 4.1   Backbone staples increase AID helical content.....	177
Figure 4.2   Crystal structures of $Ca_V\beta_{2a}$ :stapled peptide complexes .....	178
Figure 4.3   Backbone modifications decrease entropic cost of $Ca_V\beta_{2a}$ binding .....	179
Figure 4.4   Schematic of AID peptide competition experiment .....	180
Figure 4.5   AID-CAP affects $Ca_V1.2Y437A:Ca_V\beta_{2a}$ channels .....	181
Figure 4.6   $Ca_V1.2:Ca_V\beta_{2a}$ channels resist AID-CAP modulation.....	183
Figure 4.7   AID-CAP affects $Ca_V1.2:Ca_V\beta_3$ channels.....	185
Figure 4.8   S1 - Structures of $Ca_V\beta_{2a}$ :stapled peptide complexes. ....	187

## **List of Tables**

### **Chapter 2**

Table 2.1   Summary of K <sub>2P</sub> response to BL-1249 .....	75
Table 2.2   Summary of BL-1249 analogue activation of K <sub>2P</sub> 2.1 (TREK-1) and K <sub>2P</sub> 4.1 (TRAAK).....	76

### **Chapter 3**

Table 3.1   IC <sub>50</sub> values for RuR and Ru360 .....	132
Table 3.2   Supplementary table 1 - Data collection and refinement statistics.....	133
Table 3.3   Supplementary table 1 (ct'd) - Data collection and refinement statistics .....	134
Table 3.4   Supplementary table 2 - Structure Comparisons of RuR and Ru360 complexes .....	136

### **Chapter 4**

Table 4.1   AID peptide:Ca <sub>v</sub> β <sub>2a</sub> thermodynamic binding parameters .....	189
Table 4.2   Ca <sub>v</sub> 1.2 inactivation parameters and GV relationship .....	190
Table 4.3   Ca <sub>v</sub> 1.2 inactivation parameters and GV relationship (ct'd) .....	191
Table 4.4   Supplementary Table 1 - Crystallographic data collection and refinement statistics .....	193

## ***Chapter 1 : Introduction***

### ***K<sub>2P</sub> channels: pharmacological relevance and therapeutic potential***

Ion channels facilitate the flow of electricity in all neuronal processes, manifesting the physiology of thought, movement, mood and sensation<sup>1</sup>. In all organisms, a suite of ion channels controls cellular action and excitability and among these, potassium 'leak' channels are responsible for the setpoint and maintenance of cellular resting potential in between neuronal pulses (Figure 1.1A)<sup>2-4</sup>. Potassium (K<sup>+</sup>) ion channels with two-pore domains (K<sub>2P</sub>) are part of the voltage-gated ion channel (VGIC) superfamily<sup>5</sup> (Figure 1.1B) and are named K<sub>2P</sub> for their unique architecture, which distinguishes them amongst other K<sup>+</sup> channels, the largest and most diverse channel family (shaded red in figure).

K<sub>2P</sub> channels are distinct in many ways from classical potassium channels. K<sub>2P</sub>s feature a dimeric architecture, with one subunit bearing two pore-forming helical sequences (P1 and P2) flanked by four transmembrane helices, M1-M4 (Figure 1.2A, left)<sup>6</sup>. Other notable structural features of K<sub>2P</sub> channels include an extracellular cap (CAP) domain that is also absent in canonical K<sup>+</sup> channels. Each subunit bears sequences at both the N and C termini that are likely to be unstructured. The four pore helices (P1 and P2 from each subunit) combine to form a potassium selective filter capable of outward K<sup>+</sup> conduction in under most physiological membrane potentials (Figure 1.2A, right)<sup>7</sup>. In further contrast to canonical K<sup>+</sup> channels, K<sub>2P</sub> channels lack an inner gating bundle crossing and have been shown to gate exclusively through the selectivity filter 'C-type' gate<sup>8-12</sup>. Exogenous stimuli<sup>8,13</sup> are integrated through this common gating mechanism, finely tuning the cellular leak current to affect cellular excitability. In fact, such aptitude for external modulation is a defining feature of this unique channel class and is crucial to the function of these channels in a cellular context.

Since the first characterization of  $K_{2P}$  channels over twenty years prior<sup>7,14</sup>, fifteen mammalian  $K_{2P}$ s have been identified and grouped into six families according to sequence similarity and characteristic functional properties<sup>2,15</sup>. Despite sharing an overall similar topology, these families, including TWIK, TREK, TASK, THIK, TALK, and TRESK (Figure 1.2B), respond characteristically to a unique set of stimuli ranging widely from physical (external and internal pH, temperature, and mechanical stretch) to chemical (volatile anesthetics and anti-depressants, lipids, polyunsaturated fatty acids (PUFAs)) and can even be mediated by local protein-protein interactions (14-3-3, G-proteins, Protein Kinase A/C)<sup>3,16,17</sup>. Given such an important array of modalities, it is unsurprising that mis-regulation of  $K_{2P}$ s is often associated with disease, ranging from disorders of the nervous systems like migraine<sup>18</sup>, Birk-Barel syndrome<sup>19</sup>, ischemia<sup>20</sup> and facial gestalt<sup>21</sup> to disorders of cardiovascular systems resulting in arrhythmias<sup>22–26</sup> and hypertension<sup>27</sup>. Further biological and mechanistic study of these channels has been challenging due to their resistance to classical potassium channel blockers and general lack of specific chemical tools<sup>3,28–32</sup>. Despite their potential as therapeutic targets, there are no approved drugs which specifically target  $K_{2P}$ s. Combined with the need for further biological study, there is an urgent need for the development and characterization of novel,  $K_{2P}$ -specific modulators and a campaign for such molecules has begun in earnest.

### ***The TREK family: a model $K_{2P}$ system***

The most extensively studied  $K_{2P}$  family, the TREK subfamily is comprised of  $K_{2P}2.1$  (TREK-1),  $K_{2P}10.1$  (TREK-2) and  $K_{2P}4.1$  (TRAAK). These channels are thermo-, mechano-, and lipid sensitive and have been implicated as important therapeutic targets for pain, ischemia, and depression<sup>15,28,30,32,33</sup>. TREK family channels have evolved as

sensors for numerous physical and chemical stimuli, and their regulation by pH, temperature, stretch and lipids have been well characterized<sup>8,9,34,35</sup>. These channels are readily expressed in heterologous systems and their experimental adaptability has led to this family becoming an important model for understanding K<sub>2P</sub> channel biophysics and in realizing its pharmacological potential. TREK family channels have also been shown to heterodimerize<sup>36-38</sup>, forming channels with hybrid properties and increasing functional diversity in cells that express more than one type of K<sub>2P</sub> channel. Additionally, this class of K<sub>2P</sub> channels is the most structurally elucidated, with recent structures emerging of all three members in various states of activity<sup>39-44</sup>. With the clearest picture and robustness of functional characterization, this family has benefited the most in terms of the development of specific and potent chemical modulators<sup>45-48</sup>, the subject of which has been reviewed extensively<sup>3,17,49</sup>.

TREK family channels are found throughout the central nervous system, especially in the periphery (dorsal root ganglion<sup>50</sup>, nodes of Ranvier<sup>51,52</sup>), and are known to be regulated at both the transcriptional (via alternative translation initiation<sup>36,37,53,54</sup>) and translational (through post-translational modification<sup>3,17,55</sup>) levels. In terms of sequence similarity, K<sub>2P</sub>2.1 (TREK-1) and K<sub>2P</sub>10.1 (TREK-2) bear the highest similarity to each other (~65%)<sup>38,56-58</sup> and are only moderate similar to K<sub>2P</sub>4.1 (TRAAK) (~40%) – this similarity is also structurally obvious<sup>39-44</sup>. Despite their structural and functional similarities, TREK family channels differ in important ways and likely interact with different partners in distinct cellular and developmental contexts, especially at channel regions which differ greatly in sequence similarity, namely the N and C termini. Understanding and capitalizing on these



differences will continue to lead to the development of subtype specific chemical modulators for precision pharmacology.

Intriguingly, both activation and inhibition of TREK have been proposed as mechanisms for affecting distinct therapeutic outcomes. Activation of TREK channels drives the membrane potential closer to the equilibrium potential of  $K^+$ , resulting in reduced cellular excitability – this would likely have an antinociceptive effect in the periphery where many of these channels reside<sup>30</sup>. On the other side of the spectrum,  $K_{2P2.1}$  (TREK-1) knockout mice have been shown to be resistant to depression and  $K_{2P2.1}$  (TREK-1) inhibitors like spadin and norfluoxetine have shown some promising efficacy in mouse models for depression<sup>49,59,60</sup>. Pharmacologically relevant antipsychotics have also been reported to inhibit  $K_{2P2.1}$  (TREK-1). Physiologically, inhibiting  $K_{2P2.1}$  (TREK-1) would result in a less negative resting potential, but more work is needed to understand how the cellular consequences of inhibiting this channel can result in modulation of disease state.

### ***Discovering new chemical modulators of TREK channels***

TREK family channels are clearly interesting and novel targets for therapeutics, and as biologically important sensors, have a wide array of natural ligands and metabolites which are known to modulate channel activity. These natural ligands (lipids, volatile anesthetics) can be hard to work with *in vitro* and may be unadaptable between experimental systems, underscoring a need to generate new chemical matter to expand on our knowledge of  $K_{2P}$  modulation. In the development of new chemical modulators, many studies have modified natural effectors like caffeic acid to produce more potent

caffeate esters with more interesting and relevant pharmaceutical properties<sup>46,48</sup>. Spadin, although not a small-molecule, is a naturally derived peptide from the membrane protein Sortilin that has been suggested to have some efficacy in mouse models of depression<sup>49,59,60</sup>. Extensive work has been done to characterize the inhibitory effect of spadin on K<sub>2P</sub>2.1 (TREK-1), and effort has been made to improve the peptide scaffold to alter its *in vivo* efficacy and drug-like properties.

Given the potential therapeutic relevance, it is no surprise that researchers, especially pharmaceutical companies, have conducted a number of high throughput screens (HTS) resulting in chemical matter capable of targeting TREK family channels. At least a few of the known molecules affecting this family were results of screening campaigns, especially molecules like BL-1249<sup>61</sup> or ML335 and ML402<sup>42</sup>, which have industrial origins prior to their entry in the literature. Early efforts to screen in industry often relied on monitoring the phenotypic change of a disease-relevant cell-type<sup>61,62</sup>, especially since molecular targets were and continue to be challenging to isolate for screening.

The first example of one such campaign was the discovery of ML67 and ML45 series K<sub>2P</sub> modulators from a novel, yeast-based HTS platform<sup>45</sup>. In this assay, yeast were engineered such that survival (potassium transport) was linked to a K<sub>2P</sub> of interest, in this case K<sub>2P</sub>2.1 (TREK1). After screening a library of over 100,000 compounds, researchers identified both activators (ML67) and inhibitors (ML45) which were validated using electrophysiology and, in the case of ML67, improved using structure activity relationships (SAR) to ML67-33 (EC<sub>50</sub> = 36.3 ± 1 μM). Neither ML67 or ML45 class modulators display selectivity between the three TREK family members.

Other high-throughput screens against  $K_{2P}$ s have attempted to capitalize on ion flux as a readout for channel modulation, followed by electrophysiological validation after identification of hit compounds. Thallium and rubidium flux assays have been utilized in the channel field to identify new chemical matter<sup>63</sup> and in the context of  $K_{2P}$ s, such an assay has recently produced compounds with unique properties<sup>64</sup>. Dadi *et al* engineered a  $K_{2P2.1}$  (TREK-1) expressing cell-line and after screening over 76,000 compounds, report the discovery of several new activators and inhibitors, as well as new bioactive lipids like 11-deoxyprostaglandin  $F_{2\alpha}$  (11-deoxy  $PGF_{2\alpha}$ ). All of the inhibitors they identified were non-selective between  $K_{2P2.1}$  (TREK-1) and  $K_{2P10.1}$  (TREK-2), though authors do not report inhibition of  $K_{2P4.1}$  (TRAAK).

Su *et al* take a different approach to flux-based HTS, coupling  $K^+$  efflux to  $H^+$  influx, reported as fluorescence by a  $H^+$  binding dye in a cell-free system designed to produce binders to purified protein<sup>47</sup> reconstituted in liposomes. Using their liposome flux assay (LFA) platform, they screened 300,000 compounds and report two novel  $K_{2P4.1}$  (TRAAK) inhibitors that were subsequently validated using electrophysiology. Though the authors do not report using this platform to identify any  $K_{2P4.1}$  (TRAAK) activators, they did report new activator discovery for other  $K^+$  channels, demonstrating the adaptability of this high-throughput platform. TREK family selectivity of these two inhibitors is not reported, however these inhibitors do seem to be able to discriminate between at least a few more distantly related members of the mammalian  $K_{2P}$ s.

Broadly, all high throughput screening systems developed to identify TREK family modulators to date have yielded both activators and inhibitors, with wide selectivity and

efficacy profiles resulting from each screen. The obvious advantage of screening is the vast amount of chemical space that may be searched for new modulators, though electrophysiological validation is always necessary once hits have been identified. Attempts at virtual screening have shown some promise<sup>65</sup>, but are often limited to searching against known binding sites, precluding modulation through any channel state not crystallographically observed. As more molecules are identified, it will be important to characterize fully the selectivity and efficacies of these new molecules in order to unpack their unique molecular mechanisms, aiding improvement of these new molecules as potential therapies and tools for biological discovery.

### ***Pharmacological selectivity of TREK modulators, with structural perspectives***

Extensive reviews have been published on the subject of  $K_{2P}$  pharmacology<sup>3,30,32,49</sup>, up to and including a particularly thoughtful and thorough entry<sup>17</sup>, detailing broadly the important chemical modulators, with a particular focus on the molecular mechanisms governing  $K_{2P}$  modulation by small molecules. What has emerged as most relevant to this thesis, however, has been the study of small molecule selectivity between TREK family members, as such selectivity studies can shed light on key molecular differences in these closely related channels, ultimately leading to a more powerful chemical toolset for biological study and therapeutic discovery.

In general, small molecule selectivity between TREK family members is rare and limited to only a few classes of molecules (Figure 1.3). Many compound classes exhibit specificity for this mechanosensitive family but are not selective among them; examples include 2-APB<sup>66</sup>, ML67 and ML45<sup>45</sup>. Some compounds are weakly selective amongst

family members, indicating subtle differences in compound binding sites and presumably impaired propagation of signaling to the C-type gate. The fenamate class is one such example, whose principal member, BL-1249, is ~10-fold selective for K<sub>2P</sub>S2.1 (TREK-1) and 10.1 (TREK-2) over K<sub>2P</sub>4.1 (TRAAK) and seems to be able to very weakly activate more distantly related K<sub>2P</sub>S and potassium channels through a common mechanism<sup>67</sup>. In our study, we leveraged BL-1249's small window of selectivity between K<sub>2P</sub>2.1 (TREK-1) and K<sub>2P</sub>4.1 (TRAAK), shedding light on important differences between K<sub>2P</sub>2.1 (TREK-1) and K<sub>2P</sub>4.1 (TRAAK) leading to differential BL-1249 response, the results and discussions of which are detailed in chapter 2 of this thesis.

A detailed understanding of the molecular differences leading to subtype specificity in TREK family channels has been enabled largely by the few structures we have of compounds bound to various family members<sup>41-43</sup>. Perhaps the most compelling example of this is the selectivity of ML335 and ML402 for K<sub>2P</sub>S2.1 (TREK-1) and 10.1 (TREK-2) over K<sub>2P</sub>4.1 (TRAAK)<sup>42</sup>. This class of activators was found to stabilize the C-type gate by binding to a cryptic site not observed in the K<sub>2P</sub>2.1 (TREK-1) unbound state. Paired with the functional observation of activator selectivity between K<sub>2P</sub>2.1 (TREK-1) and K<sub>2P</sub>4.1 (TRAAK), structural analysis identified a key difference between the channels in the compound binding site, a lysine in K<sub>2P</sub>2.1 (TREK-1), involved in a key cation-pi interaction between the protein and the molecule. Mutation of the equivalent residue in K<sub>2P</sub>4.1 (TRAAK) (Q to K) renders the channel sensitive to ML335/402 while the K to Q mutation in K<sub>2P</sub>2.1 (TREK-1) kills activation response.

Generally, if a compound class displays selective properties, K<sub>2P</sub>4.1 (TRAAK) is found to be the odd channel out. This is consistent with the relatively low overall sequence homology between K<sub>2P</sub>2.1 (TREK-1) and 10.1 (TREK-2) versus K<sub>2P</sub>4.1 (TRAAK). In addition to the activator classes detailed above, there are a few classes of small molecules which are selective for K<sub>2P</sub>2.1 (TREK-1) and 10.1 (TREK-2) over K<sub>2P</sub>4.1 (TRAAK), including activators GI-530159<sup>68</sup> and natural product aristolochic acid<sup>69</sup>, and inhibitors like tricyclic antipsychotics<sup>70</sup> and fluoxetine/norfluoxetine, the latter of whose structure bound to K<sub>2P</sub>10.1 (TREK-2) established the 'fenestration' site as an important nexus that can be targeted for inhibition in K<sub>2P</sub>2.1 (TREK-1) and 10.1 (TREK-2)<sup>41</sup>. Additionally, recent structural studies indicate BL-1249 is also targeted to the fenestration site<sup>43</sup>, coordinating ion flow from below the selectivity filter, and establishing that both activators and inhibitors may share the same binding sites but can have opposite modes of regulation. Fenestration site selectivity in K<sub>2P</sub>2.1 (TREK-1) and 10.1 (TREK-2) over K<sub>2P</sub>4.1 (TRAAK) might also indicate that K<sub>2P</sub>4.1 (TRAAK) has a fenestration site which may be hard to target. Consequently, carefully targeting this structural difference might yield K<sub>2P</sub>4.1 (TRAAK)-specific modulators.

Rarer still are compound classes capable of discriminating between K<sub>2P</sub>2.1 (TREK-1) and K<sub>2P</sub>10.1 (TREK-2), likely because their high homology makes discrimination between these similar channels a challenging task. As mentioned previously, Dadi *et al* reported a series of inhibitors which could not discriminate between K<sub>2P</sub>2.1 (TREK-1) and K<sub>2P</sub>10.1 (TREK-2)<sup>64</sup>. However, in their screen the authors also identified activators which could discriminate between the two channels and were found to be selective for K<sub>2P</sub>10.1 (TREK-2) over K<sub>2P</sub>2.1 (TREK-1). Even more surprising, the

authors describe one activator T2A3 that seems capable of activating  $K_{2P}10.1$  (TREK-2) while simultaneously inhibiting  $K_{2P}2.1$  (TREK-1). Structural studies which aim to understand the molecular origin of this mode-switching behavior could uncover key differences between  $K_{2P}2.1$  (TREK-1) and 10.1 (TREK-2) that could be exploited for selectivity improvements.

Lastly,  $K_{2P}10.1$  (TREK-2) but not  $K_{2P}2.1$  (TREK-1) bears sensitivity to inhibition by ruthenium red (RuR). Other channels, outside the TREK subfamily, are also sensitive to RuR, including  $K_{2P}9.1$  (TASK-3). Through our own structural studies<sup>44</sup>, we have uncovered the molecular mechanisms governing this interaction using a  $K_{2P}2.1$  (TREK-1) channel bearing a mutation at the base of the CAP region of the channel, I110D. This mutation renders  $K_{2P}2.1$  (TREK-1) sensitive to RuR<sup>71</sup> and is natively an aspartate in  $K_{2P}10.1$  (TREK-2) and glutamate in  $K_{2P}9.1$  (TASK-3). This local negative charge positions ruthenium red in just the right position (deemed the 'keystone' inhibitor site) to provide an electrostatic block against outward flow of potassium.  $K_{2P}4.1$  (TRAAK) is also natively sensitive to RuR; however, the binding mode of RuR is likely different, as  $K_{2P}4.1$  (TRAAK) lacks this stabilizing negative charge at the base of its CAP region. Our studies, further detailed in chapter three, show that it is possible to coordinate ruthenium red in the keystone inhibitor site through the synthetic introduction of other local negative charge close to the keystone site. Future structural studies of  $K_{2P}4.1$  (TRAAK) in complex with RuR would help to fully clarify the mechanisms by which  $K_{2P}$ s are inhibited by RuR. Although  $K_{2P}4.1$  (TRAAK) was the first TREK family  $K_{2P}$  to be structurally characterized<sup>39</sup>, it remains the only channel in the family lacking any compound-bound structures.

### ***Modulation of protein-protein interactions – lessons from voltage-gated calcium channels (Cav)***

Like most ion channels, K<sub>2P</sub>s are known to interact with and are regulated by a wide array of cellular partners<sup>3,16,17</sup> and certain protein-protein interactions (PPIs) have been implicated as potential nodes of regulation, especially those involved in channel trafficking<sup>72,73</sup> and assembly<sup>37</sup>. Targeting PPI interfaces with small molecules can be challenging due to the large surfaces involved in protein-protein recognition and no therapies have yet been developed to specifically target these nodes in the context of K<sub>2P</sub>s or in any other type of channel. Voltage-gated calcium channels (Cav), distant relatives of K<sub>2P</sub> channels (highlighted blue, Figure 1.1B), have been used as a model for the development of channel PPI inhibitors<sup>74</sup> and the results from such studies are detailed in chapter four. By targeting the high affinity interaction of the pore-domain (Cav $\alpha$ ) and its cytosolic subunit (Cav $\beta$ ) via the  $\alpha$ -interaction domain (AID), stapled AID peptide mimetics are capable of disrupting transient interactions between Cav $\alpha$  and Cav $\beta$  in a  $\beta$  isoform-specific manner.

The development of these inhibitory peptides has only been possible due to the extensive characterization of this critical protein-protein interaction, involving functional, biophysical and structural characterization of the  $\beta$ -subunit in complex with the  $\alpha$ -subunit peptide derivatives<sup>74–79</sup>. Designing such regulators for K<sub>2P</sub> PPIs will require a similar level of characterization and the consequences of synthetically disrupting such interactions is, as of yet, completely unknown.



### ***Emergence of a poly-site model for $K_{2P}$ modulation – future directions***

With the availability of structural information, it has at last been possible to understand clearly and characterize molecular mechanisms of action for an initial set of small molecule modulators of TREK family  $K_{2P}$  channels. Though functional experiments have been important for establishing channel biophysics and the molecular mechanisms of polymodal stimulation, structure-function studies have enabled the precise enhancement of molecular interactions, providing a template for the improvement of each class of structurally characterized activator. What has emerged is a poly-site model of  $K_{2P}$  pharmacology (Figure 1.4), whereby  $K_{2P}$ s may be regulated by small molecules at least three sites, above (keystone), at the level of (cryptic pocket behind the filter) or below the selectivity filter (fenestration site). It should be noted, the modulatory lipid binding site of bioactive molecules like  $PIP_2$  has not yet been shown to be targetable by small molecules, but this may change as scientific interest and capacity for modulator screening grows. This picture remains incomplete but will resolve in time as more structural information becomes available. In particular, cryo-electron microscopy (cryo-EM) will enable the structural characterization of  $K_{2P}$  channels in complex with important cellular partners, information which has been lacking in  $K_{2P}$  crystallographic studies.

Future work aims to capitalize on the known modulator sites in the discovery of new chemical matter with the potential to utilize known sites as anchors for affecting function in novel and useful ways. Such molecules may be cleverly engineered to block or enhance various physical and chemical stimuli or even to chemically modify the channel for study in more complex cell types and tissues.

## References

- (1) Hille, B. *Ion Channels of Excitable Membranes*, 3rd ed. **2001**. Sinauer Associates, Inc.: Sunderland, MA.
- (2) Enyedi, P.; Czirják, G. Molecular Background of Leak K<sup>+</sup> Currents: Two-Pore Domain Potassium Channels. *Physiol. Rev.* **2010**, *90* (2), 559–605.
- (3) Feliciangeli, S.; Chatelain, F. C.; Bichet, D.; Lesage, F. The Family of K2P Channels: Salient Structural and Functional Properties. *J. Physiol.* **2015**, *593* (12), 2587–2603.
- (4) Lesage, F.; Barhanin, J. Molecular Physiology of PH-Sensitive Background K<sub>2P</sub> Channels. *Physiology* **2011**, *26* (6), 424–437.
- (5) Yu, F. H.; Yarov-Yarovoy, V.; Gutman, G. A.; Catterall, W. A. Overview of Molecular Relationships in the Voltage-Gated Ion Channel Superfamily. *Pharmacol. Rev.* **2005**, *57* (4), 387–395.
- (6) Goldstein, S. A. N.; Bayliss, D. A.; Kim, D.; Lesage, F.; Plant, L. D.; Rajan, S. International Union of Pharmacology. LV. Nomenclature and Molecular Relationships of Two-P Potassium Channels. *Pharmacol. Rev.* **2005**, *57* (4), 527–540.
- (7) Ketchum, K. A.; Joiner, W. J.; Sellers, A. J.; Kaczmarek, L. K.; Goldstein, S. A. N. A New Family of Outwardly Rectifying Potassium Channel Proteins with Two Pore Domains in Tandem. *Nature.* **1995**, *376* (6542), 690–695.
- (8) Bagriantsev, S. N.; Peyronnet, R.; Clark, K. A.; Honoré, E.; Minor, D. L. Multiple Modalities Converge on a Common Gate to Control K2P Channel Function. *EMBO J.* **2011**, *30* (17), 3594–3606.

- (9) Bagriantsev, S. N.; Clark, K. A.; Minor, D. L. Metabolic and Thermal Stimuli Control K2P2.1 (TREK-1) through Modular Sensory and Gating Domains. *EMBO J.* **2012**, *31* (15), 3297–3308.
- (10) Schewe, M.; Nematian-Ardestani, E.; Sun, H.; Musinszki, M.; Cordeiro, S.; Bucci, G.; de Groot, B. L.; Tucker, S. J.; Rapedius, M.; Baukrowitz, T. A Non-Canonical Voltage-Sensing Mechanism Controls Gating in K2P K<sup>+</sup> Channels. *Cell.* **2016**, *164* (5), 937–949.
- (11) Piechotta, P. L.; Rapedius, M.; Stansfeld, P. J.; Bollepalli, M. K.; Erlich, G.; Andres-Enguix, I.; Fritzenschaft, H.; Decher, N.; Sansom, M. S. P.; Tucker, S. J.; et al. The Pore Structure and Gating Mechanism of K2P Channels. *EMBO J.* **2011**, *30* (17), 3607–3619.
- (12) Cohen, A.; Ben-Abu, Y.; Hen, S.; Zilberberg, N. A Novel Mechanism for Human K2P2.1 Channel Gating - Facilitation of C-type Gating by Protonation of Extracellular Histidine Residues. *J. Biol. Chem.* **2008**, *283* (28), 19448–19455.
- (13) McClenaghan, C.; Schewe, M.; Aryal, P.; Carpenter, E. P.; Baukrowitz, T.; Tucker, S. J. Polymodal Activation of the TREK-2 K2P Channel Produces Structurally Distinct Open States. *J. Gen. Physiol.* **2016**, *147* (6), 497–505.
- (14) Lesage, F.; Guillemare, E.; Fink, M.; Duprat, F.; Lazdunski, M.; Romey, G.; Barhanin, J. TWIK-1, a Ubiquitous Human Weakly Inward Rectifying K<sup>+</sup> Channel with a Novel Structure. *EMBO J.* **1996**, *15* (5), 1004–1011.
- (15) Honoré, E. The Neuronal Background K<sup>+</sup> 2P Channels: Focus on TREK1. *Nat. Rev. Neurosci.* **2007**, *8* (4), 251–261.

- (16) Mathie, A.; Al-Moubarak, E.; Veale, E. L. SYMPOSIUM REVIEW: Gating of Two Pore Domain Potassium Channels: Gating of K2P Channels. *J. Physiol.* **2010**, *588* (17), 3149–3156.
- (17) Șterbuleac, D. Molecular Determinants of Chemical Modulation of Two-Pore Domain Potassium Channels. *Chem. Biol. Drug Des.* **2019**, *94* (3), 1596–1614.
- (18) Lafrenière, R. G.; Cader, M. Z.; Poulin, J.-F.; Andres-Enguix, I.; Simoneau, M.; Gupta, N.; Boisvert, K.; Lafrenière, F.; McLaughlan, S.; Dubé, M.-P.; et al. A Dominant-Negative Mutation in the TRESK Potassium Channel Is Linked to Familial Migraine with Aura. *Nat. Med.* **2010**, *16* (10), 1157–1160.
- (19) Barel, O.; Shalev, S. A.; Ofir, R.; Cohen, A.; Zlotogora, J.; Shorer, Z.; Mazor, G.; Finer, G.; Khateeb, S.; Zilberberg, N.; et al. Maternally Inherited Birk Barel Mental Retardation Dysmorphism Syndrome Caused by a Mutation in the Genomically Imprinted Potassium Channel KCNK9. *Am. J. Hum. Genet.* **2008**, *83* (2), 193–199.
- (20) Bayliss, D. A.; Barrett, P. Q. Emerging Roles for Two-Pore-Domain Potassium Channels and Their Potential Therapeutic Impact. *Trends Pharmacol. Sci.* **2008**, *29* (11), 566–575.
- (21) Bauer, C. K.; Calligari, P.; Radio, F. C.; Caputo, V.; Dentici, M. L.; Falah, N.; High, F.; Pantaleoni, F.; Barresi, S.; Ciolfi, A.; et al. Mutations in KCNK4 That Affect Gating Cause a Recognizable Neurodevelopmental Syndrome. *Am. J. Hum. Genet.* **2018**, *103* (4), 621–630.
- (22) Decher, N.; Ortiz-Bonnin, B.; Friedrich, C.; Schewe, M.; Kiper, A. K.; Rinné, S.; Seemann, G.; Peyronnet, R.; Zumhagen, S.; Bustos, D.; et al. Sodium Permeable

- and “Hypersensitive” TREK-1 Channels Cause Ventricular Tachycardia. *EMBO Mol. Med.* **2017**, 9 (4), 403–414.
- (23) Friedrich, C.; Rinné, S.; Zumhagen, S.; Kiper, A. K.; Silbernagel, N.; Netter, M. F.; Stallmeyer, B.; Schulze-Bahr, E.; Decher, N. Gain-of-Function Mutation in TASK-4 Channels and Severe Cardiac Conduction Disorder. *EMBO Mol. Med.* **2014**, 6 (7), 937–951.
- (24) Liang, B.; Soka, M.; Christensen, A. H.; Olesen, M. S.; Larsen, A. P.; Knop, F. K.; Wang, F.; Nielsen, J. B.; Andersen, M. N.; Humphreys, D.; et al. Genetic Variation in the Two-Pore Domain Potassium Channel, TASK-1, May Contribute to an Atrial Substrate for Arrhythmogenesis. *J. Mol. Cell. Cardiol.* **2014**, 67, 69–76.
- (25) Ma, L.; Zhang, X.; Zhou, M.; Chen, H. Acid-Sensitive TWIK and TASK Two-Pore Domain Potassium Channels Change Ion Selectivity and Become Permeable to Sodium in Extracellular Acidification. *J. Biol. Chem.* **2012**, 287 (44), 37145–37153.
- (26) Ma, L.; Zhang, X.; Chen, H. TWIK-1 Two-Pore Domain Potassium Channels Change Ion Selectivity and Conduct Inward Leak Sodium Currents in Hypokalemia. *Sci. Signal.* **2011**, 4 (176), ra37–ra37.
- (27) Ma, L.; Roman-Campos, D.; Austin, E. D.; Eyries, M.; Sampson, K. S.; Soubrier, F.; Germain, M.; Trégouët, D.-A.; Borczuk, A.; Rosenzweig, E. B.; et al. A Novel Channelopathy in Pulmonary Arterial Hypertension. *NEJM.* **2013**, 369, 351-361.
- (28) Bagal, S. K.; Brown, A. D.; Cox, P. J.; Omoto, K.; Owen, R. M.; Pryde, D. C.; Sidders, B.; Skerratt, S. E.; Stevens, E. B.; Storer, R. I.; et al. Ion Channels as Therapeutic Targets: A Drug Discovery Perspective. *J. Med. Chem.* **2013**, 56 (3), 593–624.

- (29) Lotshaw, D. P. Biophysical, Pharmacological, and Functional Characteristics of Cloned and Native Mammalian Two-Pore Domain K<sup>+</sup> Channels. *Cell Biochem. Biophys.* **2007**, *47* (2), 209–256.
- (30) Mathie, A.; Veale, E. L. Two-Pore Domain Potassium Channels: Potential Therapeutic Targets for the Treatment of Pain. *Pflüg. Arch. Eur. J. Physiol.* **2015**, *467* (5), 931–943.
- (31) Vivier, D.; Bennis, K.; Lesage, F.; Ducki, S. Perspectives on the Two-Pore Domain Potassium Channel TREK-1 (TWIK-Related K<sup>+</sup> Channel 1). A Novel Therapeutic Target? *J. Med. Chem.* **2016**, *59* (11), 5149–5157.
- (32) Es-Salah-Lamoureux, Z.; Steele, D. F.; Fedida, D. Research into the Therapeutic Roles of Two-Pore-Domain Potassium Channels. *Trends Pharmacol. Sci.* **2010**, *31* (12), 587–595.
- (33) Waxman, S. G.; Zamponi, G. W. Regulating Excitability of Peripheral Afferents: Emerging Ion Channel Targets. *Nat. Neurosci.* **2014**, *17* (2), 153–163.
- (34) Chemin, J.; Patel, A. J.; Duprat, F.; Lauritzen, I.; Lazdunski, M.; Honoré, E. A Phospholipid Sensor Controls Mechanogating of the K<sup>+</sup> Channel TREK-1. *EMBO J.* **2005**, *24* (1), 44–53.
- (35) Brohawn, S. G.; Su, Z.; MacKinnon, R. Mechanosensitivity Is Mediated Directly by the Lipid Membrane in TRAAK and TREK1 K<sup>+</sup> Channels. *Proc. Natl. Acad. Sci.* **2014**, *111* (9), 3614–3619.
- (36) Blin, S.; Ben Soussia, I.; Kim, E.-J.; Brau, F.; Kang, D.; Lesage, F.; Bichet, D. Mixing and Matching TREK/TRAAK Subunits Generate Heterodimeric K<sub>2P</sub>

- Channels with Unique Properties. *Proc. Natl. Acad. Sci.* **2016**, *113* (15), 4200–4205.
- (37) Royal, P.; Andres-Bilbe, A.; Prado, P. Á.; Verkest, C.; Wdziekonski, B.; Schaub, S.; Baron, A.; Lesage, F.; Gasull, X.; Levitz, J.; et al. Migraine-Associated TRESK Mutations Increase Neuronal Excitability through Alternative Translation Initiation and Inhibition of TREK. *Neuron*. **2019**, *101* (2), 232-245.e6.
- (38) Levitz, J.; Royal, P.; Comoglio, Y.; Wdziekonski, B.; Schaub, S.; Clemens, D. M.; Isacoff, E. Y.; Sandoz, G. Heterodimerization within the TREK Channel Subfamily Produces a Diverse Family of Highly Regulated Potassium Channels. *Proc. Natl. Acad. Sci.* **2016**, *113* (15), 4194–4199.
- (39) Brohawn, S. G.; Mármol, J. del; MacKinnon, R. Crystal Structure of the Human K2P TRAAK, a Lipid- and Mechano-Sensitive K<sup>+</sup> Ion Channel. *Science*. **2012**, *335* (6067), 436–441.
- (40) Lolicato, M.; Riegelhaupt, P. M.; Arrigoni, C.; Clark, K. A.; Minor, D. L. Transmembrane Helix Straightening and Buckling Underlies Activation of Mechanosensitive and Thermosensitive K2P Channels. *Neuron*. **2014**, *84* (6), 1198–1212.
- (41) Dong, Y. Y.; Pike, A. C. W.; Mackenzie, A.; McClenaghan, C.; Aryal, P.; Dong, L.; Quigley, A.; Grieben, M.; Goubin, S.; Mukhopadhyay, S.; et al. K2P Channel Gating Mechanisms Revealed by Structures of TREK-2 and a Complex with Prozac. *Science*. **2015**, *347* (6227), 1256–1259.

- (42) Lolicato, M.; Arrigoni, C.; Mori, T.; Sekioka, Y.; Bryant, C.; Clark, K. A.; Jr, D. L. M. K<sub>2</sub>P2.1 (TREK-1)–Activator Complexes Reveal a Cryptic Selectivity Filter Binding Site. *Nature*. **2017**, *547* (7663), 364–368.
- (43) Schewe, M.; Sun, H.; Mert, Ü.; Mackenzie, A.; Pike, A. C. W.; Schulz, F.; Constantin, C.; Vowinkel, K. S.; Conrad, L. J.; Kiper, A. K.; et al. A Pharmacological Master Key Mechanism That Unlocks the Selectivity Filter Gate in K<sup>+</sup> Channels. *Science*. **2019**, *363* (6429), 875–880.
- (44) Pope, L.; Lolicato, M.; Minor, D. L. Polynuclear Ruthenium Amines Inhibit K<sub>2</sub>P Channels via a ‘Finger in the Dam’ Mechanism. *bioRxiv*. **2019**, 863837.
- (45) Bagriantsev, S. N.; Ang, K.-H.; Gallardo-Godoy, A.; Clark, K. A.; Arkin, M. R.; Renslo, A. R.; Minor, D. L. A High-Throughput Functional Screen Identifies Small Molecule Regulators of Temperature- and Mechano-Sensitive K<sub>2</sub>P Channels. *ACS Chem. Biol.* **2013**, *8* (8), 1841–1851.
- (46) Vivier, D.; Soussia, I. B.; Rodrigues, N.; Lolignier, S.; Devilliers, M.; Chatelain, F. C.; Prival, L.; Chapuy, E.; Bourdier, G.; Bennis, K.; et al. Development of the First Two-Pore Domain Potassium Channel TWIK-Related K<sup>+</sup> Channel 1-Selective Agonist Possessing in Vivo Antinociceptive Activity. *J. Med. Chem.* **2017**, *60* (3), 1076–1088.
- (47) Su, Z.; Brown, E. C.; Wang, W.; MacKinnon, R. Novel Cell-Free High-Throughput Screening Method for Pharmacological Tools Targeting K<sup>+</sup> Channels. *Proc. Natl. Acad. Sci.* **2016**, *113* (20), 5748–5753.
- (48) Rodrigues, N.; Bennis, K.; Vivier, D.; Pereira, V.; C. Chatelain, F.; Chapuy, E.; Deokar, H.; Busserolles, J.; Lesage, F.; Eschalier, A.; et al. Synthesis and



- Structure–Activity Relationship Study of Substituted Caffeeate Esters as Antinociceptive Agents Modulating the TREK-1 Channel. *Eur. J. Med. Chem.* **2014**, *75*, 391–402.
- (49) Djillani, A.; Mazella, J.; Heurteaux, C.; Borsotto, M. Role of TREK-1 in Health and Disease, Focus on the Central Nervous System. *Front. Pharmacol.* **2019**, *10*.
- (50) Viatchenko-Karpinski, V.; Ling, J.; Gu, J. G. Characterization of Temperature-Sensitive Leak K<sup>+</sup> Currents and Expression of TRAAK, TREK-1, and TREK2 Channels in Dorsal Root Ganglion Neurons of Rats. *Mol. Brain* **2018**, *11* (1), 40.
- (51) Brohawn, S. G.; Wang, W.; Handler, A.; Campbell, E. B.; Schwarz, J. R.; MacKinnon, R. The Mechanosensitive Ion Channel TRAAK Is Localized to the Mammalian Node of Ranvier. *eLife*. **2019**, *8*, e50403.
- (52) Kanda, H.; Ling, J.; Tonomura, S.; Noguchi, K.; Matalon, S.; Gu, J. G. TREK-1 and TRAAK Are Principal K<sup>+</sup> Channels at the Nodes of Ranvier for Rapid Action Potential Conduction on Mammalian Myelinated Afferent Nerves. *Neuron*. **2019**, *104* (5), 960-971.e7.
- (53) Veale, E. L.; Al-Moubarak, E.; Bajaria, N.; Omoto, K.; Cao, L.; Tucker, S. J.; Stevens, E. B.; Mathie, A. Influence of the N Terminus on the Biophysical Properties and Pharmacology of TREK1 Potassium Channels. *Mol. Pharmacol.* **2014**, *85* (5), 671–681.
- (54) Kisselbach, J.; Seyler, C.; Schweizer, P. A.; Gerstberger, R.; Becker, R.; Katus, H. A.; Thomas, D. Modulation of K2P2.1 and K2P10.1 K<sup>+</sup> Channel Sensitivity to Carvedilol by Alternative mRNA Translation Initiation. *Br. J. Pharmacol.* **2014**, *171* (23), 5182–5194.

- (55) Plant, L. D.; Rajan, S.; Goldstein, S. A. K2P Channels and Their Protein Partners. *Curr. Opin. Neurobiol.* **2005**, *15* (3), 326–333.
- (56) Fink, M.; Duprat, F.; Lesage, F.; Reyes, R.; Romey, G.; Heurteaux, C.; Lazdunski, M. Cloning, Functional Expression and Brain Localization of a Novel Unconventional Outward Rectifier K<sup>+</sup> Channel. *EMBO J.* **1996**, *15* (24), 6854–6862.
- (57) Bang, H.; Kim, Y.; Kim, D. TREK-2, a New Member of the Mechanosensitive Tandem-Pore K<sup>+</sup> Channel Family. *J. Biol. Chem.* **2000**, *275* (23), 17412–17419.
- (58) Lesage, F.; Terrenoire, C.; Romey, G.; Lazdunski, M. Human TREK2, a 2P Domain Mechano-Sensitive K<sup>+</sup>Channel with Multiple Regulations by Polyunsaturated Fatty Acids, Lysophospholipids, and Gs, Gi, and Gq Protein-Coupled Receptors. *J. Biol. Chem.* **2000**, *275* (37), 28398–28405.
- (59) Djillani, A.; Pietri, M.; Moreno, S.; Heurteaux, C.; Mazella, J.; Borsotto, M. Shortened Spadin Analogs Display Better TREK-1 Inhibition, In Vivo Stability and Antidepressant Activity. *Front. Pharmacol.* **2017**, *8*.
- (60) Djillani, A.; Pietri, M.; Mazella, J.; Heurteaux, C.; Borsotto, M. Fighting against Depression with TREK-1 Blockers: Past and Future. A Focus on Spadin. *Pharmacol. Ther.* **2019**, *194*, 185–198.
- (61) Tertysnikova, S. BL-1249 [(5,6,7,8-Tetrahydro-Naphthalen-1-Yl)-[2-(1H-Tetrazol-5-Yl)-Phenyl]-Amine]: A Putative Potassium Channel Opener with Bladder-Relaxant Properties. *J. Pharmacol. Exp. Ther.* **2004**, *313* (1), 250–259.
- (62) Whiteaker, K. L.; Gopalakrishnan, S. M.; Groebe, D.; Shieh, C.-C.; Warrior, U.; Burns, D. J.; Coghlan, M. J.; Scott, V. E.; Gopalakrishnani, M. Validation of FLIPR

- Membrane Potential Dye for High Throughput Screening of Potassium Channel Modulators. *J. Biomol. Screen.* **2001**, 6 (5), 305–312.
- (63) Yu, H.; Li, M.; Wang, W.; Wang, X. High Throughput Screening Technologies for Ion Channels. *Acta Pharmacol. Sin.* **2016**, 37 (1), 34–43.
- (64) Dadi, P. K.; Vierra, N. C.; Days, E.; Dickerson, M. T.; Vinson, P. N.; Weaver, C. D.; Jacobson, D. A. Selective Small Molecule Activators of TREK-2 Channels Stimulate Dorsal Root Ganglion c-Fiber Nociceptor Two-Pore-Domain Potassium Channel Currents and Limit Calcium Influx. *ACS Chem. Neurosci.* **2017**, 8 (3), 558–568.
- (65) Luo, Q.; Chen, L.; Cheng, X.; Ma, Y.; Li, X.; Zhang, B.; Li, L.; Zhang, S.; Guo, F.; Li, Y.; et al. An Allosteric Ligand-Binding Site in the Extracellular Cap of K2P Channels. *Nat. Commun.* **2017**, 8 (1).
- (66) Beltrán, L.; Beltrán, M.; Aguado, A.; Gisselmann, G.; Hatt, H. 2-Aminoethoxydiphenyl Borate Activates the Mechanically Gated Human KCNK Channels KCNK 2 (TREK-1), KCNK 4 (TRAAK), and KCNK 10 (TREK-2). *Front. Pharmacol.* **2013**, 4.
- (67) Pope, L.; Arrigoni, C.; Lou, H.; Bryant, C.; Gallardo-Godoy, A.; Renslo, A. R.; Minor, D. L. Protein and Chemical Determinants of BL-1249 Action and Selectivity for K2P Channels. *ACS Chem. Neurosci.* **2018**, 9 (12), 3153-3165.
- (68) Loucif Alexandre J C; Saintot Pierre-Philippe; Liu Jia; Antonio Brett M; Zellmer Shannon G; Yoger Katrina; Veale Emma L; Wilbrey Anna; Omoto Kiyoyuki; Cao Lishuang; et al. GI-530159, a Novel, Selective, Mechanosensitive Two-pore-

- domain Potassium (K<sub>2</sub>P) Channel Opener, Reduces Rat Dorsal Root Ganglion Neuron Excitability. *Br. J. Pharmacol.* **2017**, *175* (12), 2272-2283.
- (69) Veale, E. L.; Mathie, A. Aristolochic Acid, a Plant Extract Used in the Treatment of Pain and Linked to Balkan Endemic Nephropathy, Is a Regulator of K<sub>2</sub>P Channels: Regulation of K<sub>2</sub>P Channels by Aristolochic Acid. *Br. J. Pharmacol.* **2016**, *173* (10), 1639–1652.
- (70) Thümmeler, S.; Duprat, F.; Lazdunski, M. Antipsychotics Inhibit TREK but Not TRAAK Channels. *Biochem. Biophys. Res. Commun.* **2007**, *354* (1), 284–289.
- (71) Braun, G.; Lengyel, M.; Enyedi, P.; Czirják, G. Differential Sensitivity of TREK-1, TREK-2 and TRAAK Background Potassium Channels to the Polycationic Dye Ruthenium Red: Sensitivity of K<sub>2</sub>P Channels to Ruthenium Red. *Br. J. Pharmacol.* **2015**, *172* (7), 1728–1738.
- (72) Kilisch, M.; Lytovchenko, O.; Schwappach, B.; Renigunta, V.; Daut, J. The Role of Protein–Protein Interactions in the Intracellular Traffic of the Potassium Channels TASK-1 and TASK-3. *Pflüg. Arch. - Eur. J. Physiol.* **2015**, *467* (5), 1105–1120.
- (73) Kasap, M.; Dwyer, D. S. Chapter 20 - Two-Pore Domain Potassium Channels (K<sub>2</sub>Ps) as Drug Targets in Neuroinflammation. In *Neuroinflammation (Second Edition)*; Minagar, A., Ed.; Academic Press, **2018**; pp 413–427.
- (74) Findeisen, F.; Campiglio, M.; Jo, H.; Abderemane-Ali, F.; Rumpf, C. H.; Pope, L.; Rossen, N. D.; Flucher, B. E.; DeGrado, W. F.; Minor, D. L. Stapled Voltage-Gated Calcium Channel (CaV)  $\alpha$ -Interaction Domain (AID) Peptides Act As Selective Protein–Protein Interaction Inhibitors of CaV Function. *ACS Chem. Neurosci.* **2017**, *8* (6), 1313–1326.

- (75) Petegem, F. V.; Clark, K. A.; Chatelain, F. C.; Minor, D. L. Structure of a Complex between a Voltage-Gated Calcium Channel  $\beta$ -Subunit and an  $\alpha$ -Subunit Domain. *Nature*. **2004**, 429 (6992), 671–675.
- (76) Opatowsky, Y.; Chen, C.-C.; Campbell, K. P.; Hirsch, J. A. Structural Analysis of the Voltage-Dependent Calcium Channel  $\beta$  Subunit Functional Core and Its Complex with the A1 Interaction Domain. *Neuron*. **2004**, 42 (3), 387–399.
- (77) Chen, Y.; Li, M.; Zhang, Y.; He, L.; Yamada, Y.; Fitzmaurice, A.; Shen, Y.; Zhang, H.; Tong, L.; Yang, J. Structural Basis of the  $\alpha 1$  – $\beta$  Subunit Interaction of Voltage-Gated Ca<sup>2+</sup> Channels. *Nature*. **2004**, 429 (6992), 675–680.
- (78) Petegem, F. V.; Duderstadt, K. E.; Clark, K. A.; Wang, M.; Minor, D. L. Alanine-Scanning Mutagenesis Defines a Conserved Energetic Hotspot in the CaV $\alpha$ 1 AID-CaV $\beta$  Interaction Site That Is Critical for Channel Modulation. *Structure*. **2008**, 16 (2), 280–294.
- (79) Findeisen, F.; Minor, Jr., D. L. Progress in the Structural Understanding of Voltage-Gated Calcium Channel (Ca<sub>v</sub>) Function and Modulation. *Channels*. **2010**, 4 (6), 459–474.
- (80) What is an action potential?  
<https://www.moleculardevices.com/applications/patch-clamp-electrophysiology/what-action-potential> (accessed Dec 10, 2019).
- (81) Ion channel families | IUPHAR/BPS Guide to PHARMACOLOGY  
<https://www.guidetopharmacology.org/GRAC/ReceptorFamiliesForward?type=IC> (accessed Dec 10, 2019).

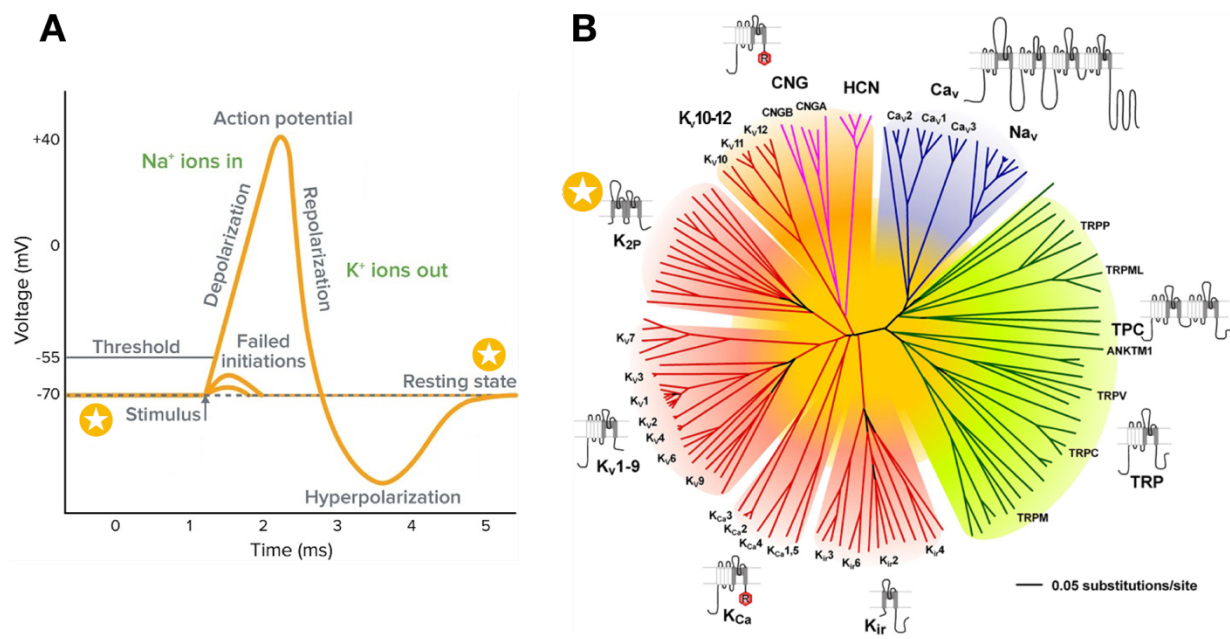


**Figure 1.1 | A suite of ion channels controls the action potential**

**A** Typical action potential, with each stage controlled by unique ion channels. K<sub>2P</sub> channels control the resting potential (starred) – figure adapted from Molecular Devices<sup>80</sup>  
**B** Dendrogram of voltage-gated ion channels (VGIC), with potassium channels shaded in red. K<sub>2P</sub> channels are denoted by star. Figure adapted from Guide to Pharmacology<sup>81</sup>

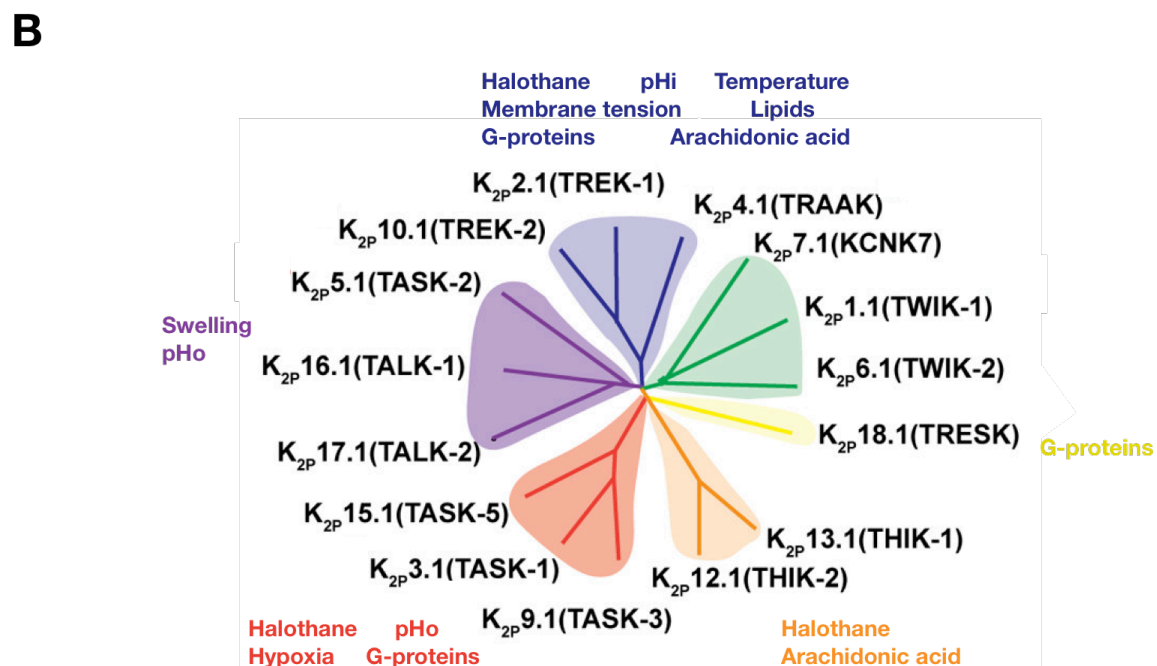
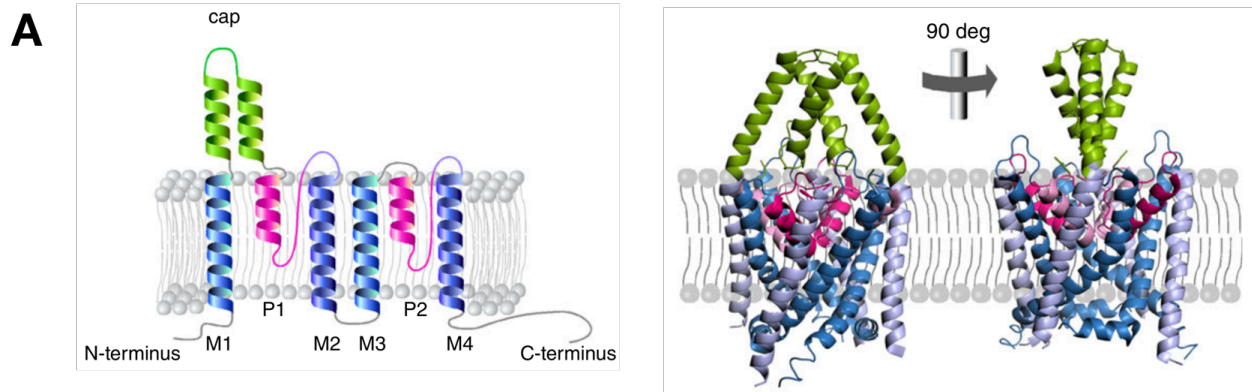


**Figure 1.2 | K<sub>2P</sub> channels are grouped according to structure and function**

**A** Diagram of K<sub>2P</sub> channel embedded in a membrane. One subunit is shown on the left. Extracellular CAP region shown in green. Helices M1-M4 (blue and purple) are separated by two pore domains P1 and P2, (pink). Dimer is depicted on the right. Figure adapted from Feliciangeli, 2014<sup>3</sup>. **B** K<sub>2P</sub> dendrogram. Families are grouped according to common stimuli and sequence similarity.

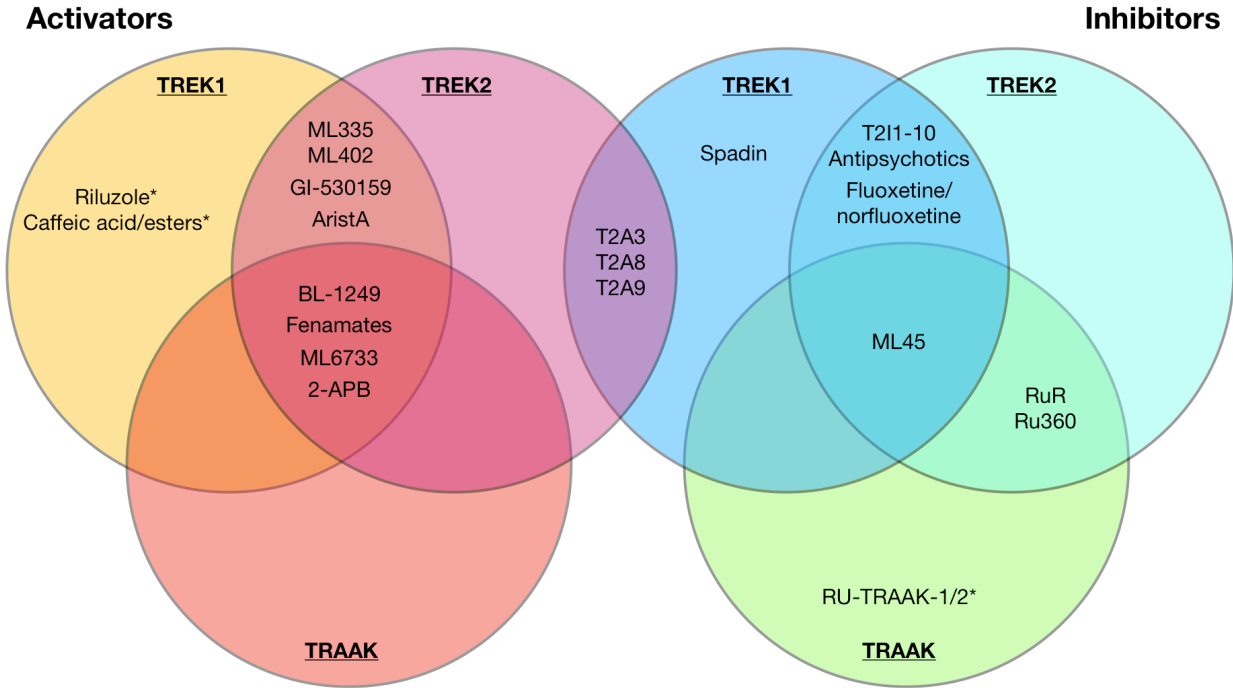


**Figure 1.3 | Selectivity profiles of small molecule modulators of TREK channels**

Small molecules reported to affect TREK family channels are grouped according to their ability to discriminate between channels (indicated in bold). Asterisks indicate report of selectivity without complete electrophysiological characterization.



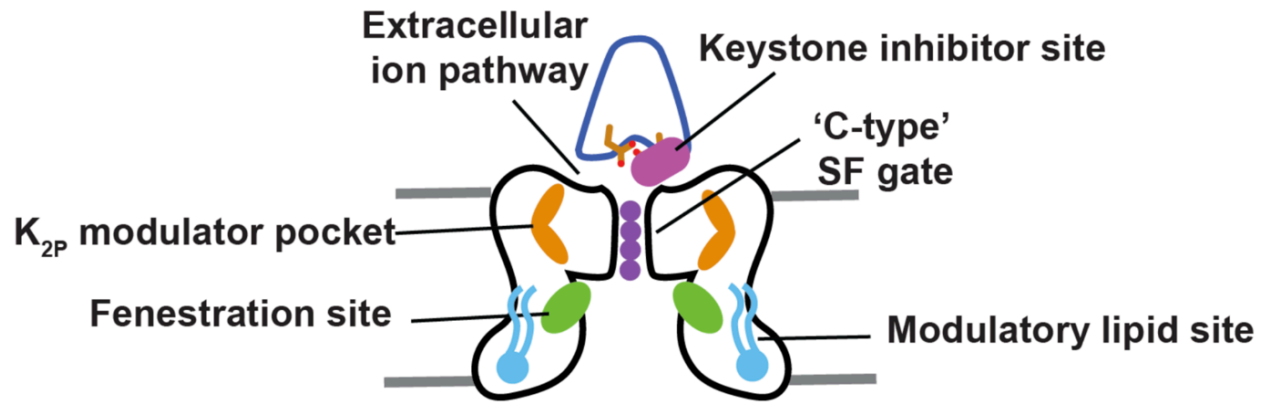


**Figure 1.4 | Unified model for  $K_{2P}$  poly-site pharmacology**

Cartoon of  $K_{2P}$  channel showing all structurally defined small molecule binding sites centered around the 'C-type' gate  $K^+$  ions (purple), including Keystone inhibitor site (maroon),  $K_{2P}$  modulator pocket (orange), fenestration site (green) and modulatory lipid site (light blue)

***Chapter 2 : Protein and chemical determinants of BL-1249 action and selectivity***

Lianne Pope, Cristina Arrigoni, Hubing Lou, Clifford Bryant, Adam R. Renslo, and

Daniel L. Minor, Jr.

## **Abstract**

K<sub>2P</sub> potassium channels generate leak currents that stabilize the resting membrane potential of excitable cells. Various K<sub>2P</sub>s are implicated in pain, ischemia, depression, migraine, and anesthetic responses, making this family an attractive target for small molecule modulator development efforts. BL-1249, a compound from the fenamate class of non-steroidal anti-inflammatory drugs is known to activate K<sub>2P</sub>2.1 (TREK-1), the founding member of the thermo- and mechanosensitive TREK subfamily; however, its mechanism of action and effects on other K<sub>2P</sub>s are not well-defined. Here, we demonstrate that BL-1249 extracellular application activates all TREK subfamily members but has no effect on other K<sub>2P</sub> subfamilies. Patch clamp experiments demonstrate that, similar to the diverse range of other chemical and physical TREK subfamily gating cues, BL-1249 stimulates the selectivity filter 'C-type' gate that controls K<sub>2P</sub> function. BL-1249 displays selectivity among the TREK subfamily, activating K<sub>2P</sub>2.1 (TREK-1) and K<sub>2P</sub>10.1 (TREK-2) ~10-fold more potently than K<sub>2P</sub>4.1 (TRAAK). Investigation of mutants and K<sub>2P</sub>2.1 (TREK-1)/ K<sub>2P</sub>4.1 (TRAAK) chimeras highlight the key roles of the C-terminal tail in BL-1249 action and identify the M2/M3 transmembrane helix interface as a key site of BL-1249 selectivity. Synthesis and characterization of a set of BL-1249 analogs demonstrates that both the tetrazole and opposing tetralin moieties are critical for function, whereas the conformational mobility between the two ring systems impacts selectivity. Together, our findings underscore the landscape of modes by which small molecules can affect K<sub>2P</sub>s and provide crucial information for the development of better and more selective K<sub>2P</sub> modulators of the TREK subfamily.

## **Introduction**

K<sub>2P</sub> (KCNK) potassium channels are members of the voltage-gated ion channel (VGIC) superfamily, make ‘background’ or ‘leak’ potassium channels that are responsible for the maintenance of cellular resting potential, and play an important role in regulating cellular excitability<sup>1-3</sup>. There are fifteen K<sub>2P</sub> subtypes that form six functionally distinct subfamilies. All K<sub>2P</sub>s comprise a dimer of subunits that each bear four transmembrane helices and two selectivity filter sequences<sup>1, 4-7</sup>. In contrast to other VGIC superfamily members, the K<sub>2P</sub> channel selectivity filter forms the principle gate that controls channel function, known as the ‘C-type gate’, rather than an intracellular barrier formed by the pore-lining helices<sup>6, 8-12</sup>. The activity of various K<sub>2P</sub> subtypes has been linked to a variety of physiological and pathological processes including pain<sup>13-15</sup>, anesthetic responses<sup>16, 17</sup>, arrhythmia<sup>18</sup>, ischemia<sup>16, 19, 20</sup>, depression<sup>21</sup>, and migraine<sup>22, 23</sup>. Yet, despite these biological links, a paucity of K<sub>2P</sub>-selective small molecule modulators has limited mechanistic and physiological studies<sup>1, 24, 25</sup>. Recent advances demonstrate that it is possible to develop subtype-selective K<sub>2P</sub> small molecule modulators<sup>6, 14, 26-30</sup>. Such compounds and the knowledge of how they engage K<sub>2P</sub>s to modulate function open a path towards elaborating new K<sub>2P</sub>-specific pharmacological tools that can enlighten channel gating mechanisms and that have potential to provide new leads for issues such as pain and ischemia<sup>25, 31, 32</sup>.

The TREK K<sub>2P</sub> subfamily, comprising K<sub>2P</sub>2.1 (TREK-1), K<sub>2P</sub>10.1 (TREK-2), and K<sub>2P</sub>4.1 (TRAAK), is regulated by diverse inputs that include temperature, stretch, pH, and lipids<sup>1-3</sup>, and stands out as the most structurally elucidated K<sub>2P</sub> subfamily<sup>4, 6, 7, 33-35</sup>. TREK subfamily structures include examples of both inhibitor:channel<sup>7</sup> and activator:channel

complexes<sup>6</sup> that highlight two points of control that can be influenced by small molecules: the transmembrane helices<sup>7</sup> and the K<sub>2P</sub> modulator pocket<sup>6</sup>. Although these examples show how a small molecule can engage with the K<sub>2P</sub> channel architecture to impact function, whether other reported TREK activators<sup>14, 26, 28, 36</sup> act via the transmembrane domains, the K<sub>2P</sub> modulator pocket, or affect other K<sub>2P</sub> channel elements remains to be elaborated.

Although not selective for K<sub>2P</sub>s, a number of fenamates, substituted derivatives of anthranilic acid<sup>37</sup>, activate members of the mechanosensitive TREK K<sub>2P</sub> subfamily<sup>38, 39</sup>. In particular, BL-1249, [(5,6,7,8-Tetrahydro-naphthalen-1-yl)-[2-(1*H*-tetrazol-5-yl)-phenyl]-amine, stimulates K<sub>2P</sub>2.1 (TREK-1)-like currents in bladder smooth muscle cells<sup>39</sup> and activates both K<sub>2P</sub>2.1 (TREK-1)<sup>18, 40</sup> and K<sub>2P</sub>10.1 (TREK-2)<sup>7</sup>. BL-1249 action is occluded by mutations that stabilize the C-type gate<sup>40</sup> and activation by BL-1249 has been shown to reverse the functional effects of a K<sub>2P</sub>2.1 (TREK-1) genetic mutation implicated in right ventricular outflow tract (RVOT) tachycardia having a compromised ion selectivity<sup>18</sup>. Nevertheless, how BL-1249 stimulates K<sub>2P</sub> activity and which elements of BL-1249 are crucial for its stimulatory effects have not yet been defined.

Here, we investigate the mechanism of action of BL-1249. Our studies show that this compound is a selective agonist of the TREK subfamily when applied extracellularly, having preferential action on K<sub>2P</sub>2.1 (TREK-1) and K<sub>2P</sub>10.1 (TREK-2) over K<sub>2P</sub>4.1 (TRAAK) and establish that its mechanism of action relies on gating at the selectivity filter C-type gate. Studies of a series of K<sub>2P</sub>2.1 (TREK-1)/K<sub>2P</sub>4.1 (TRAAK) chimeras and mutants indicate the M2/M3 helices are key to BL-1249 action and identify residues in M2 that contribute to subtype selectivity. These findings indicate that BL-1249 acts at a

separate site from the site of action of a structurally characterized activator, ML335, that directly stimulates the C-type gate via the  $K_{2P}$  modulator pocket<sup>6</sup>. Investigation of the functional properties of a set of BL-1249 analogs with respect to  $K_{2P}$  2.1 (TREK-1) and  $K_{2P}$  4.1 (TRAAK) show that both the acidic and tetralin moieties contribute to the stimulatory action of BL-1249 and indicate that the mobility of the two aryl rings relative to each other is key to the selective action of BL-1249 on  $K_{2P}$  2.1 (TREK-1).

## **Results**

### **BL-1249 external application differentially and selectively activates mechanosensitive $K_{2P}$ s**

BL-1249 activates  $K_{2P}$ 2.1 (TREK-1)<sup>18, 40</sup> and  $K_{2P}$ 10.1 (TREK-2)<sup>7</sup> but its effects on other  $K_{2P}$ s have not been characterized. Hence, we sought to define how BL-1249 affected the two channels most closely related to  $K_{2P}$ 2.1 (TREK-1),  $K_{2P}$ 10.1 (TREK-2) and  $K_{2P}$ 4.1 (TRAAK), as well as representative members of the other  $K_{2P}$  subtypes:  $K_{2P}$ 1.1 (TWIK-1),  $K_{2P}$ 3.1 (TASK-1),  $K_{2P}$ 5.1 (TASK-2),  $K_{2P}$ 9.1 (TASK-3),  $K_{2P}$ 13.1 (THIK-1), and  $K_{2P}$ 18.1 (TRESK) (Figure 1A-B). Two-electrode voltage clamp (TEVC) currents measured from *Xenopus* oocytes expressing each of the target channels showed clear activation responses after extracellular application of 10  $\mu$ M BL-1249 for only  $K_{2P}$ 2.1 (TREK-1) and  $K_{2P}$ 10.1 (TREK-2). Measurement of the dose-response curves for these channels (Figure 1C) revealed similar  $EC_{50}$ s ( $5.5 \pm 1.2 \mu$ M and  $8.0 \pm 0.8 \mu$ M for  $K_{2P}$ 2.1 (TREK-1) and  $K_{2P}$ 10.1 (TREK-2), respectively). 10  $\mu$ M BL-1249 weakly stimulated  $K_{2P}$ 4.1 (TRAAK) in agreement with observations by Mathie and colleagues<sup>28</sup>. Measurement of the dose-response uncovered a robust response at higher concentrations that indicated a ~10-fold reduction in the  $K_{2P}$ 4.1 (TRAAK)  $EC_{50}$  value relative to the other two TREK subfamily

members ( $EC_{50} = 48 \pm 10 \mu\text{M}$ , although complete saturation of the response could not be reached due to BL-1249 solubility limits, cf. Table 1) (Figure 1C). In order to test if the original  $10 \mu\text{M}$  assay had missed BL-1249 effects in other  $K_{2P}$ s, we tested concentrations of BL-1249 up to the solubility limit ( $\sim 80 \mu\text{M}$ ) against the other  $K_{2P}$  subfamily representatives. Despite the higher concentrations of BL-1249, we failed to find evidence for activation of the other  $K_{2P}$  subfamily representatives (Figure 1D). Thus, the data show that extracellular application of BL-1249 activates all members of the mechano- and thermo-sensitive TREK subfamily while sparing the other subfamilies and shows selectivity for  $K_{2P2.1}$  (TREK-1) and  $K_{2P10.1}$  (TREK-2) over  $K_{2P4.1}$  (TRAAK).

### **BL-1249 activates the $K_{2P2.1}$ (TREK-1) C-type gate**

Diverse types of physical and chemical stimuli activate  $K_{2P2.1}$  (TREK-1) by stabilizing the C-type gate and switching the channel into a 'leak' mode that is characterized by a loss of outward rectification of the potassium current<sup>6, 8</sup>. Accordingly, we used inside-out patch clamp experiments of  $K_{2P2.1}$  (TREK-1) expressed in HEK293 cells to test whether BL-1249 acts on the C-type gate. Application of  $1 \mu\text{M}$  BL-1249 caused a clear loss of rectification similar to the effects reported for both physical and chemical activators of  $K_{2P2.1}$  (TREK-1) (Figure 2A-E)<sup>6, 8</sup>. Additionally, TEVC studies of the effects of BL-1249 on  $K_{2P2.1}$  (TREK-1) channels bearing mutations that activate the C-type gate, G137I and W275S<sup>6, 10, 41</sup> demonstrated that these channels were insensitive to BL-1249 (Figure 2F). Together with previous single point concentration studies showing the insensitivity of  $K_{2P2.1}$  (TREK-1) W275S in mammalian cells<sup>40</sup>, our data provide definitive evidence that BL-1249 activates  $K_{2P2.1}$  (TREK-1) by stimulating the C-type gate. Thus, this compound

fits the mechanistic paradigm shared by varied types of activators including mechanical stretch, pH, lipids, and small molecules<sup>6, 8</sup>.

### **K<sub>2P</sub> C-terminal tail is necessary for BL-1249 action but is not the sole determinant of channel responsiveness**

Gating stimuli detected by sensors in various parts of the channel converge on the K<sub>2P</sub> selectivity filter C-type gate<sup>6, 8, 10, 12, 35</sup>. Because the C-terminal tail is the sensor for K<sub>2P</sub>2.1 (TREK-1) activation by both physiological<sup>41-46</sup> and chemical<sup>45, 47</sup> activators, we asked whether uncoupling the C-terminal tail from the channel using a triple-glycine mutant at the M4/C-terminal tail junction, K<sub>2P</sub>2.1 (TREK-1)<sub>GGG</sub><sup>41</sup>, impacted the BL-1249 response. TEVC dose response studies of K<sub>2P</sub>2.1 (TREK-1)<sub>GGG</sub> showed that the effects of BL-1249 were significantly blunted relative to wild-type channels (EC<sub>50</sub> = 19 ± 1 μM) (Figure 3A). This result contrasts previous studies of the small molecule activator ML67-33<sup>26</sup> for which uncoupling the C-terminal tail had no effect, and suggests that unlike ML67-33, the C-terminal tail plays a role in mediating the BL-1249 response.

K<sub>2P</sub>2.1 (TREK-1) C-terminal truncations have been shown to reduce potentiation by other activating stimuli<sup>42, 48</sup>. Hence, to probe the role of the C-terminal tail in the BL-1249 response further, we examined the effects of C-terminal tail truncations at residue 322, K<sub>2P</sub>2.1 (TREK-1)<sub>Δ322</sub>, equivalent to a previously described mutant called Δ89<sup>48</sup> and at residue 308, K<sub>2P</sub>2.1 (TREK-1)<sub>Δ308</sub>. Measurement of the dose-response curves for BL-1249 showed that these changes resulted in progressively reduced responses (EC<sub>50</sub> = 26 ± 8 μM and 35 ± 8 μM for K<sub>2P</sub>2.1 (TREK-1)<sub>Δ322</sub> and K<sub>2P</sub>2.1 (TREK-1)<sub>Δ308</sub>, respectively) (Figure 3B).



Given the importance of the C-terminal tail for the BL-1249 response and the fact that the C-terminal tails of K<sub>2P</sub>2.1 (TREK-1) and K<sub>2P</sub>4.1 (TRAAK) vary substantially (17.6% sequence similarity, 13.5% identity), we wondered if these differences could contribute to the different potencies observed in K<sub>2P</sub>2.1 (TREK-1) and K<sub>2P</sub>4.1 (TRAAK) BL-1249 responses. To test this possibility, we made chimeras that swapped the C-terminal tail between K<sub>2P</sub>2.1 (TREK-1) and K<sub>2P</sub>4.1 (TRAAK), TREK-1/AAK\_T and TRAAK/EK\_T. The TREK-1/AAK\_T chimera yielded channels having responses similar to K<sub>2P</sub>2.1 (TREK-1) (EC<sub>50</sub> = 7.7 ± 0.6 μM and 5.5 ± 1.2 μM for TREK-1/AAK\_T and K<sub>2P</sub>2.1 (TREK-1), respectively) (Figure 3C). By contrast, swapping the K<sub>2P</sub>2.1 (TREK-1) C-terminal tail onto K<sub>2P</sub>4.1 (TRAAK), TRAAK/EK1\_T, increased the sensitivity of K<sub>2P</sub>4.1 (TRAAK) core to BL-1249 by ~2-fold (EC<sub>50</sub> = 23 ± 4 μM and 48 ± 10 μM, for TRAAK/EK1\_T and K<sub>2P</sub>4.1 (TRAAK) respectively) (Figure 3D). Despite this modest change, it is clear that the C-terminal tail alone is not sufficient to endow the K<sub>2P</sub>4.1 (TRAAK) core with a K<sub>2P</sub>2.1 (TREK-1)-like BL-1249 response. Although the C-terminal tail is not a major locus for the selective actions of BL-1249, the strong impact that uncoupling the C-terminal tail from the core channel and C-terminal tail truncations has on the K<sub>2P</sub>2.1 (TREK-1) response to BL-1249 indicate that this channel element is an important factor that allows channel activation by BL-1249.

### **Multiple transmembrane regions contribute to BL-1249 activation**

To look for other elements that might contribute to BL-1249 responses, we constructed a set of K<sub>2P</sub>2.1 (TREK-1)/K<sub>2P</sub>4.1 (TRAAK) chimeras in which an increasing amount of one channel was spliced with the other. For the purposes of nomenclature, the channels are named using the parent N-terminal portion and the C-terminal chimera junction even

though the chimera set forms a continuum spanning the two wild type channels (Figure 4A). For example, TREK-1/AAK M4-C bears the K<sub>2P</sub>2.1 (TREK-1) sequence up to the junction with M4, whereas TRAAK/EK-1 M2-C bears K<sub>2P</sub>4.1 (TRAAK) up to the junction with M2 even though the largest portion of both of these channels comes from K<sub>2P</sub>2.1 (TREK-1).

TEVC experiments showed that all of the chimeras formed functional channels (Figures S1-S2). To test the ability of the chimeras to report on channel determinants for compound action, we examined the responses of the chimeras to two previously characterized activators, ML335 a compound that selectively activates K<sub>2P</sub>2.1 (TREK-1) but not K<sub>2P</sub>4.1 (TRAAK)<sup>6</sup> and ML67-33 an activator showing no clear preference for either channel<sup>26</sup>. The chimeras showed an essentially binary response to ML335 that was entirely dependent on the presence or absence of a lysine on the extracellular end of M4 that forms a cation- $\pi$  interaction with ML335<sup>6</sup>. Only constructs bearing a lysine at position equivalent to K<sub>2P</sub>2.1 (TREK-1) residue 271 (K<sub>2P</sub>2.1 (TREK-1), TRAAK/EK-1 M2-C, TRAAK/EK-1 M3-C, and TREK-1/AAK M4-C) robustly responded to ML335 (Figure S1A-C and G). In contrast to these results, we found no major changes with respect to the responses of the various chimeras to ML67-33 (Figure S1D-F and H). These findings are consistent with the inability of ML67-33 to discriminate between K<sub>2P</sub>2.1 (TREK-1) and K<sub>2P</sub>4.1 (TRAAK)<sup>26</sup>. Together, these studies show that this chimera set can identify selectivity determinants for activator compounds within the TREK subfamily.

We next examined how this panel of chimeras responded to BL-1249. We found that the character of the donor channel with respect to BL-1249 response became

progressively prevalent as larger portions were swapped into the recipient channel, contrasting the binary changes seen for ML335 responses (Figure 4A-C, S1G, Table 1). Further, the patterns of changes in the BL-1249 responses were not equivalent with respect to the direction of the substitution. Substituting K<sub>2P</sub>4.1 (TRAAK) sequence into K<sub>2P</sub>2.1 (TREK-1) from the C-terminal direction caused stepwise changes in EC<sub>50</sub> as the construct became dominated by the K<sub>2P</sub>4.1 (TRAAK) sequence (Figure 4A and C, clockwise in Figure 4A from K<sub>2P</sub>2.1 (TREK-1), EC<sub>50</sub> = 5.5 ± 1.2, 19 ± 3, 28 ± 2, and 39 ± 9 μM for K<sub>2P</sub>2.1 (TREK-1), TREK-1/AAK M4-C, TREK-1/AAK M3-C, and TREK-1/AAK M2-C, respectively). By contrast, substitution of K<sub>2P</sub>4.1 (TRAAK) sequence into K<sub>2P</sub>2.1 (TREK-1) from the N-terminal direction caused a loss, mild recovery, and then further loss of BL-1249 response (Figure 4A and B, counterclockwise in Figure 4A from K<sub>2P</sub>2.1 (TREK-1), EC<sub>50</sub> = 5.5 ± 1.2, 28 ± 5, 18 ± 2, 45 ± 2, and 48 ± 10 μM, for K<sub>2P</sub>2.1 (TREK-1), TRAAK/EK-1 M2-C, TRAAK/EK-1 M3-C, TRAAK/EK-1 M4-C, and K<sub>2P</sub>4.1 (TRAAK)). The complexity of the EC<sub>50</sub> changes displayed by the chimeras with respect to BL-1249 contrasted with how these chimeras responded for the case in which there is a single site responsible for compound selectivity (Figure S1G). Such a contrast suggests that multiple parts of the channel make contributions that influence BL-1249 selectivity rather than just a single site.

### **K<sub>2P</sub>2.1 (TREK-1) M2 residues contribute to BL-1249 selectivity**

In the course of converting K<sub>2P</sub>2.1 (TREK-1) to K<sub>2P</sub>4.1 (TRAAK) and vice-versa by chimeras, the M2/M3 region stood out as a point where we found both gradual changes in EC<sub>50</sub> (i.e. TREK-1/AAK M3-C → TREK-1/AAK M2-C) and stepwise changes that reversed the general EC<sub>50</sub> trend (i.e. TRAAK/EK-1 M3-C → TRAAK/EK-1 M2-C). To

investigate this issue further, we generated two chimeras in which only the M2 helix was exchanged between K<sub>2P</sub>2.1 (TREK-1) and K<sub>2P</sub>4.1 (TRAAK), TREK-1/TRAAK M2 and TRAAK/TREK-1 M2. The substitution of the K<sub>2P</sub>2.1 (TREK-1) M2 helix into K<sub>2P</sub>4.1 (TRAAK) had little effect on the BL-1249 response, yielding a channel having a response indistinguishable from K<sub>2P</sub>4.1 (TRAAK) ( $EC_{50} = 43 \pm 11 \mu\text{M}$  and  $48 \pm 10 \mu\text{M}$  for TRAAK/TREK-1 M2 and K<sub>2P</sub>4.1 (TRAAK), respectively) (Figure 5A). By contrast, the substitution of the K<sub>2P</sub>4.1 (TRAAK) M2 helix into K<sub>2P</sub>2.1 (TREK-1) caused a substantial loss in BL-1249 response ( $EC_{50} = 26 \pm 8 \mu\text{M}$  and  $5.5 \pm 1.2 \mu\text{M}$  for TREK-1/TRAAK M2 and K<sub>2P</sub>2.1 (TREK-1), respectively), indicating that elements from M2 contribute to the K<sub>2P</sub>2.1 (TREK-1) response to BL-1249.

To identify K<sub>2P</sub>2.1 (TREK-1) M2 residues that might participate in the BL-1249 response, we mapped the residues that differ between K<sub>2P</sub>2.1 (TREK-1) and K<sub>2P</sub>4.1 (TRAAK) in the context of the K<sub>2P</sub>2.1 (TREK-1) structure<sup>6</sup> (Figure 5B and C). Two K<sub>2P</sub>2.1 (TREK-1) M2 residues stood out as candidates that could explain the reduction in BL-1249 response when the entire M2 helix was replaced with M2 from K<sub>2P</sub>4.1 (TRAAK). One is at the M2/M4 interface and occurs between Phe172 and Arg297 via a  $\pi$ -cation interaction that would be lost when Phe172 is replaced with the equivalent K<sub>2P</sub>4.1 (TRAAK) residue Met134 (Figure 5C, right inset). The second is an intrasubunit  $\pi$ - $\pi$  interaction between Phe185 from M2, a site whose equivalent in K<sub>2P</sub>10.1 (TREK-2) Phe215 has a role in membrane stretch responses<sup>7</sup>, and Phe214 from M3 that would be disrupted by the replacement with the equivalent K<sub>2P</sub>4.1 (TRAAK) residue Leu147 (Figure 5C, left inset). To assess the importance of these interactions in the context of BL-1249 response, we made the K<sub>2P</sub>2.1 (TREK-1) mutants F172M and F185L and measured their

responses to BL-1249 (Figure 5D). Both changes reduced the BL-1249 response ( $EC_{50}$  =  $15 \pm 2 \mu\text{M}$  and  $27 \pm 5 \mu\text{M}$  for F172M and F185L, respectively) to levels similar to the M2 helix swap. Notably, the M2/M3 interface substitution, F185L had a larger impact on the  $EC_{50}$ , whereas the M2/M4 change F172M caused a substantial reduction in the extent to which the channel could be activated by BL-1249 (Figure 5D). Unlike the case for  $K_{2P}2.1$  (TREK-1), the two corresponding inverse mutations in  $K_{2P}4.1$  (TRAAK), M134F at the M2/M4 interface and L147F at the M2/M3 interface did not cause similar outcomes. The mutation at the M2/M4 interface had no impact on BL-1249 response ( $EC_{50}$ , M134F  $58 \pm 34 \mu\text{M}$ ), whereas the change in the M2/M3 interface conferred a modest improvement in the BL-1249 response ( $EC_{50}$ , L147F  $EC_{50} = 27 \pm 4 \mu\text{M}$ ;  $p < 0.001$  at  $35 \mu\text{M}$  ( $n = 7$ )) (Figure 5E). Taken together, these data highlight the importance of the M2 helix in BL-1249 activation. The observation that amino acid swaps in the M2/M3 interface are able to blunt the response of  $K_{2P}2.1$  (TREK-1) but enhance the response of  $K_{2P}4.1$  (TRAAK) points to the M2/M3 interface as a key element in the differential effects of BL-1249 on TREK subfamily members.

### **The BL-1249 acidic group and tetralin are critical for potency and selectivity**

Fenamates are weak  $K_{2P}$  modulators<sup>38, 39, 49</sup> and their structure-activity relationships (SAR) with respect to  $K_{2P}$  channels are poorly defined. Hence, we synthesized a set of BL-1249 derivatives in order to probe which portions of the small molecule were important for channel activation in the context of the differential responses of  $K_{2P}2.1$  (TREK-1) and  $K_{2P}4.1$  (TRAAK). BL-1249 has two ring systems, one bearing a tetrazole and a second bearing a tetralin moiety. Replacement of the tetrazole by other similar functionalities resulted in compounds having poorer potency than BL-1249 against  $K_{2P}2.1$  (TREK-1)

( $EC_{50} = 22 \pm 8 \mu\text{M}$  and  $44 \pm 10 \mu\text{M}$  for BL-1249-amide and BL-1249-acid, respectively) (Figure 6A-B, Table 2). Notably, even though BL-1249-acid was slightly less potent than BL-1249-amide (~2-fold), it had a stronger stimulatory effect on the current than either BL-1249 or BL-1249-amide, suggesting that the acidic nature of the side chain is important for BL-1249 function (Figure 6B). Curiously, unlike what we observe for the TREK subfamily, for  $K_{2P}$  18.1 (TRESK) the change from BL-1249 to BL-1249-acid has been reported to switch the functional effects of the compound from an activator to an inhibitor<sup>49</sup>. Both BL-1249-amide and BL-1249 acid retained selectivity for  $K_{2P}$ 2.1 (TREK-1) over  $K_{2P}$ 4.1 (TRAAK) (Figures 6C-D) indicating that this moiety is not the key determinant of selectivity.

To test the importance of the tetralin moiety, we synthesized a BL-1249 derivative in which this entity was replaced by a simple phenyl ring (BL-1249-Ph) (Figure 6A). This substitution proved very detrimental to activity and yielded a compound that had only a small amount of stimulatory effect against  $K_{2P}$ 2.1 (TREK-1) ( $EC_{50} > 200 \mu\text{M}$ ) and showed a similar profile against  $K_{2P}$ 4.1 (TRAAK) revealing the importance of the bicyclic tetralin ring for BL-1249 function (Figures 6B and E). Finally, we tested whether the conformation of the two aryl rings with respect to each other was important for the potency and selectivity of BL-1249. We made a BL-1249 derivative in which the tetralin structure was fused into a tricyclic scaffold to constrain the available conformations between the two aryl rings (BL-1249-tricycle) (Figure 6F). BL-1249-tricycle showed poorer activity against  $K_{2P}$ 2.1 (TREK-1) relative to BL-1249 (Figure 6G-H,  $EC_{50} = 34 \pm 6 \mu\text{M}$  versus  $5.5 \pm 1.1 \mu\text{M}$  for BL-1249-tricycle and BL-1249, respectively) but, surprisingly, retained essentially the same activity against  $K_{2P}$ 4.1 (TRAAK) (Figure 6G-H,  $EC_{50} = 42 \pm 9 \mu\text{M}$  versus  $48 \pm 10$

$\mu\text{M}$  for BL-1249-tricyclic and BL-1249, respectively). This loss in selectivity between  $\text{K}_{2\text{P}2.1}$  (TREK-1) and  $\text{K}_{2\text{P}4.1}$  (TRAAK) indicates that the ability of the aryl and tetralin rings to adopt non-co-planar conformations is key to the preferential action of BL-1249 on  $\text{K}_{2\text{P}2.1}$  (TREK-1). We also observed that BL-1249-tricyclic showed a small, but robust 'mode switch' behavior versus  $\text{K}_{2\text{P}2.1}$  (TREK-1) manifested as inhibition between 0.1-10  $\mu\text{M}$  followed by activation at higher concentrations. This behavior was not evident against  $\text{K}_{2\text{P}4.1}$  (TRAAK) and further indicates the importance of the mobility between the two ring systems for the stimulatory action of BL-1249 on  $\text{K}_{2\text{P}2.1}$  (TREK-1). Notably, other tricyclic compounds have been reported to inhibit  $\text{K}_{2\text{P}2.1}$  (TREK-1) but not  $\text{K}_{2\text{P}4.1}$  (TRAAK)<sup>50</sup> similar to the properties of BL-1249-tricyclic. Together, our studies demonstrate that both the acidic and tetralin moieties are important contributors to the stimulatory action of BL-1249 against  $\text{K}_{2\text{P}2.1}$  (TREK-1) and indicate that the mobility of the two aryl rings relative to each other is key to its selective effects on  $\text{K}_{2\text{P}2.1}$  (TREK-1) over  $\text{K}_{2\text{P}4.1}$  (TRAAK).

## ***Discussion***

Addressing the relatively poor chemical biology surrounding the  $K_{2P}$  family is an important goal that has the potential to provide tool compounds that can remove the current barriers to understanding how diverse inputs modulate  $K_{2P}$  function, as well as the physiological roles of  $K_{2P}$ s in various tissues<sup>1, 24, 25</sup>. Our studies show that the fenamic acid derivative BL-1249<sup>39</sup>, previously shown to activate  $K_{2P}2.1$  (TREK-1)<sup>18, 40</sup> and  $K_{2P}10.1$  (TREK-2)<sup>7</sup> potently and selectively activates all three members of the mechanosensitive TREK  $K_{2P}$  subfamily,  $K_{2P} 2.1$  (TREK-1),  $K_{2P} 10.1$  (TREK-2) and  $K_{2P}4.1$  (TRAAK) by potentiating the potassium currents with  $EC_{50}$ s in the low micromolar range when applied extracellularly. Similar to many  $K_{2P}$  activators<sup>6, 8, 10, 26, 41</sup>, BL-1249 enhances TREK subfamily currents by stimulating the selectivity filter C-type gate. This mode of action provides further evidence for the central role of this C-type gate in the control of  $K_{2P}$  function.

There are currently two structurally characterized examples for how small molecules can engage members of the  $K_{2P}$  family. The co-crystal structure of  $K_{2P}10.1$  (TREK-2) with inhibitor norfluoxetine shows that this inhibitor binds in a pocket underneath the P2 helix of the selectivity filter at a site that is framed by the M2, M3, and M4 transmembrane helices and that becomes accessible when the pore lining M4 helix adopts a 'down' conformation<sup>7, 51</sup>. Although the binding site is clearly demarcated, how state-dependent binding of norfluoxetine inhibits is still unclear. Interestingly, besides inhibiting the movement of the M4 helix, the structural data indicates that the primary amine of norfluoxetine is near to the lower side of the selectivity filter where it could impact ion conduction by interfering with the electrostatic environment of the pore. The other



structural example shows that a pair of related molecules, ML335 and ML402, bind to a cryptic binding site, the  $K_{2P}$  modulator pocket, situated behind the selectivity filter and sandwiched at the interface between the P1 pore helix and top of the M4 transmembrane helix of  $K_{2P}2.1$  (TREK-1)<sup>6</sup>. These activators act as wedges that stabilize the mobility of the P1/M4 interface, a site also impacted by gain-of-function mutations<sup>6, 10, 35, 41</sup>, and directly activate the C-type gate<sup>6</sup>. Understanding the extent to which other  $K_{2P}$  modulators, such as BL-1249 and ML67-33, act at the norfluoxetine site, the  $K_{2P}$  modulator pocket, or elsewhere on the channel is important for outlining the landscape of druggable sites for the  $K_{2P}$  potassium channel class.

Our studies of mutants and chimeras of  $K_{2P}2.1$  (TREK-1) and  $K_{2P}4.1$  (TRAAK) indicate that multiple channel elements that include C-terminal tail and the M2, M3, and M4 transmembrane helices contribute to BL-1249 responses. The integrity of the C-terminal tail is essential for BL-1249 stimulation (Figure 3), placing BL-1249 within a diverse class of TREK subfamily activators that are functionally dependent on this channel element including lipids<sup>42</sup>, arachidonic acid<sup>45</sup>, intracellular acidosis<sup>46</sup>, chloroform<sup>45</sup>, and temperature<sup>41</sup>. This dependence on the C-terminal tail is notably not shared by another tetrazole containing small molecule activator ML67-33<sup>26</sup>. Despite the importance of the C-terminal tail in the BL-1249 response, our data indicate that this channel element has a limited role in mediating the selective action of BL-1249 on  $K_{2P}2.1$  (TREK-1) over  $K_{2P}4.1$  (TRAAK). By contrast, we do find evidence that multiple transmembrane domains contribute to BL-1249 selectivity. Although in the context of  $K_{2P}2.1$  (TREK-1)/ $K_{2P}4.1$  (TRAAK) chimeras no single transmembrane domain emerged as the predominant contributor, we were able to identify a site in the M2/M3 interface where exchange of a

single amino acid between K<sub>2P</sub>2.1 (TREK-1) and K<sub>2P</sub>4.1 (TRAAK), F185L and L147F, respectively, was able to shift the BL-1249 phenotype in the direction of the donor channel, impairing the K<sub>2P</sub>2.1 (TREK-1) response while enhancing the K<sub>2P</sub>4.1 (TRAAK) response. Interestingly, the M2/M3 interface is also important for TREK subfamily responses to temperature<sup>35</sup> and membrane stretch<sup>52</sup>. Taken together, our findings suggest that BL-1249 does not act in the K<sub>2P</sub> modulator pocket but affects a site that is a composite of elements from multiple transmembrane helices. Although this general characteristic is shared with the norfluoxetine site, the role of the M2/M3 interface in BL-1249 selectivity suggests that BL-1249 may act outside of both structurally defined small molecule sites.

Our studies of a small set of BL-1249 derivatives show that the two defining moieties of BL-1249, the tetrazole and the tetralin groups, contribute to the stimulatory effect of BL-1249 TREK subfamily channels. The acidic nature at the tetrazole site and the hydrophobicity of the tetralin ring are both crucial for the potency of BL-1249 (Figure 6). Whether or not the two rings are constrained is key for the compound to discriminate between K<sub>2P</sub>2.1 (TREK-1) and K<sub>2P</sub>4.1 (TRAAK) as demonstrated by the properties of BL-1249-tricycle. This dependence on the ability of the ring systems to adopt non-coplanar conformations in order to achieve selectivity within the TREK subfamily suggests that further exploration of strategies to modify the conformational preferences between the two ring systems might be a means to achieve better subtype discrimination. Interestingly, the importance of the tetrazole is a property shared by BL-1249 and ML67-33<sup>26</sup> and both compounds share the general architecture of a hydrophobic ring system linked to the tetrazole. However, ML67-33 is not selective within the TREK

subfamily and rather than having hydrophobic moieties that can adopt a non-coplanar conformation has an acridine ring system that is constrained, not unlike BL-1249-tricycle. This commonality between ML67-33 and BL-1249-tricycle lends further support to the idea that constrained versus conformationally adaptable hydrophobic ring systems are an important property for the tetrazole-bearing class of TREK subfamily activators. These shared features suggest that further optimization of hydrophobic scaffolds bearing tetrazoles or other acidic groups could provide a path towards the development of other TREK family modulators.

The actions of multiple diverse physical and chemical activators of the TREK subfamily converge at the C-type gate<sup>6, 8-10, 12, 26, 41</sup>. Our observation that BL-1249 also stimulates the C-type gate fits this paradigm. Our data support the idea that the BL-1249 site of action is not in the K<sub>2P</sub> modulator pocket, the chemical modulator site closest to the C-type gate, but appears to reside among the transmembrane helices and supports the notion that changes in the channel architecture distant from the selectivity filter can impact the C-type gate<sup>6, 35</sup>.

Elaboration of small molecule modulators for the TREK subfamily provides essential chemical biology tools for unraveling channel function and may offer new paths for treating issues such as pain<sup>14, 25</sup> and arrhythmia<sup>18</sup>. Our study, together with recent structural work<sup>6, 7</sup>, paints a complex landscape in which there are multiple points for small molecules to intervene in K<sub>2P</sub> function. Given the growing and diverse list of small molecules that influence various K<sub>2P</sub>s<sup>14, 26-28, 36, 50, 53-57</sup>, further definition of the types of sites with which small molecules can bind and impact K<sub>2P</sub> function through combined

efforts of structural, functional, and computational studies will be crucial for defining how precise chemical control of  $K_{2P}$  activity can be achieved.

## **Materials and Methods**

### **Molecular Biology**

Constructs for murine K<sub>2</sub>P<sub>S</sub>, including: K<sub>2</sub>P<sub>2</sub>.1 (TREK-1) (Gene ID: 16526), K<sub>2</sub>P<sub>10</sub>.1 (TREK-2) (Gene ID: 72258), K<sub>2</sub>P<sub>4</sub>.1 (TRAAK) (Gene ID: 16528), K<sub>2</sub>P<sub>5</sub>.1 (TASK-2) (Gene ID: 16529), K<sub>2</sub>P<sub>3</sub>.1 (TASK-1) (Gene ID: 16527), K<sub>2</sub>P<sub>9</sub>.1 (TASK-3) (Gene ID: 223604), K<sub>2</sub>P<sub>18</sub>.1 (TRESK) (Gene ID: 332396) in pGEMHE/pMO were used for *Xenopus* oocyte experiments as previously described<sup>10, 26</sup>. Murine K<sub>2</sub>P<sub>2</sub>.1 (TREK-1) (Gene ID: 16526) was expressed in HEK-293 cells using a pIRES-EGFP construct as previously described<sup>26</sup>. Murine K<sub>2</sub>P<sub>13</sub>.1 (THIK-1) (Gene ID: 217826) and K<sub>2</sub>P<sub>1</sub>.1 (TWIK-1) (Gene ID: 16525) were cloned into pGEMHE/pMO for use in *Xenopus* oocytes. Chimeras were designed using EMBOSS Needle pairwise sequence alignment tool<sup>58</sup> to match homologous helices in K<sub>2</sub>P<sub>2</sub>.1 (TREK-1) and K<sub>2</sub>P<sub>4</sub>.1 (TRAAK) and were assembled using the Gibson assembly method<sup>59</sup>. Chimera boundaries are Thr152, TREK-1/AAK M2-C; Trp199, TREK-1/AAK M3-C; and Y272, TREK-1/AAK M4-C, Thr114, TRAAK/EK-1 M2-C; Trp161, TRAAK/EK-1 M3-C; and Tyr234 K<sub>2</sub>P<sub>4</sub>.1 (TRAAK). All sequences were verified using DNA sequencing.

### **Patch clamp electrophysiology**

Mouse K<sub>2</sub>P<sub>2</sub>.1 was expressed from a previously described pIRES2-EGFP vector in HEK293T cells (ATCC CRL-1573<sup>TM</sup>). 70% confluent cells were transfected (in 35-mm diameter wells) with LipofectAMINE 2000 (Invitrogen) for 6 h, and plated onto coverslips coated with Matrigel (BD Biosciences).

Voltage-dependent activation of  $K_{2P2.1}$  was recorded on excised patches in inside-out configuration (50 kHz sampling) in the absence and presence of 1  $\mu$ M BL-1249. Pipette solution contained the following: 150 mM KCl, 3.6 mM  $CaCl_2$ , 10 mM HEPES (pH 7.4 with KOH). Bath solution contained the following: 150 mM RbCl, 2 mM EGTA and 10 mM HEPES (pH 7.4 with RbOH), and was continuously perfused at 200 ml per hour during the experiment. TREK-1 currents were elicited by a 10 mV voltage step protocol from  $-100$  mV to  $+100$  mV, from a  $-80$  mV holding potential. Data were analysed using Clampfit 9 and Origin 7.

### **Two-electrode voltage-clamp (TEVC) electrophysiology**

*Xenopus laevis* oocytes were harvested in accordance with UCSF IACUC protocol **AN129690** and digested in calcium-free ND-96 (96 mM NaCl, 2 mM KCl, 3.8 mM  $MgCl_2$ ) immediately following harvest, as previously described<sup>6, 10</sup>. Digested oocytes were maintained in standard ND96 (96 mM NaCl, 2 mM KCl, 1.8 mM  $CaCl_2$ , 2 mM  $MgCl_2$ , 10 mM HEPES, pH 7.4) with antibiotics (100 units  $ml^{-1}$  Penicillin, 100  $\mu$ g  $ml^{-1}$  Streptomycin, 50  $\mu$ g  $ml^{-1}$  Gentimycin). Defolliculated stage V-VI oocytes were injected with 0.2-6.0 ng of mRNA in 50 nL and currents were recorded 24-48 hours after injection. mRNA was synthesized from plasmid DNA using mMessage mMachin Kit (T7 promoter, Ambion, Life Technologies) and purified using RNEasy Kit (Qiagen). Injected oocytes were impaled with two standard microelectrodes (0.2 – 1.0  $M\Omega$ ) filled with 3M KCl and subjected to constant perfusion of standard ND96 during recording. Currents were amplified using the GeneClamp 500B (MDS Analytical Technologies) amplifier controlled by the pClamp software (Molecular Devices). Data were digitized at 1 kHz using Digidata 1332A (MDS Analytical Technologies). For all experiments with small molecules, basal

currents were evoked using 1s long ramps from -150 to +50 mV under constant perfusion of ND96. Once stabilized basal currents were recorded, compounds were perfused at various concentrations in standard ND96 and currents were allowed to increase to stabilization before recording final current. Fold activation upon compound application is expressed as  $I/I_0$  (0 mV), derived from the current at 0 mV in presence of compound divided by the basal current at 0 mV in standard ND96 without compound. Data were analyzed and plotted using Graphpad Prism Version 5 (GraphPad Software, San Diego California USA, [www.graphpad.com](http://www.graphpad.com)). In cases where saturation could not be reached due to BL-1249 solubility limits,  $EC_{50}$  was estimated using an upper bound of  $I/I_0$  was set to 15 for the fits. In the case of BL-1249-acid  $EC_{50}$  estimation, upper bound of  $I/I_0$  was set to 20 to account for the strong stimulation of BL-1249-acid.

### **BL-1249 analogue chemical synthesis**

Complete methods for the synthesis of BL-1249 analogs, BL-1249-acid, BL-1249-amide, BL-1249-Ph, and BL-1249-tricycle are found in the supplementary material and are available online.

## **Acknowledgements**

We thank P. Riegelhaupt for input in the early stages of this project and K. Brejc for comments on the manuscript. This work was supported by grant NIH- R01-MH093603 to D.L.M. and an American Heart Foundation Postdoctoral fellowship to C.A.

## **Author Contributions**

L.P., C.A., H.L. and D.L.M. conceived the study and designed the experiments. L.P. and H.L. performed two-electrode voltage-clamp electrophysiology experiments. C.A. performed patch clamp electrophysiology experiments. L.P., and C.A. analyzed the electrophysiology data. L.P. and H.L. performed molecular biology experiments. C.B. and A.G.-G. synthesized and purified the compounds. C.B., A.G.-G., and A.R.R. designed the synthetic routes. D.L.M. analyzed data and provided guidance and support. L.P., C.A., C.B., A.R.R., and D.L.M. wrote the paper.

## **Conflict of Interest**

The authors declare no financial interests.

## **Supporting Information**

A supplementary file containing supplementary figures, methods, and references accompanies this manuscript.



## References

- (1) Feliciangeli, S., Chatelain, F. C., Bichet, D., and Lesage, F. The family of K channels: salient structural and functional properties, *J Physiol.* **2014.** 593, 2587.
- (2) Enyedi, P., and Czirjak, G. Molecular background of leak K<sup>+</sup> currents: two-pore domain potassium channels, *Physiological reviews.* **2010.** 90, 559-605.
- (3) Renigunta, V., Schlichthorl, G., and Daut, J. Much more than a leak: structure and function of K(2)p-channels, *Pflugers Arch.* **2015.** 467, 867-894.
- (4) Brohawn, S. G., del Marmol, J., and MacKinnon, R. Crystal structure of the human K2P TRAAK, a lipid- and mechano-sensitive K<sup>+</sup> ion channel, *Science.* **2012.** 335, 436-441.
- (5) Miller, A. N., and Long, S. B. Crystal structure of the human two-pore domain potassium channel K2P1, *Science.* **2012.** 335, 432-436.
- (6) Lolicato, M., Arrigoni, C., Mori, T., Sekioka, Y., Bryant, C., Clark, K. A., and Minor, D. L., Jr. K2P2.1 (TREK-1)-activator complexes reveal a cryptic selectivity filter binding site, *Nature.* **2017.** 547, 364-368.
- (7) Dong, Y. Y., Pike, A. C., Mackenzie, A., McClenaghan, C., Aryal, P., Dong, L., Quigley, A., Grieben, M., Goubin, S., Mukhopadhyay, S., Ruda, G. F., Clausen, M. V., Cao, L., Brennan, P. E., Burgess-Brown, N. A., Sansom, M. S., Tucker, S. J., and Carpenter, E. P. K2P channel gating mechanisms revealed by structures of TREK-2 and a complex with Prozac, *Science.* **2015.** 347, 1256-1259.
- (8) Schewe, M., Nematian-Ardestani, E., Sun, H., Musinszki, M., Cordeiro, S., Bucci, G., de Groot, B. L., Tucker, S. J., Rapedius, M., and Baukrowitz, T. A Non-

- canonical Voltage-Sensing Mechanism Controls Gating in K2P K(+) Channels, *Cell*. **2016**. 164, 937-949.
- (9) Zilberberg, N., Ilan, N., and Goldstein, S. A. KCNKO: opening and closing the 2-P-domain potassium leak channel entails "C-type" gating of the outer pore, *Neuron*. **2001**. 32, 635-648.
- (10) Bagriantsev, S. N., Peyronnet, R., Clark, K. A., Honore, E., and Minor, D. L., Jr. Multiple modalities converge on a common gate to control K2P channel function, *EMBO J*. **2011**. 30, 3594-3606.
- (11) Cohen, A., Ben-Abu, Y., Hen, S., and Zilberberg, N. A novel mechanism for human K2P2.1 channel gating. Facilitation of C-type gating by protonation of extracellular histidine residues, *J Biol Chem*. **2008**. 283, 19448-19455.
- (12) Piechotta, P. L., Rapedius, M., Stansfeld, P. J., Bollepalli, M. K., Ehrlich, G., Andres-Enguix, I., Fritzenschaft, H., Decher, N., Sansom, M. S., Tucker, S. J., and Baukrowitz, T. The pore structure and gating mechanism of K2P channels, *EMBO J*. **2011**. 30, 3607-3619.
- (13) Devilliers, M., Busserolles, J., Lolignier, S., Deval, E., Pereira, V., Alloui, A., Christin, M., Mazet, B., Delmas, P., Noel, J., Lazdunski, M., and Eschalier, A. Activation of TREK-1 by morphine results in analgesia without adverse side effects, *Nat Commun*. **2013**. 4, 2941.
- (14) Vivier, D., Soussia, I. B., Rodrigues, N., Lolignier, S., Devilliers, M., Chatelain, F. C., Prival, L., Chapuy, E., Bourdier, G., Bennis, K., Lesage, F., Eschalier, A., Busserolles, J., and Ducki, S. Development of the first Two-Pore Domain Potassium Channel TREK-1 (TWIK-Related K<sup>+</sup> Channel 1)-selective agonist

- possessing in vivo anti-nociceptive activity, *Journal of medicinal chemistry*. **2017**. 60, 1076.
- (15) Alloui, A., Zimmermann, K., Mamet, J., Duprat, F., Noel, J., Chemin, J., Guy, N., Blondeau, N., Voilley, N., Rubat-Coudert, C., Borsotto, M., Romey, G., Heurteaux, C., Reeh, P., Eschalier, A., and Lazdunski, M. TREK-1, a K<sup>+</sup> channel involved in polymodal pain perception, *Embo J*. **2006**. 25, 2368-2376.
- (16) Heurteaux, C., Guy, N., Laigle, C., Blondeau, N., Duprat, F., Mazzuca, M., Lang-Lazdunski, L., Widmann, C., Zanzouri, M., Romey, G., and Lazdunski, M. TREK-1, a K<sup>+</sup> channel involved in neuroprotection and general anesthesia, *Embo J*. **2004**. 23, 2684-2695.
- (17) Lazarenko, R. M., Fortuna, M. G., Shi, Y., Mulkey, D. K., Takakura, A. C., Moreira, T. S., Guyenet, P. G., and Bayliss, D. A. Anesthetic activation of central respiratory chemoreceptor neurons involves inhibition of a THIK-1-like background K(+) current, *J Neurosci*. **2010**. 30, 9324-9334.
- (18) Decher, N., Ortiz-Bonnin, B., Friedrich, C., Schewe, M., Kiper, A. K., Rinne, S., Seemann, G., Peyronnet, R., Zumhagen, S., Bustos, D., Kockskamper, J., Kohl, P., Just, S., Gonzalez, W., Baukowitz, T., Stallmeyer, B., and Schulze-Bahr, E. Sodium permeable and "hypersensitive" TREK-1 channels cause ventricular tachycardia, *EMBO molecular medicine*. **2017**. 9, 403-414.
- (19) Laigle, C., Confort-Gouny, S., Le Fur, Y., Cozzone, P. J., and Viola, A. Deletion of TRAAK potassium channel affects brain metabolism and protects against ischemia, *PloS one*. **2012**. 7, e53266.

- (20) Wu, X., Liu, Y., Chen, X., Sun, Q., Tang, R., Wang, W., Yu, Z., and Xie, M. Involvement of TREK-1 activity in astrocyte function and neuroprotection under simulated ischemia conditions, *Journal of molecular neuroscience*. **2013**. *MN* 49, 499-506.
- (21) Heurteaux, C., Lucas, G., Guy, N., El Yacoubi, M., Thummler, S., Peng, X. D., Noble, F., Blondeau, N., Widmann, C., Borsotto, M., Gobbi, G., Vaugeois, J. M., Debonnel, G., and Lazdunski, M. Deletion of the background potassium channel TREK-1 results in a depression-resistant phenotype, *Nat Neurosci*. **2006**. 9, 1134-1141.
- (22) Andres-Enguix, I., Shang, L., Stansfeld, P. J., Morahan, J. M., Sansom, M. S., Lafreniere, R. G., Roy, B., Griffiths, L. R., Rouleau, G. A., Ebers, G. C., Cader, Z. M., and Tucker, S. J. Functional analysis of missense variants in the TRESK (KCNK18) K channel, *Scientific reports*. **2012**. 2, 237.
- (23) Lafreniere, R. G., Cader, M. Z., Poulin, J. F., Andres-Enguix, I., Simoneau, M., Gupta, N., Boisvert, K., Lafreniere, F., McLaughlan, S., Dube, M. P., Marcinkiewicz, M. M., Ramagopalan, S., Ansorge, O., Brais, B., Sequeiros, J., Pereira-Monteiro, J. M., Griffiths, L. R., Tucker, S. J., Ebers, G., and Rouleau, G. A. A dominant-negative mutation in the TRESK potassium channel is linked to familial migraine with aura, *Nat. Med*. **2010**. 16, 1157-1160.
- (24) Mathie, A., and Veale, E. L. Two-pore domain potassium channels: potential therapeutic targets for the treatment of pain, *Pflug Arch Eur J Phy*. **2015**. 467, 931-943.

- (25) Vivier, D., Bennis, K., Lesage, F., and Ducki, S. Perspectives on the Two-Pore Domain Potassium Channel TREK-1 (TWIK-Related K(+) Channel 1). A Novel Therapeutic Target?, *Journal of medicinal chemistry*. **2016**. 59, 5149-5157.
- (26) Bagriantsev, S. N., Ang, K. H., Gallardo-Godoy, A., Clark, K. A., Arkin, M. R., Renslo, A. R., and Minor, D. L., Jr. A high-throughput functional screen identifies small molecule regulators of temperature- and mechano-sensitive K2P channels, *ACS chemical biology*. **2013**. 8, 1841-1851.
- (27) Su, Z. W., Brown, E. C., Wang, W. W., and MacKinnon, R. Novel cell-free high-throughput screening method for pharmacological tools targeting K<sup>+</sup> channels, *P Natl Acad Sci*. **2016**. USA 113, 5748-5753.
- (28) Loucif, A. J. C., Saintot, P. P., Liu, J., Antonio, B. M., Zellmer, S. G., Yoger, K., Veale, E. L., Wilbrey, A., Omoto, K., Cao, L., Gutteridge, A., Castle, N. A., Stevens, E. B., and Mathie, A. GI-530159, a novel, selective, mechanosensitive two-pore-domain potassium (K2P) channel opener, reduces rat dorsal root ganglion neuron excitability, *British journal of pharmacology*. **2017**. 175, 2272.
- (29) Coburn, C. A., Luo, Y., Cui, M., Wang, J., Soll, R., Dong, J., Hu, B., Lyon, M. A., Santarelli, V. P., Kraus, R. L., Gregan, Y., Wang, Y., Fox, S. V., Binns, J., Doran, S. M., Reiss, D. R., Tannenbaum, P. L., Gotter, A. L., Meinke, P. T., and Renger, J. J. Discovery of a pharmacologically active antagonist of the two-pore-domain potassium channel K2P9.1 (TASK-3), *ChemMedChem*. **2012**. 7, 123-133.
- (30) Rodrigues, N., Bennis, K., Vivier, D., Pereira, V., F, C. C., Chapuy, E., Deokar, H., Busserolles, J., Lesage, F., Eschalier, A., and Ducki, S. Synthesis and structure-activity relationship study of substituted caffeate esters as antinociceptive agents

- modulating the TREK-1 channel, *European journal of medicinal chemistry*. **2014**. 75, 391-402.
- (31) Bayliss, D. A., and Barrett, P. Q. Emerging roles for two-pore-domain potassium channels and their potential therapeutic impact, *Trends Pharmacol Sci*. **2008**. 29, 566-575.
- (32) Yekkirala, A. S., Roberson, D. P., Bean, B. P., and Woolf, C. J. Breaking barriers to novel analgesic drug development, *Nature reviews. Drug discovery*. **2017**. 16, 545.
- (33) Brohawn, S. G., Campbell, E. B., and MacKinnon, R. Domain-swapped chain connectivity and gated membrane access in a Fab-mediated crystal of the human TRAAK K<sup>+</sup> channel, *Proc Natl Acad Sci U S A*. **2013**. 110, 2129-2134.
- (34) Brohawn, S. G., Campbell, E. B., and MacKinnon, R. Physical mechanism for gating and mechanosensitivity of the human TRAAK K<sup>+</sup> channel, *Nature*. **2014**. 516, 126-130.
- (35) Lolicato, M., Riegelhaupt, P. M., Arrigoni, C., Clark, K. A., and Minor, D. L., Jr. Transmembrane helix straightening and buckling underlies activation of mechanosensitive and thermosensitive K(2P) channels, *Neuron*. **2014**. 84, 1198-1212.
- (36) Dadi, P. K., Vierra, N. C., Days, E. L., Dickerson, M., Vinson, P. N., Weaver, C. D., and Jacobson, D. A. Selective small molecule activators of TREK-2 channels stimulate DRG c-fiber nociceptor K<sub>2</sub>P currents and limit calcium influx, *ACS chemical neuroscience*. **2016**. 8, 558.

- (37) Graham, G. G. (2016) Fenamates, In *Compendium of Inflammatory Diseases* (Parnham, M. J., Ed.), pp 477-482, Springer Basel, Basel.
- (38) Takahira, M., Sakurai, M., Sakurada, N., and Sugiyama, K. Fenamates and diltiazem modulate lipid-sensitive mechano-gated 2P domain K(+) channels, *Pflugers Arch.* **2005.** 451, 474-478.
- (39) Tertysnikova, S., Knox, R. J., Plym, M. J., Thalody, G., Griffin, C., Neelands, T., Harden, D. G., Signor, L., Weaver, D., Myers, R. A., and Lodge, N. J. BL-1249 [(5,6,7,8-tetrahydro-naphthalen-1-yl)-[2-(1H-tetrazol-5-yl)-phenyl]-amine]: a putative potassium channel opener with bladder-relaxant properties, *The Journal of pharmacology and experimental therapeutics.* **2005.** 313, 250-259.
- (40) Veale, E. L., Al-Moubarak, E., Bajaria, N., Omoto, K., Cao, L., Tucker, S. J., Stevens, E. B., and Mathie, A. Influence of the N terminus on the biophysical properties and pharmacology of TREK1 potassium channels, *Molecular pharmacology.* **2014.**85, 671-681.
- (41) Bagriantsev, S. N., Clark, K. A., and Minor, D. L., Jr. Metabolic and thermal stimuli control K(2P)2.1 (TREK-1) through modular sensory and gating domains, *EMBO J.* **2012.** 31, 3297-3308.
- (42) Chemin, J., Patel, A. J., Duprat, F., Lauritzen, I., Lazdunski, M., and Honore, E. A phospholipid sensor controls mechanogating of the K+ channel TREK-1, *EMBO J.* **2005.** 24, 44-53.
- (43) Chemin, J., Patel, A. J., Duprat, F., Sachs, F., Lazdunski, M., and Honore, E. Up- and down-regulation of the mechano-gated K(2P) channel TREK-1 by PIP (2) and other membrane phospholipids, *Pflugers Arch.* **2007.** 455, 97-103.

- (44) Murbartian, J., Lei, Q., Sando, J. J., and Bayliss, D. A. Sequential phosphorylation mediates receptor- and kinase-induced inhibition of TREK-1 background potassium channels, *J Biol Chem.* **2005.** *280,* 30175-30184.
- (45) Patel, A. J., Honore, E., Maingret, F., Lesage, F., Fink, M., Duprat, F., and Lazdunski, M. A mammalian two pore domain mechano-gated S-like K<sup>+</sup> channel, *Embo J.* **1998.***17,* 4283-4290.
- (46) Honore, E., Maingret, F., Lazdunski, M., and Patel, A. J. An intracellular proton sensor commands lipid- and mechano-gating of the K(+) channel TREK-1, *EMBO J.* **2002.** *21,* 2968-2976.
- (47) Lotshaw, D. P. Biophysical, pharmacological, and functional characteristics of cloned and native mammalian two-pore domain K<sup>+</sup> channels, *Cell biochemistry and biophysics.* **2007.** *47,* 209-256.
- (48) Maingret, F., Honore, E., Lazdunski, M., and Patel, A. J. Molecular basis of the voltage-dependent gating of TREK-1, a mechano-sensitive K(+) channel, *Biochem Biophys Res Commun.* **2002.** *292,* 339-346.
- (49) Monteillier, A., Loucif, A., Omoto, K., Stevens, E. B., Lainez, S., Saintot, P. P., Cao, L., and Pryde, D. C. Investigation of the structure activity relationship of flufenamic acid derivatives at the human TRESK channel K2P18.1, *Bioorganic & medicinal chemistry letters.* **2016.** *26,* 4919-4924.
- (50) Thummler, S., Duprat, F., and Lazdunski, M. Antipsychotics inhibit TREK but not TRAAK channels, *Biochem Biophys Res Commun.* **2007.** *354,* 284-289.



- (51) McClenaghan, C., Schewe, M., Aryal, P., Carpenter, E. P., Baukrowitz, T., and Tucker, S. J. Polymodal activation of the TREK-2 K2P channel produces structurally distinct open states, *J Gen Physiol.* **2016.** 147, 497-505.
- (52) Aryal, P., Jarerattanachat, V., Clausen, M. V., Schewe, M., McClenaghan, C., Argent, L., Conrad, L. J., Dong, Y. Y., Pike, A. C. W., Carpenter, E. P., Baukrowitz, T., Sansom, M. S. P., and Tucker, S. J. Bilayer-Mediated Structural Transitions Control Mechanosensitivity of the TREK-2 K2P Channel, *Structure.* **2017.** 25, 708-718 e702.
- (53) Braun, G., Lengyel, M., Enyedi, P., and Czirjak, G. Differential sensitivity of TREK-1, TREK-2 and TRAAK background potassium channels to the polycationic dye ruthenium red, *British journal of pharmacology.* **2015.** 172, 1728-1738.
- (54) Chokshi, R. H., Larsen, A. T., Bhayana, B., and Cotten, J. F. Breathing Stimulant Compounds Inhibit TASK-3 Potassium Channel Function Likely by Binding at a Common Site in the Channel Pore, *Molecular pharmacology.* **2015.** 88, 926-934.
- (55) Luethy, A., Boghosian, J. D., Srikantha, R., and Cotten, J. F. Halogenated Ether, Alcohol, and Alkane Anesthetics Activate TASK-3 Tandem Pore Potassium Channels Likely through a Common Mechanism, *Molecular pharmacology.* **2017.** 91, 620-629.
- (56) Kennard, L. E., Chumbley, J. R., Ranatunga, K. M., Armstrong, S. J., Veale, E. L., and Mathie, A. Inhibition of the human two-pore domain potassium channel, TREK-1, by fluoxetine and its metabolite norfluoxetine, *British journal of pharmacology.* **2005.** 144, 821-829.

- (57) Patel, A. J., Honore, E., Lesage, F., Fink, M., Romey, G., and Lazdunski, M. Inhalational anesthetics activate two-pore-domain background K<sup>+</sup> channels, *Nat Neurosci.* **1999.** 2, 422-426.
- (58) Rice, P., Longden, I., and Bleasby, A. EMBOSS: the European Molecular Biology Open Software Suite, *Trends Genet.* **2000.** 16, 276-277.
- (59) Gibson, D. G., Young, L., Chuang, R. Y., Venter, J. C., Hutchison, C. A., 3rd, and Smith, H. O. Enzymatic assembly of DNA molecules up to several hundred kilobases, *Nature methods.* **2009.** 6, 343-345.

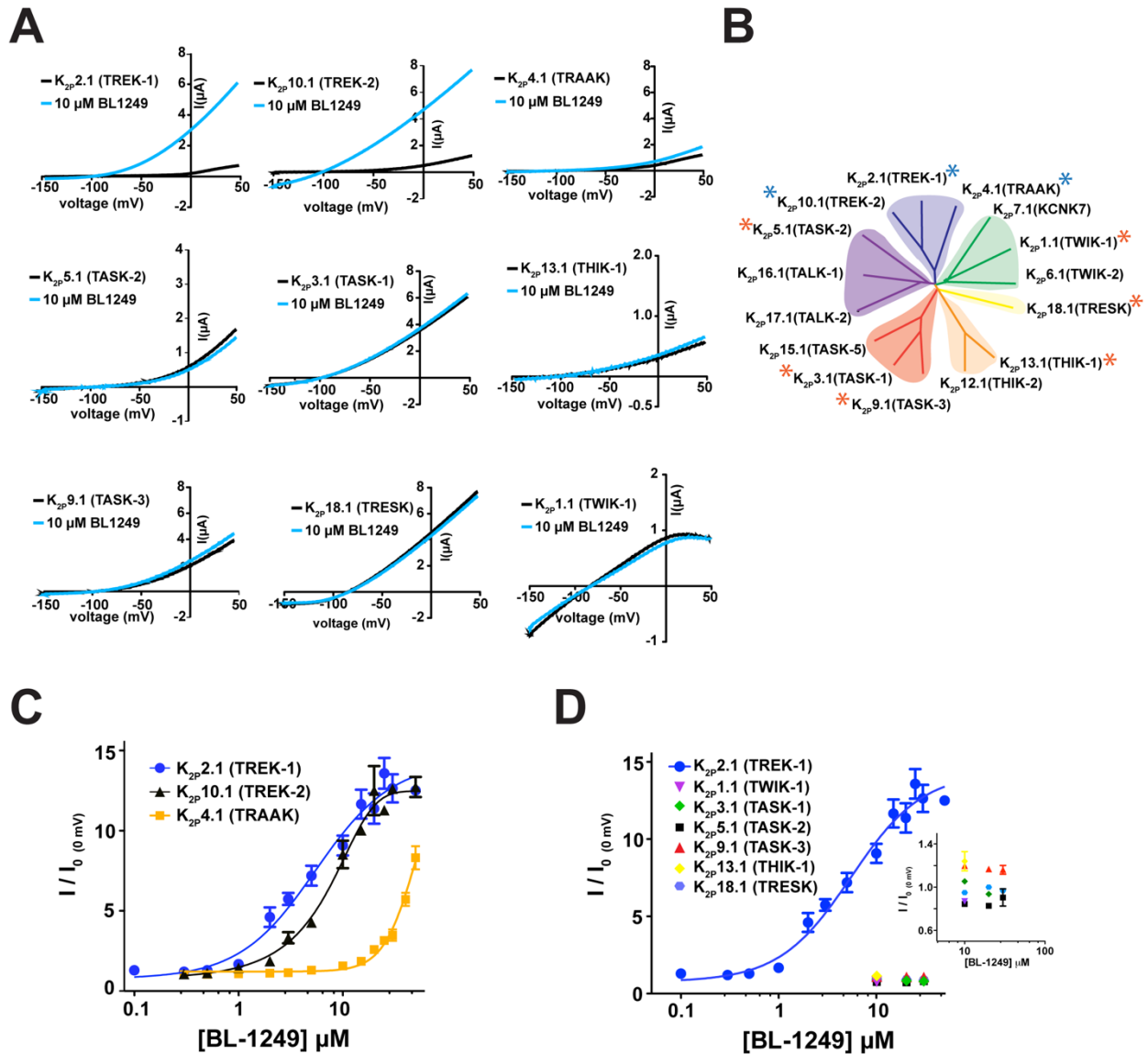


**Figure 2.1 | External application of BL-1249 selectively activates mechanosensitive  $K_{2P}$ s**

**A**, Exemplar current traces for specified  $K_{2P}$ s (black) with 10  $\mu$ M BL-1249 (light blue) as measured via TEVC in *Xenopus* oocytes. **B**,  $K_{2P}$  channel phylogenetic tree. Stars denote assayed representative  $K_{2P}$ s. Blue stars indicate BL-1249 responsive channels. **C**, BL-1249 dose-response curves for  $K_{2P}2.1$ (TREK-1) (blue circles),  $K_{2P}10.1$ (TREK-2) (black triangles), and  $K_{2P}4.1$ (TRAAK) (orange squares). ( $EC_{50} = 5.5 \pm 1.2 \mu$ M,  $8.0 \pm 0.8 \mu$ M and  $48 \pm 10 \mu$ M, respectively). **D**, BL-1249 responses of indicated  $K_{2P}$ s. Inset shows expanded view of poorly responsive  $K_{2P}$ s. Error bars are s.e.m.

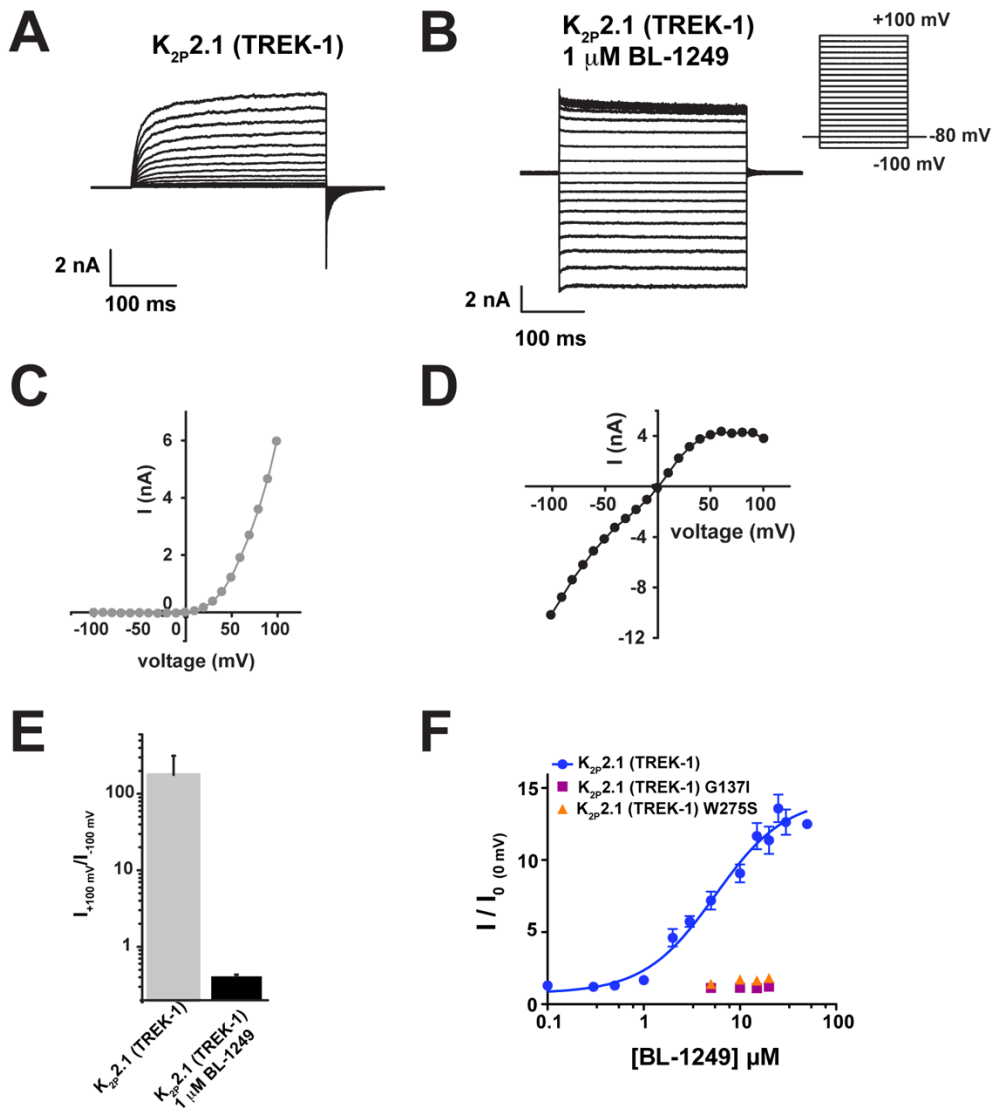


**Figure 2.2 | BL-1249 activates the K2P2.1 (TREK-1) C-type gate**

**A**, and **B**, Exemplar current traces for **A**, K<sub>2P</sub>2.1 (TREK-1) and **B**, K<sub>2P</sub>2.1 (TREK-1) with 1 μM BL-1249 in HEK293 inside-out patches in 150 mM K<sup>+</sup><sub>[out]</sub>/150 mM Rb<sup>+</sup><sub>[in]</sub>. Inset shows voltage protocol. **C**, and **D**, Current-voltage relationships for **C**, K<sub>2P</sub>2.1 (TREK-1) and **D**, K<sub>2P</sub>2.1 (TREK-1) with 1 μM BL-1249. **E**, Rectification coefficients ( $I_{+100\text{mV}}/I_{-100\text{mV}}$ ) from recordings ( $n \geq 3$ ) made in ('A'-'D'). **F**, Dose-response curves in *Xenopus* oocytes for K<sub>2P</sub>2.1 (TREK-1) (blue circles), K<sub>2P</sub>2.1 (TREK-1) G137I (purple squares), and K<sub>2P</sub>2.1 (TREK-1) W275S (orange triangles) K<sub>2P</sub>2.1 (TREK-1):  $5.5 \pm 1.2 \mu\text{M}$ , G137I and W275S  $>60 \mu\text{M}$ . K<sub>2P</sub>2.1 (TREK-1) data are from Figure 1C. Error bars are s.e.m..

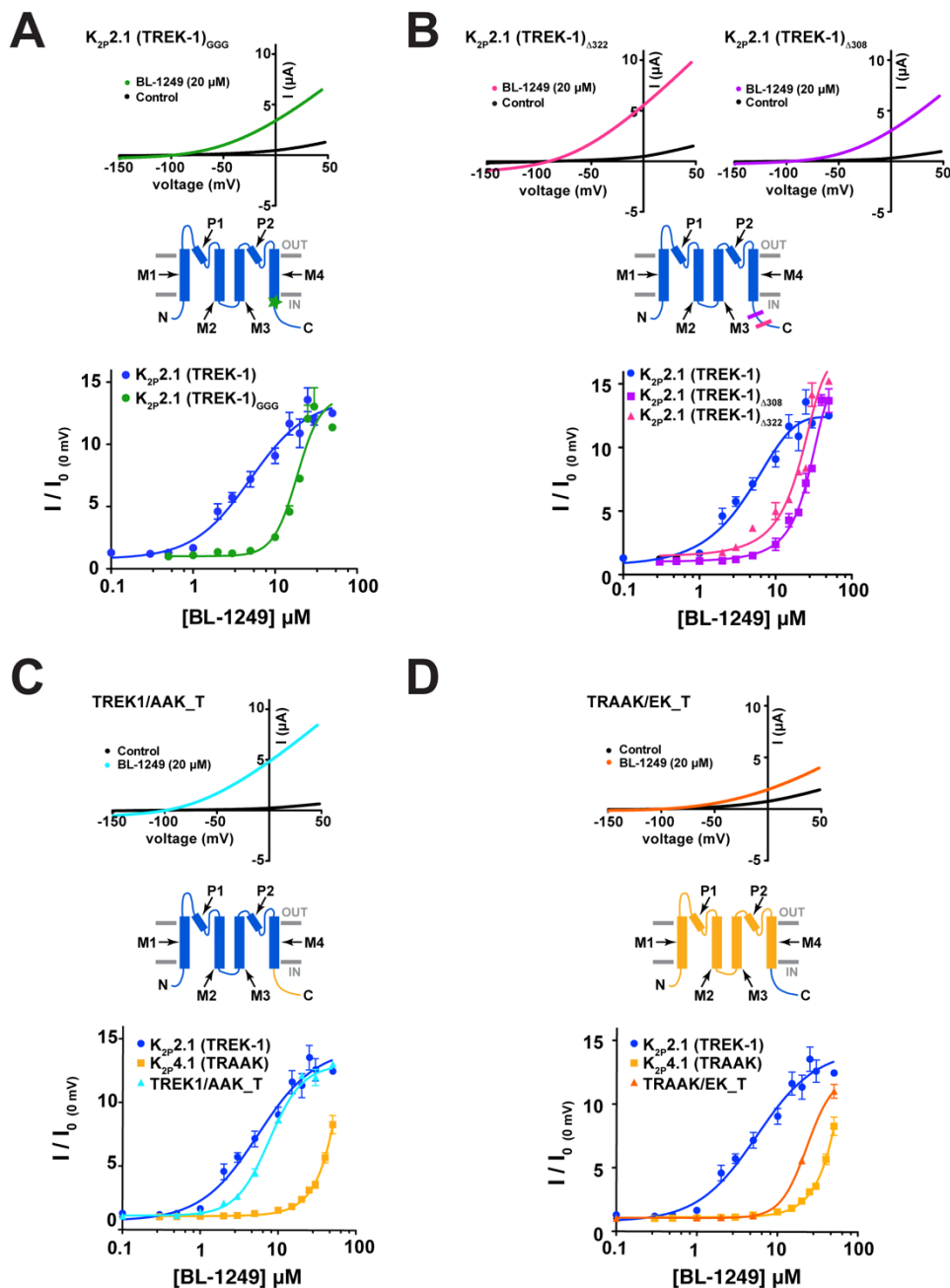


**Figure 2.3 | K2P2.1(TREK 1) C-terminus affects BL-1249 response**

**A**, Exemplar current traces for  $K_{2P2.1}(\text{TREK-1})_{\text{GGG}}$  (black) with 20  $\mu\text{M}$  BL-1249 (green) and BL-1249 dose-response curves for  $K_{2P2.1}(\text{TREK-1})$  (blue circles) and  $K_{2P2.1}(\text{TREK-1})_{\text{GGG}}$  (green circles) ( $\text{EC}_{50} = 5.5 \pm 1.2 \mu\text{M}$  and  $19 \pm 1 \mu\text{M}$ , respectively). Green star in cartoon indicates site of GGG mutation. **B**, Exemplar current traces for  $K_{2P2.1}(\text{TREK-1})_{\Delta 322}$  (magenta) and  $K_{2P2.1}(\text{TREK-1})_{\Delta 308}$  (purple) with 20  $\mu\text{M}$  BL-1249 and BL-1249 dose-response curves for  $K_{2P2.1}(\text{TREK-1})$  (blue circles),  $K_{2P2.1}(\text{TREK-1})_{\Delta 322}$  (purple squares), and  $K_{2P2.1}(\text{TREK-1})_{\Delta 308}$  (magenta triangles). ( $\text{EC}_{50} = 5.5 \pm 1.2 \mu\text{M}$ ,

26 ± 8 μM, and 35 ± 8 μM, respectively). Magenta and purple lines in cartoon indicates site of Δ322 and Δ308 truncations, respectively. **C**, Exemplar current traces for TREK-1/AAK\_T (black) and with 20 μM BL-1249 (cyan). BL-1249 dose-response curves for K<sub>2P</sub>2.1(TREK-1) (blue circles), K<sub>2P</sub>4.1(TRAACK) (light orange squares), and TRAAK/EK1\_T (light blue triangles). (EC<sub>50</sub> = 5.5 ± 1.2 μM, 48 ± 10 μM, and 7.7 ± 0.6 μM, respectively). Cartoon indicates TREK-1/AAK\_T channel regions from K<sub>2P</sub>2.1 (blue) and K<sub>2P</sub>4.1 (yellow). **D**, Exemplar current traces for TRAAK/EK\_T (black) and with 20 μM BL-1249 (orange). BL-1249 dose-response curves for K<sub>2P</sub>2.1(TREK-1) (blue circles), K<sub>2P</sub>4.1(TRAACK) (light orange squares), and TRAAK/EK\_T (orange triangles) (EC<sub>50</sub> = 5.5 ± 1.2 μM, 48 ± 10 μM, and 23 ± 4 μM, respectively). Cartoon indicates TRAAK/EK\_T channel regions from K<sub>2P</sub>2.1 (blue) and K<sub>2P</sub>4.1 (light orange). In **A-D**, K<sub>2P</sub>2.1(TREK-1) and K<sub>2P</sub>4.1(TRAACK) data are from Figure 1C. Error bars are s.e.m.

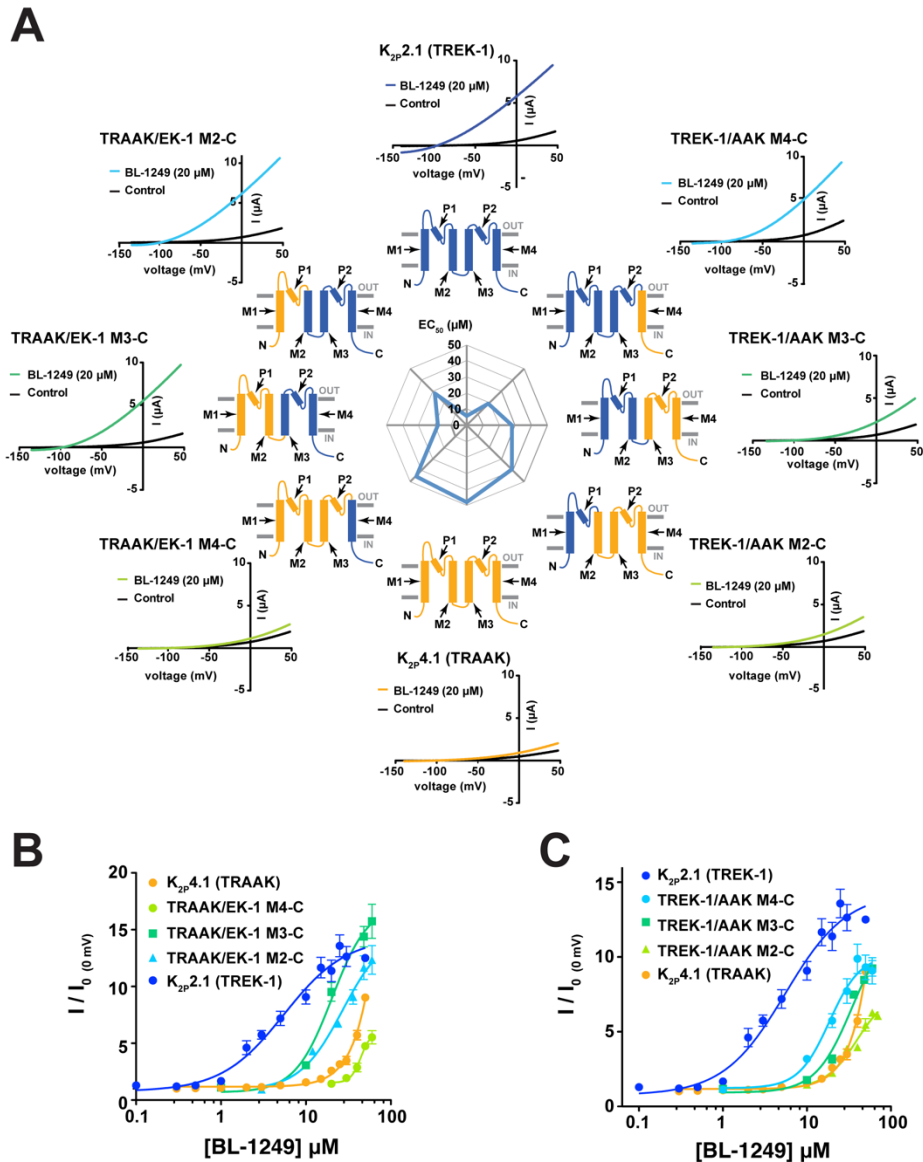


**Figure 2.4 | BL-1249 responses of TREK-1/TRAAK chimeras**

**A**, Exemplar current traces for BL-1249 responses for  $K_{2P}2.1$ (TREK-1) (blue),  $K_{2P}4.1$ (TRAAK) (light orange), and chimeras TREK-1/AAK M4-C (light blue), TREK-1/AAK M3-C (green), TREK-1/AAK M2-C (light green), TRAAK/EK-1 M4-C (light green), TRAAK/EK-1 M3-C (green), TRAAK/EK-1 M2-C (light blue) Black and colored traces show basal and currents with 20  $\mu$ M BL-1249, respectively. Cartoon schematics show channel portions from  $K_{2P}2.1$ (TREK-1) (blue) and  $K_{2P}4.1$ (TRAAK) (light orange). **B**, and **C**, Dose-response curves for  $K_{2P}2.1$ (TREK-1),  $K_{2P}4.1$ (TRAAK) and the indicated chimeras. ( $EC_{50} = 5.5 \pm 1.2 \mu$ M,  $48 \pm 10 \mu$ M,  $19 \pm 3 \mu$ M,  $28 \pm 3 \mu$ M,  $39 \pm 9 \mu$ M,  $45 \pm 2 \mu$ M,  $18 \pm 2 \mu$ M,  $28 \pm 5 \mu$ M, for  $K_{2P}2.1$ (TREK-1),  $K_{2P}4.1$ (TRAAK), TREK-1/AAK M4-C, TREK-1/AAK M3-C, TREK-1/AAK M2-C, TRAAK/EK1 M4-C, and TRAAK/EK1 M3-C, TRAAK/EK1 M2-C, respectively).  $K_{2P}2.1$ (TREK-1) and  $K_{2P}4.1$ (TRAAK) data are from Figure 1C. Error bars are s.e.m..

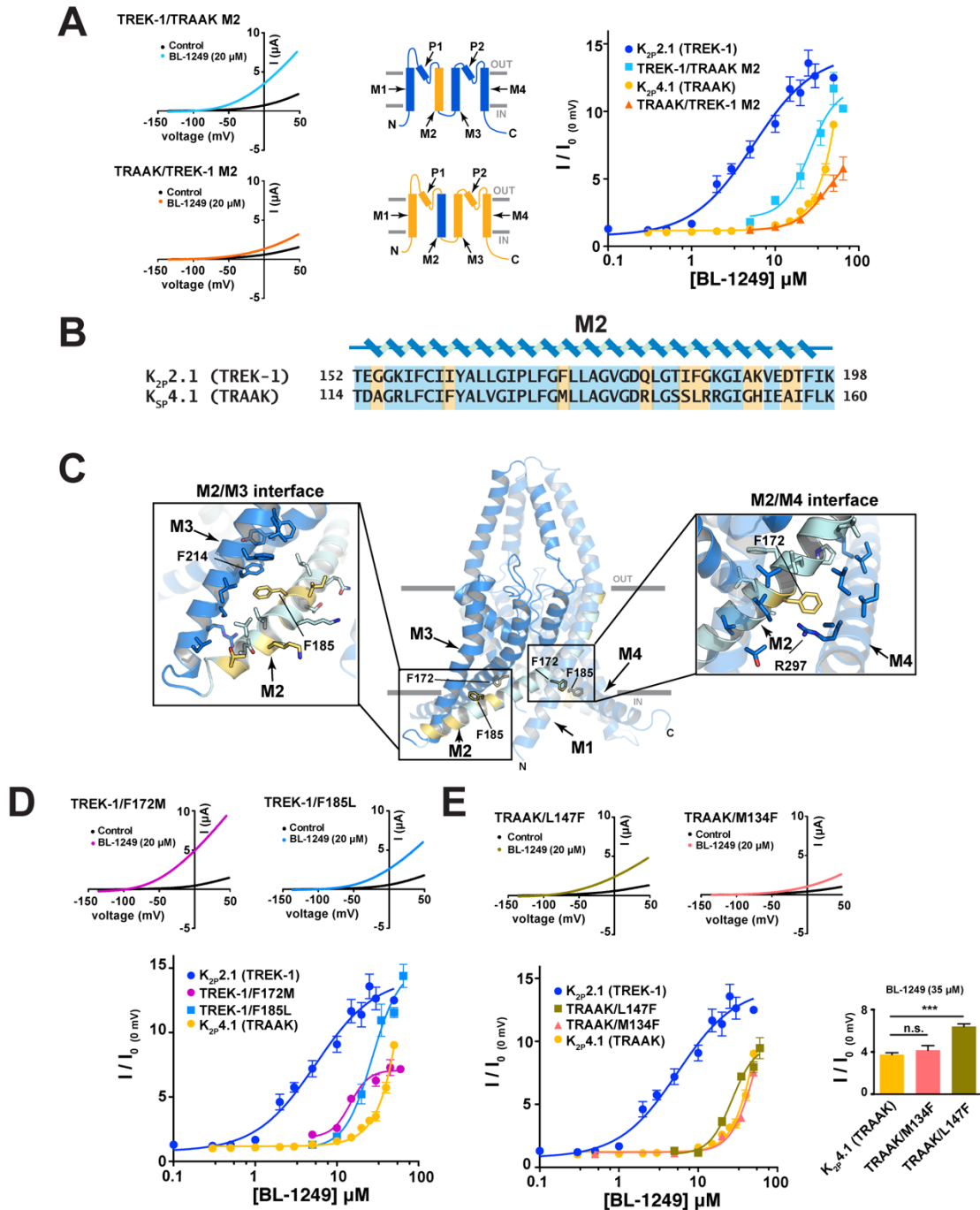


**Figure 2.5 | M2 residues contribute to BL-1249 selectivity between K<sub>2P</sub>2.1 (TREK 1) and K<sub>2P</sub>4.1 (TRAAK)**

**A**, Exemplar current traces for TREK-1/TRAAK M2 (light blue) and TRAAK/TREK-1 M2 (orange) with 20  $\mu$ M BL-1249 (left). Insets depict M2 helix swap. BL-1249 dose-response curves (right) for K<sub>2P</sub>2.1 (TREK-1) (blue circles), TREK-1/TRAAK M2 (light blue squares), K<sub>2P</sub>4.1 (TRAAK) (light orange circles) and TRAAK/TREK-1 M2 (orange triangles).



( $EC_{50} = 5.5 \pm 1.2 \mu\text{M}$ ,  $26 \pm 8 \mu\text{M}$ ,  $48 \pm 10 \mu\text{M}$  and  $43 \pm 11 \mu\text{M}$ , respectively). **B**, Alignment of  $K_{2P}2.1$  (TREK-1) and  $K_{2P}4.1$  (TRAAK) M2 sequences. Non-conserved residues are highlighted in yellow. **C**,  $K_{2P}2.1$ (TREK-1) (PDB 6CQ6)<sup>6</sup> structure. Residues that differ from  $K_{2P}4.1$  (TRAAK) are highlighted yellow. Panel insets show the environment surrounding the highlighted M2 residues. **D**, Exemplar current traces for TREK-1/F172M (pink) and TREK-1/F185L (light blue) with 20  $\mu\text{M}$  BL-1249. BL-1249 dose-response curves for  $K_{2P}2.1$ (TREK-1) (blue circles), TREK-1/F172M (pink circles),  $K_{2P}2.1$  (F185L) (light blue squares) and  $K_{2P}4.1$ (TRAAK) (light orange circles). ( $EC_{50} = 5.5 \pm 1.2 \mu\text{M}$ ,  $15 \pm 2 \mu\text{M}$ ,  $27 \pm 5 \mu\text{M}$  and  $48 \pm 10 \mu\text{M}$ , respectively). **E**, Exemplar current traces for TRAAK/M134F (orange triangles) and TRAAK/L147F (olive green squares) with 20  $\mu\text{M}$  BL-1249. BL-1249 dose-response curves for  $K_{2P}2.1$  (TREK-1) (blue circles), TRAAK/M134F (orange triangles), TRAAK/L147F (olive green squares) and  $K_{2P}4.1$ (TRAAK) (light orange circles). ( $EC_{50} = 5.5 \pm 1.2 \mu\text{M}$ ,  $58 \pm 34 \mu\text{M}$ ,  $27 \pm 4 \mu\text{M}$  and  $48 \pm 10 \mu\text{M}$ , respectively).  $K_{2P}2.1$ (TREK-1) and  $K_{2P}4.1$ (TRAAK) data are from Figure 1C. Inset compares responses at 35  $\mu\text{M}$  BL-1249. \*\*\* indicates  $p < 0.001$  for a one-way ANOVA test. 'n.s.' no significant difference. Error bars are s.e.m.



(TREK-1) (blue) and  $K_{2P4.1}$ (TRAAK) (light orange) (bottom). **F**, Chemical structure of BL-1249-tricycle. **G**, Exemplar current traces for  $K_{2P2.1}$  (TREK-1) and  $K_{2P4.1}$  (TRAAK) with 25  $\mu$ M BL-1249-tricycle (purple). **H**, Dose-response of  $K_{2P2.1}$  (TREK-1) (blue) and  $K_{2P4.1}$  (TRAAK) (light orange) for BL-1249-tricycle ( $EC_{50}$ = 34  $\pm$  6  $\mu$ M and 42  $\pm$  9  $\mu$ M, respectively). Error bars are s.e.m.

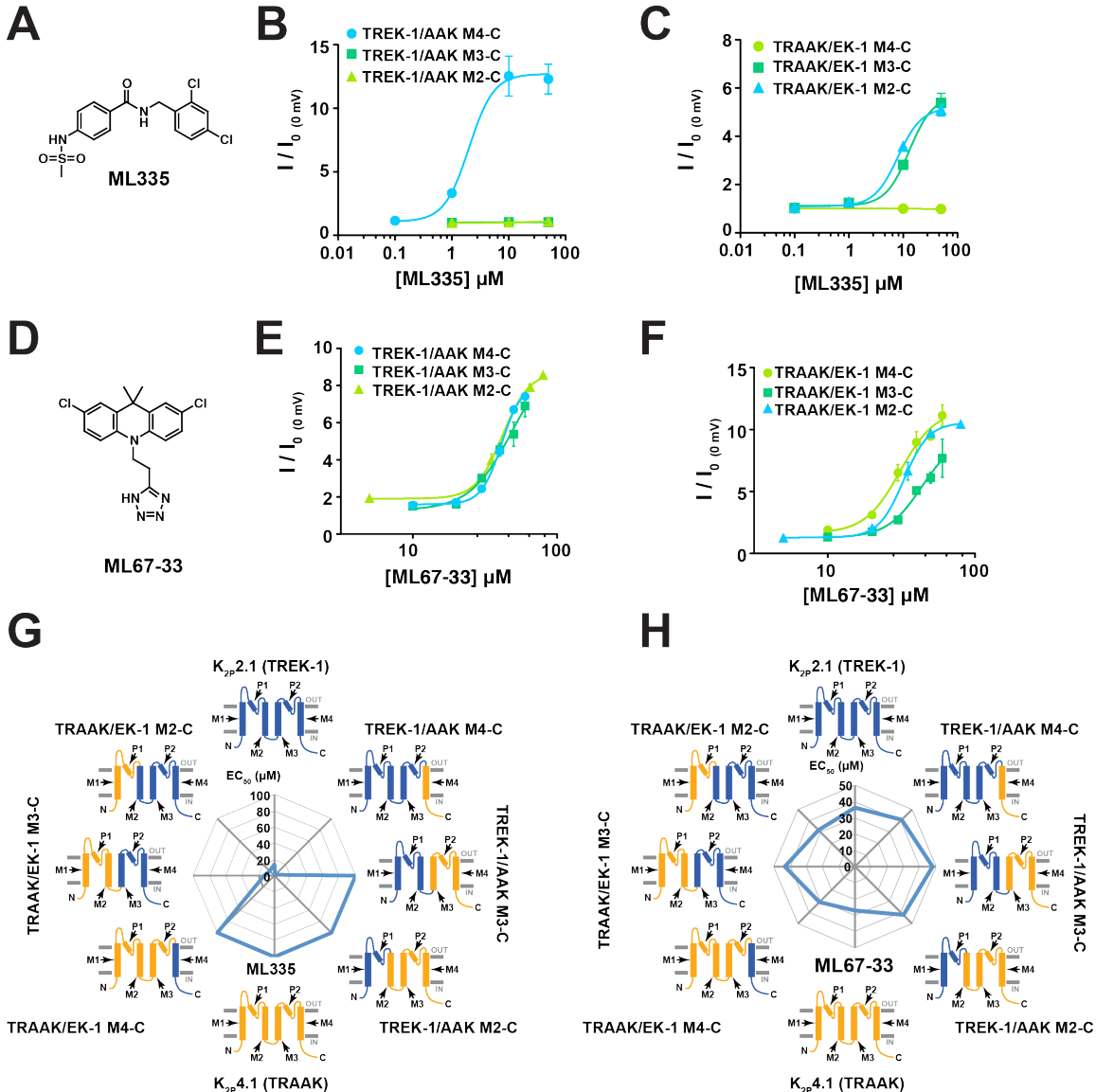


**Figure 2.7 | Supplementary Figure 1 - Responses of TREK-1/TRAAK chimeras to ML355 and ML67-33 activators.**

**A**, ML355 chemical structure. **B**, and **C**, ML355 dose-response curves for: TREK-1/AAK M4-C (light blue), TREK-1/AAK M3-C (green), and TREK-1/AAK M2-C (light green) ( $EC_{50} = .0 \pm 0.6 \mu\text{M}$ ,  $>100 \mu\text{M}$ , and  $>100 \mu\text{M}$ , respectively), and TRAAK/EK-1 M4-C (light green), TRAAK/EK-1 M3-C (green), and TRAAK/EK-1 M2-C (light blue) ( $EC_{50} = >100 \mu\text{M}$ ,  $13 \pm 2 \mu\text{M}$ , and  $8 \pm 1 \mu\text{M}$  respectively). **D**, ML67-33 chemical structure. **E**, and **F**, ML67-33 dose-response curves for: TREK-1/AAK M4-C (light blue), TREK-1/AAK M3-C (green), and TREK-1/AAK M2-C (light green), ( $EC_{50} = 42 \pm 3 \mu\text{M}$ ,  $49 \pm 22 \mu\text{M}$ , and  $42 \pm 3 \mu\text{M}$ , respectively), and TRAAK/EK-1 M4-C (light green), TRAAK/EK-1 M3-C (green), TRAAK/EK-1 M2-C (light blue), ( $EC_{50} = 31 \pm 3 \mu\text{M}$ ,  $44 \pm 14 \mu\text{M}$ , and  $33 \pm 1 \mu\text{M}$ , respectively). **G** and **H**, Spider plot of  $EC_{50}$ s for the indicated chimeras. Cartoon

schematics show channel portions from K<sub>2P</sub>2.1(TREK-1) (blue) and K<sub>2P</sub>4.1(TRAAK) (light orange). Error bars are s.e.m.

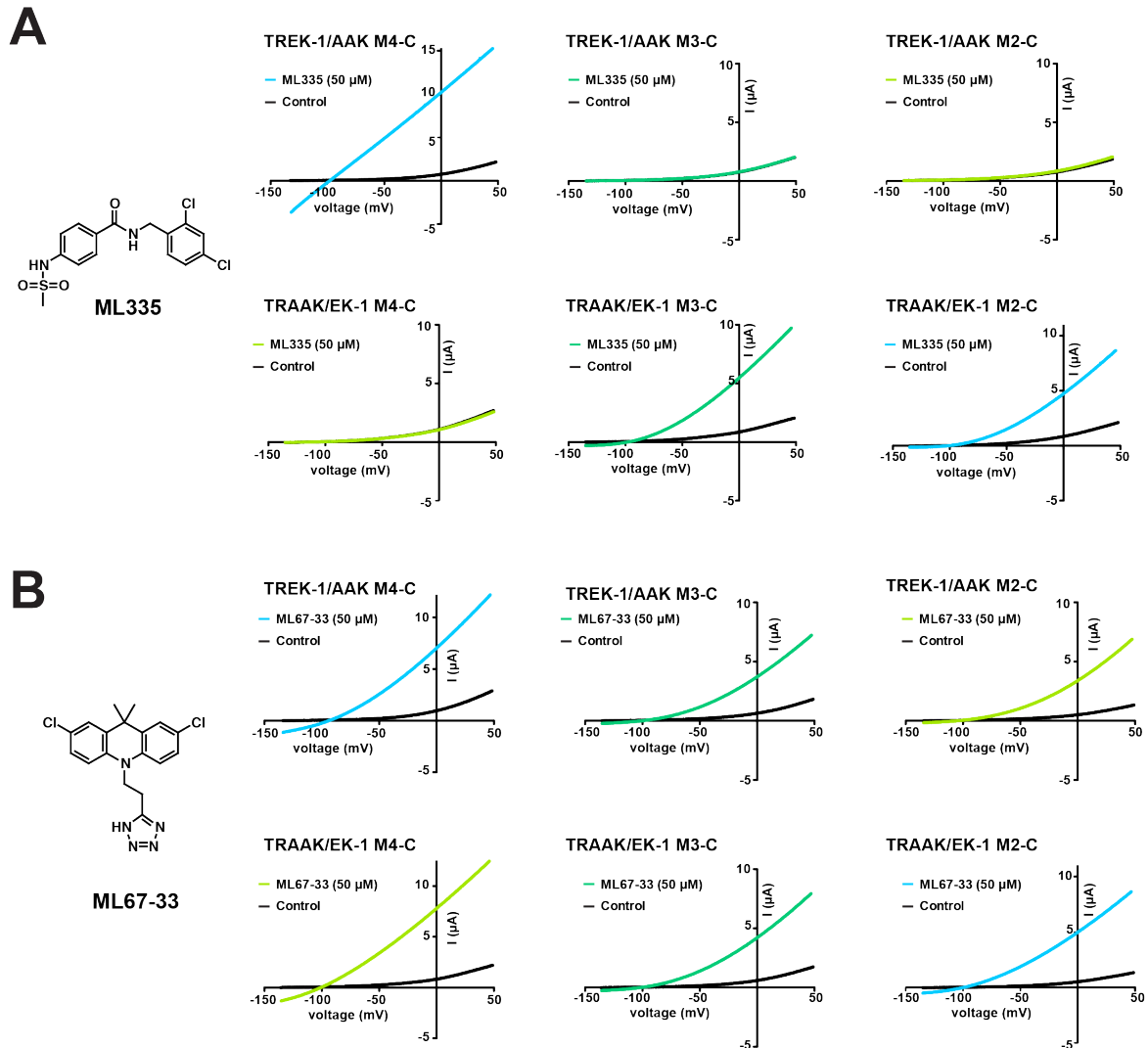


**Figure 2.8 | Supplementary Figure 2 - Exemplar responses of TREK-1/TRAAK chimeras to ML355 and ML67-33 activators**

**A**, Chemical structure of ML335 and exemplars for responses of TREK-1/AAK M4-C (light blue), TREK-1/AAK M3-C (green), TREK-1/AAK M2-C (light green), TRAAK/EK-1 M4-C (light green), TRAAK/EK-1 M3-C (green), and TRAAK/EK-1 M2-C (light blue) to 50  $\mu$ M ML335. **B**, Chemical structure of ML67-33 and exemplars for responses to 50  $\mu$ M ML67-33. Colors are as in 'A'.

**Table 2.1 | Summary of K2P response to BL-1249**

Background	Mutant	EC <sub>50</sub> (μM)	n (≥)
	-	5.5 ± 1.2	3
<b>K<sub>2</sub>P2.1 (TREK-1)</b>	K <sub>2</sub> P2.1 (TREK-1) <sub>GGG</sub>	19 ± 1	3
	K <sub>2</sub> P2.1 (TREK-1) <sub>Δ322</sub>	26 ± 8*	2
	K <sub>2</sub> P2.1 (TREK-1) <sub>Δ308</sub>	35 ± 8*	2
	TREK-1/AAK_T	7.7 ± 0.6	2
	TREK-1/AAK M4-C	19 ± 3	3
	TREK-1/AAK M3-C	28 ± 2	3
	TREK-1/AAK M2-C	39 ± 9	3
	TREK-1/TRAAK M2	26 ± 8	3
	F172M	15 ± 2	3
F185L	27 ± 5	3	
<b>K<sub>2</sub>P10.1 (TREK-2)</b>	-	8.0 ± 0.8	3
<b>K<sub>2</sub>P4.1 (TRAAK)</b>	-	48 ± 10*	3
	TRAAK/EK1_T	23 ± 4	2
	TRAAK/EK1 M4-C	45 ± 2	3
	TRAAK/EK1 M3-C	18 ± 2	3
	TRAAK/EK1 M2-C	28 ± 5	3
	TRAAK/TREK-1 M2	43 ± 11	3
	M134F	58 ± 34*	2
	L147F	27 ± 4	3

\*Denotes experiments where complete saturation of the response could not be reached due to BL-1249 solubility limits. For these cases, fits were imposed with an upper boundary of 15 (Fold Activation, I/I<sub>0</sub>) to estimate EC<sub>50</sub> and error.

Data derived from at least two independent experiments with each data point averaged from at least three oocytes

**Table 2.2 | Summary of BL-1249 analogue activation of K2P2.1 (TREK-1) and K2P4.1 (TRAAK)**

Compound	K <sub>2P</sub> 2.1 (TREK-1) EC <sub>50</sub> (μM)	n (≥)	K <sub>2P</sub> 4.1 (TRAAK) EC <sub>50</sub> (μM)	n (≥)
	-			
BL-1249	5.5 ± 1.2	3	48 ± 10*	3
BL-1249 amide	22 ± 8	3	>200	3
BL-1249-acid	44 ± 10**	4	>200	2
BL-1249-Ph	>200	3	>200	3
BL-1249-tricycle	34 ± 6	2	42 ± 9	3

\* EC<sub>50</sub> estimated imposing with an upper boundary of 15 (Fold Activation, I/I<sub>0</sub>)

\*\* EC<sub>50</sub> estimated imposing with an upper boundary of 20 (Fold Activation, I/I<sub>0</sub>)

Data derived from at least two independent experiments with each data point averaged from at least three oocytes



***Chapter 3 : Polynuclear ruthenium amines inhibit  $K_{2PS}$  via a 'finger in the dam'  
mechanism***

Lianne Pope, Marco Lolicato and Daniel L. Minor, Jr.

## ***Abstract***

The trinuclear ruthenium amine Ruthenium Red (RuR) inhibits diverse ion channels including  $K_{2P}$  potassium channels, TRPs, the mitochondrial calcium uniporter, CALHMs, ryanodine receptors, and Piezos. Despite this extraordinary array, there is very limited information for how RuR engages its targets. Here, using X-ray crystallographic and electrophysiological studies of an RuR-sensitive  $K_{2P}$ ,  $K_{2P2.1}$  (TREK-1) I110D, we show that RuR acts by binding an acidic residue pair comprising the 'Keystone inhibitor site' under the  $K_{2P}$  CAP domain archway above the channel pore. We further establish that Ru360, a dinuclear ruthenium amine not known to affect  $K_{2PS}$ , inhibits RuR-sensitive  $K_{2PS}$  using the same mechanism. Structural knowledge enabled a generalizable RuR 'super-responder' design strategy for creating  $K_{2PS}$  having nanomolar sensitivity. Together, the data define a 'finger in the dam' inhibition mechanism acting at a novel  $K_{2P}$  inhibitor binding site. These findings highlight the polysite nature of  $K_{2P}$  pharmacology and provide a new framework for  $K_{2P}$  inhibitor development.

## **Introduction**

Ruthenium red (RuR)<sup>1</sup> (Figure 1A) is a trinuclear oxo-bridged ruthenium amine polycation with many biological applications<sup>2</sup>, including a ~50 year legacy of use as an inhibitor of diverse ion channels, such as select members of the K<sub>2P</sub> (KCNK) family<sup>3-6</sup>, numerous TRP channels<sup>7-14</sup>, the mitochondrial calcium uniporter (MCU)<sup>15-18</sup>, CALHM calcium channels<sup>19-21</sup>, ryanodine receptors<sup>22, 23</sup>, and Piezo channels<sup>24, 25</sup>. Despite this remarkably wide range of ion channel targets and the recent boom in ion channel structural biology, structural understanding of how RuR acts on any ion channel is limited to a recent cryo-EM study of the CALHM2 channel that provides few molecular details regarding the coordination chemistry that underlies RuR binding<sup>21</sup>. In the case of K<sub>2P</sub>S, functional studies have established that a negatively charged residue at the base of the K<sub>2P</sub> extracellular domain that forms an archway over the channel pore, the CAP domain, comprises a key RuR sensitivity determinant in the natively RuR sensitive channels K<sub>2P</sub>9.1 (TASK-3)<sup>4-6</sup> and K<sub>2P</sub>10.1 (TREK-2)<sup>3</sup>. Further, installation of a negatively charged amino acid at the equivalent CAP domain site in a non-RuR sensitive channel is sufficient to confer RuR sensitivity<sup>3</sup>. The archway above the selectivity filter extracellular mouth made by the K<sub>2P</sub> CAP domain creates a pair of water-filled portals, the extracellular ion pathway (EIP), through which ions exit the channel under physiological conditions<sup>26-29</sup>. Although the EIP has been proposed as the site of RuR action<sup>3,6</sup>, the mechanism by which RuR inhibits K<sub>2P</sub>S remains unresolved and to date there is no direct structural evidence indicating that the EIP can be targeted by RuR or any other class of small molecule or protein-based inhibitors.

K<sub>2</sub>PS produce an outward 'leak' potassium current that plays a critical role in stabilizing the resting membrane potential of diverse cell types in the nervous, cardiovascular, and immune systems<sup>30-32</sup>. There are fifteen K<sub>2</sub>P subtypes comprising six subfamilies in which the channel monomers assemble into dimers wherein each subunit contributes two conserved pore forming domains to make the channel pore<sup>26-29,31,33</sup>. A range of physical and chemical signals control K<sub>2</sub>P function<sup>30-32</sup> and various K<sub>2</sub>P subtypes have emerging roles in a multitude of physiological responses and pathological conditions such as action potential propagation in myelinated axons<sup>34,35</sup>, anesthetic responses<sup>36,37</sup>, microglial surveillance<sup>38</sup>, sleep duration<sup>39</sup>, pain<sup>40-42</sup>, arrhythmia<sup>43</sup>, ischemia<sup>36,44,45</sup>, cardiac fibrosis<sup>46</sup>, depression<sup>47</sup>, migraine<sup>48</sup>, intraocular pressure regulation<sup>49</sup>, and pulmonary hypertension<sup>50</sup>. Although there have been recent advances in identifying new K<sub>2</sub>P modulators<sup>28,42,51-55</sup> and in defining key structural aspects of K<sub>2</sub>P channel pharmacology<sup>27,28,56</sup>, as is the case with many ion channel classes, pharmacological agents targeting K<sub>2</sub>PS remain poorly developed and limit the ability to probe K<sub>2</sub>P mechanism and biological functions<sup>57</sup>.

Here, we present X-ray crystal structures of a K<sub>2</sub>P2.1 (TREK-1) mutant bearing a single change at the site that controls K<sub>2</sub>P channel RuR sensitivity, K<sub>2</sub>P2.1 I110D, alone and complexed with two different polynuclear ruthenium amines, RuR and the dinuclear ruthenium amine, Ru360<sup>58</sup>, an inhibitor of the mitochondrial calcium uniporter<sup>15,59,60</sup> not previously known to affect potassium channels. The structures show that the negatively charged residues at position 110 comprise 'the Keystone inhibitor site' on the ceiling of the CAP archway to which positively charged RuR and Ru360 bind through ionic interactions. This interaction holds the polybasic compounds directly over the mouth of

the channel pore, blocks one EIP arm, and prevents channel function. Functional studies corroborated by a crystal structure of K<sub>2P</sub>2.s I110D bound simultaneously to RuR and a small molecule activator of the channel selectivity filter 'C-type gate', ML335<sup>28</sup>, establish that polynuclear ruthenium amine inhibition of K<sub>2P</sub>s is unaffected by C-type gate activation. Using molecular recognition principles derived from the structures of the K<sub>2P</sub>:RuR and K<sub>2P</sub>:Ru360 complexes, we demonstrate a general design strategy for endowing any K<sub>2P</sub> channel with nanomolar RuR sensitivity. Our work establishes that polynuclear ruthenium compounds act through a 'finger in the dam' mechanism to inhibit K<sub>2P</sub> function by binding under the CAP domain archway at the Keystone inhibitor site and blocking the pore. The structural definition of this new modulatory site demonstrates the importance of electronegativity and specific sidechain geometry for polynuclear amine molecular recognition, defines a new small molecule binding site that augments the rich, polysite pharmacology of K<sub>2P</sub> modulation, and opens a path for targeting the Keystone inhibitor site and EIP for the development of new K<sub>2P</sub> modulators.

## Results

### A single site in the K<sub>2P</sub> CAP domain confers RuR sensitivity

K<sub>2P</sub>2.1 (TREK-1) is the founding member of the thermo- and mechanosensitive subgroup of K<sub>2P</sub>S<sup>31,61</sup>. Although this channel is resistant to RuR inhibition (Figure 1B and D, Table 1)<sup>3</sup>, two electrode voltage clamp (TEVC) recordings in *Xenopus* oocytes of outward current inhibition by RuR under physiological ionic conditions showed that installation of a point mutation I110D at the base of the K<sub>2P</sub>2.1 (TREK-1) CAP domain conferred sub-micromolar RuR sensitivity to K<sub>2P</sub>2.1 (TREK-1) (IC<sub>50</sub> = 0.287 ± 0.054 μM)(Figures. 1C-D, Table 1). This inhibition followed a 1:1 RuR:channel stoichiometry, in agreement with K<sub>2P</sub> studies using other recording protocols<sup>3,5</sup>, and validates previous studies showing that this point mutant renders K<sub>2P</sub>2.1 (TREK-1) sensitive to RuR<sup>3</sup>. Importantly, the response of K<sub>2P</sub>2.1 I110D to RuR matched that of the closely-related, natively-RuR sensitive K<sub>2P</sub>10.1 (TREK-2)<sup>3</sup> in which there are native aspartate residues at the K<sub>2P</sub>2.1 Ile110 analogous site (Figures 1D and S1A, Table 1) (IC<sub>50</sub> = 0.287 ± 0.054 and 0.23 ± 0.06 μM for K<sub>2P</sub>2.1 I110D and K<sub>2P</sub>10.1 (TREK-2)<sup>3</sup>, respectively), suggesting that the I110D change to K<sub>2P</sub>2.1 (TREK-1) captures the essence of the requirements for RuR inhibition.

Because another natively-RuR sensitive K<sub>2P</sub>, K<sub>2P</sub>9.1 (TASK-3), has a glutamate at the K<sub>2P</sub>2.1 I110D equivalent site (Figure S1A) that is essential for its RuR response<sup>4-6</sup>, we asked whether I110E would also render K<sub>2P</sub>2.1 (TREK-1) sensitive to RuR. Indeed, TEVC measurements showed that RuR inhibited K<sub>2P</sub>2.1 I110E (IC<sub>50</sub> = 13.6 ± 2.7 μM, Table 1) (Figures 1D and S1B, Table 1). RuR inhibition was ~50 fold weaker than that observed for K<sub>2P</sub>2.1 I110D, indicating that the I110D and I110E changes are not equivalent even

though both bear similar negative charges. Further, introduction of a positively charged residue, K<sub>2P</sub>2.1 I110K, yielded channels as insensitive to RuR as K<sub>2P</sub>2.1 (TREK-1) (Figures 1D and S1C). RuR inhibition was essentially independent of voltage for K<sub>2P</sub>2.1 I110D and K<sub>2P</sub>2.1 I110E (Figures S1D-G), consistent with prior reports of RuR inhibition of other K<sub>2P</sub>S<sup>62</sup>. Together, these results provide key support for the idea that a negative charge at the K<sub>2P</sub> CAP domain base is a crucial determinant of RuR inhibition of K<sub>2P</sub>S<sup>3-6</sup>. Importantly, the observation of the ~50 fold difference between the RuR sensitivity of two essentially equivalently negatively charged residues in the same structural context, K<sub>2P</sub>2.1 I110D and K<sub>2P</sub>2.1 I110E (Figure 1D, Table 1) indicates that electrostatics is not the sole factor contributing to the RuR:channel interaction and points to a role for the detailed geometry of the interaction of the negatively charged residues with RuR.

### **Structural definition of the K<sub>2P</sub> RuR binding site**

To understand how RuR inhibits K<sub>2P</sub> channels, we determined the X-ray crystal structures of K<sub>2P</sub>2.1 I110D alone and bound to RuR at resolutions of 3.40Å and 3.49Å, respectively (Table S1) on the background of the previously crystallized construct K<sub>2P</sub>2.1 (TREK-1)<sub>cryst</sub><sup>28</sup>. Apart from the I110D change, the overall structure of K<sub>2P</sub>2.1 I110D was essentially identical to K<sub>2P</sub>2.1 (TREK-1)<sub>cryst</sub> (RMSD<sub>Cα</sub> = 0.575Å). Importantly, K<sub>2P</sub>2.1 I110D was structurally similar to the natively-RuR sensitive K<sub>2P</sub>10.1 (TREK-2)<sup>28</sup> (RMSD<sub>Cα</sub> = 0.938Å), especially in the neighborhood of K<sub>2P</sub>10.1 (TREK-2) Asp140 (Figure S2A, Table S2), the residue that is fundamental to K<sub>2P</sub>10.1 (TREK-2) RuR sensitivity<sup>3</sup>. Hence, when taken together with the functional similarity to K<sub>2P</sub>10.1 (TREK-2), the K<sub>2P</sub>2.1 I110D:RuR complex should capture the essential elements that contribute to the RuR response of natively RuR-sensitive K<sub>2P</sub>S.

The K<sub>2P</sub>2.1 I110D:RuR complex structure shows that RuR binds under the CAP domain archway directly above the selectivity filter at a site we term the 'Keystone inhibitor site' due to the location of the I110D residues at the peak of the CAP archway ceiling (Figures 1E and S2B-C). RuR binds with a 1:1 stoichiometry to the channel that matches expectations from functional studies (Table 1)<sup>3,5,62</sup>. To facilitate description of this and other RuR complexes, we designate the three RuR ruthenium amine centers as Ru<sub>A</sub>, Ru<sub>B</sub>, and Ru<sub>C</sub>. RuR binds at ~45° angle relative to the CAP and selectivity filter in a pose that places one of the terminal ruthenium-amine moieties, Ru<sub>A</sub>, directly above the column of selectivity filter ions in a position that overlaps with the S0 ion site from the K<sub>2P</sub>2.1 I110D structure (Figures 1F and S2B). The Ru<sub>B</sub> and Ru<sub>C</sub> moieties block one EIP arm (Figures 1E-F). Notably, the observed pose is very different from the previously proposed horizontal RuR binding pose in which the Ru<sub>B</sub> moiety sits above the column of selectivity filter ions<sup>6</sup>. The I110D carboxylates coordinate RuR directly through electrostatic interactions with all three ruthenium-amine moieties using a multipronged set of interactions (Figure 1F and G). Such direct coordination suggests why K<sub>2P</sub>2.1 I110D and K<sub>2P</sub>2.1 I110E have different magnitude RuR responses, as the extra methylene groups in K<sub>2P</sub>2.1 I110E would not allow the same type of direct coordination observed for the smaller aspartate pair (Figure 1G). Besides direct electrostatic interactions, there are van der Waals contacts between Ru<sub>C</sub> and the side chain of CAP residue Val107 from chain A, Ru<sub>A</sub> and Ru<sub>B</sub> with Asn111 from each chain of the dimer, Ru<sub>A</sub> with Asp256 from chain B, and Ru<sub>B</sub> with Gly255 from chain B. Apart from a slight reorientation of the I110D sidechains and CAP to accommodate RuR (Figure S2D), there are only minor conformational changes with respect to the unbound K<sub>2P</sub>2.1 I110D



( $\text{RMSD}_{\text{C}\alpha} = 0.688\text{\AA}$ )(Table S2). Hence, RuR binds to an essentially pre-organized electronegative binding site at the CAP base.

### **K<sub>2P</sub> RuR binding is independent of C-type gate activation**

Activation of the selectivity filter, 'C-type' gate is central to K<sub>2P</sub> function<sup>28,63-66</sup>. Because RuR binds directly above the selectivity filter and overlaps with the S0 ion, we asked whether C-type gate activation by mutation, G137I<sup>63,67</sup> or by a small molecule activator, ML335<sup>28</sup>, would impact RuR inhibition of K<sub>2P</sub>2.1 I110D (Figure 2A-B). TEVC experiments showed that RuR inhibits K<sub>2P</sub>2.1 I110D/G137I with an IC<sub>50</sub> (IC<sub>50</sub> = 0.154 ± 0.023 μM) that is very similar to that for K<sub>2P</sub>2. I110D, indicating that C-type gate activation does not influence RuR block of the channel (Figure 2C, Table 1).

Before assessing whether RuR inhibition was influenced by ML335 activation, we first measured the activation of K<sub>2P</sub>2.1 I110D by ML335. The I110D change is >15Å from the K<sub>2P</sub> modulator pocket that forms the ML335 binding site and is not expected to impact ML335 activation. In line with these expectations, there was no difference in the response of K<sub>2P</sub>2.1 I110D to ML335 activation relative to K<sub>2P</sub>2.1 (TREK-1) (EC<sub>50</sub> (ML335) = 11.8 ± 2.3 and 14.3 ± 2.7 μM for K<sub>2P</sub>2. I110D and K<sub>2P</sub>2.1 (TREK-1)<sup>28</sup>, respectively) (Figures S3A-B). Importantly, similar to the observations with the G137I C-type gate activation mutant, pharmacological C-type gate activation by saturating amounts of ML335 had minimal impact on the RuR response relative to K<sub>2P</sub>2.1 I110D (IC<sub>50</sub> = 0.173 ± 0.021 μM, Table 1). Together, these data demonstrate that RuR inhibition is essentially independent of C-type gate activation (Figures 2A-D, Table 1) and are consistent with the observed position of RuR above the selectivity filter.

To see whether there might be structural differences in the interaction of RuR with an activated C-type gate, we determined the structure of the K<sub>2P</sub>2.1 I110D:RuR:ML335 complex at 3.00Å resolution (Figures 2E and S3C-D, Table S1). This structure is very similar to the K<sub>2P</sub>2.1 I110D:RuR complex (Figures S3C-E) (RMSD<sub>C $\alpha$</sub>  = 0.507Å) and to the previously determined K<sub>2P</sub>2.1:ML335 complex<sup>28</sup> (RMSD<sub>C $\alpha$</sub>  = 0.480Å) (Table S2). The structure shows that RuR binds to the Keystone inhibitor site using a pose that is very similar to that in the K<sub>2P</sub>2.1 I110D:RuR complex. Both I110D sidechains coordinate multiple Ru centers through direct interactions to RuR (Figures 2F-G) like those in the K<sub>2P</sub>2.1 I110D:RuR complex and there are van der Waals contacts with residues in the CAP and selectivity filter outer mouth. These fundamental similarities in binding to the Keystone inhibitor site are consistent with the similar IC<sub>50</sub>s measured with or without ML335 C-type gate activation (Figures 2C-D, Table 1).

### **Polynuclear ruthenium compounds inhibit K<sub>2P</sub>s at a common site**

The dinuclear oxo-bridged ruthenium compound, Ru360 (Figure 3A)<sup>58</sup>, has many characteristics in common with RuR (cf. Figure 1A). Ru360 is best known as an inhibitor of the mitochondrial calcium uniporter (MCU)<sup>15,59,60</sup>, a property it shares with RuR<sup>68</sup>. Yet, despite its structural similarity to RuR and the fact that both Ru360 and RuR inhibit MCU, Ru360 has not been reported to block K<sub>2P</sub> channels. To ask whether Ru360 might inhibit RuR-sensitive K<sub>2P</sub> channels, we used TEVC to measure the Ru360 responses of K<sub>2P</sub>2.1 (TREK-1), K<sub>2P</sub>2.1 I110D, and the natively RuR sensitive K<sub>2P</sub>s, K<sub>2P</sub>10.1 (TREK-2)<sup>3</sup> and K<sub>2P</sub>9.1 (TASK-3)<sup>4-6</sup>. Application of 100  $\mu$ M Ru360 to K<sub>2P</sub>2.1 (TREK-1) had no effect, consistent with the insensitivity of this channel to RuR (Figures 3B and F). However, in stark contrast, Ru360 inhibited all of the RuR sensitive K<sub>2P</sub>s with micromolar potency (IC<sub>50</sub>

=  $11.3 \pm 1.8$ ,  $2.8 \pm 1.2$ , and  $15.6 \pm 2.7$   $\mu\text{M}$  for  $\text{K}_{2\text{P}2.1}$  I110D,  $\text{K}_{2\text{P}10.1}$  (TREK-2), and  $\text{K}_{2\text{P}9.1}$  (TASK-3), respectively) (Figures 3C-F, Table 1). Similar to RuR inhibition, Ru360 block of  $\text{K}_{2\text{P}}\text{S}$  was independent of voltage (Figures S4A-D). For both  $\text{K}_{2\text{P}2.1}$  I110D and  $\text{K}_{2\text{P}10.1}$  (TREK-2) the Ru360  $\text{IC}_{50}\text{s}$  are >10-fold weaker than those for RuR. Because there is a reported 30-fold discrepancy in the  $\text{IC}_{50}$  of RuR for  $\text{K}_{2\text{P}9.1}$  (TASK-3) in the literature ( $0.35 \mu\text{M}^5$  vs.  $10 \mu\text{M}^6$ ) that precluded a direct comparison with our Ru360 data, we measured inhibition of  $\text{K}_{2\text{P}9.1}$  (TASK-3) by RuR to resolve whether RuR and Ru360 had similar or different  $\text{IC}_{50}\text{s}$  for  $\text{K}_{2\text{P}9.1}$  (TASK-3). Our TEVC experiments measured a sub-micromolar  $\text{IC}_{50}$  for RuR inhibition of  $\text{K}_{2\text{P}9.1}$  (TASK-3) ( $\text{IC}_{50} = 0.114 \pm 0.021 \mu\text{M}$ ) (Figures S4E-F, Table 1) that agrees with other *Xenopus* oocyte TEVC studies<sup>5</sup>. These data establish that, as with the other polynuclear ruthenium-sensitive  $\text{K}_{2\text{P}}\text{S}$  we studied, Ru360 is a weaker inhibitor of  $\text{K}_{2\text{P}9.1}$  (TASK-3) than RuR. The uniformly weaker potency of Ru360 versus RuR against  $\text{K}_{2\text{P}}\text{S}$  correlates with the fact that Ru360 carries half the positive charge of RuR (+3 versus +6) and underscores the important role that electrostatics plays in the binding of these polycations.

To understand the details of how Ru360 inhibits  $\text{K}_{2\text{P}}\text{S}$ , we determined of a 3.51Å resolution X-ray crystal structure of the  $\text{K}_{2\text{P}2.1}$  I110D:Ru360 complex (Figures 3G-H, Table S1). As with the RuR complexes, the  $\text{K}_{2\text{P}2.1}$  I110D:Ru360 complex has a channel structure that is overall very similar to the structure of the  $\text{K}_{2\text{P}2.1}$  I110D in the absence of the inhibitor ( $\text{RMSD}_{\text{C}\alpha} = 0.665\text{\AA}$ ) and to the  $\text{K}_{2\text{P}2.1}$  I110D:RuR complex ( $\text{RMSD}_{\text{C}\alpha} = 0.561\text{\AA}$ ) (Figure S4G, Table S2). Ru360 binds to the Keystone inhibitor site in a pose that matches RuR (Figures 3H and S4G-I). Notably, even though Ru360 has one fewer ruthenium atoms than RuR, one of the Ru360 ruthenium-amine moieties, denoted  $\text{Ru}_A$ ,

occupies essentially the same site as the RuR Ru<sub>A</sub> moiety and overlaps with the S0 ion site (Figure 3H), while the other ruthenium amine, Ru<sub>B</sub>, overlaps the position of the RuR Ru<sub>B</sub> moiety and blocks one EIP arm. There are essentially no conformational changes between K<sub>2P</sub>2.1 I110D and the K<sub>2P</sub>2.1 I110D:Ru360 complex except for a change near the base of the CAP helices similar to that seen in the RuR complexes (Figure S4I). The Keystone inhibitor site acidic sidechains directly coordinate the Ru360 Ru<sub>A</sub> and Ru<sub>B</sub> centers (Figure 3I). Ru360 also makes van der Waals contacts to the upper part of the selectivity filter and part of the CAP from chain A similar to those made by RuR (cf. Figures 1G, 2G, and 3I). Together, these data demonstrate that Ru360 inhibits RuR-sensitive K<sub>2P</sub>s and reveals the common mode by which polynuclear ruthenium amines affect K<sub>2P</sub> channels by binding to the Keystone inhibitor site, blocking ion exit from the selectivity filter, and obstructing one EIP arm.

### **Protein engineering creates RuR super-responders**

Because the electronegative nature of the Keystone inhibitor site is a key determinant of K<sub>2P</sub> channel sensitivity to polynuclear ruthenium compounds, we wanted to test whether increasing the electronegative character of surrounding portions of the EIP would also affect RuR block. To identify candidate sites, we looked for elements on the floor of the RuR and Ru360 binding site that made close contacts with the inhibitors. This analysis identified the backbone atoms of the selectivity filter outer mouth residues Asn147 and Asp256 as the nearest neighbors (Figures 1G, 2G, 3G, and 4A). As we cannot easily change the backbone atoms, we considered changing the properties of the sidechains from these positions. Sequence comparison of representatives from each K<sub>2P</sub> subtype (Figure S5A) shows that the two sites have very different conservation patterns. The

Asn147 site shows a range of amino acid types. This variability contrasts with the strict conservation at the Asp256 site. Because all  $K_{2P}$ s have aspartate at the 256 position regardless of whether or not they RuR-sensitive, we reasoned that the negatively charged sidechain at this site has no influence on RuR binding. By contrast, the amino acid diversity at the Asn147 site indicated that this site might have different properties than the Asp256 site. Hence, we tested whether replacing Asn147 with a negatively charged residue would impact  $K_{2P2.1}$  (TREK-1) RuR sensitivity. TEVC experiments showed that RuR inhibited both  $K_{2P2.1}$  N147D and  $K_{2P2.1}$  N147E (Figures 4C-F), demonstrating that the presence of an acidic residue at the Keystone inhibitor site is not the only means by which a  $K_{2P}$  channel can acquire RuR sensitivity. Notably, there was a marked difference in the  $IC_{50}$ s between the two mutants with N147E having a much greater susceptibility to RuR inhibition than N147D ( $IC_{50} = 0.0733 \pm 0.0165$  and  $47.7 \pm 6.3 \mu\text{M}$  for  $K_{2P2.1}$  N147E and  $K_{2P2.1}$  N147D, respectively) (Figures 4G-I, Table 1). Similar to RuR inhibition of other  $K_{2P}$ s, RuR block of  $K_{2P2.1}$  N147E was essentially voltage independent, whereas  $K_{2P2.1}$  N147D showed a mild voltage-dependence (Figures S5B-E).

Because both N147D and N147E changes were able to confer RuR sensitivity to  $K_{2P2.1}$  (TREK-1) (Figure 4F, Table 1), we asked whether having negatively charged residues on both the ceiling (residue 110) and floor (residue 147) of the RuR binding site would result in enhanced RuR inhibition. TEVC measurements of the RuR responses of  $K_{2P2.1}$  I110D/N147D and  $K_{2P2.1}$  I110D/N147E revealed that both double mutants had similar  $IC_{50}$ s ( $IC_{50} = 0.0127 \pm 0.0023$  and  $0.0126 \pm 0.0034 \mu\text{M}$  for  $K_{2P2.1}$  I110D/N147D and  $K_{2P2.1}$  I110D/N147E, respectively) (Figures S5F-G, Table 1). Similar to the I110D

and N147E mutants, the response of both double mutant channels to RuR was essentially independent of voltage (Figures S5H-J).

The  $IC_{50}$ s values of the double mutants were an order of magnitude better than that of  $K_{2P2.1}$  I110D alone and three orders of magnitude better than  $K_{2P2.1}$  N147D. Hence, we turned to double mutant cycle analysis<sup>69,70</sup> to assess the extent of synergy between the two sites with respect to RuR inhibition. This analysis uncovered a strong positive cooperativity for the I110D/N147D pair ( $\Delta\Delta G = -4.1$  kcal mol<sup>-1</sup>) (Figure S6A). By contrast, the enhanced RuR response of the I110D/N147E combination resulted from essentially additive contributions of the two negatively charged residues ( $\Delta\Delta G = -0.3$  kcal mol<sup>-1</sup>) (Figure S6B). The fact that the two double mutant pairs do not behave equivalently even though both comprise two sets of acidic sidechains, together with the observation that there is a substantial difference in the impact of I110D versus I110E alone on the RuR sensitivity of  $K_{2P2.1}$  (TREK-1) (Figure 1E, Table 1) reinforces the idea that RuR molecular recognition requires both general electrostatic interactions and the direct coordination from the acidic sidechains. Taken together, our results indicate that details of these two factors tune the strength of the RuR interaction with the channel. Because of the largely conserved nature of the  $K_{2P}$  architecture in the region of the CAP and selectivity filter<sup>26-29</sup>, installing acidic residues simultaneously at the equivalents of the  $K_{2P2.1}$  (TREK-1) Ile110 and Asn147 positions should endow any  $K_{2P}$  of interest sensitive to nanomolar concentrations of RuR.

## ***Discussion***

Polynuclear ruthenium compounds have been used for nearly 50 years to control the function of various ion channels<sup>3-20,22-25</sup>. Yet, despite this widespread application in the study of a multitude of diverse ion channels, there is only limited visualization of how such compounds might interact with and affect the function of their targets<sup>21</sup>. The K<sub>2P</sub>:RuR and K<sub>2P</sub>:Ru360 complexes presented here provide the first detailed structural views of how this class of inorganic polycations can inhibit ion channel function. The structures demonstrate general molecular recognition principles in which a channel uses acidic sidechains to coordinate both trinuclear, RuR, and dinuclear, Ru360, ruthenium amines through direct, multipronged electrostatic interactions. Both compounds block the flow of ions through the channel using a ‘finger in the dam’ mechanism that exploits the unique archway architecture that the K<sub>2P</sub> CAP domain creates above the K<sub>2P</sub> channel mouth (Figure 5A).

K<sub>2P</sub>PS are the only potassium channel family that bears a CAP domain, an extracellular dimerization domain positioned directly above the channel pore<sup>26,29</sup>. The structures presented here show that a pair of aspartic acids located on the underside of the CAP archway at a site that controls the RuR response of natively-RuR sensitive K<sub>2P</sub>S, K<sub>2P</sub>10.1 (TREK-2) and K<sub>2P</sub>9.1 (TASK-3)<sup>4-6</sup> and of the RuR-sensitive mutant K<sub>2P</sub>2.1 I110D (Figure 1E)<sup>3</sup>, create a polycation binding site, the Keystone inhibitor site. This site forms the primary point of interaction with a single RuR or Ru360 that plugs one arm of the bifurcated EIP created by the CAP domain archway (Figures 1E-F, 2E-F, 3G-H). This structural observation defines an unambiguous mechanism of action for how polyruthenium amines inhibit K<sub>2P</sub>PS, as holding a large polycation above the channel pore

would both physically block ion exit as well as provide an electrostatic barrier to permeant ion movement (Figure 5A). Ru360 a dinuclear oxo-bridged ruthenium amine inhibitor of the mitochondrial calcium uniporter<sup>15,59,60</sup> that had not previously been reported to affect potassium channels also inhibits engineered, K<sub>2P</sub>2.1 I110D, and natively-RuR sensitive K<sub>2PS</sub>, K<sub>2P</sub>10.1 (TREK-2), and K<sub>2P</sub>9.1 (TASK-3), in a manner similar to RuR (Figure 3E-F). Hence, even though RuR and Ru360 bind to a largely pre-formed binding site, there is sufficient plasticity to permit the binding of different types of polyruthenium cations. Consistent with a binding site positioned above the selectivity filter and outside of the transmembrane electric field, polynuclear ruthenium amine inhibition of K<sub>2PS</sub> is independent of voltage (Figures S1E-G, S4A-B, S5B-E and H-J) and the C-type gate activation (Figure 2D). Together, the data define a mechanism of action in which polynuclear ruthenium amines inhibit K<sub>2P</sub> function by preventing ion flow out of the K<sub>2P</sub> selectivity filter and through the EIP (Figure 5A).

Although many ion channels lack the extracellular archway made by the K<sub>2P</sub> CAP domain, the structures of the K<sub>2P</sub>:polyruthenium amine complexes reveal general molecular recognition principles that are likely to be shared with RuR and Ru360 sensitive ion channels. The requirement to have a negatively charged residue at the Keystone inhibitor site for RuR (Figure 1E)<sup>3-6</sup> and Ru360 (Figure 3F) responses, together with the observation that inhibitor potency is proportional to the total charge (Table 1) highlights the importance of electrostatic interactions for recognizing ruthenium polycations. The multipronged direct coordination of the RuR and Ru360 ruthenium amine moieties (Figures 1G, 2G, and 3G) shows the important role that direct coordination by acidic sidechains plays in binding both compounds. The observation that equivalently charged



residues having different sidechain geometries, aspartate and glutamate, display differential effects on RuR potency at the Keystone inhibitor site (Figure 1D and Table 1) highlights the importance of direct ligand coordination for tuning the strength of the interaction with polynuclear ruthenium amines. It should be noted that K<sub>2P</sub>4.1 (TRAAK) is inhibited by RuR but lacks a negatively charged residue in the Keystone inhibitor site (Figure S1A) and binds RuR with a higher stoichiometry than observed for the K<sub>2P</sub> channels studied here (Table 1)<sup>3,62</sup>. These differences suggest that RuR inhibition of K<sub>2P</sub>4.1 (TRAAK) occurs using a mechanism different from the ‘finger in the dam’ mechanism. Given the importance of direct interactions between RuR and Ru360 and the acidic sidechains in the target channels studied here and the fact that acidic residues are key to the RuR sensitivity of other channels<sup>25,71</sup>, we expect that similar types of multipronged coordination by sidechain carboxylates are likely to contribute to the RuR and Ru360 block of other polynuclear ruthenium amine sensitive channels such as K<sub>2P</sub>4.1 (TRAAK), TRPs<sup>7-14</sup>, the mitochondrial calcium uniporter (MCU)<sup>15-18</sup>, CALHM calcium channels<sup>19-21</sup>, ryanodine receptors<sup>22,23</sup>, and Piezo channels<sup>24,25</sup>, even if the details of where the inhibitor binds to the channel differ.

K<sub>2P</sub> channels can be modulated by a number of different small molecules and lipids<sup>57</sup>. When placed in the context of previous structural studies of K<sub>2P</sub> modulator interactions<sup>27,28,56</sup>, our studies highlight an emerging picture of the complex, multisite structural pharmacology that contributes to the control of K<sub>2P</sub> function. The discovery of the Keystone inhibitor site reveals that there are at least four control sites that span from the inner leaflet of the bilayer to the extracellular parts of the channel through which exogenous molecules affect channel function (Figure 5B). These include a modulatory

lipid binding site in the bilayer inner leaflet<sup>28</sup>, the fenestration site residing at the intersection of the movable M4 transmembrane helix and the lower part of the selectivity filter that can be targeted by both small molecule activators and inhibitors<sup>27,56</sup>, the K<sub>2P</sub> modulator pocket site<sup>28</sup>, and the Keystone inhibitor site. Exploring the degree of conformational coupling among these modulatory sites will be important for understanding the extent of synergistic or antagonistic actions within the various classes of K<sub>2P</sub> modulators. Acquiring this type of knowledge will be crucial for creating new interventions that could offer exquisite control of K<sub>2P</sub> function.

The ‘finger in the dam’ inhibitory mechanism defined here provides a blueprint for the development of small molecule or protein-based K<sub>2P</sub> modulators that could reach through the EIP to the Keystone inhibitor site. In this regard, designing compounds having moieties that interact with the Keystone inhibitor site but that also make contacts to non-conserved features of CAP exterior could yield subtype-selective modulators. Biologics, such as nanobodies, may be particularly suited to this type of molecular recognition mode. Further, given the highly conserved nature of the K<sub>2P</sub> channel architecture in the region of the CAP and selectivity filter<sup>26-29</sup>, the strategies we used to develop RuR super-responders should be applicable to other K<sub>2P</sub> subfamily members to create subtypes endowed with RuR sensitivity. Such RuR-sensitive channels could be used to dissect the roles of various K<sub>2P</sub>S in their native physiological settings.

## **Significance**

Ruthenium Red (RuR) is a trinuclear, oxo-bridged ruthenium amine polycation that has many biological applications, including a ~50 year legacy as an inhibitor of diverse classes of ion channels. RuR inhibits select members of the K<sub>2P</sub> (KCNK) family, numerous

TRP channels, the mitochondrial calcium uniporter, CALHM calcium channels, ryanodine receptors, and Piezo channels. Despite this remarkably wide range of ion channel targets, there are extremely limited structural data describing how RuR binds to any ion channel target. Our studies show how two polyruthenium compounds, RuR and Ru360, inhibit  $K_{2P}$  channels through a 'finger in the dam' mechanism in which these polycations bind at a novel site, the 'Keystone inhibitor site', formed by acidic residue pair under the  $K_{2P}$  CAP domain archway above the channel pore. This series of structures, together with functional studies, outline the molecular recognition principles that govern how RuR and Ru360 bind to specific sites of proteins using a mixture of electrostatics and polyvalent coordination by acidic sidechains. These principles are likely to control RuR and Ru360 binding to a wide range of diverse ion channel targets. Moreover, we show that we can use knowledge of these factors to engineer RuR 'super-responder'  $K_{2P}$ s that have RuR sensitivity in the low nanomolar range. The protein engineering strategy we define should be generally applicable to any  $K_{2P}$  of interest and provide a new method for dissecting the function of specific  $K_{2P}$ s in complex settings such as neurons, the brain, and the cardiovascular system. Together, the data define a 'finger in the dam' inhibition mechanism acting at a novel  $K_{2P}$  inhibitor binding site. These findings highlight the polysite nature of  $K_{2P}$  pharmacology and provide a new framework for  $K_{2P}$  inhibitor development.

## **Materials and Methods**

### **Molecular Biology**

Murine K<sub>2P</sub>2.1 (TREK-1) (Gene ID 16526), K<sub>2P</sub>10.1 (TREK-2) (Gene ID: 72258), and K<sub>2P</sub>9.1 (TASK-3) (Gene ID: 223604) were each expressed from in a pGEMHE/pMO vector for two-electrode voltage clamp (TEVC) experiments as described previously<sup>28,55</sup>. A previously described version of murine K<sub>2P</sub>2.1 (TREK-1) in a *Pichia pastoris* pPicZ plasmid, K<sub>2P</sub>2.1(TREK-1)<sub>CRYST</sub><sup>28</sup>, encoding residues 21-322 and bearing the following mutations: K84R, Q85E, T86K, I88L, A89R, Q90A, A92P, N95S, S96D, T97Q, N119A, S300C, E306A, was used for structural studies. Mutants of K<sub>2P</sub>2.1 (TREK-1) and K<sub>2P</sub>2.1(TREK-1)<sub>CRYST</sub> were generated using site-directed mutagenesis (PFU Turbo AD, Agilent) and verified by sequencing of the complete gene.

### **Two-electrode voltage clamp (TEVC) electrophysiology**

*Xenopus laevis* oocytes were harvested according to UCSF IACUC Protocol AN129690 and digested using collagenase (Worthington Biochemical Corporation, #LS004183, 0.7-0.8 mg mL<sup>-1</sup>) in Ca<sup>2+</sup>-free ND96 (96 mM NaCl, 2 mM KCl, 3.8 mM MgCl<sub>2</sub>, 5 mM HEPES pH 7.4) immediately post-harvest, as previously reported<sup>28,55</sup>. Oocytes were maintained at 18°C in ND96 (96 mM NaCl, 2 mM KCl, 1.8 mM CaCl<sub>2</sub>, 2 mM MgCl<sub>2</sub>, 5 mM HEPES pH 7.4) supplemented with antibiotics (100 units mL<sup>-1</sup> penicillin, 100 µg mL<sup>-1</sup> streptomycin, 50 µg mL<sup>-1</sup> gentimycin) and used for experiments within one week of harvest. mRNA for oocyte injection was prepared from plasmid DNA using mMessage Machine T7 Transcription Kit (Thermo Fisher Scientific), purified using RNEasy kit (Qiagen), and stored as stocks and dilutions in RNase-free water at -80°C.

Defolliculated stage V-VI oocytes were microinjected with 50 nL of 0.1-6 ng mRNA

and currents were recorded within 24-48 hours of injection. Oocytes were impaled by two standard microelectrodes (0.3-3.0 M $\Omega$ ), filled with 3M KCl and subjected to constant perfusion of ND96. Currents were elicited from a -80 mV holding potential using a 500 ms ramp ranging from -140 to +50 mV.

Recording solutions containing Ruthenium red (RuR) (Millipore-Sigma, R2751) and Ru360 (Millipore-Sigma, Calbiochem – 557440) were prepared immediately prior to use. RuR was weighed and dissolved directly into ND96 at 200  $\mu$ M in ND96 and then diluted into ND96 for tested experimental concentrations. The pH of the stock solution was checked to ensure no change occurred. Due to its instability in aqueous solutions, Ru360 solutions were covered with aluminum foil to minimize exposure to light and to avoid degradation. RuR and Ru360 were determined to be stable in recording solutions for duration of typical experiment length by measuring UV absorbance at 536 nm and 363 nm, respectively, before and after length of the recording session. ML335 was synthesized as described previously<sup>28</sup>. ML335 recording solutions were prepared from a DMSO stock stored at -20°C (final DMSO concentration was 0.1%).

Data were recorded using a GeneClamp 500B (MDS Analytical Technologies) amplifier controlled by pClamp software (Molecular Devices), and digitized at 1 kHz using Digidata 1332A (MDS Analytical Technologies). For each recording, control solution (ND96) was perfused over a single oocyte until current was stable before switching to solutions containing the test compounds at various concentrations and again allowed to stabilize before recording final, stabilized trace. Fractional block at the potential of interest was determined as  $\frac{I-I_B}{I_0-I_B}$  in which I is the measured current,  $I_0$  is the current in the absence

of the test compound, and  $I_B$  is the basal current derived from an average of uninjected oocytes ( $n=14$ ). For dose-response curves, each point is an average of at least three oocytes recorded from at least two independent batches of oocytes. Representative traces and dose response plots were generated in Graphpad Prism Version 5 (GraphPad Software, San Diego California USA, [www.graphpad.com](http://www.graphpad.com)). Inhibition  $IC_{50}$ s were estimated using an auto-fitted Hill equation with a Hill coefficient = -1.0.

### **Protein expression**

$K_{2P2.1_{CRYST}}$  I110D was expressed as a fusion protein having in series from the channel C-terminus a 3C protease site, green fluorescent protein (GFP), and His<sub>10</sub> tag as described previously for  $K_{2P2.1_{cryst}}$ <sup>28</sup>. Linearized plasmid DNA (*PmeI*) was introduced into *Pichia pastoris* strain SMD1163H via electroporation. Strains with highest incorporation were selected for on YPD plates containing 1-2 mg mL<sup>-1</sup> zeocin. Individual colonies were screened using fluorescence size exclusion chromatography (FSEC)<sup>72</sup> to identify strain with highest expression level as described previously<sup>28</sup>. The best FSEC candidate was used to inoculate a starter culture (60-120 mL) in minimal media (1% glycerol, 100 mM potassium phosphate pH 6.0, 0.4 mg L<sup>-1</sup> biotin, 1X YNB from Invitrogen) supplemented with 1 mg mL<sup>-1</sup> zeocin and cultured in shaker flask for 2 days at 29°C. The starter culture was then used to inoculate a large scale (6-12L) culture in shaker flasks containing minimal media without zeocin. Cells were grown at 29°C over two days in minimal media containing 1% glycerol. Cells were centrifuged at 3000g (6 min, 20°C) and pellet was resuspended in minimal induction media (100 mM potassium phosphate pH 6.0, 0.4 mg L<sup>-1</sup> biotin, 1X YNB) containing 0.5% methanol. After 24 hrs, 0.5% methanol was added to

each flask. Cells were harvested (6000g, 20 min, 4°C) two days after induction, snap-frozen in liquid nitrogen, and stored at -80°C.

### **Protein Purification**

Purified K<sub>2</sub>P2.1<sub>cryst</sub> I110D was obtained from preparations using 100-200g of cell mass cryo-milled (Retsch, MM400) in liquid nitrogen (5 x 3 min, 25 Hz). All purification steps were carried out at 4°C and purification conditions were similar to those previously reported for K<sub>2</sub>P2.1<sub>cryst</sub><sup>28</sup>. Cell powder was solubilized at a ratio of 3 grams of cells per mL of lysis buffer containing 200 mM KCl, 21 mM octyl glucose neopentyl glycol (OGNG, Anatrace), 30 mM *n*-heptyl-β-D-thioglucopyranoside (HTG, Anatrace), 0.1% cholesterol hemisuccinate (CHS, Anatrace), 100 mM Tris-Cl, pH 8.2, 1 mM PMSF and 0.1 mg/mL DNaseI. Following 3 hour membrane solubilization, the sample was centrifuged at 40,000g for 45 min at 4°C. After centrifugation, supernatant was incubated with anti-GFP nanobodies immobilized on CNBr-activated sepharose resin (GE Healthcare, 17-0430-01) at a ratio of 1 mL resin per 10 g of cells and gently rotated on an orbital rocker for 3 hours. Resin was collected in a gravity column (Econo-Pac, 1.5 x 12 cm, BioRad) and washed with 10 CV each, buffers A-C (A-C: 200 mM KCl, 50 mM Tris-Cl pH 8.0, 15 mM HTG; A: 10 mM OGNG, 0.018% CHS; B: 5 mM OGNG, 0.018% CHS; C: 3.85 mM OGNG, 0.0156% CHS), applied in series to reduce the detergent concentration and wash away cell debris (30 CV total). The GFP-affinity tag was cleaved overnight on column using two CV of buffer C supplemented with 350 mM KCl, 1 mM EDTA and 3C protease<sup>73</sup>. Cleaved protein was eluted from resin with two CV of size-exclusion buffer (SEC: 200 mM KCl, 20 mM Tris-Cl pH 8.0, 2.1 mM OGNG, 15 mM HTG, 0.012% CHS), concentrated and applied to a Superdex 200 (GE, 10/300) pre-equilibrated with SEC buffer. Peak fractions were

evaluated by SDS-PAGE (15% acrylamide) for purity, pooled and concentrated for crystallization.

### **Crystallization, structure determination, and refinement**

Purified  $K_{2P2.1_{\text{cryst}}}$ -I110D was concentrated to  $6 \text{ mg mL}^{-1}$  before crystallization using hanging-drop vapor diffusion at  $4^{\circ}\text{C}$  using a mixture of  $0.2 \text{ }\mu\text{L}$  protein to  $0.1 \text{ }\mu\text{L}$  reservoir solution, over  $100 \text{ }\mu\text{L}$  reservoir of 20-25% PEG400, 200 mM KCl, 100 mM HEPES pH 8.0 or 7.1 and 1-2 mM  $\text{CdCl}_2$ . Crystals appeared within 1-2 days and grew to full size within 2 weeks. Crystals were cryoprotected in solution containing 200 mM KCl, 0.2% OGNG, 15 mM HTG, 0.02% CHS, 100 mM HEPES pH 8.0 or 7.1 and 1-2 mM  $\text{CdCl}_2$ , with 5% increase in PEG400 up to final concentration of 38% before flash freezing in liquid nitrogen. For compound bound structures, cryoprotected crystals were also soaked in final cryoprotection solution containing 1 mM each RuRed, RuRed+ML335 or Ru360, sourced as described in TEVC methods, for at least 1 hour prior to flash freezing in liquid nitrogen.

Datasets were collected at 100 K using synchrotron radiation at APS GM/CAT beamline 23-IDB/D Chicago, Illinois using a wavelength of  $1.0332 \text{ \AA}$ , processed with XDS<sup>74</sup> and scaled and merged with Aimless<sup>75</sup>. Highest resolution structures were obtained from crystals that were soaked with the ruthenium compounds. Structure determination of low resolution datasets from complexes obtained by co-crystallization indicated that there was no difference in the RuR position in complexes made by either soaking or co-crystallization. Final resolution cutoff was  $3.40 \text{ \AA}$ ,  $3.49 \text{ \AA}$ ,  $3.00 \text{ \AA}$  and  $3.51 \text{ \AA}$  for  $K_{2P2.1_{\text{cryst}}}$  I110D,  $K_{2P2.1_{\text{cryst}}}$  I110D:RuR,  $K_{2P2.1_{\text{cryst}}}$  I110D:RuR:ML335 and  $K_{2P2.1_{\text{cryst}}}$  I110D:Ru360 structures, respectively, using the  $\text{CC}_{1/2}$  criterion<sup>76</sup>.  $K_{2P2.1_{\text{cryst}}}$



I110D was solved by molecular replacement utilizing K<sub>2</sub>P4.1 (G124I) structure (PDB: 4RUE) as search model. For compound bound structures, the K<sub>2</sub>P2.1<sub>cryst</sub>-I110D model was used as the molecular replacement search model. Electron density maps were improved through several cycles of manual model rebuilding, using COOT<sup>77</sup>, REFMAC (CCP4), and PHENIX<sup>78</sup>.

### Mutant cycle analysis

Double mutant cycle analysis<sup>69,70</sup> was carried out using the equation  $\Omega = \frac{IC_{50}^{WT} * IC_{50}^{X'Y'}}{IC_{50}^{X'} * IC_{50}^{Y'}}$  in which  $\Omega$  is the coupling factor<sup>70</sup> and  $IC_{50}^{WT}$ ,  $IC_{50}^{X'}$ ,  $IC_{50}^{Y'}$  and  $IC_{50}^{X'Y'}$  are the  $IC_{50}$  values for the wild-type, each single mutant of the X-Y pair, and the double mutant, respectively. As wild type K<sub>2</sub>P2.1 (TREK-1) is unaffected by RuR, the free energy of the interaction is zero and hence,  $K_a$  and  $K_d = 1$ . Coupling energy,  $\Delta\Delta G_{\Omega}$ , was calculated as  $\Delta\Delta G_{\Omega} = RT \ln \Omega$  where  $R=1.987 \text{ cal mol}^{-1} \text{ deg}^{-1}$  and  $T= 298\text{K}$ .

## References

- (1) J. M. Fletcher, B. F. Greenfield, C. J. Hardy, D. Scargill, J. L. Woodhead, Ruthenium Red. *J. Chem. Soc.* **1961**. 2000-2006.
- (2) M. J. Clarke, Ruthenium metallopharmaceuticals. *Coordin Chem Rev.* **2002**. 232, 69-93
- (3) G. Braun, M. Lengyel, P. Enyedi, G. Czirjak, Differential sensitivity of TREK-1, TREK-2 and TRAAK background potassium channels to the polycationic dye ruthenium red. *British journal of pharmacology.* **2015**. 172, 1728-1738.
- (4) B. Musset *et al.*, Effects of divalent cations and spermine on the K<sup>+</sup> channel TASK-3 and on the outward current in thalamic neurons. *J Physiol.* **2006**. 572, 639-657.
- (5) G. Czirjak, P. Enyedi, Ruthenium red inhibits TASK-3 potassium channel by interconnecting glutamate 70 of the two subunits. *Molecular pharmacology.* **2003**. 63, 646-652.
- (6) W. Gonzalez *et al.*, An extracellular ion pathway plays a central role in the cooperative gating of a K(2P) K<sup>+</sup> channel by extracellular pH. *J Biol Chem.* **2013**. 288, 5984-5991.
- (7) M. J. Caterina *et al.*, The capsaicin receptor: a heat-activated ion channel in the pain pathway. *Nature.* **1997**. 389, 816-824.
- (8) R. Strotmann, C. Harteneck, K. Nunnenmacher, G. Schultz, T. D. Plant, OTRPC4, a nonselective cation channel that confers sensitivity to extracellular osmolarity. *Nat Cell Biol.* **2000**. 2, 695-702.

- (9) A. D. Guler *et al.*, Heat-evoked activation of the ion channel, TRPV4. *J Neurosci.* **2002.** 22, 6408-6414.
- (10) M. J. Caterina, T. A. Rosen, M. Tominaga, A. J. Brake, D. Julius, A capsaicin-receptor homologue with a high threshold for noxious heat. *Nature.* **1999.** 398, 436-441.
- (11) T. Voets *et al.*, Molecular determinants of permeation through the cation channel TRPV4. *J Biol Chem.* **2002.** 277, 33704-33710.
- (12) M. Arif Pavel *et al.*, Function and regulation of TRPP2 ion channel revealed by a gain-of-function mutant. *Proc Natl Acad Sci U S A.* **2016.** 113, E2363-2372.
- (13) T. Voets *et al.*, TRPM6 forms the Mg<sup>2+</sup> influx channel involved in intestinal and renal Mg<sup>2+</sup> absorption. *J Biol Chem.* **2004.** 279, 19-25.
- (14) G. M. Story *et al.*, ANKTM1, a TRP-like channel expressed in nociceptive neurons, is activated by cold temperatures. *Cell.* **2003.** 112, 112, 819-829.
- (15) Y. Kirichok, G. Krapivinsky, D. E. Clapham, The mitochondrial calcium uniporter is a highly selective ion channel. *Nature.* **2004.** 427, 360-364.
- (16) D. Chaudhuri, Y. Sancak, V. K. Mootha, D. E. Clapham, MCU encodes the pore conducting mitochondrial calcium currents. *eLife.* **2013.** 2, e00704.
- (17) R. Rahamimoff, E. Alnaes, Inhibitory action of Ruthenium red on neuromuscular transmission. *Proc Natl Acad Sci U S A.* **1973.** 70, 3613-3616.
- (18) C. L. Moore, Specific inhibition of mitochondrial Ca<sup>++</sup> transport by ruthenium red. *Biochem Biophys Res Commun.* **1971.** 42, 298-305.

- (19) Z. Ma *et al.*, Calcium homeostasis modulator 1 (CALHM1) is the pore-forming subunit of an ion channel that mediates extracellular Ca<sup>2+</sup> regulation of neuronal excitability. *Proc Natl Acad Sci U S A.* **2012.** 109, E1963-1971.
- (20) U. Dreses-Werringloer *et al.*, CALHM1 controls the Ca(2)(+)-dependent MEK, ERK, RSK and MSK signaling cascade in neurons. *J Cell Sci.* **2013.** 126, 1199-1206.
- (21) W. Choi, N. Clemente, W. Sun, J. Du, W. Lu, The structures and gating mechanism of human calcium homeostasis modulator 2. *Nature.* **2019.** 576, 163-167.
- (22) J. Ma, Block by ruthenium red of the ryanodine-activated calcium release channel of skeletal muscle. *J Gen Physiol.* **1993.** 102, 1031-1056.
- (23) J. S. Smith *et al.*, Purified ryanodine receptor from rabbit skeletal muscle is the calcium-release channel of sarcoplasmic reticulum. *J Gen Physiol.* **1988.** 92, 1-26.
- (24) B. Coste *et al.*, Piezo proteins are pore-forming subunits of mechanically activated channels. *Nature.* **2012.** 483, 176-181.
- (25) Q. C. Zhao *et al.*, Ion Permeation and Mechanotransduction Mechanisms of Mechanosensitive Piezo Channels. *Neuron.* **2016.** 89, 1248-1263.
- (26) S. G. Brohawn, J. del Marmol, R. MacKinnon, Crystal structure of the human K2P TRAAK, a lipid- and mechano-sensitive K<sup>+</sup> ion channel. *Science.* **2012.** 335, 436-441.
- (27) Y. Y. Dong *et al.*, K2P channel gating mechanisms revealed by structures of TREK-2 and a complex with Prozac. *Science.* **2015.** 347, 1256-1259.

- (28) M. Lolicato *et al.*, K2P2.1 (TREK-1)-activator complexes reveal a cryptic selectivity filter binding site. *Nature*. **2017**. 547, 364-368.
- (29) A. N. Miller, S. B. Long, Crystal structure of the human two-pore domain potassium channel K2P1. *Science*. **2012**. 335, 432-436.
- (30) P. Enyedi, G. Czirjak, Molecular background of leak K<sup>+</sup> currents: two-pore domain potassium channels. *Physiological reviews*. **2010**. 90, 559-605.
- (31) S. Felicangeli, F. C. Chatelain, D. Bichet, F. Lesage, The family of K channels: salient structural and functional properties. *J Physiol*. **2014**. 593, 2587-2603.
- (32) V. Renigunta, G. Schlichthorl, J. Daut, Much more than a leak: structure and function of K(2)p-channels. *Pflugers Arch*. **2015**. 467, 867-894.
- (33) K. E. J. Rödström *et al.*, A unique lower X-gate in TASK channels traps inhibitors within the vestibule. *bioRxiv*, **2019**. 706168.
- (34) H. Kanda *et al.*, TREK-1 and TRAAK Are Principal K(+) Channels at the Nodes of Ranvier for Rapid Action Potential Conduction on Mammalian Myelinated Afferent Nerves. *Neuron*. **2019**. 104, 960-971.
- (35) S. G. Brohawn *et al.*, The mechanosensitive ion channel TRAAK is localized to the mammalian node of Ranvier. *eLife*. **2019**. 8, e50403.
- (36) C. Heurteaux *et al.*, TREK-1, a K<sup>+</sup> channel involved in neuroprotection and general anesthesia. *Embo J*. **2004**. 23, 2684-2695.

- (37) R. M. Lazarenko *et al.*, Anesthetic activation of central respiratory chemoreceptor neurons involves inhibition of a THIK-1-like background K(+) current. *J Neurosci.* **2010.** *30*, 9324-9334.
- (38) C. Madry *et al.*, Microglial Ramification, Surveillance, and Interleukin-1beta Release Are Regulated by the Two-Pore Domain K(+) Channel THIK-1. *Neuron.* **2018.** *97*, 299-312 e296.
- (39) K. Yoshida *et al.*, Leak potassium channels regulate sleep duration. *Proc Natl Acad Sci U S A.* **2018.** *115*, E9459-E9468.
- (40) A. Alloui *et al.*, TREK-1, a K<sup>+</sup> channel involved in polymodal pain perception. *Embo J.* **2006.** *25*, 2368-2376.
- (41) M. Devilliers *et al.*, Activation of TREK-1 by morphine results in analgesia without adverse side effects. *Nat Commun.* **2013.** *4*, 2941.
- (42) D. Vivier *et al.*, Development of the first Two-Pore Domain Potassium Channel TREK-1 (TWIK-Related K<sup>+</sup> Channel 1)-selective agonist possessing in vivo anti-nociceptive activity. *Journal of medicinal chemistry.* **2017.** *60*, 1076-1088.
- (43) N. Decher *et al.*, Sodium permeable and "hypersensitive" TREK-1 channels cause ventricular tachycardia. *EMBO molecular medicine.* **2017.** *9*, 403-414.
- (44) C. Laigle, S. Confort-Gouny, Y. Le Fur, P. J. Cozzone, A. Viola, Deletion of TRAAK potassium channel affects brain metabolism and protects against ischemia. *PloS one.* **2012.** *7*, e53266.

- (45) X. Wu *et al.*, Involvement of TREK-1 activity in astrocyte function and neuroprotection under simulated ischemia conditions. *Journal of molecular neuroscience*. **2013**. 49, MN 499-506.
- (46) D. M. Abraham *et al.*, The two-pore domain potassium channel TREK-1 mediates cardiac fibrosis and diastolic dysfunction. *J Clin Invest*. **2018**. 128, 4843-4855.
- (47) C. Heurteaux *et al.*, Deletion of the background potassium channel TREK-1 results in a depression-resistant phenotype. *Nat Neurosci*. **2006**. 9, 9, 1134-1141.
- (48) P. Royal *et al.*, Migraine-Associated TRESK Mutations Increase Neuronal Excitability through Alternative Translation Initiation and Inhibition of TREK. *Neuron*. **2019**. 101, 101, 232-245 e236.
- (49) O. Yarishkin *et al.*, TREK-1 channels regulate pressure sensitivity and calcium signaling in trabecular meshwork cells. *J Gen Physiol*. **2018**. 150, 1660-1675.
- (50) M. Lambert *et al.*, Loss of KCNK3 is a hallmark of RV hypertrophy/dysfunction associated with pulmonary hypertension. *Cardiovasc Res*. **2018**. 114, 880-893.
- (51) S. N. Bagriantsev *et al.*, A high-throughput functional screen identifies small molecule regulators of temperature- and mechano-sensitive K2P channels. *ACS chemical biology*. **2013**. 8, 1841-1851.
- (52) F. Tian *et al.*, A Small-Molecule Compound Selectively Activates K2P Channel TASK-3 by Acting at Two Distant Clusters of Residues. *Molecular pharmacology*. **2019**. 96, 26-35.

- (53) P. D. Wright *et al.*, Pranlukast is a novel small molecule activator of the two-pore domain potassium channel TREK2. *Biochem Biophys Res Commun.* **2019.** 520, 35-40.
- (54) Z. W. Su, E. C. Brown, W. W. Wang, R. MacKinnon, Novel cell-free high-throughput screening method for pharmacological tools targeting K<sup>+</sup> channels. *P Natl Acad Sci USA.* **2016.** 113, 5748-5753.
- (55) L. Pope *et al.*, Protein and Chemical Determinants of BL-1249 Action and Selectivity for K<sub>2</sub>P Channels. *ACS chemical neuroscience.* **2018.** 9, 3153-3165.
- (56) M. Schewe *et al.*, A pharmacological master key mechanism that unlocks the selectivity filter gate in K(+) channels. *Science.* **2019.** 363, 875-880.
- (57) D. Sterbuleac, Molecular determinants of chemical modulation of two-pore domain potassium channels. *Chem Biol Drug Des.* **2019.** 94, 1596-1614.
- (58) W. L. Ying, J. Emerson, M. J. Clarke, D. R. Sanadi, Inhibition of mitochondrial calcium ion transport by an oxo-bridged dinuclear ruthenium ammine complex. *Biochemistry.* **1991.** 30, 4949-4952.
- (59) J. M. Baughman *et al.*, Integrative genomics identifies MCU as an essential component of the mitochondrial calcium uniporter. *Nature.* **2011.** 467, 341-345.
- (60) K. Oxenoid *et al.*, Architecture of the mitochondrial calcium uniporter. *Nature.* **2016.** 533, 269-273.
- (61) D. Douguet, E. Honore, Mammalian Mechanoelectrical Transduction: Structure and Function of Force-Gated Ion Channels. *Cell.* **2019.** 179, 340-354.



- (62) G. Czirjak, P. Enyedi, Formation of functional heterodimers between the TASK-1 and TASK-3 two-pore domain potassium channel subunits. *J Biol Chem.* **2002.** *277,* 5426-5432.
- (63) S. N. Bagriantsev, K. A. Clark, D. L. Minor, Jr., Metabolic and thermal stimuli control K(2P)2.1 (TREK-1) through modular sensory and gating domains. *EMBO J.* **2012.** *31,* 3297-3308.
- (64) S. N. Bagriantsev, R. Peyronnet, K. A. Clark, E. Honore, D. L. Minor, Jr., Multiple modalities converge on a common gate to control K2P channel function. *EMBO J.* **2011.** *30,* 3594-3606.
- (65) P. L. Piechotta *et al.*, The pore structure and gating mechanism of K2P channels. *EMBO J.* **2011.** *30,* 3607-3619.
- (66) M. Schewe *et al.*, A Non-canonical Voltage-Sensing Mechanism Controls Gating in K2P K(+) Channels. *Cell.* **2016.** *164,* **164,** 937-949.
- (67) M. Lolicato, P. M. Riegelhaupt, C. Arrigoni, K. A. Clark, D. L. Minor, Jr., Transmembrane helix straightening and buckling underlies activation of mechanosensitive and thermosensitive K(2P) channels. *Neuron.* **2014.** *84,* 1198-1212.
- (68) T. E. Gunter, D. R. Pfeiffer, Mechanisms by which mitochondria transport calcium. *Am J Physiol.* **1990.** *258,* C755-786.
- (69) P. J. Carter, G. Winter, A. J. Wilkinson, A. R. Fersht, The use of double mutants to detect structural changes in the active site of the tyrosyl-tRNA synthetase (*Bacillus stearothermophilus*). *Cell.* **1984.** *38,* 835-840.

- (70) P. Hidalgo, R. MacKinnon, Revealing the architecture of a K<sup>+</sup> channel pore through mutant cycles with a peptide inhibitor. *Science*. **1995**. 268, 307-310.
- (71) Q. Zhao *et al.*, Structure and mechanogating mechanism of the Piezo1 channel. *Nature*. **2018**. 554, 487-492.
- (72) T. Kawate, E. Gouaux, Fluorescence-detection size-exclusion chromatography for precrystallization screening of integral membrane proteins. *Structure*. **2006**. 14, 673-681.
- (73) D. Shaya *et al.*, Voltage-gated sodium channel (NaV) protein dissection creates a set of functional pore-only proteins. *Proc Natl Acad Sci U S A*. **2011**. 108, 12313-12318.
- (74) W. Kabsch, Xds. *Acta crystallographica. Section D, Biological crystallography*. **2010**. 66, 125-132.
- (75) P. R. Evans, G. N. Murshudov, How good are my data and what is the resolution? *Acta crystallographica. Section D, Biological crystallography*. **2013**. 69, 1204-1214.
- (76) K. Diederichs, P. A. Karplus, Better models by discarding data? *Acta crystallographica. Section D, Biological crystallography*. **2013**. 69, 1215-1222.
- (77) P. Emsley, K. Cowtan, Coot: model-building tools for molecular graphics. *Acta crystallographica. Section D, Biological crystallography*. **2004**. 60, 2126-2132.
- (78) P. D. Adams *et al.*, PHENIX: a comprehensive Python-based system for macromolecular structure solution. *Acta crystallographica. Section D, Biological crystallography*. **2010**. 66, 213-221.

(79) A. C. Wallace, R. A. Laskowski, J. M. Thornton, LIGPLOT: a program to generate schematic diagrams of protein-ligand interactions. *Protein Eng.* **1995.** 8, 127-134.

## **Acknowledgements**

We thank V. Nguyen for help in the initial stages of this project, Z. Wong for technical assistance, A. Natale for help with structure comparisons, M. Grabe and for helpful discussions, and Y. Kirichok and members of the Minor lab for comments on the manuscript. This work was supported by grant NIH-R01-MH093603 to D.L.M.

## **Author Contributions**

L.P. and D.L.M. conceived the study and designed the experiments. L.P. performed molecular biology experiments, two-electrode voltage clamp recordings, expressed, purified, and crystallized the proteins, and collected diffraction data. L.P. and M.L. determined the structures. L.P. and M.L. analyzed the data. D.L.M. analyzed data and provided guidance and support. L.P., M.L., and D.L.M. wrote the paper.

## **Competing interests**

The other authors declare no competing interests.

## **Data and materials availability**

Coordinates and structure factors for the structures of K<sub>2</sub>P2.1 I110D (6V36), K<sub>2</sub>P2.1 I110D:RuR (6V3I), K<sub>2</sub>P2.1 I110D:RuR:ML335 (6V37), and K<sub>2</sub>P2.1 I110D:Ru360 (6V3C) are deposited with RCSB and will be released immediately upon publication.

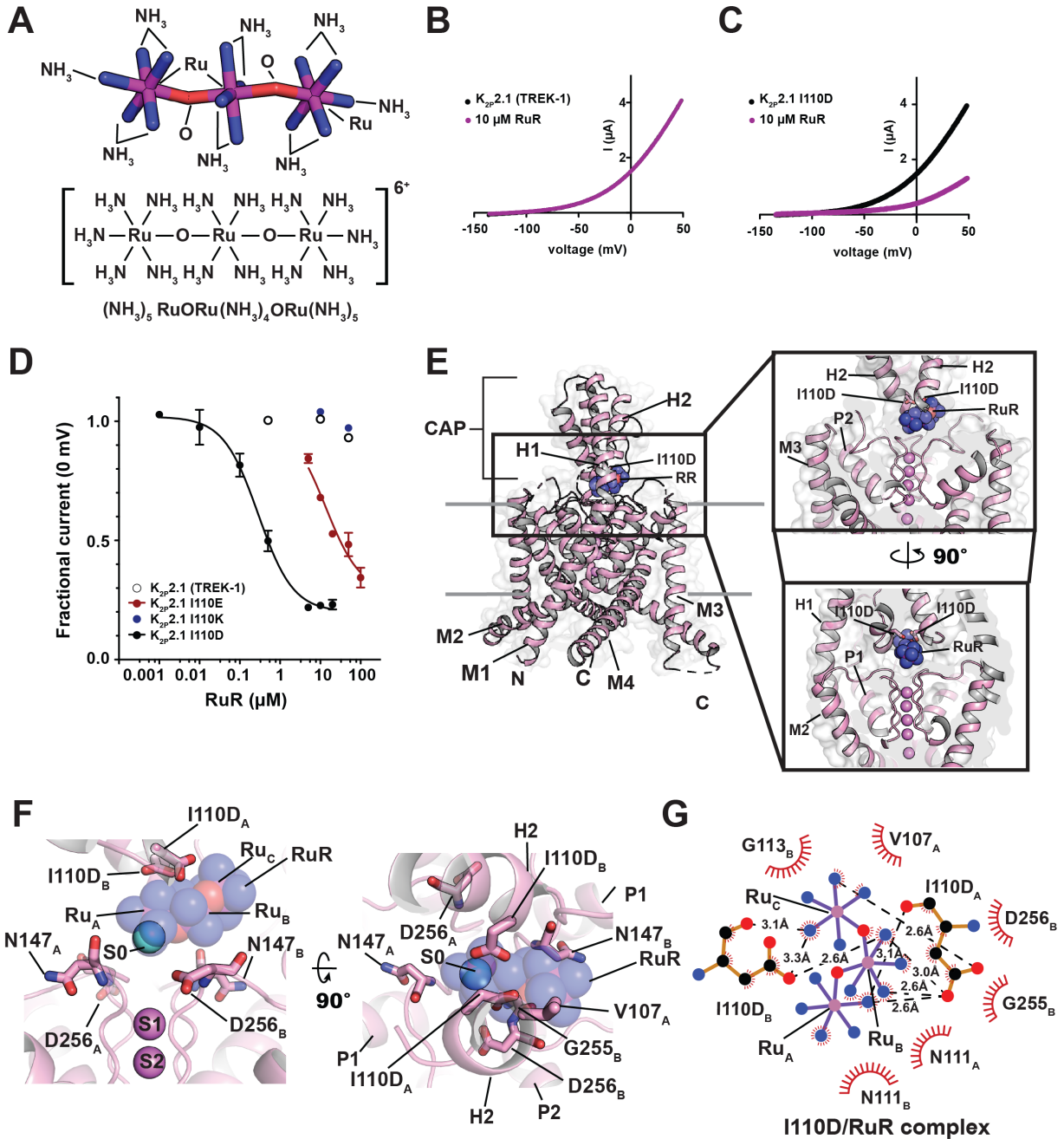


**Figure 3.1 | Functional and structural analysis of the  $K_{2P2.1}$  I110D:RuR complex.**

(A) Ruthenium Red (RuR) structure (B) and (C) Exemplar TEVC recordings of (B)  $K_{2P2.1}$  (TREK-1) and (C)  $K_{2P2.1}$  I110D responses to 10  $\mu\text{M}$  RuR (magenta). (D) Dose-response curves for  $K_{2P2.1}$  (TREK-1) (open white circles),  $K_{2P2.1}$  I110D (black),  $K_{2P2.1}$  I110E (red), and  $K_{2P2.1}$  I110K to RuR. (E) Structure of the  $K_{2P2.1}$  I110D:RuR complex. Inset shows the location of the RuR binding site. I110D is shown as sticks. (F) Close up view of  $K_{2P2.1}$  I110D:RuR interactions. S0 ion (cyan) from the  $K_{2P2.1}$  I110D structure is indicated, RuR is shown in space filling in panels (E) and (F). (G) LigPLOT<sup>79</sup> diagram of the I110D/RuR complex

K<sub>2</sub>P2.1 I110D:RuR interactions showing ionic interactions (dashed lines) and van der Waals contacts (red)  $\leq 5\text{\AA}$ .

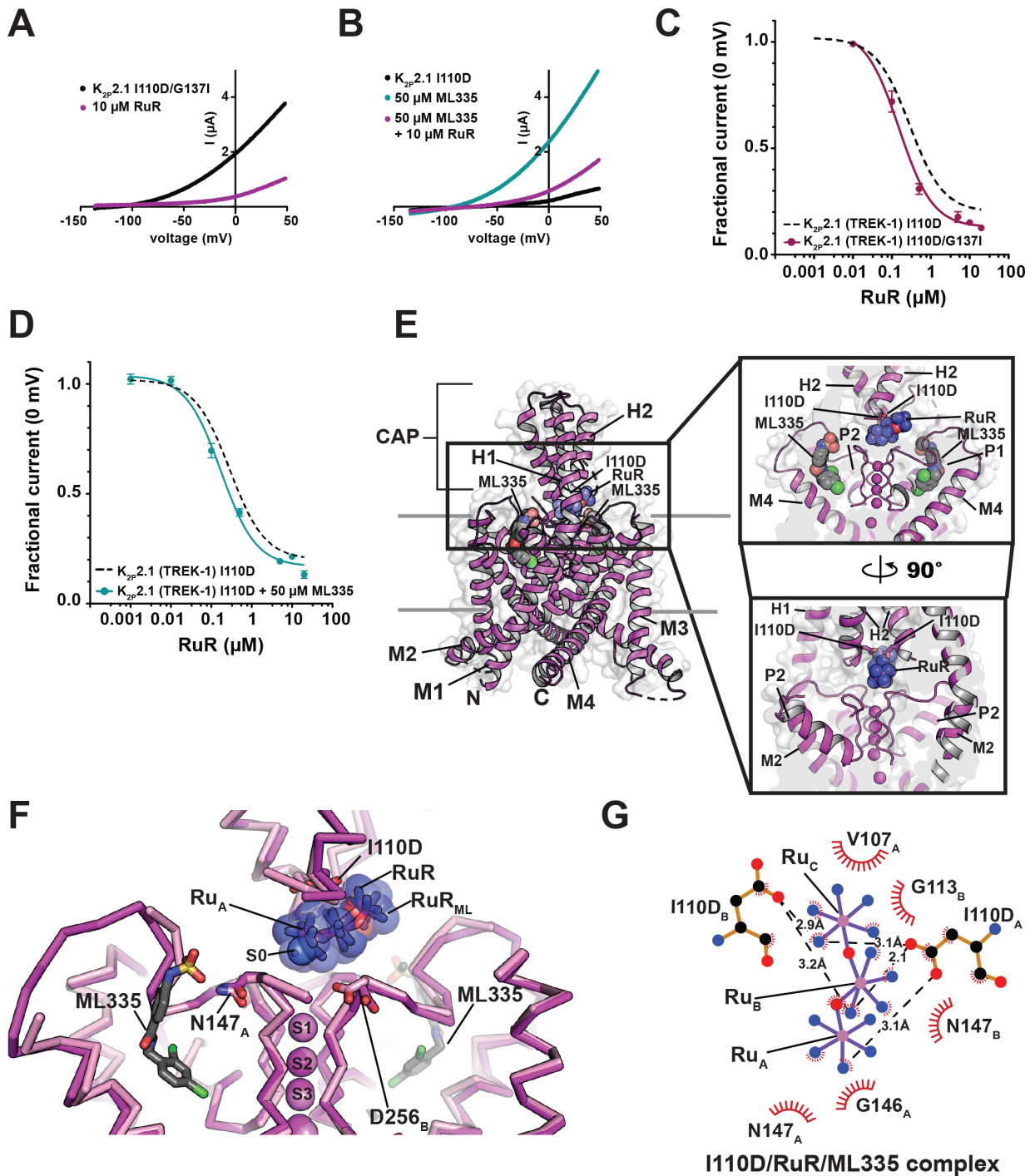


**Figure 3.2 | Functional and structural analysis of C-type gate activated  $K_{2P2.1}$  I110D:RuR complexes.**

(A) and (B) Exemplar TEVC recordings of: (A)  $K_{2P2.1}$  I110D/G137I (black) and in the presence of 10  $\mu$ M RuR (magenta), and (B)  $K_{2P2.1}$  I110D alone (black) in the presence of 50  $\mu$ M ML335 (cyan), and in the presence of 50  $\mu$ M ML335 + 10  $\mu$ M RuR (magenta).

(C) and (D) RuR dose-response curves for (C)  $K_{2P2.1}$  I110D/G137I (magenta), and (D)  $K_{2P2.1}$  I110D in the presence of 50  $\mu$ M ML335 (cyan). Dashed lines show RuR response of  $K_{2P2.1}$  I110D from Figure 1D. (E) Structure of the  $K_{2P2.1}$  I110D:ML335 RuR complex. Inset shows the location of the RuR binding site. I110D is shown as sticks. ML335 (grey) is shown as space filling. (F) Superposition of RuR binding site from the  $K_{2P2.1}$  I110D:RuR (pink) and  $K_{2P2.1}$  I110D:ML335:RuR (magenta) RuR and RuR<sub>ML</sub> indicate RuR from the  $K_{2P2.1}$  (TREK-1) I110D:RuR and  $K_{2P2.1}$  I110D:ML335:RuR structures, respectively. ML335 is shown as sticks. (G) LigPLOT<sup>79</sup> diagram of  $K_{2P2.1}$  I110D:RuR interactions from the  $K_{2P2.1}$  I110D:ML335:RuR complex showing ionic interactions (dashed lines) and van der Waals contacts (red)  $\leq 5\text{\AA}$ .



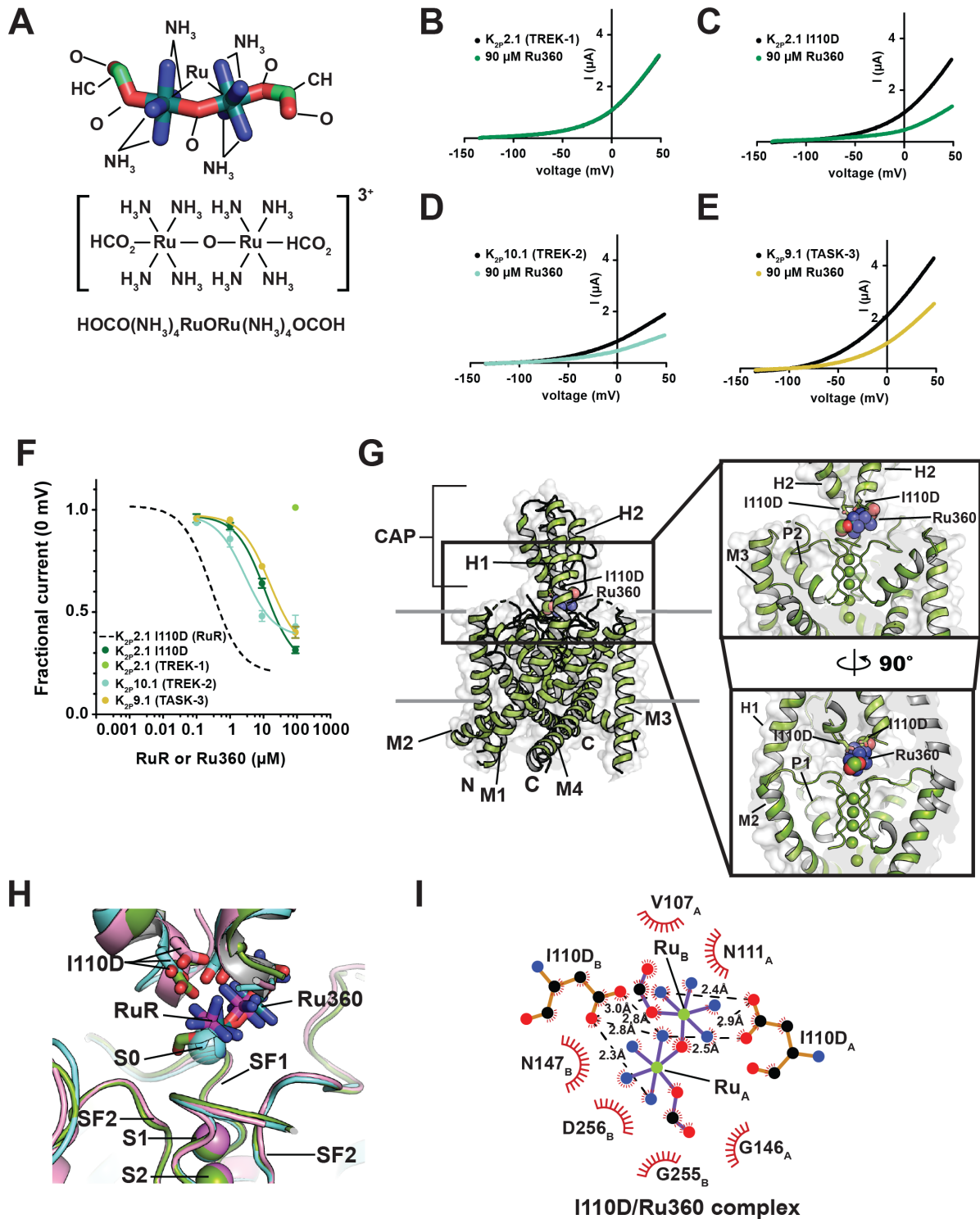


**Figure 3.3 | Functional and structural analysis of K<sub>2P</sub>:Ru360: interactions.**

(A) Ru360 (RuR) structure. (B-D) Exemplar TEVC recordings of (B) K<sub>2P</sub>2.1 (TREK-1), (C) K<sub>2P</sub>2.1 I110D, (D) K<sub>2P</sub>10.1 (TREK-2), and (E) K<sub>2P</sub>9.1 (TASK-3) alone (black) and in

the presence of 90  $\mu$ M Ru360 (green, teal, and olive, respectively). **(F)** Ru360 dose-response curves for K<sub>2P</sub>2.1 I110D (green), K<sub>2P</sub>2.1 (TREK-1) (light green), K<sub>2P</sub>10.1 (TREK-2) (teal), and K<sub>2P</sub>9.1 (TASK-3) (olive). Dashed line shows RuR dose-response for K<sub>2P</sub>2.1 I110D from Figure 1D. **(G)** Structure of the K<sub>2P</sub>2.1 I110D:Ru360 complex. Inset shows the location of the Ru360 binding site. I110D is shown as sticks. **(H)** Close up view of K<sub>2P</sub>2.1 I110D (cyan), K<sub>2P</sub>2.1 I110D:RuR (pink), and K<sub>2P</sub>2.1 I110D:Ru360 Keystone inhibitor sites. RuR and Ru360 are shown as sticks. S0 ion from the K<sub>2P</sub>2.1 I110D structure is shown as a sphere. **(I)** LigPLOT<sup>79</sup> diagram of K<sub>2P</sub>2.1 I110D:Ru360 interactions showing ionic interactions (dashed lines) and van der Waals contacts (red)  $\leq 5\text{\AA}$ .

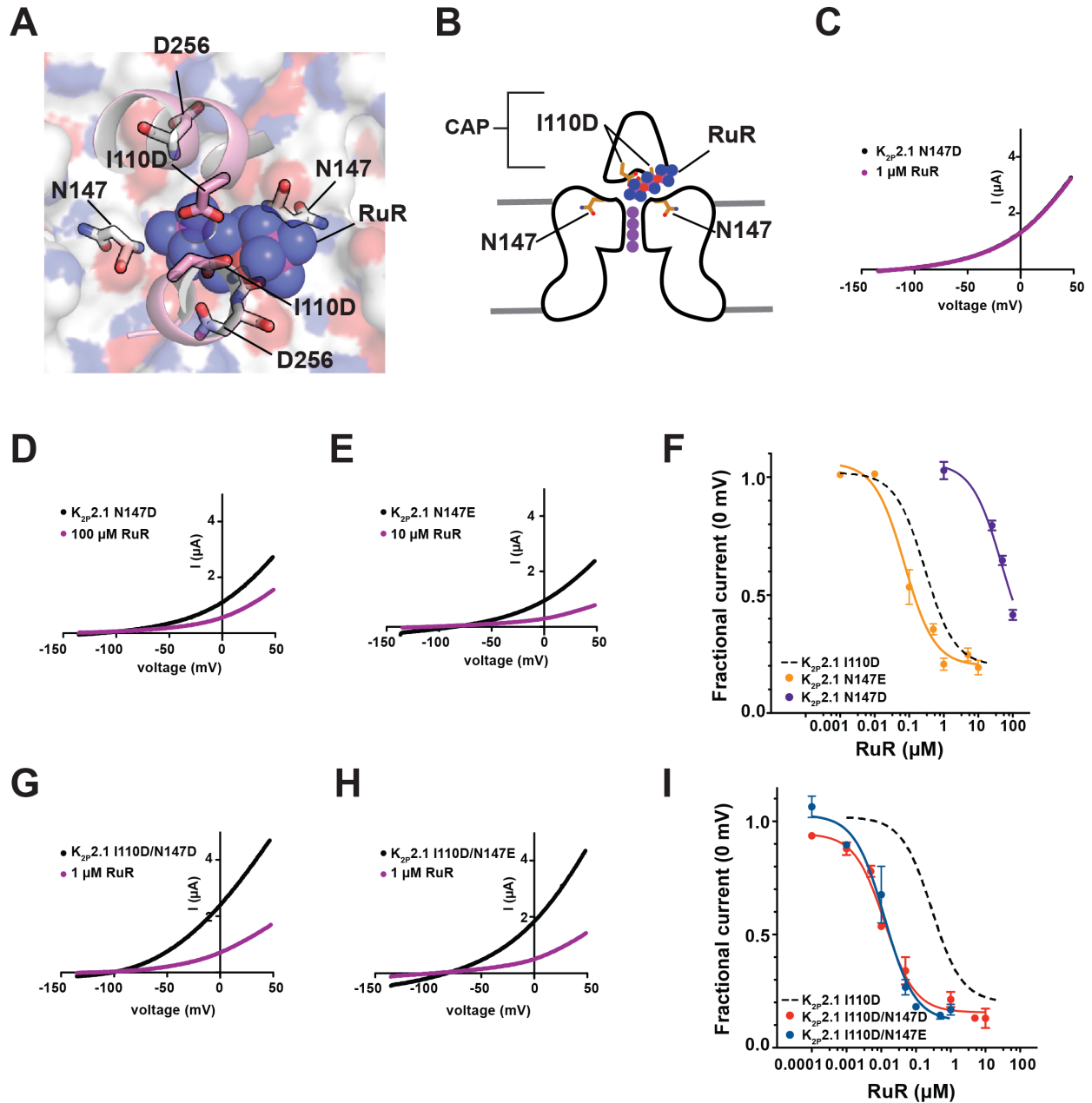


**Figure 3.4 | Engineering  $K_{2P}$  RuR super-responders**

(A) View through the  $K_{2P}2.1$  (TREK-1) CAP to the floor of the Keystone inhibitor site. CAP H2 helix (pink) is shown as a cartoon. RuR is shown as semi-transparent spheres. Surface (white) shows the top of the selectivity filter. I110D, N147, and D256 are shown as sticks. (B) Cartoon depiction of the elements framing the Keystone inhibitor site. Locations of CAP, I110D, and N147 are indicated. Selectivity filter potassium ions are shown as purple circles. (C-E) TEVC recordings of (C)  $K_{2P}2.1$  N147D alone (black) and in the presence of 1  $\mu M$  RuR (magenta), (D)  $K_{2P}2.1$  N147D alone (black) and in the presence of 100  $\mu M$  RuR (magenta) and (E)  $K_{2P}2.1$  N147E alone (black) and in the

presence of 10  $\mu$ M RuR (magenta). **(F)** RuR response of K<sub>2P</sub>2.1 N147D (purple) and K<sub>2P</sub>2.1 N147E (orange). Dashed line shows K<sub>2P</sub>2.1 I110D response to RuR, from Figure 1D. **(G)** and **(H)** TEVC recordings of **(G)** K<sub>2P</sub>2.1 I110D/N147D alone (black) and in the presence of 1  $\mu$ M RuR (magenta), and **(H)** K<sub>2P</sub>2.1 I110D/N147E alone (black) and in the presence of 1  $\mu$ M RuR (magenta). **(I)** RuR dose-response of K<sub>2P</sub>2.1 I110D/N147D (red) and K<sub>2P</sub>2.1 I110D/N147E (blue). Dashed line shows K<sub>2P</sub>2.1 I110D response to RuR, from Figure 1D.

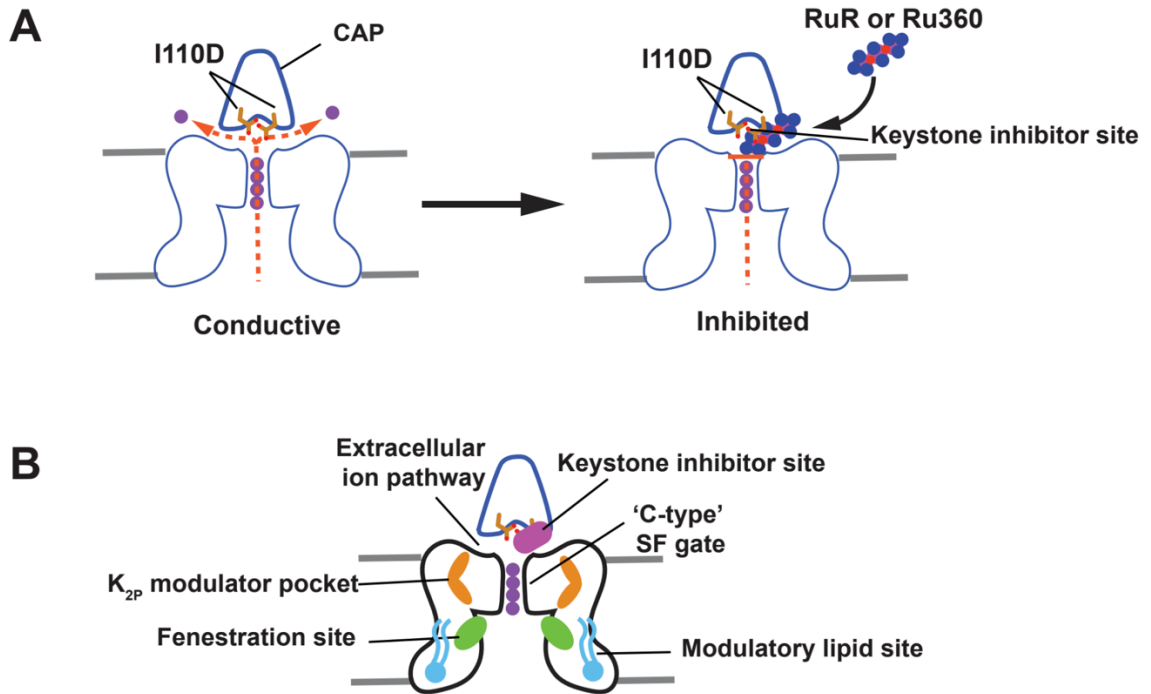


**Figure 3.5 | Mechanisms of small molecule  $K_{2P}$  modulation**

(**A**) Cartoon diagram depicting the ‘finger in the dam’ mechanism of  $K_{2P}$  inhibition by polynuclear ruthenium amines. Ion flow is indicated by the dashed orange lines. Potassium ions are shown as purple circles. (**B**) Polysite model of  $K_{2P}$  modulation. Diagram shows structurally defined sites for  $K_{2P}$  modulators: Keystone inhibitor site (magenta),  $K_{2P}$  modulator pocket (orange)<sup>28</sup>, fenestration site (green)<sup>27,56</sup>, and modulatory lipid site (cyan)<sup>28</sup>. Extracellular ion pathway (EIP) and selectivity filter ‘C-type’ gate are indicated. CAP is outlined in blue and shows the position of the negatively charged residues required for the Keystone inhibitor site (sticks).

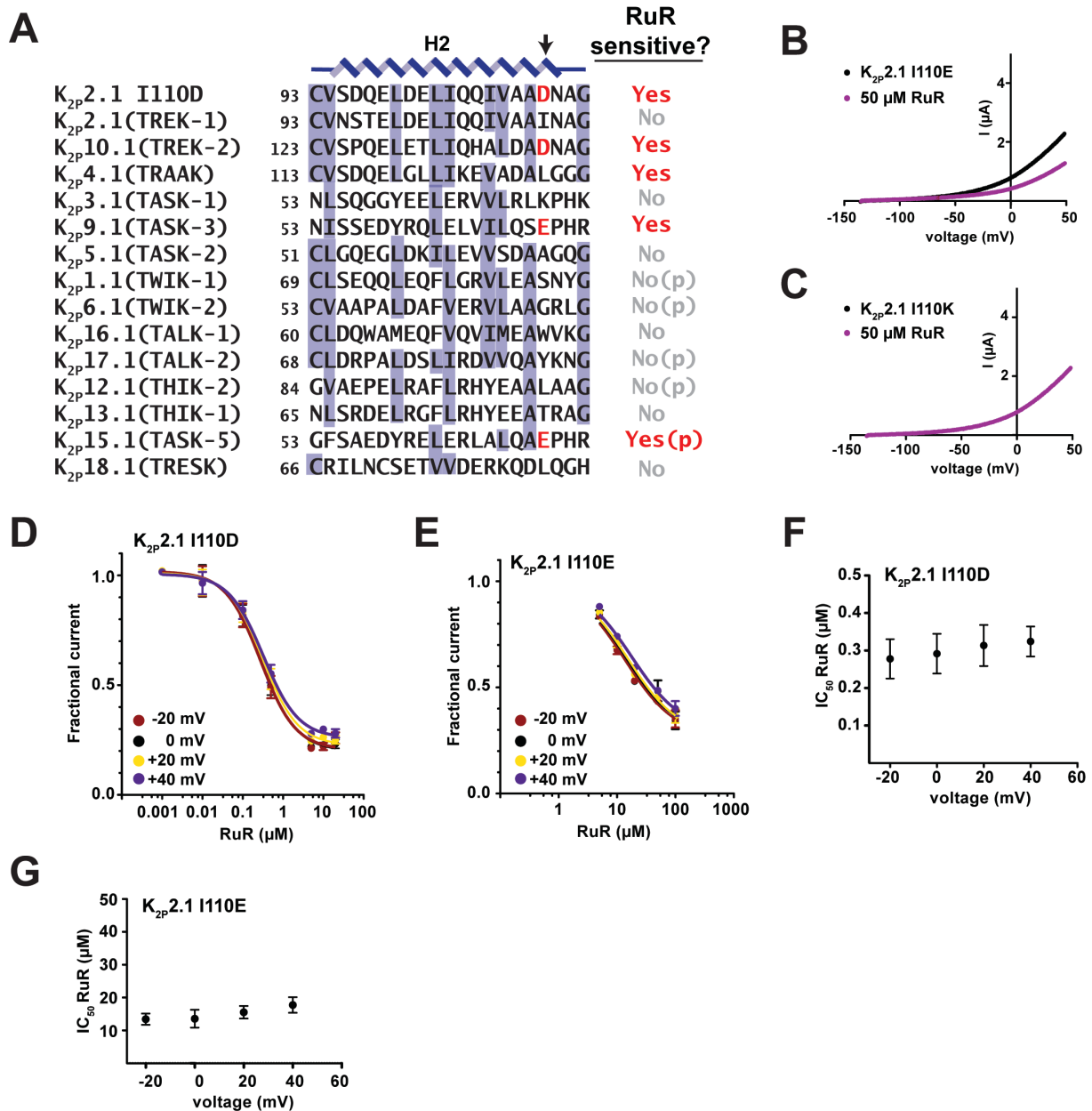


**Figure 3.6 | S1 - K<sub>2p</sub> CAP sequences and K<sub>2p</sub>2.1 CAP mutant functional properties**

(A) CAP H2 helix sequences for the indicated K<sub>2p</sub> channels. Measured<sup>3-6</sup> or predicted (p) Ruthenium Red (RuR) sensitivity is indicated. Arrow indicates the position of the RuR sensitivity determinant (amino acids highlighted in red). K<sub>2p</sub>2.1 I110D, K<sub>2p</sub>2.1 (TREK-1) AAD47569.1, K<sub>2p</sub>10.1 (TREK-2) BAF83207, K<sub>2p</sub>4.1 (TRAAK) AAI10328.1, K<sub>2p</sub>3.1 (TASK-1) NP\_002237.1, K<sub>2p</sub>9.1 (TASK-3) NP\_001269463.1, K<sub>2p</sub>5.1 (TASK-2) NP\_003731.1, K<sub>2p</sub>1.1 (TWIK-1) NP\_002236.1, K<sub>2p</sub>6.1 (TWIK-2) NP\_004814.1, K<sub>2p</sub>16.1 (TALK-1) NP\_001128577.1, K<sub>2p</sub>17.1 (TALK-2) AAK28551.1, K<sub>2p</sub>12.1 (THIK-2) NP\_071338.1, K<sub>2p</sub>13.1 (THIK-1) NP\_071337.2, K<sub>2p</sub>15.1 (TASK-5) EAW75900.1, K<sub>2p</sub>18.1 (TRESK) NP\_862823.1. K<sub>2p</sub>15.1 (TASK-5) cannot be functionally expressed<sup>29</sup>.

(B) and (C) Exemplar TEVC recordings of (B)  $K_{2P2.1} I110E$  and (C)  $K_{2P2.1} I110K$  responses to 50  $\mu M$  RuR (magenta). (D-G) Analysis of the voltage-dependence of RuR inhibition of  $K_{2P2.1} I110D$  and  $K_{2P2.1} I110E$ . (D) and (E) Dose-response curves at -20 mV (red), 0 mV (black), +20 mV (yellow), and +40 mV (purple) for (D)  $K_{2P2.1} I110D$  and (E)  $K_{2P2.1} I110E$ . (F) and (G) RuR  $IC_{50}$  ( $\mu M$ ) as a function of voltage for (D)  $K_{2P2.1} I110D$  and (E)  $K_{2P2.1} I110E$ . Error bars are SEM.

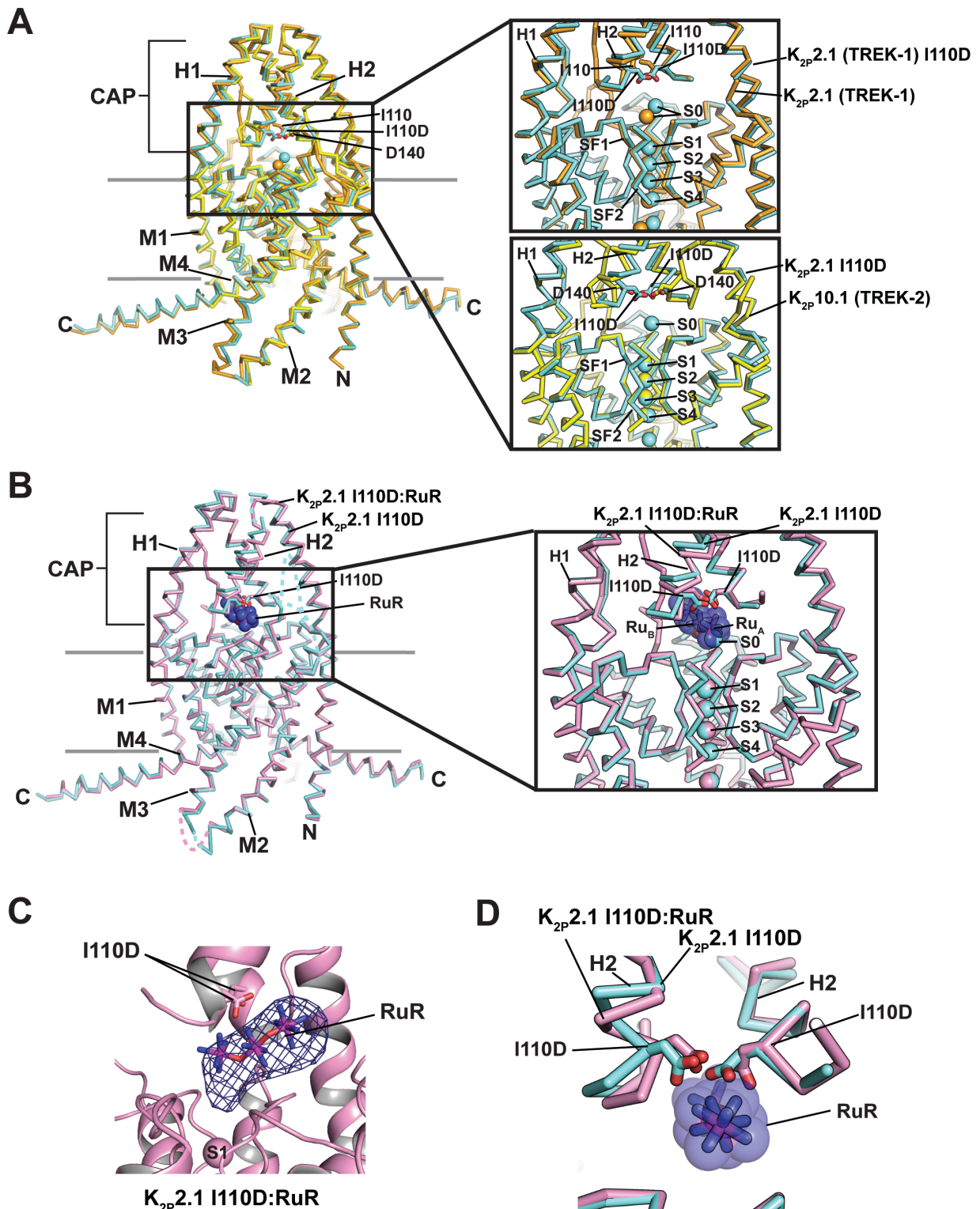
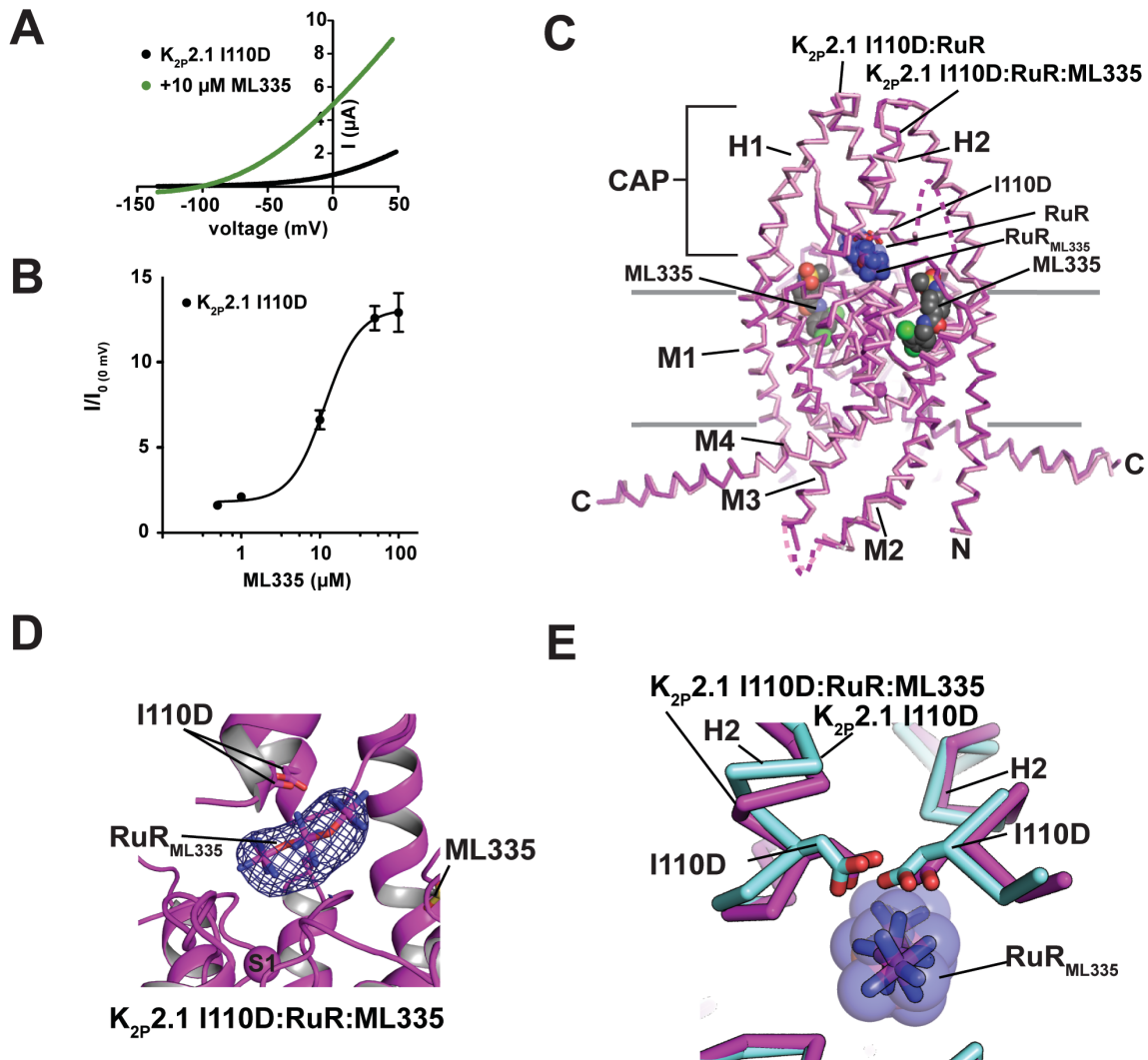


**Figure 3.7 | S2 - K<sub>2P</sub>2.1 I110D structures and structure comparisons**

(A) Superposition of K<sub>2P</sub>2.1 (TREK-1) (orange) (PDB:6CQ6)(27), K<sub>2P</sub>2.1 I110D (cyan), and K<sub>2P</sub>10.1 (TREK-2) (PDB:4BW5) (yellow)<sup>28</sup>.

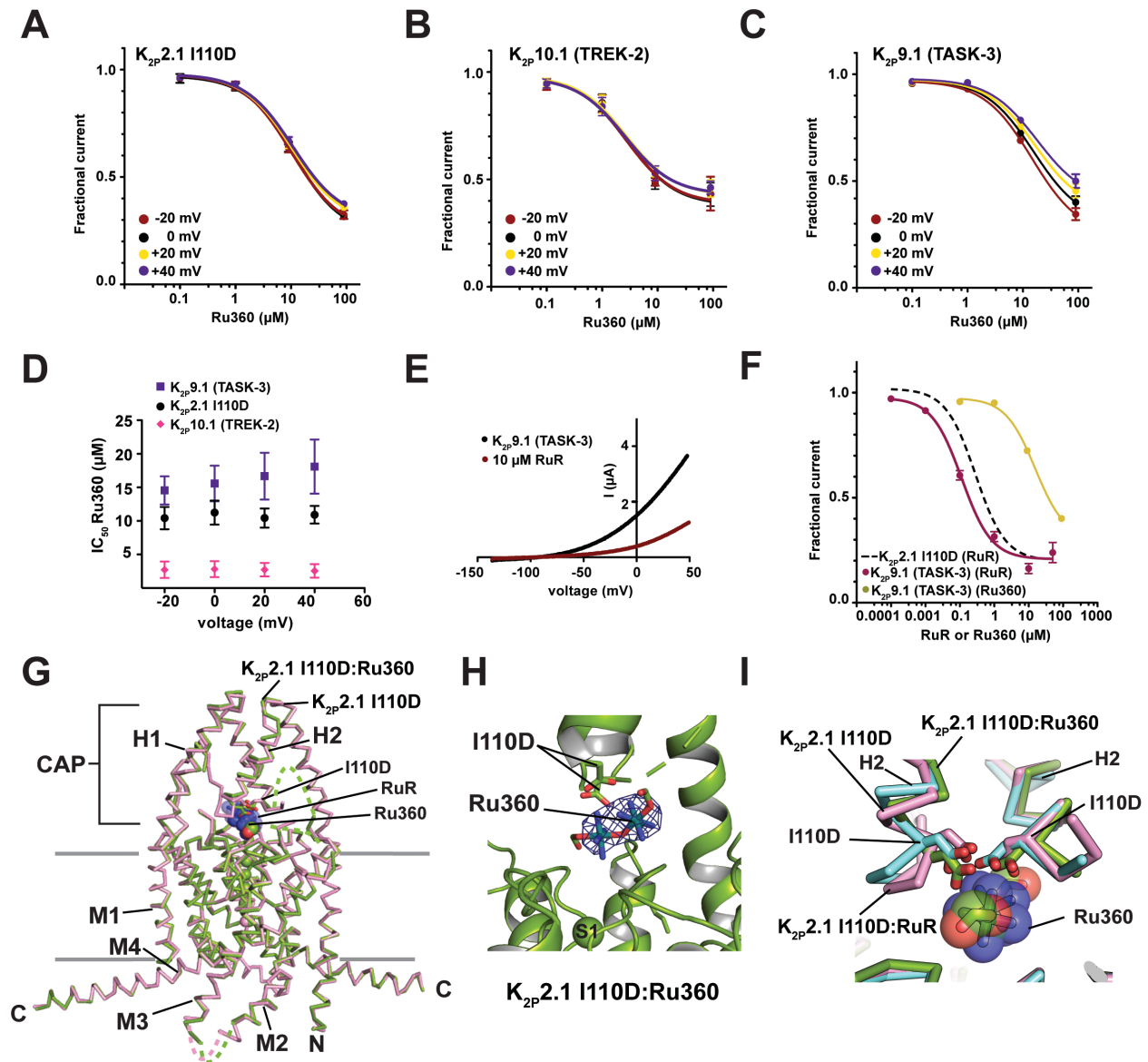


the I110D mutation. Top, K<sub>2P</sub>2.1 (TREK-1) and K<sub>2P</sub>2.1 I110D; Bottom K<sub>2P</sub>2.1 I110D and K<sub>2P</sub>10.1 (TREK-2). **(B)** Superposition of K<sub>2P</sub>2.1 I110D (cyan) and K<sub>2P</sub>2.1 I110D:RuR (pink). Inset shows area around the Keystone inhibitor site. RuR is shown as sticks with a semi-transparent surface. **(C)** Exemplar Fo-Fc density ( $3\sigma$ )(dark blue) for the K<sub>2P</sub>2.1 I110D:RuR complex (pink). RuR is shown as sticks. **(D)** Close up view of K<sub>2P</sub>2.1 I110D (cyan) and K<sub>2P</sub>2.1 I110D:RuR (pink) showing conformational changes in the Keystone inhibitor site. RuR is shown as sticks with a semi-transparent surface.



**Figure 3.8 | S3 -  $K_{2P}2.1$  I110D ML335 response and structure of the  $K_{2P}2.1$  I110D:RuR:ML335 complex**

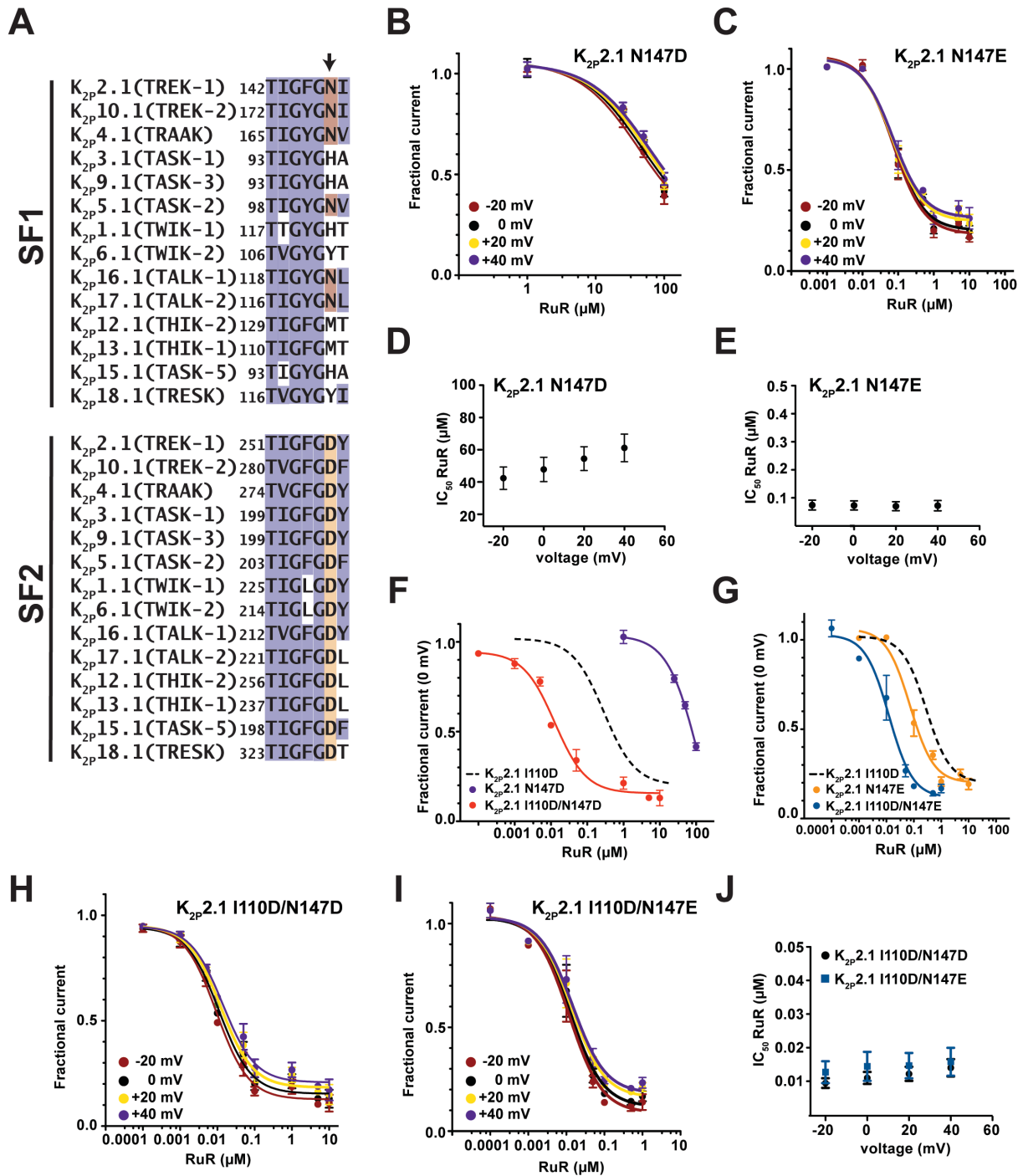
(A) Exemplar two-electrode voltage clamp recordings of the response of  $K_{2P}2.1$  I110D (black) to 10  $\mu$ M ML335 (green). (B) ML335 dose-response curve for  $K_{2P}2.1$  I110D.  $EC_{50} = 11.8 \pm 2.3 \mu$ M, matching that of  $K_{2P}2.1$  (TREK-1) ( $14.3 \pm 2.7 \mu$ M<sup>28</sup>). (C) Superposition of  $K_{2P}2.1$  I110D:RuR (pink) and  $K_{2P}2.1$  I110D:RuR:ML335 (magenta). I110D is shown as sticks. RuR and ML335 are shown in space filling representation. (D) Exemplar Fo-Fc density ( $3\sigma$ ) (dark blue) for the  $K_{2P}2.1$  I110D:RuR:ML335 complex (magenta), and (I110D, RuR, Ru360, and ML335 are shown as sticks. S1 selectivity filter ion is labeled. (E) Close up view of  $K_{2P}2.1$  I110D (cyan) and  $K_{2P}2.1$  I110D:RuR:ML335 (magenta) CAP base.



**Figure 3.9 | S4 - Ru360 inhibits  $K_{2P}$  channels**

(A-C) Ru360 dose-response curves at -20 mV (red), 0 mV (black), +20 mV (yellow), and +40 mV (purple) for (A)  $K_{2P}2.1$  I110D, (B)  $K_{2P}10.1$  (TREK-2), and (C)  $K_{2P}9.1$  (TASK-3). (D) RuR  $IC_{50}$  ( $\mu$ M) voltage-dependence for  $K_{2P}2.1$  I110D (black circles),  $K_{2P}10.1$  (TREK-2) (pink diamonds), and  $K_{2P}9.1$  (TASK-3) (purple squares). (E) Exemplar TEVC recordings of  $K_{2P}9.1$  (TASK-3) alone (black) and in the presence of 10  $\mu$ M RuR (dark red). (F)  $K_{2P}9.1$  (TASK-3) dose-response curves for RuR (dark red) and Ru360 (olive) (from Figure 3F). Dashed line shows RuR dose-response for  $K_{2P}2.1$  I110D from Figure 1D. (G) Superposition of  $K_{2P}2.1$  I110D:RuR (pink) and  $K_{2P}2.1$  I110D:Ru360 (green). I110D is shown as sticks. (H) Exemplar Fo-Fc density ( $3\sigma$ ) (dark blue) for the  $K_{2P}2.1$  I110D:Ru360 complex (green). I110D and Ru360 are

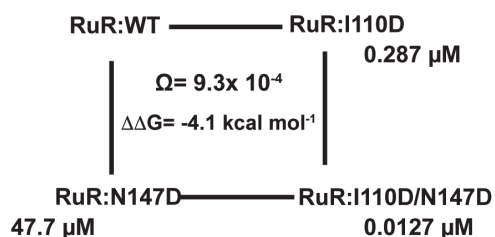
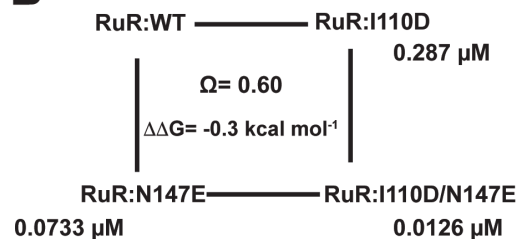
shown as sticks. S1 selectivity filter ion is labeled. (I) Close up view of  $K_{2P2.1}$  I110D:Ru360 (green),  $K_{2P2.1}$  I110D (cyan), and  $K_{2P2.1}$  I110D:RuR (pink) CAP base. RuR and Ru360 are shown in space filling representation.



**Figure 3.10 | S5 - K<sub>2P</sub> selectivity filter (SF) sequences and RuR responses of K<sub>2P</sub>2.1 SF mutants**

(A) Sequence alignment of the selectivity filter 1 (SF1) and selectivity filter 2 (SF2) sequences of the following human K<sub>2P</sub> channels. K<sub>2P</sub>2.1 (TREK-1) AAD47569.1, K<sub>2P</sub>10.1 (TREK-2) BAF83207, K<sub>2P</sub>4.1 (TRAAK) AAI10328.1, K<sub>2P</sub>3.1 (TASK-1) NP\_002237.1, K<sub>2P</sub>9.1 (TASK-3) NP\_001269463.1, K<sub>2P</sub>5.1 (TASK-2) NP\_003731.1, K<sub>2P</sub>1.1 (TWIK-1) NP\_002236.1, K<sub>2P</sub>6.1 (TWIK-2) NP\_004814.1, K<sub>2P</sub>16.1 (TALK-1) 129

NP\_001128577.1, K<sub>2P</sub>17.1 (TALK-2) AAK28551.1, K<sub>2P</sub>12.1 (THIK-2) NP\_071338.1, K<sub>2P</sub>13.1 (THIK-1) NP\_071337.2, K<sub>2P</sub>15.1 (TASK-5) EAW75900.1, K<sub>2P</sub>18.1 (TRESK) NP\_862823.1. SF1 and SF2 sequence and numbers for K<sub>2P</sub>2.1 (TREK-1)<sub>cryst</sub> (PDB:6CQ6)<sup>28</sup> are identical to that of K<sub>2P</sub>2.1 (TREK-1) AAD47569.1. **(B-C)** RuR dose-response curves at -20 mV (red), 0 mV (black), +20 mV (yellow), and +40 mV (purple) for **(B)** K<sub>2P</sub>2.1 N147D and **(C)** K<sub>2P</sub>2.1 N147E. **(D-E)** IC<sub>50</sub> voltage dependence for **(D)** K<sub>2P</sub>2.1 N147D and **(E)** K<sub>2P</sub>2.1 N147E. **(F-G)** RuR dose-response curves for **(F)** K<sub>2P</sub>2.1 N147D (purple) and K<sub>2P</sub>2.1 I110D/N147D (red) and **(G)** K<sub>2P</sub>2.1 I110E (orange) and K<sub>2P</sub>2.1 I110D/N147E (blue). Dashed lines show RuR response of K<sub>2P</sub>2.1 I110D from Fig. 1D. **(H-I)** RuR dose-response curves at -20 mV (red), 0 mV (black), +20 mV (yellow), and +40 mV (purple) for **(H)** K<sub>2P</sub>2.1 I110D/N147D and **(I)** K<sub>2P</sub>2.1 I110D/N147E. **(J)** IC<sub>50</sub> voltage dependence for K<sub>2P</sub>2.1 I110D/N147D (black circles) and K<sub>2P</sub>2.1 I110D/N147E (blue squares). Error bars are SEM.

**A****B**

**Figure 3.11 | S6 - Double mutant cycle analysis**

Double mutant cycle analysis<sup>69,70</sup> for the RuR responses of **(A)** K<sub>2P</sub>2.1 I110D/N147D and **(B)** K<sub>2P</sub>2.1 I110D/N147E.  $\Omega = \frac{IC_{50} X' Y'}{IC_{50} X' * IC_{50} Y'}$ , as  $\Delta\Delta G_{\Omega} = RTLn\Omega$  where R=1.987 cal mol<sup>-1</sup> deg<sup>-1</sup> and T= 298K.

**Table 3.1 | IC<sub>50</sub> values for RuR and Ru360**

Inhibitor	Construct	EC <sub>50</sub> (μM)	n	
RuR	K <sub>2P</sub> 2.1 (TREK-1)	K <sub>2P</sub> 2.1 (TREK-1)	>100	3
		K <sub>2P</sub> 2.1 I110D	0.287 ± 0.054	3
		K <sub>2P</sub> 2.1 I110E	13.6 ± 2.7	3
		K <sub>2P</sub> 2.1 I110K	>100	
		K <sub>2P</sub> 2.1 I110D/G137I	0.154 ± 0.023	3
		K <sub>2P</sub> 2.1 I110D + 50 μM ML335	0.173 ± 0.021	3
		K <sub>2P</sub> 2.1 N147D	47.7 ± 6.3**	2
		K <sub>2P</sub> 2.1 N147E	0.0733 ± 0.0165	3
		K <sub>2P</sub> 2.1 I110D/N147D	0.0127 ± 0.0023	3
	K <sub>2P</sub> 2.1 I110D/N147E	0.0126 ± 0.0034	3	
	Other K <sub>2P</sub> S	K <sub>2P</sub> 10.1 (TREK-2) [D135]*	0.23 ± 0.06 μM (Braun et al., 2015)	3
		K <sub>2P</sub> 9.1 (TASK-3) [E70]*	0.114 ± 0.021 μM	3
	Ru360	K <sub>2P</sub> 2.1 (TREK-1)	K <sub>2P</sub> 2.1 (TREK-1)	>100
K <sub>2P</sub> 2.1 I110D			11.3 ± 1.8	3
Other K <sub>2P</sub> S		K <sub>2P</sub> 10.1 (TREK-2) [D135]*	2.8 ± 1.2	3
		K <sub>2P</sub> 9.1 (TASK-3) [E70]*	15.6 ± 2.7	3

n = number of oocytes

Errors are SEM.

\*' residue at the K<sub>2P</sub>2.1 (TREK-1) I110D equivalent position

\*\* Lower bound constrained to 0.2



**Table 3.2 | Supplementary table 1 - Data collection and refinement statistics**

	<b>K<sub>2</sub>P2.1 (TREK-1) I110D (PDB:6V36)</b>	<b>K<sub>2</sub>P2.1 (TREK-1) I110D:RuR (PDB:6V3I)</b>
<b>Data collection</b>		
Space group	P2 <sub>1</sub> 2 <sub>1</sub> 2 <sub>1</sub>	P2 <sub>1</sub> 2 <sub>1</sub> 2 <sub>1</sub>
Cell dimensions		
<i>a</i> , <i>b</i> , <i>c</i> (Å)	69.19/120.40/128.35	67.95/120.3/127.82
$\alpha$ , $\beta$ , $\gamma$ (°)	90/90/90	90/90/90
Resolution (Å)	46.7 – 3.40 (3.67 - 3.40)	46.6 - 3.49 (3.82 - 3.49)
<i>R</i> <sub>merge</sub>	0.072 (5.87)	0.089 (3.80)
<i>I</i> / $\sigma$ ( <i>I</i> )	9.6 (0.5)	9.8 (0.8)
<i>CC</i> <sub>1/2</sub>	0.999 (0.128)	1.000 (0.331)
Completeness (%)	99.9 (100.0)	100.0 (100.0)
Redundancy	6.5 (6.7)	8.8 (9.0)
<b>Refinement</b>		
Resolution (Å)	15.00 - 3.40	15.00 – 3.49
No. reflections	14468	13484
<i>R</i> <sub>work</sub> / <i>R</i> <sub>free</sub>	28.6/31.6	26.5/32.7
No. atoms	4124	4192
Protein	4066	4092
Ligand/ion	55	98
K <sup>+</sup>	6	5
Cd <sup>++</sup>	3	3
Lipid	46	63
ML335	0	0
RuR	0	1
Ru360	0	0
Water	3	2
<i>B</i> factors		
Protein	227.94	191.96
Ligand/ion	195.40	196.35
R.M.S. deviations		
Bond lengths (Å)	0.004	0.004
Bond angles (°)	0.913	0.760
Ramachandran		
Favored (%)	94.6	93.9
Allowed (%)	4.8	5.1
Outliers (%)	0.6	1.0

Each dataset was derived from a single crystal.

<sup>a</sup> Values in parentheses are for highest-resolution shell.

**Table 3.3 | Supplementary table 1 (ct'd) - Data collection and refinement statistics**

	<b>K<sub>2</sub>P2.1 (TREK-1) I110D:RuR:ML335 (PDB: 6V37)</b>	<b>K<sub>2</sub>P2.1 (TREK-1) I110D:Ru360 (PDB:6V3C)</b>
<b>Data collection</b>		
Space group	P2 <sub>1</sub> 2 <sub>1</sub> 2 <sub>1</sub>	P2 <sub>1</sub> 2 <sub>1</sub> 2 <sub>1</sub>
Cell dimensions		
<i>a</i> , <i>b</i> , <i>c</i> (Å)	67.02/118.74/129.04	67.74/120.71/127.27
$\alpha$ , $\beta$ , $\gamma$ (°)	90/90/90	90/90/90
Resolution (Å)	46.5 - 3.00 (3.18 - 3.00)	46.4 - 3.51 (3.85 - 3.51)
<i>R</i> <sub>merge</sub>	0.085 (2.45)	0.110 (8.64)
<i>I</i> / $\sigma$ ( <i>I</i> )	16.8 (1.2)	10.8 (0.4)
<i>CC</i> <sub>1/2</sub>	0.996 (0.553)	1.000 (0.149)
Completeness (%)	100.0 (100.0)	100.0 (100.0)
Redundancy	13.2 (13.7)	13.3 (13.7)
<b>Refinement</b>		
Resolution (Å)	14.99 – 3.00	14.98 – 3.51
No. reflections	21051	12595
<i>R</i> <sub>work</sub> / <i>R</i> <sub>free</sub>	26.7/31.4	31.0/32.6
No. atoms	4309	4063
Protein	4180	3993
Ligand/ion	127	68
K <sup>+</sup>	5	5
Cd <sup>++</sup>	3	3
Lipid	82	43
ML335	1	0
RuR	1	0
Ru360	0	1
Water	2	2
<b><i>B</i> factors</b>		
Protein	145.60	200.63
Ligand/ion	150.32	182.87
<b>R.M.S. deviations</b>		
Bond lengths (Å)	0.003	0.002
Bond angles (°)	0.628	0.559
<b>Ramachandran</b>		
Favored (%)	92.5	96.6
Allowed (%)	6.7	3.4
Outliers (%)	0.8	0.0

Each dataset was derived from a single crystal.

<sup>a</sup> Values in parentheses are for highest-resolution shell.

**Table 3.4 | Supplementary table 2 - Structure Comparisons of RuR and Ru360 complexes**

		RMSD (Å)
K <sub>2P</sub> 2.1 I110D		K <sub>2P</sub> 2.1 (TREK-1) (6CQ6)(27) 0.575
K <sub>2P</sub> 2.1 I110D		K <sub>2P</sub> 10.1 (TREK-2) (4BW5)(26) 0.938
K <sub>2P</sub> 2.1 I110D	<b>Versus</b>	K <sub>2P</sub> 2.1 I110D:RuR 0.688
K <sub>2P</sub> 2.1 I110D		K <sub>2P</sub> 2.1 I110D:Ru360 0.665
K <sub>2P</sub> 2.1 I110D:RuR:ML335		K <sub>2P</sub> 2.1 I110D:RuR 0.507
K <sub>2P</sub> 2.1 I110D:RuR:ML335		K <sub>2P</sub> 2.1 (TREK-1):ML335 (6CQ8)(27) 0.480
K <sub>2P</sub> 2.1 I110D:Ru360		K <sub>2P</sub> 2.1 I110D:RuR 0.561

RMSDs were calculated using C $\alpha$  atoms in the specified residue ranges after optimal translational and rotational alignment of those atoms. Calculations were performed with the MDAnalysis python package version 0.19.2 (78). Residue ranges include all of the  $\alpha$ -helical portions of the structures as follows: K<sub>2P</sub>2.1 (TREK-1): 45-93, 96-110, 126-190, 206-259, 268-300; K<sub>2P</sub>10.1 (TREK-2): 75-123, 126-140, 156-220, 236-289, 299-331. 4BW5 comparison is for chains A and B from the asymmetric unit.

***Chapter 4 : Stapled voltage-gated calcium channel (Ca<sub>v</sub>)  $\alpha$ -interaction domain (AID) peptides act as selective protein-protein interaction inhibitors of Ca<sub>v</sub> function***

Felix Findeisen, Marta Campiglio, Hyunil Jo, Fayal Abderemane-Ali, Christine H. Rumpf, Lianne Pope, Nathan D. Rossen, Bernhard E. Flucher, William F. DeGrado, and Daniel L. Minor, Jr

## **Abstract**

For many voltage-gated ion channels (VGICs) creation of a properly functioning ion channel requires the formation of specific protein-protein interactions between the transmembrane pore-forming subunits and cytoplasmic accessory subunits. Despite the importance of such protein-protein interactions in VGIC function and assembly, their potential as sites for VGIC modulator development has been largely overlooked. Here, we develop meta-xylyl (m-xylyl) stapled peptides that target a prototypic VGIC high affinity protein-protein interaction, the interaction between the voltage-gated calcium channel ( $\text{Ca}_V$ ) pore-forming subunit  $\alpha$ -interaction domain (AID) and cytoplasmic  $\beta$ -subunit ( $\text{Ca}_V\beta$ ). We show using circular dichroism spectroscopy, X-ray crystallography, and isothermal titration calorimetry that the m-xylyl staples enhance AID helix formation, are structurally compatible with native-like AID: $\text{Ca}_V\beta$  interactions, and reduce the entropic penalty associated with AID binding to  $\text{Ca}_V\beta$ . Importantly, electrophysiological studies reveal that stapled AID peptides act as effective inhibitors of the  $\text{Ca}_V\alpha_1$ : $\text{Ca}_V\beta$  interaction that modulate  $\text{Ca}_V$  function in an  $\text{Ca}_V\beta$  isoform-selective manner. Together, our studies provide a proof-of-concept demonstration of the use of protein-protein interaction inhibitors to control VGIC function and point to strategies for improved AID-based  $\text{Ca}_V$  modulator design.

## **Introduction**

Voltage-gated ion channels (VGICs) control electrical signaling in the brain, heart, and nervous system<sup>1</sup>. Many members of this protein superfamily are multi-protein complexes comprising both transmembrane pore-forming subunits and cytoplasmic regulatory subunits<sup>2</sup>. VGIC cytoplasmic subunits can exert strong control over channel function by conferring distinct biophysical properties to the resulting channel complex and by affecting channel biogenesis and plasma membrane trafficking<sup>1, 3-5</sup>. Although the importance of such subunits for VGIC function is well established, with the exception of a few cases<sup>6-9</sup>, their potential as targets for the development of agents that could control channel function has been largely overlooked<sup>10-12</sup>. Protein-protein interaction antagonists have been shown to be effective modulators of diverse protein classes<sup>13-17</sup> but have not yet been developed and validated for any ion channel system. Hence, we asked whether we could advance this type of reagent against the exemplar VGIC high-affinity protein-protein interaction formed between the voltage-gated calcium channel pore-forming  $Ca_V\alpha_1$  and cytoplasmic  $Ca_V\beta$  subunits for which there is a wealth of structural information to guide design<sup>18</sup>.

High-voltage  $Ca_V$ s ( $Ca_V1$ s and  $Ca_V2$ s) are the principal agents of calcium influx in excitable cells, are vital components of the machinery that regulates muscle contraction, vascular tone, hormone and neurotransmitter release, and synaptic function and provide a prototypical example of the pivotal role of cytoplasmic subunits in VGIC function<sup>1, 19-21</sup>.  $Ca_V1$ s and  $Ca_V2$ s are made from at least four main components<sup>18, 22, 23</sup>: a  $Ca_V\alpha_1$  pore forming subunit, a cytoplasmic  $Ca_V\beta$  subunit<sup>20, 21</sup>, the extracellular  $Ca_V\alpha_2\delta$  subunit<sup>24</sup>, and a calcium sensor protein, such as calmodulin<sup>25</sup>. The  $Ca_V\alpha_1:Ca_V\beta$  interaction is central to

the formation of properly functioning native  $\text{Ca}_V\text{S}$ <sup>20, 21</sup>, controls  $\text{Ca}_V$  trafficking to the plasma membrane<sup>3, 26-30</sup>, and affects a number of  $\text{Ca}_V$  biophysical properties including voltage-dependent activation and the rate of channel inactivation<sup>20, 21, 31-39</sup>.  $\text{Ca}_V\alpha_1$  and  $\text{Ca}_V\beta$  associate through a high affinity ( $K_d \sim \text{nM}$ )<sup>40-45</sup> interaction between a short peptide segment on the  $\text{Ca}_V$  intracellular I-II loop, known as the  $\alpha$ -interaction domain (AID), and a groove in  $\text{Ca}_V\beta$  termed the  $\alpha$ -binding pocket (ABP)<sup>20, 46-49</sup>.

$\text{Ca}_V\text{S}$  are validated targets for drugs treating cardiovascular diseases, epilepsy, and chronic pain<sup>19, 50</sup>. Well-studied modifiers of  $\text{Ca}_V$  function such as small molecule drugs and peptide toxins largely target the pore-forming subunit<sup>19, 50-52</sup>. Because of the central role of the AID:ABP protein-protein interaction in  $\text{Ca}_V$  function, there has been an interest in establishing whether interfering with this interaction might provide an alternative strategy for  $\text{Ca}_V$  modulation<sup>45, 53</sup>. Previous studies suggesting that the  $\text{Ca}_V\alpha_1:\text{Ca}_V\beta$  interaction is labile<sup>54-57</sup> and studies showing that blocking  $\text{Ca}_V\beta$  action is a productive means to affect  $\text{Ca}_V$  function<sup>8, 9</sup> support such an approach.

Because stapled-peptide strategies have been particularly effective at targeting protein-protein interactions in which one partner is single  $\alpha$ -helix<sup>17, 58</sup>, such as in the AID:ABP case, we pursued the stapled-peptide strategy to develop AID-based inhibitors of the AID:ABP interaction and  $\text{Ca}_V$  function. Previously, we and others demonstrated that chemical crosslinking of  $i$  and  $i+4$  cysteines could be useful for  $\alpha$ -helical peptide stabilization<sup>59, 60</sup>. Here, we expand this cysteine crosslinking strategy to constrain an N-terminal capping motif<sup>61, 62</sup> appended to the AID. Our studies demonstrate that stapling AID peptides with a meta-xylyl bridge<sup>59, 63</sup> between two engineered cysteines creates AID



peptides having enhanced helical content that bind  $Ca_v\beta$  in a native-like manner. We find that the macrocyclic constrained cap acts as an effective means to enhance helix content and that importantly, the enhanced AID peptide is a potent inhibitor of  $Ca_v$  currents that causes  $Ca_v\beta$  isoform-specific inhibition of the AID:ABP interaction.

## Results

### AID Backbone modifications increase alpha-helical content of AID

Structural studies have shown that there is essentially no conformational change between the apo- and AID-bound  $\text{Ca}_v\beta$  ABP<sup>46-48</sup>. By contrast, the  $\text{Ca}_v$  AID peptide undergoes a large conformational change between an unbound disordered state and the  $\text{Ca}_v\beta$ -bound helical conformation<sup>45, 47, 64, 65</sup>. This binding event involves a substantial entropic penalty,  $\sim -14 \text{ cal mol}^{-1} \text{ K}^{-1}$ <sup>45</sup>, that due to the essentially unchanged structure of the ABP, must arise from the entropic cost of ordering the AID. In order to overcome this problem, we pursued a chemical stabilization strategy to enhance the helical structure of the AID unbound state (Figure 1A).

Previously, we and others demonstrated that introduction of m-xylyl linker between two cysteines ( $i, i+4$ ) by thiol alkylation<sup>63</sup> could be used to stabilize the  $\alpha$ -helical conformation in peptides<sup>59, 60</sup>. This cysteine alkylation strategy has the advantage of not requiring unnatural amino acids. To date, all strategies for stapled peptide synthesis have focused on introduction of linkers along one  $\alpha$ -helix face, an approach that can buttress the structure but that does not restrain the  $\alpha$ -helix polar ends. To address this issue, we introduced an N-terminal capping motif<sup>61, 62</sup> into two AID peptides, AID-CAP and AID-CEN (Figure 1B). This capping motif includes an  $\text{N}_{\text{Cap}}$  position serine intended to stabilize the structure through hydrogen bonds to the exposed amide protons at the helix N-terminus, an  $\text{N}_1$  position proline to act as a helix initiator, and an  $\text{N}_3$  position glutamate placed to contribute hydrogen bonds to the  $\text{N}_{\text{Cap}}$  serine and amide backbone (Figure 1B). In the case of AID-CAP, two cysteines were included to make a macrocyclic capping box sequence, Cys-Ser-Pro-Leu-Glu-Cys, in which the cysteine residues should allow facile

macrocyclization with *m*-xylyl bromide (Figure 1B). AID-CEN bears an unconstrained capping motif and a more conventional (*i*, *i*+4) crosslinking motif within the helix (K435C and D439C) (Figure 1B). In both peptides, cysteine positions for staple attachment were chosen to reside on the exposed AID surface based on structures of the Ca<sub>v</sub>β-AID complexes in order to avoid introducing interfering interactions.

Circular dichroism (CD) studies of AID-CAP and AID-CEN indicated that *m*-xylyl staple incorporation affected the secondary structure to different extents depending on the staple location (Figure 1C). The *m*-xylyl staple in AID-CEN caused a modest change that reduced the intensity of the signal at 208 nm relative to the unmodified AID. By contrast, AID-CAP displayed the hallmark double minima associated with α-helical structure that was absent in the unmodified AID peptide<sup>66</sup> and that indicates that the N-terminal cap site is a potent element for stabilizing the AID helical conformation.

### **X-ray crystal structures show that Ca<sub>v</sub>β<sub>2a</sub>:stapled AID complexes are similar to native complexes**

To investigate the structural integrity of the backbone staple designs, we crystallized and determined the structure of AID-CAP and AID-CEN bound to a unimolecular Ca<sub>v</sub>β<sub>2a</sub> construct previously used for extensive Ca<sub>v</sub>β<sub>2a</sub>:AID thermodynamic binding studies<sup>45</sup>. Crystals of the AID-CAP complex grew in the H3 space group having one molecule in the asymmetric unit and diffracted X-rays to 1.9 Å (Table S1). Structure solution by molecular replacement ( $R/R_{\text{free}} = 18.5/23.0\%$ ) revealed a Ca<sub>v</sub>β<sub>2a</sub>:AID structure similar to that determined previously for the unconstrained AID<sup>48</sup> (RMSD<sub>Cα</sub> = 1.2 Å) (Figure 2A) except for a few minor differences. The Ca<sub>v</sub>β<sub>2a</sub> α1 helix is longer by ten residues (Figure S1A)

and there is a moderate divergence in the angle of the  $\alpha 2$  helix. This element precedes the disordered V2/HOOK domain and extends from the SH3 domain far from the AID binding site (Figure S1A) and is affected by crystal lattice contacts. Excluding the  $\alpha 2$  helix from the comparison, the structures of the  $\text{Ca}_V\beta_{2a}:\text{AID}$ - and  $\text{Ca}_V\beta_{2a}:\text{AID-CAP}$  complexes are essentially identical ( $\text{RMSD}_{\text{C}\alpha} = 0.55 \text{ \AA}$  over residues 43-127, 217-273, 295-414).

The structure of the  $\text{Ca}_V\beta_{2a}:\text{AID-CAP}$  complex (Figure 2A) reveals that the AID-CAP peptide binds to the  $\alpha$ -binding pocket (ABP) in a manner that is identical to the wild-type AID (Figure S1A) using the main hydrophobic anchors Tyr437, Trp440, and Ile441, and interactions with two buried water molecules coordinated by the sidechain of Ty437 (Figure S1B)<sup>45-48</sup>. The m-xylyl linker connecting the  $i \rightarrow i+5$  cysteines was clearly visible in the electron density (Figure 2B). This moiety makes no interactions with  $\text{Ca}_V\beta$ , indicating that its effects are only on the AID conformational properties as intended. The N-terminal AID-CAP residue, Cys427, adopts a non-helical conformation that occupies the  $\beta$ -backbone conformation portion of the Ramachandran plot. Subsequent residues form a regular  $\alpha$ -helix. Within the m-xylyl stabilized region, the Glu431 sidechain contacts the backbone nitrogen of Ser428, satisfying the backbone requirement for this otherwise free functional group and the intention of the sequence design. The cysteine members of the m-xylyl staple, Cys427 and Cys432, have sidechain  $\chi 1$  angles of ( $+60^\circ$ ) and meta ( $-180^\circ$ ), respectively, resulting in a 5.9  $\text{\AA}$  distance between the Cys427 and Cys432 sulfurs, that allows for unstrained connection through the meta-xylene functional group.

We also obtained crystals of the  $\text{Ca}_V\beta_{2a}:\text{AID-CEN}$  complex that grew in the  $\text{P}2_12_12_1$  spacegroup, diffracted X-rays to 1.8  $\text{\AA}$ , and were solved by molecular replacement

( $R/R_{\text{free}} = 15.8/19.6\%$ ) (Figure 2C, Table S1). In this structure,  $\text{Ca}_V\beta_{2a}$  has an extended C-tail (residues 417-425) (Figure S1A) but otherwise, the  $\text{Ca}_V\beta_{2a}$  component is essentially unchanged from the  $\text{Ca}_V\beta_{2a}$  core<sup>48</sup> ( $\text{RMSD}_{\text{C}\alpha} = 0.4 \text{ \AA}$  over residues 43-127, 217-273, 295-414) or  $\text{Ca}_V\beta_{2a}$  in the  $\text{Ca}_V\beta_{2a}:\text{AID-CAP}$  complex (Figure 2C,  $\text{RMSD}_{\text{C}\alpha} = 0.4 \text{ \AA}$  over residues 43-127, 217-273, 295-414). As with the  $\text{Ca}_V\beta_{2a}:\text{AID-CAP}$  complex, the AID-CEN backbone forms a regular  $\alpha$ -helix and the  $\text{Ca}_V\beta_{2a}:\text{AID-CEN}$  interaction is unaltered from the native structure (Figure S1B). Density for the  $i \rightarrow i+4$  m-xylyl backbone staple was well resolved (Figure 2D) and shows that, similar to the situation with AID-CAP, the m-xylyl staple plays no direct role in  $\text{Ca}_V\beta$  binding. The cysteine anchors for the m-xylyl staple, Cys435 and Cys439, have sidechain  $\chi_1$  angles of  $-180^\circ$  and  $-161^\circ$ , respectively. This conformation leads to a  $6.5 \text{ \AA}$  distance between the Cys435 and Cys439 sulfurs. The  $\sim 20^\circ$  deviation from the regular low energy conformers of Cys439 suggests that there is a small energetic cost for liganding the anchor atoms at a  $6.5 \text{ \AA}$  distance. Comparison of the N-terminal capping motifs in the  $\text{Ca}_V\beta_{2a}:\text{AID-CAP}$  and  $\text{Ca}_V\beta_{2a}:\text{AID-CEN}$  complexes shows that the designed hydrogen bond network among the  $\text{N}_{\text{Cap}}$ ,  $\text{N}_2$ ,  $\text{N}_3$ , and  $\text{N}_4$  positions is well formed in the presence of the AID-CAP m-xylyl staple (Figure S1C). This network is also present in the unconstrained capping motif in AID-CEN, but has longer hydrogen bonds and slightly different interactions for Glu431 (Figure S1D). Together, the structural data demonstrate that the m-xylyl staple is compatible with the helical conformation of the AID and in the case of AID-CAP helps to organize the N-terminal capping motif.

### **AID helix staples lower the entropic cost of ligand binding**

Having determined that the backbone staples are able to affect AID helix content (Figure 1) and are structurally compatible with the  $\text{Ca}_v\beta$ -AID interaction (Figure 2), we used isothermal titration calorimetry (ITC) to investigate whether the AID staples impacted binding thermodynamics. Experiments measuring  $\text{Ca}_v1.2$  AID binding to the  $\text{Ca}_v\beta_{2a}$  core yielded an affinity in good agreement with prior measurements  $K_d = 6.6 \pm 2.0$  nM vs.  $5.3$  nM<sup>45</sup> (Figure 3A, Table 1). This binding reaction is driven by a favorable enthalpic component ( $\Delta H = -15.6 \pm 2.4$  kcal mol<sup>-1</sup>) that is opposed by a large entropic cost ( $\Delta S = -16.7 \pm 6.0$  cal mol<sup>-1</sup> K<sup>-1</sup>) that most likely results from the requirement to reduce the degrees of freedom of the highly disordered ligand upon binding.

ITC measurements with AID-CEN and AID-CAP revealed that both peptides bind  $\text{Ca}_v\beta_{2a}$  with affinities similar to wild type AID,  $5.2 \pm 1.5$  nM and  $5.1 \pm 1.6$  nM, respectively (Figure 3B and C, Table 1) but that incorporation of the m-xylyl moiety affects the thermodynamic binding parameters of the  $\text{Ca}_v\beta_{2a}$ :AID interaction. Consistent with the incorporation of the m-xylyl staple and decrease in random coil as seen by CD (Figure 1), the entropic cost of complex formation was reduced relative to the wild type for both stapled peptides ( $\Delta S = 2.2 \pm 0.5$  and  $-4.6 \pm 4.1$  cal mol<sup>-1</sup> K<sup>-1</sup> for AID-CEN and AID-CAP, respectively). However, this reduction of the unfavorable entropic component was offset by a binding enthalpy reduction ( $\Delta H = -10.2 \pm 0.1$  and  $-12.3 \pm 1.4$  kcal mol<sup>-1</sup>, AID-CEN and AID-CAP, respectively). Because neither m-xylyl staple contributes to the AID:ABP interaction, and there are no obvious changes in ABP interaction site contacts (Figure S1A and S1B), this result appears to be an example of enthalpy-entropy compensation<sup>67</sup> and may originate in the loss of some of the favorable enthalpy of helix formation<sup>68</sup> due

to the pre-ordering of the helical structure in the unbound state. Even though the effects of enthalpy-entropy compensation left the binding affinity unaffected, the data demonstrate that the inclusion of the staple was effective at reducing the disorder of the unbound AID as designed.

### **Stapled AID peptides compete with mutant but not wild-type Cav1.2:Ca $v\beta$ <sub>2a</sub> complexes**

Because AID-CAP and AID-CEN had similar affinities for Ca $v\beta$  but the AID-CAP had the highest amount of helical structure, we focused on testing whether AID-CAP could affect Ca $v$  function. Ca $v\beta$  binding to the pore-forming Ca $v\alpha_1$  subunit AID is known to cause clear changes to channel gating properties, such as the extent and speed of inactivation and the channel activation potential ( $V_{1/2}$ )<sup>20, 45, 64</sup>. We were concerned that the tight interaction between Ca $v\alpha_1$  and Ca $v\beta$  subunits might be difficult to compete with an exogenous peptide, particularly because the Ca $v$ 1.2:Ca $v\beta$ <sub>2a</sub> interaction has been shown to be long-lived unless it is weakened by ABP-AID interface mutations<sup>69</sup>. Hence, we first performed competition experiments using a Ca $v\alpha_1$  subunit bearing an AID mutation that lowers the Ca $v\beta$  affinity by ~1000 fold (Y437A,  $K_d$  = 5.3 vs. 5263 nM for wild-type and Y437A, respectively<sup>45</sup>). To test the ability of AID peptides to interfere with Ca $v$  function, we measured the response of pre-assembled, functional, plasma membrane Ca $v$  complexes expressed in *Xenopus* oocytes to competitor peptides (Figure 4), similar to the approach we used previously to uncover the direct competition between calcium sensor proteins on Ca $v$ s<sup>70</sup>. Two principal inactivation processes govern Ca $v$  function, voltage-dependent inactivation (VDI)<sup>71, 72</sup> and calcium-dependent inactivation (CDI)<sup>25, 72</sup>,

<sup>73</sup>. Because VDI is essentially absent with  $\text{Ca}_V\beta_{2a}$ <sup>20</sup> and CDI requires  $\text{Ca}_V\beta$ <sup>64</sup>, we measured CDI over the course of 30 minutes post-injection to monitor functional consequences of AID peptide injection on  $\text{Ca}_V\beta_{2a}$  containing channels (Figure 4).

One functional signature of the interaction of  $\text{Ca}_V1.2$  with  $\text{Ca}_V\beta_{2a}$  is the extent and speed of inactivation, which are more complete and faster, respectively, in the presence of  $\text{Ca}_V\beta_{2a}$  (Table 2). Prior to peptide injection,  $\text{Ca}_V1.2\text{-Y437A}:\text{Ca}_V\beta_{2a}$  channels were essentially functionally identical to wild-type  $\text{Ca}_V1.2:\text{Ca}_V\beta_{2a}$  channels (Table 2). Within 30 minutes of injection of 400  $\mu\text{M}$  AID or AID-CAP peptides, we observed substantial and similar changes from both peptides with respect to the extent of channel inactivation 300 ms after activation ( $t_{i300}$ ) ( $t_{i300}$  decreased from  $64.9 \pm 1.9\%$  to  $44.8 \pm 2.1\%$  and  $65.5 \pm 1.3\%$  to  $43.1 \pm 3.7\%$  for AID and AID-CAP, respectively) (Figure 5 A-C). In fact, at 30 minutes after peptide injection, the extent of inactivation was indistinguishable from  $\text{Ca}_V1.2$  expressed in the absence of  $\text{Ca}_V\beta$  ( $t_{i300} = 47.9 \pm 1.2\%$ ,  $44.8 \pm 2.1\%$ , and  $43.1 \pm 3.7\%$ , for no  $\text{Ca}_V\beta$ , AID (30'), and AID-CAP (30'), respectively), suggesting that the peptides had interfered completely with  $\text{Ca}_V\beta$  binding. By contrast, injection of an AID mutant peptide in which the three most important residues for binding to  $\text{Ca}_V\beta$  were mutated to alanine (Y437A/W440A/I441, termed 'HotA'<sup>45</sup>) showed no specific effects on fractional inactivation and had effects indistinguishable from water injection (Figure 5) ( $t_{i300}$  decreased from  $68.8 \pm 1.0\%$  to  $63.7 \pm 1.3\%$  and  $67.2 \pm 1.9\%$  to  $59.8 \pm 2.6\%$  for HotA and water, respectively, Figure 5 and Table 2). In addition to the  $t_{i300}$  changes, the fraction of the fast inactivation component decreased after injection of either AID or AID-CAP to levels similar to  $\text{Ca}_V1.2$  expressed without a  $\text{Ca}_V\beta$  subunit (Figure 5C).



A second functional signature of the interaction of  $\text{Ca}_v\beta_{2a}$  with  $\text{Ca}_v1.2$  is a hyperpolarizing shift of  $\sim 10$  mV in the channel activation ( $V_{1/2} = 18.1 \pm 1.0$  mV and  $8.1 \pm 1.2$  mV, for  $\text{Ca}_v1.2$  without and with  $\text{Ca}_v\beta_{2a}$ , respectively, Table 2). In  $\text{Ca}_v1.2$  Y437A: $\text{Ca}_v\beta_{2a}$  channels, competition with both the AID and AID-CAP peptides reduced this effect of  $\text{Ca}_v\beta$  on channel activation ( $V_{1/2} = 15.1 \pm 2.0$  mV and  $16.9 \pm 1.0$  mV, for AID and AID-CAP, respectively) (Figure 5D, Table 2). By contrast, oocytes co-expressing  $\text{Ca}_v1.2$ -Y437A: $\text{Ca}_v\beta_{2a}$  that were injected either with water or the HotA peptide did not show any changes in gating characteristics. These observations are consistent with the notion that AID and AID-CAP peptide injection counteracted the effect of  $\text{Ca}_v\beta_{2a}$  on the voltage-dependency of channel activation and suggest that the observed effects arise from disruption of the  $\text{Ca}_v1.2$ : $\text{Ca}_v\beta_{2a}$  interaction.

Recordings from  $\text{Ca}_v1.2$ -Y437A: $\text{Ca}_v\beta_{2a}$  expressing oocytes challenged by AID or AID-CAP also showed consistently higher rundown, compared to recordings from water or HotA peptide injected oocytes (Figure 5E and Table 2). This increased rundown may reflect some enhanced internalization of channel once the  $\text{Ca}_v1.2$ : $\text{Ca}_v\beta$  interaction is lost or possible inhibition of the formation of new complexes. Subtraction of the water-injected baseline revealed that the AID and AID-CAP induced rundown of  $I_{\max}$  reached steady state on the timescale of minutes (Figure 5F) and that the AID-CAP peptide was more potent than the unstapled wild-type. The rundown process could be well fit by a single exponential (Figure 5F) ( $\tau = 5.3 \pm 0.9$  and  $4.1 \pm 0.4$  min for AID and AID-CAP, respectively). All of the observed characteristic changes caused by AID and AID-CAP injection are consistent with a disruption of the  $\text{Ca}_v1.2$ : $\text{Ca}_v\beta_{2a}$  interaction.

Given that the AID-CAP peptide performed better than the AID, we next asked whether AID-CAP could compete with  $\text{Ca}_V\beta_{2a}$  bound to an unaltered channel. Contrasting the results with  $\text{Ca}_V1.2\text{-Y437A}$ , the effects of 400  $\mu\text{M}$  AID-CAP injection into wild-type  $\text{Ca}_V1.2$  expressing oocytes were not different from the effects seen with water or similar concentration injections of HotA on  $\text{Ca}_V1.2\text{-Y437A}:\text{Ca}_V\beta_{2a}$ . Increasing the injected AID-CAP concentration to 2.8 mM did not cause functional effects that were different from the negative controls with the exception of inducing a slight increase in channel rundown (Figure 6). Thus, unlike the situation in which the AID:ABP interaction is weakened by the Y437A mutation in the  $\text{Ca}_V1.2$   $\alpha_1$ -subunit AID, native  $\text{Ca}_V1.2:\text{Ca}_V\beta_{2a}$  complexes appear to be sufficiently stable to resist kinetic competition by the injected peptides.

### **Stapled AID peptides compete with functional $\text{Ca}_V1.2/\text{Ca}_V\beta_3$ complexes in oocytes**

$\text{Ca}_V\beta_{2a}$  bears an N-terminal palmitoylation site<sup>74</sup> that anchors it to the plasma membrane making it different from other  $\text{Ca}_V\beta$  isoforms. This membrane tethering should increase the effective concentration<sup>75</sup> of the AID:ABP interaction and could thwart the ability of AID peptides to compete with the native AID:ABP interaction. To test this idea, we examined whether AID and AID-CAP peptides could affect wild-type  $\text{Ca}_V1.2$  co-expressed with non-palmitoylated isoform  $\text{Ca}_V\beta_3$  that shares a conserved structure and ABP-AID interface with  $\text{Ca}_V\beta_{2a}$ <sup>45, 46</sup>. By strong contrast with the  $\text{Ca}_V1.2:\text{Ca}_V\beta_{2a}$  results (Figure 6), injection of AID or AID-CAP into oocytes expressing  $\text{Ca}_V1.2:\text{Ca}_V\beta_3$  channels at the maximal peptide concentration that was ineffective against  $\text{Ca}_V1.2:\text{Ca}_V\beta_{2a}$  channels (2.8 mM, Figure 7) resulted in a striking change of the channel properties compared to

the control HotA peptide (Figure 7A, Table 2). Over the course of 30 minutes, competition with AID and AID-CAP decreased the extent of inactivation ( $t_{i300}$  from  $73.4 \pm 2.0\%$  to  $49.8 \pm 1.9\%$  and from  $73.2 \pm 1.5\%$  to  $48.3 \pm 4.1\%$ , respectively, Figure 7B), prolonged  $\tau$  of inactivation (Figure 7C), and shifted the activation  $V_{1/2}$  (from  $6.3 \pm 1.6$  to  $20.5 \pm 2.8$  mV and from  $10.4 \pm 2.2$  to  $21.0 \pm 2.0$  mV for AID-CAP and AID, in contrast to HotA, from  $6.7 \pm 2.9$  to  $8.6 \pm 3.3$  mV Figure 7D). Following injection with both the AID-CAP and AID peptides there was also a clear change in channel inactivation kinetics, which changed from one having two components to a monoexponential process. Similar to the Cav1.2-Y437A:Cav $\beta_{2a}$  experiments, injection of AID and AID-CAP peptides resulted in strongly increased current rundown, consistent with a loss of active channels on the plasma membrane (Figure 7E). All of these functional changes are consistent with the near complete disruption of the Cav1.2 $\alpha_1$ :Cav $\beta_3$  interaction and are absent in currents from oocytes expressing Cav1.2:Cav $\beta_3$  challenged with the HotA peptide. The nearly similar performance of the AID and AID-CAP peptides matches their comparable affinities for Cav $\beta$  (Figure 3 and Table 1). There is a slight advantage for the AID-CAP version that suggests that the peptide staple improves the performance of the peptide in a cellular setting (Figure 7).

Measurement of the time constant for the loss of channels by fitting to a single exponential yields  $\tau = 5.3 \pm 0.7$  min and  $4.6 \pm 0.4$  min for AID-CAP and AID, respectively. These values are notably similar to those measured for Cav1.2 Y437A:Cav $\beta_{2a}$  complexes ( $5.3 \pm 0.9$  min and  $4.1 \pm 0.4$  min, respectively, Figure 7F) and are within a factor of three of the reported  $k_{off}$  for dissociation of purified Cav2.2 I-II loop peptide and Cav $\beta_{2b}$  ( $\tau = 2.1$

min)<sup>44</sup>. These observations, together with the similar binding properties of all AID and Cav $\beta$  isoforms<sup>45</sup> suggest that the functional effects we observe are driven by dissociation of Cav $\beta$  from the channel. Taken together, our data demonstrate that it is possible to use exogenous AID peptides to disrupt Cav $\alpha$ :Cav $\beta$  interactions. Differences in the labile nature of the AID:Cav $\beta$  interaction lead to Cav $\beta$  isoform-specific effects even though the target AID:ABP interactions are strictly conserved.

## **Discussion**

The function, regulation, and biogenesis of many VGIC superfamily members rely on the formation of protein-protein complexes between VGIC pore-forming and cytoplasmic subunits<sup>1, 76</sup>. Well-studied examples of how this class of protein-protein interactions can affect VGIC biophysical properties and cellular targeting have been elaborated for Cav1 and Cav2 pore-forming subunits with Cav $\beta$ <sup>20, 23, 45-48</sup> and the interaction of Kv1 and Kv4 voltage gated potassium channels with either Kv $\beta$ <sup>4, 77</sup> or KChIPs<sup>4, 78</sup>, respectively. In particular, application of Cav1 AID peptides to channel containing membrane patches has been reported to modulate Cav1.2 channels in a manner consistent with competition of the Cav $\alpha_1$ :Cav $\beta$  interaction<sup>55</sup> and comprehensive structural and functional studies have shown that cortisone can modulate Kv1 channels by competing with the Kv1-Kv $\beta$  interaction<sup>6, 7</sup>. These initial studies suggest that antagonists of the protein-protein interactions between pore-forming and cytoplasmic VGIC components may offer an alternative strategy to control channel function that contrasts the classical approaches that target the pore-forming subunit<sup>19, 50-52, 79</sup>.

Targeting protein-protein interactions remains challenging<sup>14, 16</sup>. Nevertheless, notable successes have been made in developing protein-protein interaction antagonists for a variety of cellular targets such as Bcl-X<sub>L</sub>, p53, and estrogen receptors<sup>14-17</sup>. Despite the many successes with intracellular targets, there has been little successful development reported regarding VGIC protein-protein interaction antagonists. Two studies have detailed the search for compounds that would affect Cav $\alpha$ -Cav $\beta$ <sup>53</sup> and Kv4-KChIP interactions<sup>80</sup>, but neither validated the reported compounds as authentic protein-protein interaction antagonists. Given such lack of progress targeting ion channel protein-protein

interactions as a point of pharmacological intervention and questions about the degree to which interactions between pore-forming and cytoplasmic subunits may be labile there has been reasonable skepticism about whether targeting such interactions can be a viable strategy to control channel function in cellular settings<sup>12, 19</sup>. Our studies here, using a classic paradigm for cytoplasmic subunit modulation, that of the Cav $\alpha_1$ :Cav $\beta$  interaction, now validate the concept of using protein-protein antagonists to control a VGIC and should open a path to further development of this type of strategy to control channel function.

Protein-protein interactions involving the binding of an  $\alpha$ -helix to a partner protein represent one of the most attractive architectures for protein-protein interaction antagonist development<sup>15</sup> as the interaction surface is limited and there are a variety of strategies for improving the properties of the  $\alpha$ -helical partner. The AID:ABP interaction presents an example of this sort of interaction in an ion channel complex. The  $\alpha$ -helical element of the complex, the AID, lacks structure in its unbound state<sup>45, 47, 64, 65</sup> and binds to a well-defined Cav $\beta$  cleft, the ABP, that undergoes minimal conformational change<sup>46-48</sup>. Because  $\alpha$ -helix stabilization strategies have proven successful for targeting many protein-protein interactions mediated by a similar general architecture<sup>15</sup> and the binding energy of the AID:ABP is focused into a hotspot in the center of the AID helix<sup>45</sup>, we reasoned that pursuing a stapled peptide strategy<sup>58</sup> to enhance the stability of the AID helix, might provide a first step in the development of Cav $\beta$ -directed inhibitors of Cav function.

Incorporation of an m-xylyl staple, a strategy used previously to stabilize the protease inhibitor calpastatin<sup>59</sup> and  $\beta$ -catenin<sup>60</sup>, enhanced AID helix formation when placed at

either N-terminal (AID-CAP) or central (AID-CEN) positions (Figure 1C). The AID-CAP configuration proved superior for inducing helical content. We attribute this effect to the stabilization of an engineered helix cap by the m-xylyl staple (Figure S1C) and the importance of helix nucleation<sup>81, 82</sup>. Our crystallographic studies show that neither m-xylyl staple position altered the way the AID peptides bind Cav $\beta$  (Figure 2). As anticipated, m-xylyl staple incorporation reduced the entropic penalty of Cav $\beta$  binding (Table 1) in a manner consistent with reduction of disorder in the unbound AID. Nevertheless, despite this effect, lack of interference of the staples with Cav $\beta$  complex formation, and lack of conformational change in the Cav $\beta$  ABP, there was a concomitant reduction in the large enthalpic gain of complex formation that resulted in no measurable change in Cav $\beta$  binding affinity between the unconstrained and stapled AIDs (Table 1). Such entropy-enthalpy compensation effects are not uncommon in protein-ligand recognition and design efforts<sup>67</sup>. In the case of the stapled AIDs, the ordering of the helical conformation may have traded away some of the gain in favorable enthalpy associated with the formation of helical backbone interactions<sup>68</sup> that would otherwise be associated with the binding reaction. The structural information obtained here should enable strategies using other crosslinking sites or the combination of multiple staples to provide a path towards more efficacious peptide-based Cav $\alpha$ :Cav $\beta$  protein-protein interaction inhibitors. Notably, even in the absence of affinity enhancement effects, the helical staples may offer advantages, as our cell-based assays indicated that the stapled peptide outperformed the unstapled AID (Figures 5 and 7). Hence, there may be multiple layers of benefit to helix stabilization in a cellular context that go beyond the effects on binding affinity.

Two challenges to targeting the AID:ABP interaction are competition with a nanomolar native interaction<sup>45</sup> and the fact that the AID:ABP interface comprises well-conserved interactions among the isoforms of both partners<sup>45</sup>. Despite these challenges, our functional studies showed that injection of either wild-type AID or AID-CAP into *Xenopus* oocytes expressing Ca<sub>v</sub>1.2-Y437A:Ca<sub>v</sub>β<sub>2a</sub> or Ca<sub>v</sub>1.2:Ca<sub>v</sub>β<sub>3</sub> channel complexes resulted in biophysical changes that were consistent with loss of Ca<sub>v</sub>β modulation and binding. Such changes were absent for Ca<sub>v</sub>1.2:Ca<sub>v</sub>β<sub>2a</sub> channels in which the Ca<sub>v</sub>β component is anchored to the membrane via palmitoylation<sup>74</sup>. The biophysical parameter changes were also accompanied by a reduction of channels at the cell membrane as indicated by the changes in the I<sub>max</sub> parameter. Notably, such changes could also be observed for Ca<sub>v</sub>1.2:Ca<sub>v</sub>β<sub>2a</sub>, although to a lesser extent than with Ca<sub>v</sub>1.2-Y437A:Ca<sub>v</sub>β<sub>2a</sub> or Ca<sub>v</sub>1.2:Ca<sub>v</sub>β<sub>3</sub>, suggesting that the peptides may not only affect channels at the membrane, but may inhibit the formation or membrane incorporation of newly assembled channels or may influence channel destruction by the ERAD system<sup>30</sup>. Interestingly, the time constants measured for the I<sub>max</sub> changes are close to the intrinsic dissociation rates reported for the AID-Ca<sub>v</sub>β interaction<sup>44</sup> and suggest that some of the competitive effects of the peptides may be governed by the intrinsic dissociation rates of Ca<sub>v</sub>β from the pore-forming subunit. Together, our data demonstrate that the AID:ABP interaction can be targeted effectively in a cellular context. Importantly, despite the high similarity in the residues that contribute to the AID:ABP interface and the corresponding similar interaction affinities for AID-Ca<sub>v</sub>β pairs<sup>45</sup>, our findings show that it is possible to achieve some degree of isoform selective specificity. This selectivity appears to originate in factors outside of the ABP-AID interface that contribute to the diverse functional effects of the



different  $\text{Ca}_v\beta$  isoforms, that likely affect how  $\text{Ca}_v\beta$  engages the channel, and that are related to the  $\text{Ca}_v\beta$  off rate. Thus, our studies with stapled AID peptides show that it is possible to antagonize a paradigmatic protein-protein interaction central to VGIC function, for  $\text{Ca}_v$  current regulation and achieve specificity between different  $\text{Ca}_v\beta$  isoforms.

VGICs have well-established important roles in the generation of bioelectrical signals in excitable tissues such as brain, heart, and muscle<sup>1</sup> and also have an emerging set of 'non-classical' roles in insulin secretion<sup>83</sup>, cancer<sup>84-86</sup>, and gene regulation<sup>87, 88</sup>. Because of these diverse functions and a general lack of specific means for controlling channel function, there remains a need to develop new molecular tools that can be used to probe VGIC biology<sup>51, 89, 90</sup>. Due to the importance of protein-protein interactions between pore-forming and cytoplasmic VGIC subunits for the biogenesis and trafficking of many VGICs, further development of such VGIC protein-protein interaction antagonists may open new means to study the dynamics of channel complexes, the steps associated with channel assembly, and the roles of these processes in native settings excitable tissues such as muscles and neurons.

## **Materials and Methods**

### **Molecular Biology**

Human Ca<sub>v</sub>1.2 ( $\alpha_1$ C77, GenBank Z34815), human Ca<sub>v</sub>1.2-Y437A, rat Ca<sub>v</sub> $\beta_{2a}$  (GenBank NM\_053851), Ca<sub>v</sub> $\beta_3$  (GenBank NM\_001101715), and Ca<sub>v</sub> $\alpha_2\delta$ -1 (GenBank NM\_00182276) were used for two-electrode voltage clamp experiments in *Xenopus* oocytes. For constructing Ca<sub>v</sub>1.2-Y437A, the mutation in position 437 of Ca<sub>v</sub>1.2 was introduced by SOE-PCR (Splicing by Overlap-PCR). Briefly, the I-II loop cDNA sequence of Ca<sub>v</sub>1.2 was PCR amplified with overlapping mutagenesis primers in separate PCR reactions using pcDNA3.1-Ca<sub>v</sub>1.2 as template. The two separate PCR products were then used as templates for a final PCR reaction with flanking primers to connect the nucleotide sequences. This fragment was then HpaI/PpuMI digested and cloned into the respective sites of pcDNA3.1-Ca<sub>v</sub>1.2.

### **Protein expression and purification**

Ca<sub>v</sub> $\beta_{2a}$  expression and purification were done as previously described<sup>45</sup>. For complex formation with stapled peptides, 155  $\mu$ M Ca<sub>v</sub> $\beta_{2a}$  in buffer A (150 mM KCl, 1mM TCEP pH7.4, 10 mM HEPES/KOH pH 7.4) was mixed with an equal volume of peptide in buffer A, creating a molar ratio of protein:peptide of 1:1.2. Unbound peptide was removed using a Superdex200 HR10/30 gel filtration column run in buffer A. The Ca<sub>v</sub> $\beta_{2a}$ /peptide complex was concentrated (Amicon filter, MWCO 10 kDa) to 8 mg/ml as determined by absorbance<sup>91</sup>.

### **Peptide synthesis and purification**

All the AID peptides were synthesized using an automated peptide synthesizer (0.1 mmol scale). Fmoc-solid phase peptide synthesis was employed on Chemmatrix

Rinkamde resin (substitution level: ~0.5 mmol/g). Deprotection was performed with 20% 4-methyl piperidine in DMF and coupling reactions were done in a mixture of Fmoc-amino acid (5 eq), HCTU (4.95 eq), and DIPEA (10eq) in DMF at 70 °C for 5 min. The peptide was cleaved from the resin by treatment with the cleavage cocktail (TFA: EDT: thioanisole = 95:2.5:2.5) and the crude product was obtained by cold ether precipitation after removal of TFA. The crude peptide was purified by reverse phase (RP)-HPLC C4 column and lyophilized.

### **Peptide crosslinking**

Peptide crosslinking was performed as described previously<sup>59</sup>. Briefly, a solution of cysteine containing peptide (0.1 mM) was incubated with TCEP(1.5eq) in  $\text{NH}_4\text{HCO}_3$  buffer (100 mM, pH=8.0) for 30 min. Then m,m'-dibromoxylene solution (2 or 3 eq, 1 mM in DMF) was added and stirred at room temperature. The reaction progress was monitored by mass spectrometry. When the reaction is complete, the reaction mixture was quenched by 1M HCl solution to acidic pH (pH 3 or 4) and purified by RP-HPLC.

### **Crystallization and Refinement**

The  $\text{Ca}_v\beta_{2a}$ /ASPL complex was crystallized by hanging drop vapor diffusion at 4°C by mixing equal volumes of protein in buffer A and well solution containing 1.5-1.7 M  $(\text{NH}_4)_2\text{SO}_4$ , 5 mM  $\beta$ -mercaptoethanol and 0.1 M HEPES, pH 7. The  $\text{Ca}_v\beta_{2a}$ /CSPE complex was crystallized by hanging drop vapor diffusion at 4°C by mixing equal volumes of protein in buffer A and well solution containing 34-37 % PEG400, 0.1 M  $\text{MgCl}_2$  and 0.1 M MES, pH 6.3. After flash-freezing in well solution plus 20% glycerol, diffraction data were collected at Beamline 8.3.1 (Advanced Light Source, Lawrence Berkeley National Laboratories), indexed using MOSFLM 7.0.4<sup>92</sup> and scaled using SCALA<sup>93</sup>. Molecular

replacement with PHASER<sup>94</sup> using a model derived from 1T3S yielded starting phases. The initial model was improved by iterative cycles of manual building in COOT<sup>95</sup> and refinement against native data using Refmac5<sup>96</sup>. TLS-tensors were added in the final cycle of refinement. Data collection and final model refinement statistics are summarized in Table S1.

### **Circular Dichroism**

Circular dichroism spectra were measured in a 2 mm path length quartz cuvette (Hellma), 50 mM KCl and 10 mM KH<sub>2</sub>PO<sub>4</sub>/K<sub>2</sub>HPO<sub>4</sub>, pH 7.3 using an Aviv Model 215 spectropolarimeter (Aviv Biomedical) equipped with a peltier temperature controller. Wavelength scans from 320 to 190 nm were taken at 4°C. Each point was determined in triplicate from the same sample and subtracted by the average of a triplicate buffer scan. Each sample was checked for purity by HPLC. Molar ellipticity was calculated as follows:  $\theta = 100(\Delta m)/CnI$ , where  $\Delta m$  is the CD signal in millidegrees after buffer subtraction, C is the millimolar peptide concentration, n is the number of residues in the peptide, and I is the cuvette path length in centimeters.

### **Isothermal Calorimetry**

Titration were performed at 15°C using a VP-ITC Microcalorimeter (MicroCal). Samples were dialyzed overnight at 4°C (Slide-A-Lyzer, 2 kDa molecular weight cut-off, Thermo Scientific) against 150 mM KCl and 10 mM K-phosphate, pH 7.3. After 30' centrifugation at 40,000 rpm at 4 °C, protein concentrations were determined by absorbance at 280 nm<sup>97</sup>. All samples were degassed for 5' prior to loading into the calorimeter. Cav1.2 Cav $\beta$ <sub>2a</sub> core at a concentration of 2  $\mu$ M was titrated with 20  $\mu$ M modified or unmodified AID peptide with one 4  $\mu$ l injection followed by 29 injections of 10

$\mu$ l titrant. To correct the baseline either heat of dilution from titrations of injectant into buffer was subtracted. Data were processed with MicroCal Origin 7.0 using a single site binding model.

### **Electrophysiology**

Details of two-electrode voltage clamp have been described previously<sup>64</sup>. In short, linearized cDNA was translated into capped mRNA using the T7 mMessenger kit (Ambion). 50 nl of a mRNA mixture containing an equimolar ratio of  $Ca_{V\alpha_1}$  and  $Ca_{V\alpha_2\delta-1}$ , and a lower amount of  $Ca_V\beta$  were microinjected into *Xenopus* oocytes 48-72 hours prior to recording. After injection the oocytes were kept at 18°C in ND96 medium supplemented with penicillin (100 U ml<sup>-1</sup>) and streptomycin (100  $\mu$ g ml<sup>-1</sup>). Prior studies established that with injections of an equimolar ratio of  $Ca_{V\alpha_1}$  and  $Ca_V\beta$  RNA there is an excess of free  $Ca_V\beta$ <sup>64</sup>. To avoid an excess of free  $Ca_V\beta$  in the cytoplasm the optimal  $Ca_{V\alpha_1}/Ca_V\beta$  RNA ratio was determined for each RNA preparation. Different  $Ca_{V\alpha_1}/Ca_V\beta$  molar ratios were titrated for every RNA preparation and the highest  $Ca_{V\alpha_1}/Ca_V\beta$  RNA ratio at which the channel currents displayed the same extent and speed of inactivation as oocytes injected with equimolar ratio of  $Ca_{V\alpha_1}/Ca_V\beta$  used for peptide injection experiments (1:10 to 1:100 for  $Ca_V\beta_{2a}:Ca_V1.2$ ; 1:1 for  $Ca_V\beta_3:Ca_V1.2$ ).

For experiments that involved peptide injections into oocytes, 5 minutes before the first recording, 50 nl of a mixture of 0.1M BAPTA and the test substance (peptide or water) was injected. Recording solutions contained 40 mM  $Ca(NO_3)_2$ , 50 mM NaOH, 1 mM KOH, and 10 mM HEPES, adjusted to pH 7.4 using  $HNO_3$ . Electrodes were filled with 3 M KCl and had resistances of 0.3-2.0 M $\Omega$ . Leak currents were subtracted using a P/4 protocol.

Currents were analyzed with Clampfit 8.2 (Axon Instruments). All results are from at least two independent oocyte batches. The  $t_{i300}$  values were calculated from normalized currents at +20 mV and represent the percentage of inactivation after 300 milliseconds. Inactivation  $\tau$  values at +20 mV,  $G_{max}$ ,  $K_a$ ,  $V_{1/2}$ , and  $V_{rev}$  were calculated as described<sup>64</sup>.

### **Statistical analysis**

Data are expressed as mean  $\pm$  S.E.M. Statistical differences between samples were determined using One-way Analysis of Variance or Kruskal-Wallis One Way Analysis of Variance on Ranks (when data were not normally distributed), and Two-way Analysis of Variance associated with a Holm-Sidak post-hoc test when needed. A value of  $p < 0.05$  was considered significant.

## References

- (1) Hille, B. *Ion Channels of Excitable Membranes*, 3rd ed. **2001**. Sinauer Associates, Inc., Sunderland, MA.
- (2) Yu, F. H., Yarov-Yarovoy, V., Gutman, G. A., and Catterall, W. A. Overview of molecular relationships in the voltage-gated ion channel superfamily, *Pharmacol Rev.* **2005**. *57*, 387-395.
- (3) Simms, B. A., and Zamponi, G. W. Trafficking and stability of voltage-gated calcium channels, *Cell Mol Life Sci.* **2012**. *69*, 843-856.
- (4) Pongs, O., and Schwarz, J. R. Ancillary subunits associated with voltage-dependent K<sup>+</sup> channels, *Physiol Rev.* **2010**. *90*, 755-796.
- (5) Schwappach, B. An overview of trafficking and assembly of neurotransmitter receptors and ion channels, *Mol Membr Biol.* **2008**. *25*, 270-278.
- (6) Pan, Y., Levin, E. J., Quick, M., and Zhou, M. Potentiation of the Kv1 family K(+) channel by cortisone analogues, *ACS chemical biology.* **2012**. *7*, 1641-1646.
- (7) Pan, Y., Weng, J., Kabaleeswaran, V., Li, H., Cao, Y., Bhosle, R. C., and Zhou, M. Cortisone dissociates the Shaker family K<sup>+</sup> channels from their beta subunits, *Nat Chem Biol.* **2008**. *4*, 708-714.
- (8) Yang, T., Suhail, Y., Dalton, S., Kernan, T., and Colecraft, H. M. Genetically encoded molecules for inducibly inactivating CaV channels, *Nat Chem Biol.* **2007**. *3*, 795-804.
- (9) Yang, T., He, L. L., Chen, M., Fang, K., and Colecraft, H. M. Bio-inspired voltage-dependent calcium channel blockers, *Nature communications.* **2013**. *4*, 2540.

- (10) Rouwette, T., Avenali, L., Sondermann, J., Narayanan, P., Gomez-Varela, D., and Schmidt, M. Modulation of nociceptive ion channels and receptors via protein-protein interactions: implications for pain relief, *Channels*. **2015**. *9*, 175-185.
- (11) Subramanyam, P., and Colecraft, H. M. Ion channel engineering: perspectives and strategies, *J Mol Biol*. **2015**. *427*, 190-204.
- (12) Kohout, S. C., and Isacoff, E. Y. To dislodge an enzyme from an ion channel, try steroids, *Nat Chem Biol*. **2008**. *4*, 650-651.
- (13) Laraia, L., McKenzie, G., Spring, D. R., Venkitaraman, A. R., and Huggins, D. J. Overcoming Chemical, Biological, and Computational Challenges in the Development of Inhibitors Targeting Protein-Protein Interactions, *Chem Biol*. **2015**. *22*, 689-703.
- (14) Wells, J. A., and McClendon, C. L. Reaching for high-hanging fruit in drug discovery at protein-protein interfaces, *Nature*. **2007**. *450*, 1001-1009.
- (15) Azzarito, V., Long, K., Murphy, N. S., and Wilson, A. J. Inhibition of alpha-helix-mediated protein-protein interactions using designed molecules, *Nature chemistry*. **2013**. *5*, 161-173.
- (16) Milroy, L. G., Grossmann, T. N., Hennig, S., Brunsveld, L., and Ottmann, C. Modulators of protein-protein interactions, *Chemical reviews*. **2014**. *114*, 4695-4748.
- (17) Cromm, P. M., Spiegel, J., and Grossmann, T. N. Hydrocarbon stapled peptides as modulators of biological function, *ACS chemical biology*. **2015**. *10*, 1362-1375.



- (18) Findeisen, F., and Minor, D. L., Jr. Progress in the structural understanding of voltage-gated calcium channel (CaV) function and modulation, *Channels*. **2010**. *4*, 459-474.
- (19) Zamponi, G. W., Striessnig, J., Koschak, A., and Dolphin, A. C. The Physiology, Pathology, and Pharmacology of Voltage-Gated Calcium Channels and Their Future Therapeutic Potential, *Pharmacol Rev*. **2015**. *67*, 821-870.
- (20) Buraei, Z., and Yang, J. The {beta} Subunit of Voltage-Gated Ca<sup>2+</sup> Channels, *Physiol Rev*. **2010**. *90*, 1461-1506.
- (21) Buraei, Z., and Yang, J. Structure and function of the beta subunit of voltage-gated Ca<sup>2+</sup>(+) channels, *Biochim Biophys Acta*. **2013**. *1828*, 1530-1540.
- (22) Van Petegem, F., and Minor, D. L. The structural biology of voltage-gated calcium channel function and regulation, *Biochem Soc Trans*. **2006**. *34*, 887-893.
- (23) Wu, J., Yan, Z., Li, Z., Yan, C., Lu, S., Dong, M., and Yan, N. Structure of the voltage-gated calcium channel Cav1.1 complex, *Science*. **2015**. *350*, aad2395.
- (24) Dolphin, A. C. (2013) The alpha2delta subunits of voltage-gated calcium channels, *Biochim Biophys Acta*. **2013**. *1828*, 1541-1549.
- (25) Ben-Johny, M., and Yue, D. T. Calmodulin regulation (calmodulation) of voltage-gated calcium channels, *J Gen Physiol*. **2014**. *143*, 679-692.
- (26) Fang, K., and Colecraft, H. M. Mechanism of auxiliary beta-subunit-mediated membrane targeting of L-type (Ca(V)1.2) channels, *J Physiol*. **2015**. *589*, 4437-4455.
- (27) Bichet, D., Cornet, V., Geib, S., Carlier, E., Volsen, S., Hoshi, T., Mori, Y., and De Waard, M. The I-II loop of the Ca<sup>2+</sup> channel alpha1 subunit contains an

- endoplasmic reticulum retention signal antagonized by the beta subunit, *Neuron*. **2000**. 25, 177-190.
- (28) Bourdin, B., Marger, F., Wall-Lacelle, S., Schneider, T., Klein, H., Sauve, R., and Parent, L. Molecular determinants of the CaVbeta-induced plasma membrane targeting of the CaV1.2 channel, *J Biol Chem*. **2010**. 285, 22853-22863.
- (29) Kanevsky, N., and Dascal, N. Regulation of maximal open probability is a separable function of Ca(v)beta subunit in L-type Ca<sup>2+</sup> channel, dependent on NH2 terminus of alpha1C (Ca(v)1.2alpha), *J Gen Physiol*. **2006**. 128, 15-36.
- (30) Altier, C., Garcia-Caballero, A., Simms, B., You, H., Chen, L., Walcher, J., Tedford, H. W., Hermosilla, T., and Zamponi, G. W. The Cavbeta subunit prevents RFP2-mediated ubiquitination and proteasomal degradation of L-type channels, *Nat Neurosci*. **2011**. 14, 173-180.
- (31) He, L. L., Zhang, Y., Chen, Y. H., Yamada, Y., and Yang, J. Functional modularity of the beta-subunit of voltage-gated Ca<sup>2+</sup> channels, *Biophys J*. **2007**. 93, 834-845.
- (32) Berrou, L., Bernatchez, G., and Parent, L. Molecular determinants of inactivation within the I-II linker of alpha1E (CaV2.3) calcium channels, *Biophys J*. **2001**. 80, 215-228.
- (33) Berrou, L., Dodier, Y., Raybaud, A., Tousignant, A., Dafi, O., Pelletier, J. N., and Parent, L. The C-terminal residues in the alpha-interacting domain (AID) helix anchor CaV beta subunit interaction and modulation of CaV2.3 channels, *J Biol Chem*. **2005**. 280, 494-505.

- (34) Perez-Reyes, E., Castellano, A., Kim, H. S., Bertrand, P., Bagstrom, E., Lacerda, A. E., Wei, X. Y., and Birnbaumer, L. Cloning and expression of a cardiac/brain beta subunit of the L-type calcium channel, *J Biol Chem.* **1992.** 267, 1792-1797.
- (35) Yamaguchi, H., Okuda, M., Mikala, G., Fukasawa, K., and Varadi, G. Cloning of the beta(2a) subunit of the voltage-dependent calcium channel from human heart: cooperative effect of alpha(2)/delta and beta(2a) on the membrane expression of the alpha(1C) subunit, *Biochem Biophys Res Commun.* **2000.** 267, 156-163.
- (36) Neely, A., Wei, X., Olcese, R., Birnbaumer, L., and Stefani, E. Potentiation by the beta subunit of the ratio of the ionic current to the charge movement in the cardiac calcium channel, *Science.* **1993.** 262, 575-578.
- (37) Takahashi, S. X., Miriyala, J., Tay, L. H., Yue, D. T., and Colecraft, H. M. A CaV{beta} SH3/Guanylate Kinase Domain Interaction Regulates Multiple Properties of Voltage-gated Ca<sup>2+</sup> Channels, *J Gen Physiol.* **2005.** 126, 365-377.
- (38) De Waard, M., and Campbell, K. P. Subunit regulation of the neuronal alpha 1A Ca<sup>2+</sup> channel expressed in *Xenopus* oocytes, *J Physiol.* **1995.** 485, 619-634.
- (39) Colecraft, H. M., Alseikhan, B., Takahashi, S. X., Chaudhuri, D., Mittman, S., Yegnasubramanian, V., Alvania, R. S., Johns, D. C., Marban, E., and Yue, D. T. Novel functional properties of Ca(2+) channel beta subunits revealed by their expression in adult rat heart cells, *J Physiol.* **2002.** 541, 435-452.
- (40) Bell, D. C., Butcher, A. J., Berrow, N. S., Page, K. M., Brust, P. F., Nesterova, A., Stauderman, K. A., Seabrook, G. R., Nurnberg, B., and Dolphin, A. C. Biophysical properties, pharmacology, and modulation of human, neuronal L-type (alpha(1D), Ca(V)1.3) voltage-dependent calcium currents, *J Neurophysiol.* **2001.** 85, 816-827.

- (41) Canti, C., Davies, A., Berrow, N. S., Butcher, A. J., Page, K. M., and Dolphin, A. C. Evidence for two concentration-dependent processes for beta-subunit effects on alpha1B calcium channels, *Biophys J.* **2001.** *81*, 1439-1451.
- (42) Geib, S., Sandoz, G., Cornet, V., Mabrouk, K., Fund-Saunier, O., Bichet, D., Villaz, M., Hoshi, T., Sabatier, J. M., and De Waard, M. The interaction between the I-II loop and the III-IV loop of Cav2.1 contributes to voltage-dependent inactivation in a beta -dependent manner, *J Biol Chem.* **2002.** *277*, 10003-10013.
- (43) Opatowsky, Y., Chomsky-Hecht, O., Kang, M. G., Campbell, K. P., and Hirsch, J. A. The voltage-dependent calcium channel beta subunit contains two stable interacting domains, *J Biol Chem.* **2003.** *278*, 52323-52332.
- (44) Butcher, A. J., Leroy, J., Richards, M. W., Pratt, W. S., and Dolphin, A. C. The importance of occupancy rather than affinity of CaV{beta} subunits for the calcium channel I-II linker in relation to calcium channel function, *J Physiol.* **2006.** *574*, 387-398.
- (45) Van Petegem, F., Duderstadt, K. E., Clark, K. A., Wang, M., and Minor, D. L., Jr. Alanine-Scanning Mutagenesis Defines a Conserved Energetic Hotspot in the Ca(V)alpha(1) AID-Ca(V)beta Interaction Site that Is Critical for Channel Modulation, *Structure.* **2008.** *16*, 280-294.
- (46) Chen, Y. H., Li, M. H., Zhang, Y., He, L. L., Yamada, Y., Fitzmaurice, A., Shen, Y., Zhang, H., Tong, L., and Yang, J. Structural basis of the alpha1-beta subunit interaction of voltage-gated Ca<sup>2+</sup> channels, *Nature.* **2004.** *429*, 675-680.

- (47) Opatowsky, Y., Chen, C. C., Campbell, K. P., and Hirsch, J. A. Structural Analysis of the Voltage-Dependent Calcium Channel beta Subunit Functional Core and Its Complex with the alpha1 Interaction Domain, *Neuron*. **2004**. 42, 387-399.
- (48) Van Petegem, F., Clark, K. A., Chatelain, F. C., and Minor, D. L., Jr. Structure of a complex between a voltage-gated calcium channel beta-subunit and an alpha-subunit domain, *Nature*. **2004**. 429, 671-675.
- (49) Almagor, L., Chomsky-Hecht, O., Ben-Mocha, A., Hendin-Barak, D., Dascal, N., and Hirsch, J. A. The role of a voltage-dependent Ca<sup>2+</sup> channel intracellular linker: a structure-function analysis, *J Neurosci*. **2012**. 32, 7602-7613.
- (50) Catterall, W. A., and Swanson, T. M. Structural Basis for Pharmacology of Voltage-Gated Sodium and Calcium Channels, *Mol Pharmacol*. **2015**. 88, 141-150.
- (51) Zamponi, G. W. Targeting voltage-gated calcium channels in neurological and psychiatric diseases, *Nat Rev Drug Discov*. **2016**. 15, 19-34.
- (52) Kalia, J., Milescu, M., Salvatierra, J., Wagner, J., Klint, J. K., King, G. F., Olivera, B. M., and Bosmans, F. From foe to friend: Using animal toxins to investigate ion channel function, *J Mol Biol*. **2014**. 427, 158-175.
- (53) Young, K., Lin, S., Sun, L., Lee, E., Modi, M., Hellings, S., Husbands, M., Ozenberger, B., and Franco, R. Identification of a calcium channel modulator using a high throughput yeast two-hybrid screen, *Nat Biotechnol*. **1998**. 16, 946-950.
- (54) Jangsangthong, W., Kuzmenkina, E., Bohnke, A. K., and Herzig, S. Single-channel monitoring of reversible L-type Ca(2+) channel Ca(V)alpha(1)-Ca(V)beta subunit interaction, *Biophys J*. **2011**. 101, 2661-2670.

- (55) Hohaus, A., Poteser, M., Romanin, C., Klugbauer, N., Hofmann, F., Morano, I., Haase, H., and Groschner, K. Modulation of the smooth-muscle L-type Ca<sup>2+</sup> channel alpha1 subunit (alpha1C-b) by the beta2a subunit: a peptide which inhibits binding of beta to the I-II linker of alpha1 induces functional uncoupling, *Biochem J.* **2000.** 348, 657-665.
- (56) Campiglio, M., Di Biase, V., Tuluc, P., and Flucher, B. E. Stable incorporation versus dynamic exchange of beta subunits in a native Ca<sup>2+</sup> channel complex, *Journal of cell science.* **2013.** 126, 2092-2101.
- (57) Hidalgo, P., Gonzalez-Gutierrez, G., Garcia-Olivares, J., and Neely, A. The alpha1-beta-subunit interaction that modulates calcium channel activity is reversible and requires a competent alpha-interaction domain, *J Biol Chem.* **2006.** 281, 24104-24110.
- (58) Verdine, G. L., and Hilinski, G. J. Stapled peptides for intracellular drug targets, *Methods Enzymol.* **2012.** 503, 3-33.
- (59) Jo, H., Meinhardt, N., Wu, Y., Kulkarni, S., Hu, X., Low, K. E., Davies, P. L., DeGrado, W. F., and Greenbaum, D. C. Development of alpha-helical calpain probes by mimicking a natural protein-protein interaction, *J Am Chem Soc.* **2012.** 134, 17704-17713.
- (60) Diderich, P., Bertoldo, D., Dessen, P., Khan, M. M., Pizzitola, I., Held, W., Huelsken, J., and Heinis, C. Phage Selection of Chemically Stabilized alpha-Helical Peptide Ligands, *ACS chemical biology.* **2016.** 11, 1422-1427.
- (61) Aurora, R., and Rose, G. D. Helix capping, *Protein Sci.* **1998.** 7, 21-38.

- (62) Mahon, A. B., and Arora, P. S. End-Capped alpha-Helices as Modulators of Protein Function, *Drug Discov Today Technol.* **2012.** 9, e57-e62.
- (63) Timmerman, P., Beld, J., Puijk, W. C., and Meloen, R. H. Rapid and quantitative cyclization of multiple peptide loops onto synthetic scaffolds for structural mimicry of protein surfaces, *Chembiochem.* **2005.** 6, 821-824.
- (64) Findeisen, F., and Minor, D. L., Jr. Disruption of the IS6-AID Linker Affects Voltage-gated Calcium Channel Inactivation and Facilitation, *J Gen Physiol.* **2009.** 133, 327-343.
- (65) Arias, J. M., Murbartian, J., Vitko, I., Lee, J. H., and Perez-Reyes, E. Transfer of beta subunit regulation from high to low voltage-gated Ca<sup>2+</sup> channels, *FEBS Lett.* **2005.** 579, 3907-3912.
- (66) Berova, N., Nakanishi, K., and Woody, R. W. Circular Dichroism: Principles and Applications, 2nd ed., **2000.** Wiley-VCH, New York.
- (67) Chodera, J. D., and Mobley, D. L. Entropy-enthalpy compensation: role and ramifications in biomolecular ligand recognition and design, *Annual review of biophysics.* **2013.** 42, 121-142.
- (68) Scholtz, J. M., Marqusee, S., Baldwin, R. L., York, E. J., Stewart, J. M., Santoro, M., and Bolen, D. W. Calorimetric determination of the enthalpy change for the alpha-helix to coil transition of an alanine peptide in water, *Proc Natl Acad Sci U S A.* **1991.** 88, 2854-2858.
- (69) Zhang, Y., Chen, Y. H., Bangaru, S. D., He, L., Abele, K., Tanabe, S., Kozasa, T., and Yang, J. Origin of the voltage dependence of G-protein regulation of P/Q-type Ca<sup>2+</sup> channels, *J Neurosci.* **2008.** 28, 14176-14188.

- (70) Findeisen, F., Rumpf, C. H., and Minor, D. L., Jr. Apo states of calmodulin and CaBP1 control CaV1 voltage-gated calcium channel function through direct competition for the IQ domain, *J Mol Biol.* **2013.** 425, 3217-3234.
- (71) Stotz, S. C., Jarvis, S. E., and Zamponi, G. W. Functional roles of cytoplasmic loops and pore lining transmembrane helices in the voltage-dependent inactivation of HVA calcium channels, *J Physiol.* **2004.** 554, 263-273.
- (72) Cens, T., Rousset, M., Leyris, J. P., Fesquet, P., and Charney, P. Voltage- and calcium-dependent inactivation in high voltage-gated Ca(2+) channels, *Prog Biophys Mol Biol.* **2006.** 90, 104-117.
- (73) Halling, D. B., Aracena-Parks, P., and Hamilton, S. L. Regulation of voltage-gated Ca<sup>2+</sup> channels by calmodulin, *Sci STKE.* **2005,** 315, re15.
- (74) Chien, A. J., Gao, T., Perez-Reyes, E., and Hosey, M. M. Membrane targeting of L-type calcium channels. Role of palmitoylation in the subcellular localization of the beta2a subunit, *J Biol Chem.* **1998.** 273, 23590-23597.
- (75) Jencks, W. P. On the attribution of additivity of binding energies, *Proc Natl Acad Sci U S A.* **1981.** 78, 4046-4050.
- (76) Trimmer, J. S. Regulation of ion channel expression by cytoplasmic subunits, *Curr Opin Neurobiol.* **1998.** 8, 370-374.
- (77) Long, S. B., Campbell, E. B., and Mackinnon, R. Crystal structure of a mammalian voltage-dependent Shaker family K<sup>+</sup> channel, *Science.* **2005.** 309, 897-903.
- (78) Pioletti, M., Findeisen, F., Hura, G. L., and Minor, D. L., Jr. Three-dimensional structure of the KChIP1-Kv4.3 T1 complex reveals a cross-shaped octamer, *Nat Struct Mol Biol.* **2006.** 13, 987-995.



- (79) Ahern, C. A., Payandeh, J., Bosmans, F., and Chanda, B. The hitchhiker's guide to the voltage-gated sodium channel galaxy, *J Gen Physiol.* **2016.** *147,* 1-24.
- (80) Bowlby, M. R., Chanda, P., Edris, W., Hinson, J., Jow, F., Katz, A. H., Kennedy, J., Krishnamurthy, G., Pitts, K., Ryan, K., Zhang, H., and Greenblatt, L. Identification and characterization of small molecule modulators of KChIP/Kv4 function, *Bioorganic & medicinal chemistry.* **2005.** *13,* 6112-6119.
- (81) Austin, R. E., Maplestone, R. A., Sefler, A. M., Liu, K., Hruzewicz, W. N., Liu, C. W., Cho, H. S., Wemmer, D. E., and Bartlett, P. A. Template for stabilization of a peptide alpha-helix: Synthesis and evaluation of conformational effects by circular dichroism and NMR, *JACS.* **1997.** *119,* 6461-6472.
- (82) Wang, D., Chen, K., Dimartino, G., and Arora, P. S. (2006) Nucleation and stability of hydrogen-bond surrogate-based alpha-helices, *Organic & biomolecular chemistry.* **2006.** *4,* 4074-4081.
- (83) Yang, S. N., Shi, Y., Yang, G., Li, Y., Yu, J., and Berggren, P. O. Ionic mechanisms in pancreatic beta cell signaling, *Cell Mol Life Sci.* **2014.** *71,* 4149-4177.
- (84) Black, J. A., and Waxman, S. G. Noncanonical roles of voltage-gated sodium channels, *Neuron.* **2013.** *80,* 280-291.
- (85) Wulff, H., Castle, N. A., and Pardo, L. A. Voltage-gated potassium channels as therapeutic targets, *Nat Rev Drug Discov.* **2009.** *8,* 982-1001.
- (86) Pardo, L. A., and Stuhmer, W. The roles of K(+) channels in cancer, *Nature reviews. Cancer.* **2014.** *14,* 39-48.

- (87) Etemad, S., Obermair, G. J., Bindreither, D., Benedetti, A., Stanika, R., Di Biase, V., Burtscher, V., Koschak, A., Kofler, R., Geley, S., Wille, A., Lusser, A., Flockerzi, V., and Flucher, B. E. Differential neuronal targeting of a new and two known calcium channel beta4 subunit splice variants correlates with their regulation of gene expression, *J Neurosci.* **2014.** *34*, 1446-1461.
- (88) Tadmouri, A., Kiyonaka, S., Barbado, M., Rousset, M., Fablet, K., Sawamura, S., Bahembera, E., Pernet-Gallay, K., Arnoult, C., Miki, T., Sadoul, K., Gory-Faure, S., Lambrecht, C., Lesage, F., Akiyama, S., Khochbin, S., Baulande, S., Janssens, V., Andrieux, A., Dolmetsch, R., Ronjat, M., Mori, Y., and De Waard, M. Cacnb4 directly couples electrical activity to gene expression, a process defective in juvenile epilepsy, *EMBO J.* **2012.** *31*, 3730-3744.
- (89) Isacoff, E. Y., Jan, L. Y., and Minor, D. L., Jr. Conduits of life's spark: a perspective on ion channel research since the birth of neuron, *Neuron.* **2013.** *80*, 658-674.
- (90) Minor, D. L., Jr. Searching for interesting channels: pairing selection and molecular evolution methods to study ion channel structure and function, *Mol Biosyst.* **2009.** *5*, 802-810.
- (91) Edelhoch, H. Spectroscopic determination of tryptophan and tyrosine in proteins, *Biochemistry.* **1967.** *6*, 1948-1954.
- (92) Leslie, A. G. W. Recent changes to the MOSFLM package for processing film and image plate data, Joint CCP4 + ESF-EAMCB Newsletter of Protein Crystallography. **1992.** *26*.
- (93) Evans, P. R. An introduction to data reduction: space-group determination, scaling and intensity statistics, *Acta Crystallogr D Biol Crystallogr.* **2011.** *67*, 282-292.

- (94) McCoy, A. J., Grosse-Kunstleve, R. W., Adams, P. D., Winn, M. D., Storoni, L. C., and Read, R. J. Phaser crystallographic software, *J Appl Crystallogr.* **2007.** *40*, 658-674.
- (95) Emsley, P., and Cowtan, K. Coot: model-building tools for molecular graphics, *Acta Crystallogr D Biol Crystallogr.* **2004.** *60*, 2126-2132.
- (96) Collaborative Computational Project, N. The CCP4 suite: Programs for protein crystallography, *Acta Crystallogr D Biol Crystallogr.* **1994.** *50*, 760-763.

## **Acknowledgements**

We thank M. Grabe for insightful discussions and comments on the manuscript. This work was supported by NIH grants R01-HL080050 to D.L.M and R01-GM54616 to W.F.D. and Austrian Science Fund (FWF) W01101 to B.E.F.

## **Coordinates and structure factors**

Coordinates and structure factors for have been deposited for the Cav $\beta_{2a}$ :Cav1.2 AID-CAP complex (5V2P) and Cav $\beta_{2a}$ :AID-CEN complex (5V2Q) and will be immediately available upon publication.

## **Competing financial interests statement**

The authors declare no competing financial interests.

## **Author contributions.**

M.C. F.F. H.J. W.F.D. and D.L.M. conceived the study and designed the experiments. F.F. M.C. H.J. C.H.R. L.P., F.A.A. and N.D.R. performed the experiments. F.F. purified, crystallized and determined the structures AID-Cav $\beta$  complexes, performed the CD experiments, and analyzed the data. F.F. M.C., F.A.A., and N.D.R. performed electrophysiological experiments and analyzed the data. H.J. and W.F.D. designed and synthesized the peptides. D.L.M analyzed the data and provided guidance and support throughout. F.F. M.C., H.J., F.A.A., B.E.F., W.F.D. and D.L.M. wrote the paper.

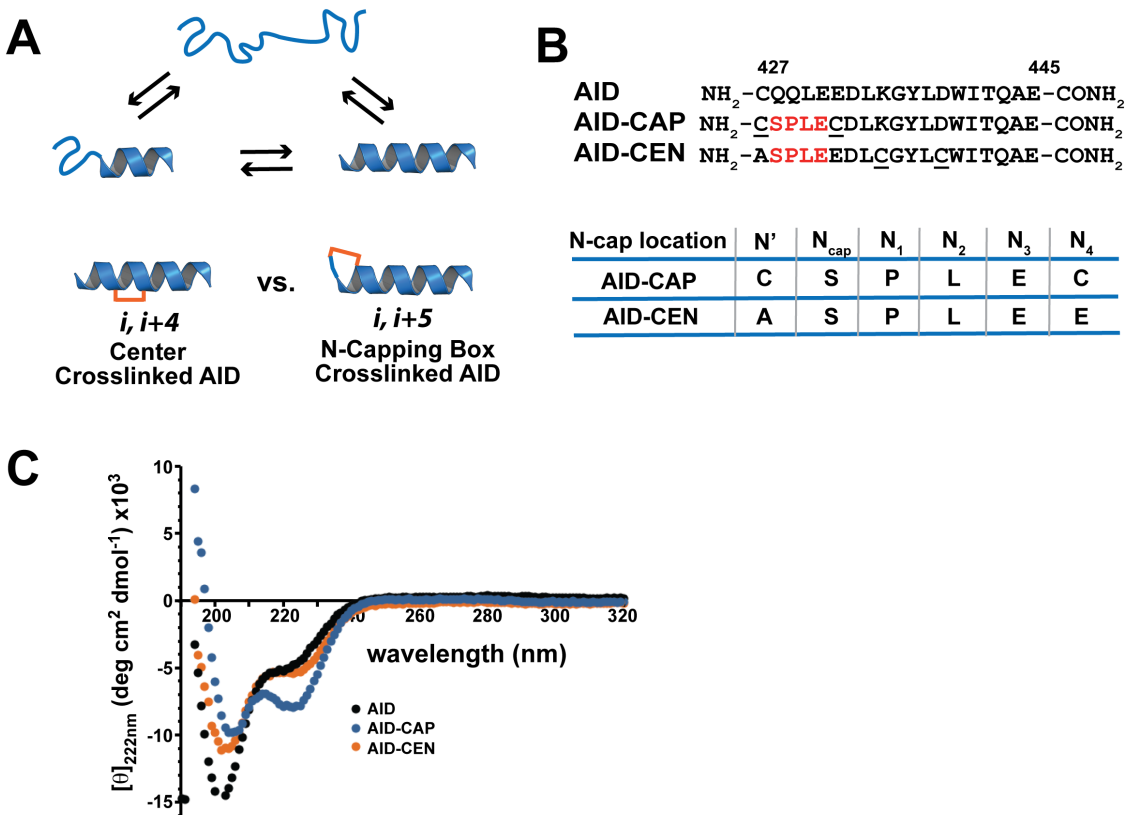


**Figure 4.1 | Backbone staples increase AID helical content**

**A**, Schematic showing the conformational ensemble of the native AID (top) versus the desired effect of incorporating the m-xylyl backbone staple. **B**, AID, AID-CAP and AID-CEN peptide sequences. The capping box residues are highlighted in red. Underline denotes m-xylyl linker crosslinking positions. **C**, Circular dichroism spectra of AID (black), AID-CAP (blue) and AID-CEN (orange) at 70  $\mu$ M and 4°C.

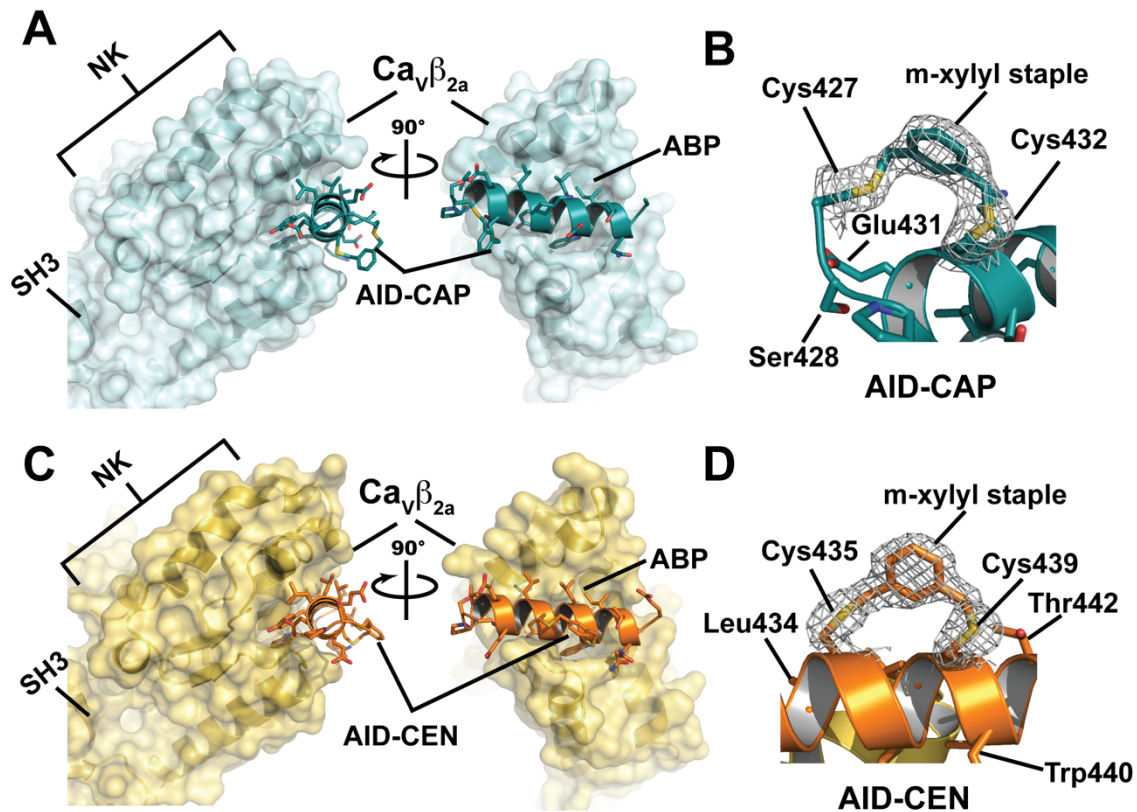


**Figure 4.2 | Crystal structures of  $Ca_v\beta_{2a}$ :stapled peptide complexes**

**A**, Structure of the  $Ca_v\beta_{2a}$ :AID-CAP complex.  $Ca_v\beta_{2a}$  (cyan) is shown in surface rendering. AID-CAP (deep teal) is shown as a cartoon having sidechains shown as sticks. Locations of the AID-CAP and ABP, nucleotide kinase (NK) and SH3 domains of  $Ca_v\beta_{2a}$  are indicated. **B**, 2Fo-Fc electron density ( $1.0 \sigma$ ) for the AID-CAP m-xylyl staple. Select AID-CAP residues are indicated. **C**, Structure of the  $Ca_v\beta_{2a}$ :AID-CEN complex.  $Ca_v\beta_{2a}$  (yellow orange) is shown in surface rendering. AID-CEN (orange) is shown as a cartoon having sidechains shown as sticks. Locations of the AID-CEN and ABP, nucleotide kinase (NK) and SH3 domains of  $Ca_v\beta_{2a}$  are indicated. **D**, 2Fo-Fc electron density ( $1.0 \sigma$ ) for the AID-CEN m-xylyl staple. Select AID-CAP residues are indicated.

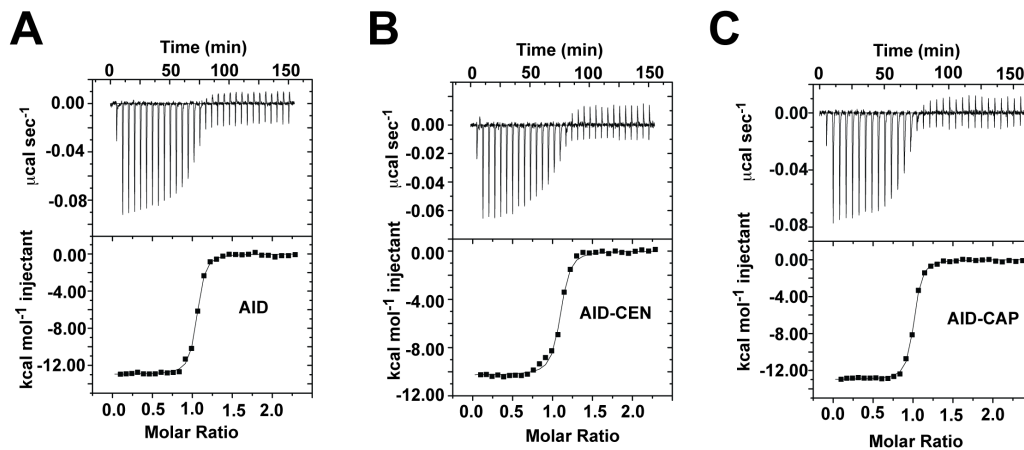


**Figure 4.3 | Backbone modifications decrease entropic cost of  $\text{Ca}_v\beta_{2a}$  binding**  
 Exemplar ITC titrations for **A**, 20  $\mu\text{M}$  AID into 2  $\mu\text{M}$   $\text{Ca}_v\beta_{2a}$ . **B**, 20  $\mu\text{M}$  AID-CEN into 2  $\mu\text{M}$   $\text{Ca}_v\beta_{2a}$  core and **C**, 20  $\mu\text{M}$  AID-CAP-peptide into 2  $\mu\text{M}$   $\text{Ca}_v\beta_{2a}$ .

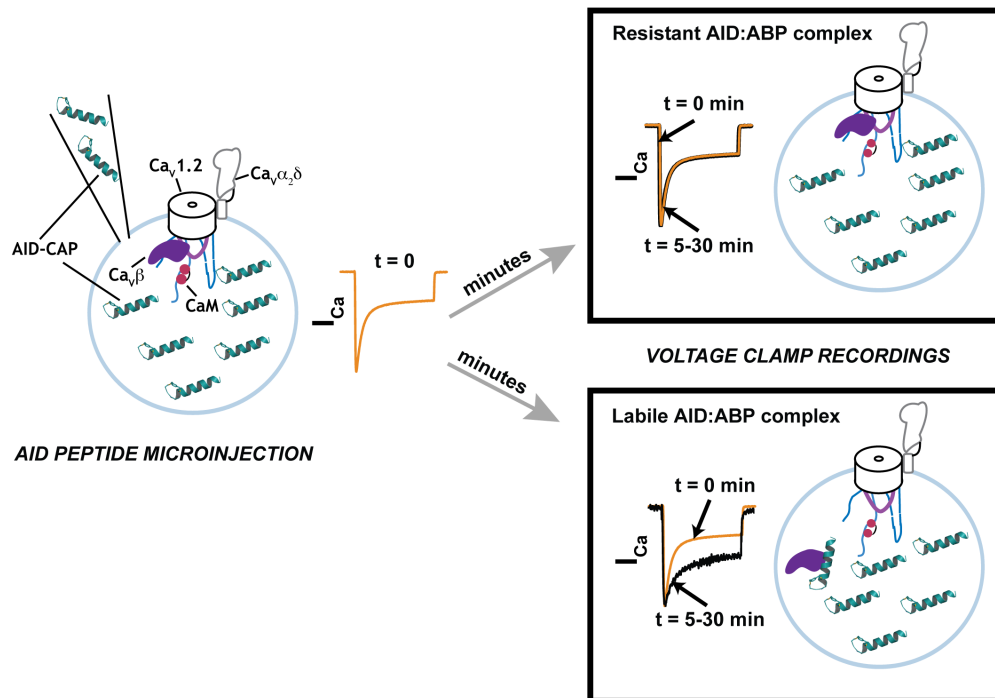


**Figure 4.4 | Schematic of AID peptide competition experiment**

*Xenopus* oocytes expressing Ca<sub>v</sub> channels (complexes of Ca<sub>v</sub>1.2 (black lines), Ca<sub>v</sub>β (purple), Ca<sub>v</sub>α<sub>2</sub>δ (grey lines), and CaM (red) (left) are injected with AID-CAP peptide at t=0 and initial channel properties are recorded using two-electrode voltage clamp. Panels show two possible outcomes. Resistant complexes have no changes in channel biophysical properties (orange vs. black lines). Labile channel complexes in which the AID competitor peptide can capture released Ca<sub>v</sub>β leaving an unoccupied I-II loop (purple) show biophysical changes. For simplicity, changes in channel current amplitude, an additional possible outcome for labile complexes, is not depicted.



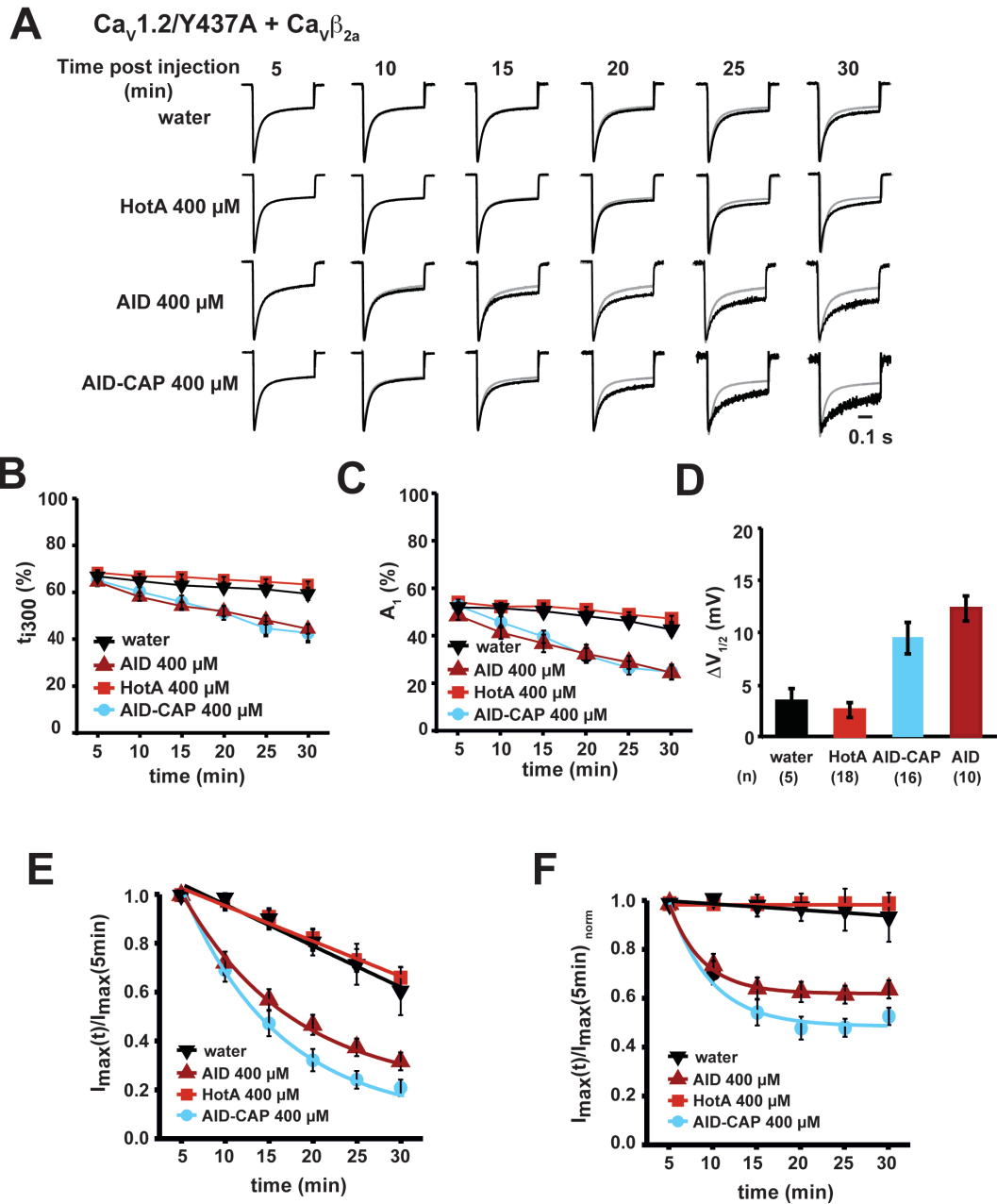


**Figure 4.5 | AID-CAP affects  $\text{Ca}_v1.2/\text{Y437A}:\text{Ca}_v\beta_{2a}$  channels**

**A**, Exemplar normalized  $I_{\text{Ca}}$  traces at a test potential of +20 mV for *Xenopus* oocytes expressing  $\text{Ca}_v1.2\text{-Y437A}:\text{Ca}_v\beta_{2a}$  channels recorded after injection of water, 400  $\mu\text{M}$  HotA, 400  $\mu\text{M}$  AID-CAP, or 400  $\mu\text{M}$  AID at the indicated post-injection times. Grey curves at times 10, 15, 20, 25, and 30 minutes show initial 5 minute response. **B**, Fractional inactivation after 300 ms ( $t_{i300}$ ) and **C**,  $A_1$ , the relative amplitude of the fast inactivation component for  $\text{Ca}_v1.2\text{-Y437A}:\text{Ca}_v\beta_{2a}$  currents as a function of post-injection time for water (inverted black triangles), 400  $\mu\text{M}$  HotA (red squares), 400  $\mu\text{M}$  AID (maroon triangles), or 400  $\mu\text{M}$  AID-CAP (blue circles). **D**, Change in half maximal activation

potential ( $\Delta V_{1/2}$ ) between recordings at 5 and 30 minutes post-injection. **E**,  $I_{\max}(t)/I_{\max(5\text{min})}$  and **F**,  $I_{\max}(t)/I_{\max(5\text{min})}$  normalized to  $I_{\max}(t)/I_{\max(5\text{min})}$  of HotA injection as a function of post-injection time. Symbols are as in 'B' and 'C'. Lines in 'F' show fit to  $I(t) = A \exp(-t/\tau) + C$  (exponential) or  $I(t) = mt + C$  (linear), where  $I$  is the recorded current,  $A$  is the amplitude of the loss of current (for exponential fit),  $m$  is the slope factor (linear fit), and  $C$  is the residual current after 30 minutes. Results for AID and AID-CAP are statistically different from HotA in all panels ( $P < 0.001$ ). AID and AID-CAP results are not statistically different from each other except in panels 5E and 5F where ( $P < 0.001$ ).

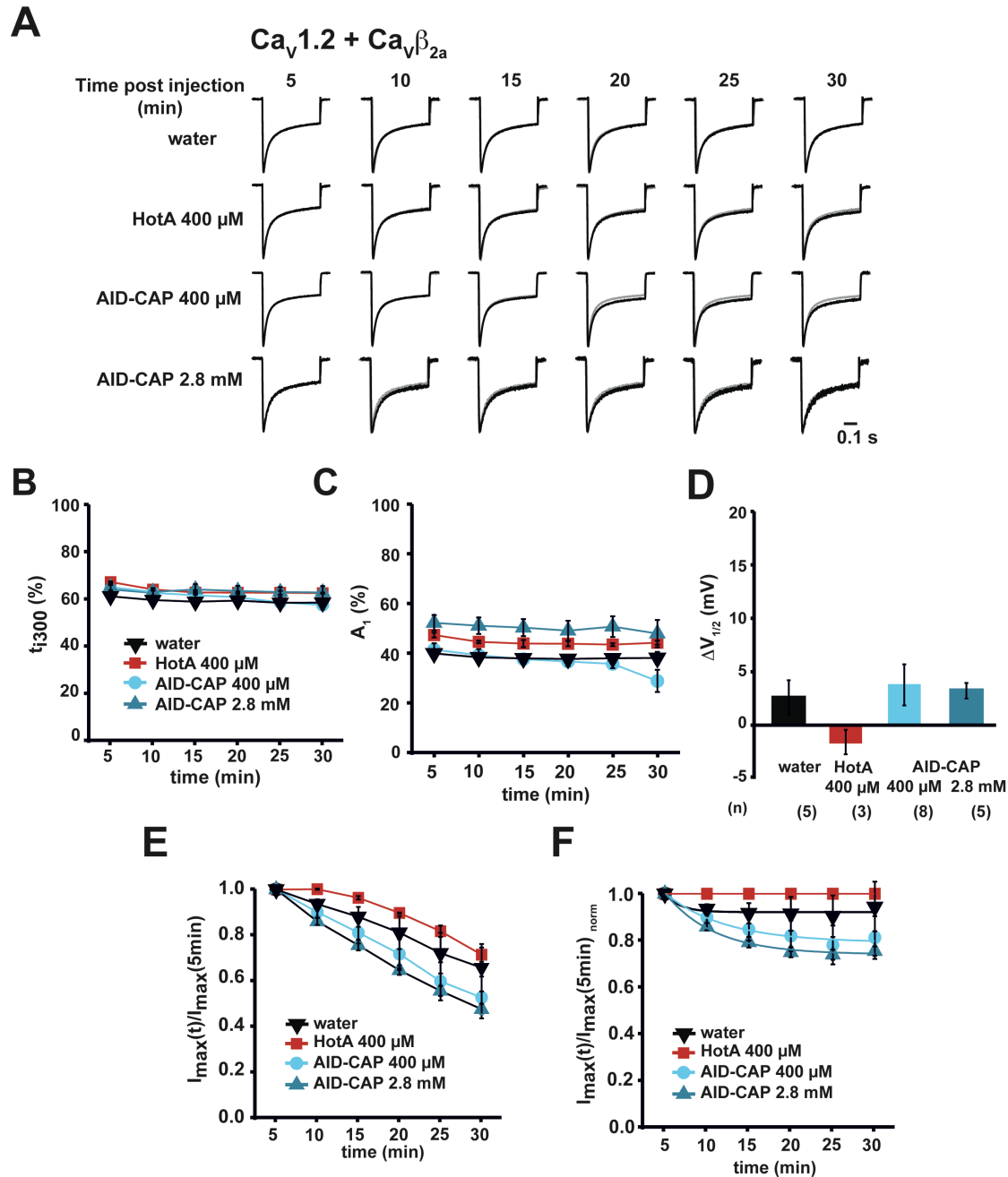


**Figure 4.6 |  $\text{Cav}1.2:\text{Cav}\beta_{2a}$  channels resist AID-CAP modulation**

**A**, Exemplar normalized  $I_{\text{Ca}}$  traces at a test potential of +20 mV for *Xenopus* oocytes expressing  $\text{Cav}1.2:\text{Cav}\beta_{2a}$  channels recorded after injection of water, 400  $\mu\text{M}$  HotA, 400  $\mu\text{M}$  AID-CAP, or 2.8 mM AID-CAP at the indicated post-injection times. Grey curves at times 10, 15, 20, 25, and 30 minutes show initial 5 minute response. **B** and **C**, post-injection values of **B**, Fractional inactivation after 300 ms ( $t_{i300}$ ) and **C**,  $A_1$ , the relative amplitude of the fast inactivation component for  $\text{Cav}1.2\text{-Y437A}:\text{Cav}\beta_{2a}$  currents as a function of post-injection time for water (inverted black triangles), 400  $\mu\text{M}$  HotA (red squares), 400  $\mu\text{M}$  AID-CAP (blue circles) or 2.8 mM AID-CAP (teal triangles). **D**, Change

in half maximal activation potential ( $\Delta V_{1/2}$ ) between recordings 5 and 30 minutes post-injection. **E**,  $I_{\max}(t)/I_{\max(5\text{min})}$  and **F**,  $I_{\max}(t)/I_{\max(5\text{min})}$  normalized to HotA njection as a function of post-injection time. Symbols are as in 'B' and 'C'. Lines in 'F' show fit  $t$  to  $I(t) = A \exp(-t/\tau) + C$  (exponential) or  $I(t) = mt + C$  (linear), where  $I$  is the recorded current,  $A$  is the amplitude of the loss of current (for exponential fit),  $m$  is the slope factor (linear fit), an  $C$  is the residual current after 30 minutes. There are no statistically significant differences in the results shown in the panels, except for 6E and 6F where the AID-CAP 2.8 mM results are statistically significant from Hot A ( $P = 0.034$ ).

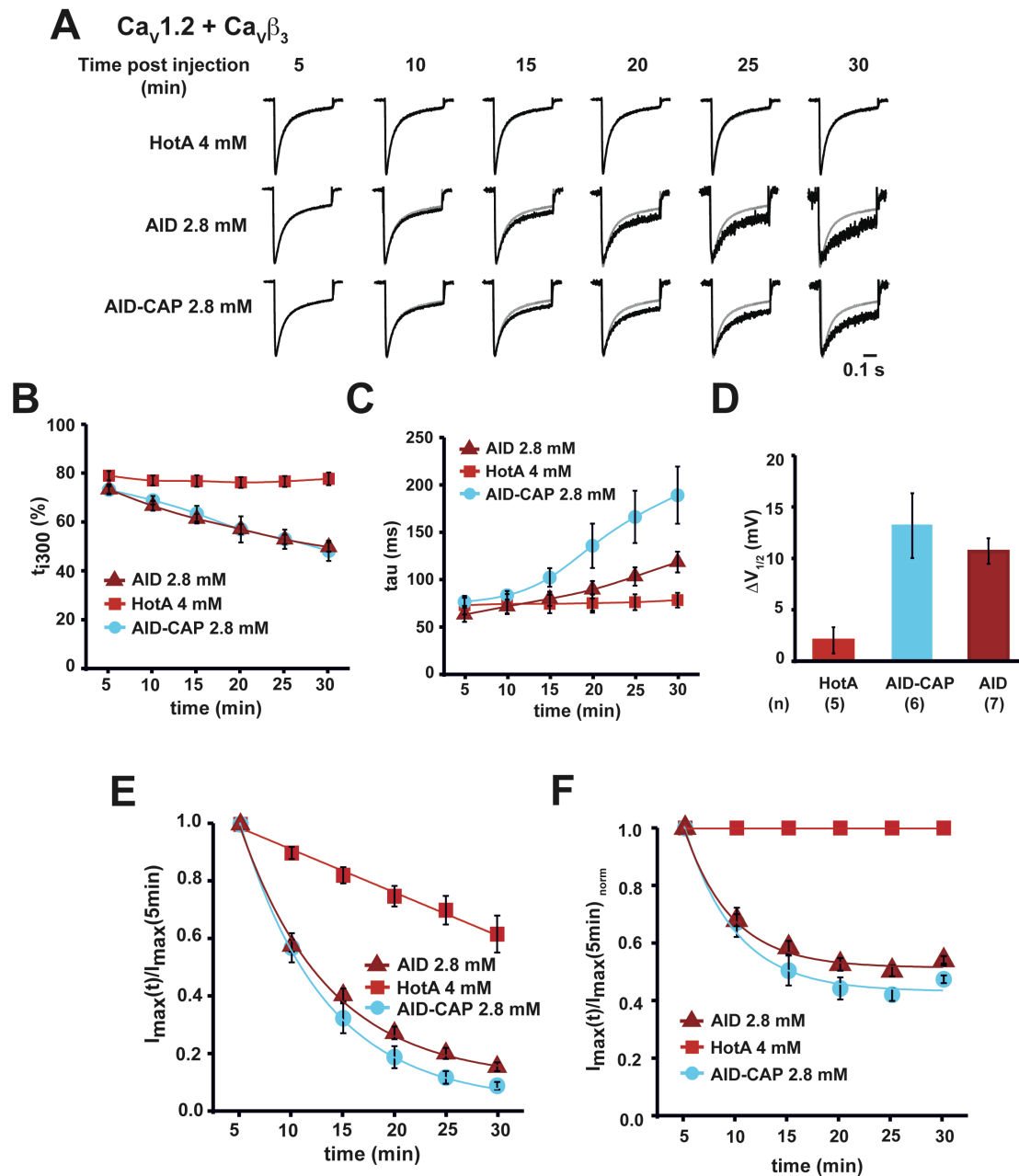


**Figure 4.7 | AID-CAP affects  $\text{Ca}_v1.2:\text{Ca}_v\beta_3$  channels**

**A**, Exemplar normalized  $I_{\text{Ca}}$  traces at a test potential of +20 mV for *Xenopus* oocytes expressing  $\text{Ca}_v1.2:\text{Ca}_v\beta_3$  channels recorded after injection of 4 mM HotA, 2.8 mM AID-CAP, or 2.8 mM AID at the indicated post-injection times. Grey curves at times 10, 15, 20, 25, and 30 minutes show initial 5 minute response. **B** and **C**, post-injection values of **B**, Fractional inactivation after 300 ms ( $t_{300}$ ) and **C**,  $\tau$ , the fast inactivation time constant of  $\text{Ca}_v1.2:\text{Ca}_v\beta_3$  currents as a function of post-injection time for 4 mM HotA (red squares), 2.8 mM AID (maroon triangles), or 2.8 mM AID-CAP (blue circles). **D**, Change in half maximal activation potential ( $\Delta V_{1/2}$ ) between recordings 5 and 30 minutes post-injection.

**E**,  $I_{\max}(t)/I_{\max(5\text{min})}$  and **F**,  $I_{\max}(t)/I_{\max(5\text{min})}$  normalized to HotA injection as a function of post-injection time. Symbols are as in 'B' and 'C'. Lines in 'F' show fit to  $I(t) = A \exp(-t/\tau) + C$  (exponential) or  $I(t) = mt + C$  (linear), where  $I$  is the recorded current,  $A$  is the amplitude of the loss of current (for exponential fit),  $m$  is the slope factor (linear fit), and  $C$  is the residual current after 30 minutes. Because of the switch in inactivation behavior, to facilitate comparisons, values from monoexponential fits of the channel kinetics were used for 'C'. Results for AID and AID-CAP are statistically different from HotA in all panels ( $P < 0.001$  for Panels 7B, 7E and 7F;  $P < 0.05$  for Panels 7C and 7D). AID and AID-CAP results are not statistically different from each other except in panels 7C, 7E, and 7F where ( $P < 0.001$ ).

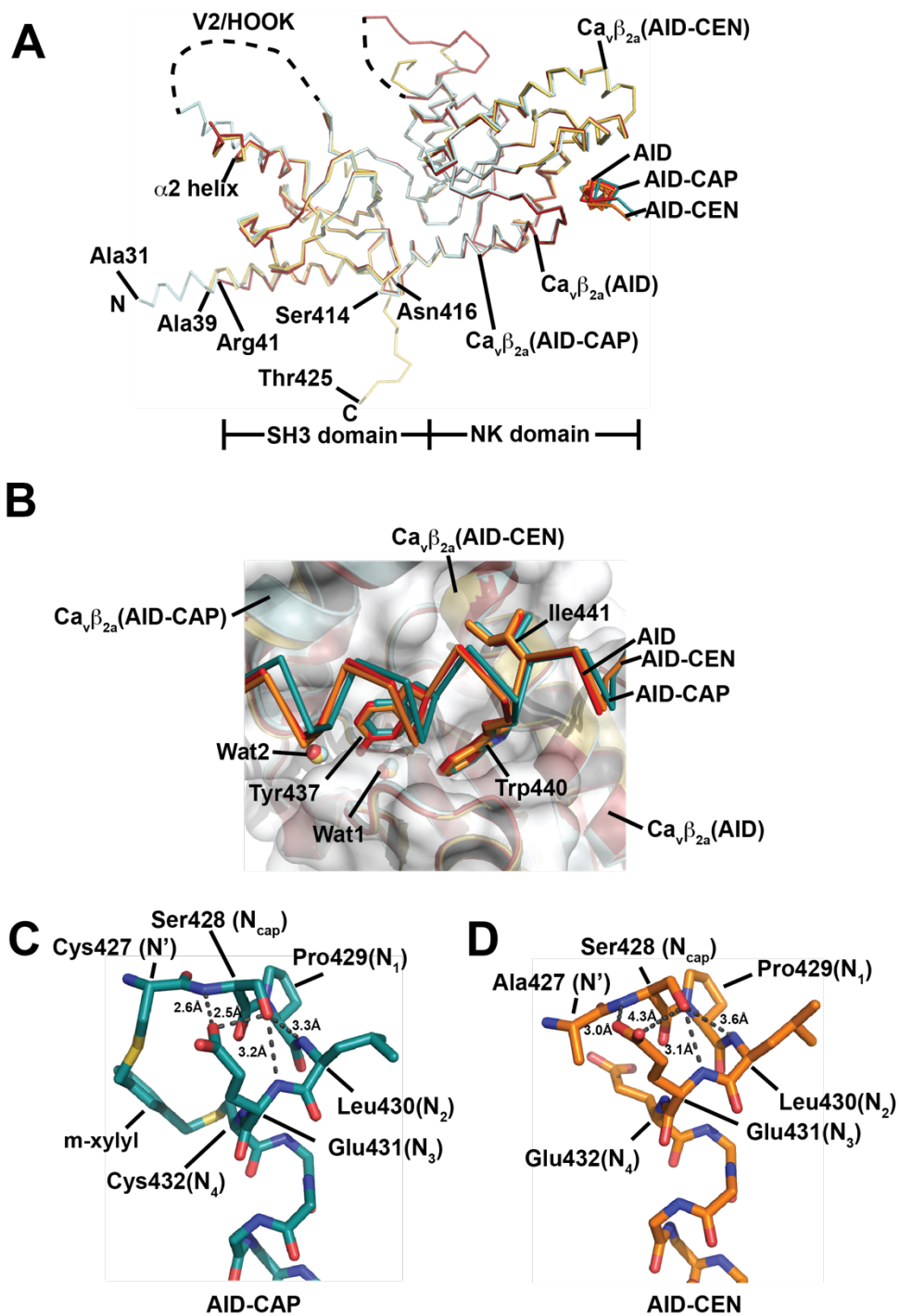


**Figure 4.8 | S1 - Structures of  $Ca_v\beta_{2a}$ :stapled peptide complexes.**

**A**, Superposition of  $Ca_v\beta_{2a}$ :AID-CAP (cyan),  $Ca_v\beta_{2a}$ :AID-CEN (yellow orange), and  $Ca_v\beta_{2a}$ :AID (firebrick) (1T0H)<sup>1</sup> complexes shown as wireframe. First and last  $Ca_v\beta_{2a}$  residues in each structure are labeled and are as follows:  $Ca_v\beta_{2a}$ :AID-CAP, Ala31 and

Ser414; Cav $\beta$ <sub>2a</sub>:AID-CEN Ala39 and Thr425; and Cav $\beta$ <sub>2a</sub>:AID, Arg41 and Asn416. N- and C- termini representing the maximal respective termini are indicated. Locations of Cav $\beta$ <sub>2a</sub> SH3 and NK (also known as GK) domain are indicated. AID-CAP (deep teal), AID-CEN (orange), and AID (red) peptides are labeled. Dashed lines denote loop regions lacking electron density. **B**, Close-up view of AID-ABP interaction from the superposition in '**A**'. AID peptides are shown as wireframe. Hotspot residues, Tyr437, Trp440, and Ile441<sup>48,45</sup>, are shown as sticks and are labeled. Buried water molecules, Wat1 and Wat2, are shown and colored according to the parent structure. Cav $\beta$ <sub>2a</sub> from each complex is shown as a cartoon. Surface (white) is from the Cav $\beta$ <sub>2a</sub>:AID structure (1T0H)<sup>48</sup>. **C**, and **D**, Close up view of the N-terminal capping motif residues in the **C**, AID-CAP, and **D**, AID-CEN structures. Sidechains and identities for N-cap positions N', N<sub>cap</sub>, N<sub>1</sub>, N<sub>2</sub>, N<sub>3</sub>, and N<sub>4</sub> are shown. Hydrogen bonds in the N-terminal capping motif and distances are shown.



**Table 4.1 | AID peptide:Ca<sub>v</sub>β<sub>2a</sub> thermodynamic binding parameters**

<b>AID peptide</b>	<b>n</b>	<b>K<sub>d</sub> (nM)</b>	<b>N</b>	<b>ΔH (kcal mol<sup>-1</sup>)</b>	<b>ΔS (cal mol<sup>-1</sup> K<sup>-1</sup>)</b>	<b>K<sub>d</sub> / K<sub>d</sub> Cav1.2 AID</b>
<b>Cav1.2 AID</b>	3	6.6 ± 2.0	0.94 ± 0.07	-15.6 ± 2.4	-16.7 ± 6.0	1
<b>AID-CEN</b>	2	5.2 ± 1.5	1.05 ± 0.03	-10.2 ± 0.1	2.2 ± 0.5	0.79 ± 0.33
<b>AID-CAP</b>	3	5.1 ± 1.6	1.02 ± 0.10	-12.3 ± 1.4	-4.6 ± 4.1	0.77 ± 0.34

**Table 4.2 | Cav1.2 inactivation parameters and GV relationship**

	$t_{i300}$ (%)	$A_1$ (%)	$\tau_1$ (ms)	$A_2$ (%)	
Cav1.2:Cav $\beta_{2a}$	68.4 ± 1.1	49.4 ± 1.9	25.4 ± 1.2	21.3 ± 1.2	
Cav1.2-Y437A:Cav $\beta_{2a}$	66.0 ± 3.2	51.6 ± 3.7	31.2 ± 4.6	22.5 ± 3.9	
Cav1.2:Cav $\beta_3$	75.9 ± 1.1	70.3 ± 0.9	59.8 ± 2.5		
		59.9 ± 1.9	33.9 ± 3.0	25.4 ± 1.6	
Cav1.2, no Cav $\beta$	47.9 ± 1.2	26.8 ± 3.6	75.5 ± 10.3	48.4 ± 4.8	
Cav1.2-Y437A:Cav $\beta_{2a}$	water 5 min	67.2 ± 1.9	51.9 ± 2.2	28.0 ± 1.5	19.7 ± 1.2
	water 30 min	59.8 ± 2.6	42.6 ± 2.6	31.6 ± 2.9	23.7 ± 1.6
	HotA, 5 min	68.8 ± 1.0	54.0 ± 1.2	33.2 ± 1.4	20.0 ± 1.3
	HotA, 30 min	63.7 ± 1.3	47.2 ± 1.2	34.5 ± 1.7	22.0 ± 1.0
	AID-CAP, 5 min	65.5 ± 1.3	52.7 ± 1.3	32.9 ± 1.7	18.8 ± 1.1
	AID-CAP, 30 min	43.1 ± 3.7	24.8 ± 3.2	52.8 ± 8.2	38.2 ± 3.0
	AID, 5 min	64.9 ± 1.9	48.5 ± 1.8	35.0 ± 1.5	24.1 ± 1.6
	AID, 30 min	44.8 ± 2.1	24.5 ± 3.0	53.3 ± 14.4	31.0 ± 1.9
	water 5 min	60.8 ± 1.0	40.0 ± 1.1	34.6 ± 3.9	27.1 ± 0.8
	water 30 min	58.1 ± 1.4	38.3 ± 2.5	37.3 ± 3.0	27.1 ± 2.0
Cav1.2:Cav $\beta_{2a}$	HotA, 5 min	66.8 ± 0.3	47.5 ± 1.0	28.4 ± 0.7	24.6 ± 1.0
	HotA, 30 min	62.1 ± 0.2	44.4 ± 0.8	33.5 ± 2.3	24.7 ± 0.6
	AID-CAP 400 $\mu$ M, 5 min	63.7 ± 1.9	41.6 ± 2.5	33.0 ± 2.3	28.9 ± 1.8
	AID-CAP 400 $\mu$ M, 30 min	57.1 ± 1.6	33.1 ± 2.0	35.0 ± 1.7	28.6 ± 2.0
	AID-CAP 2.8 mM, 5 min	64.6 ± 1.3	52.4 ± 3.1	29.2 ± 3.3	19.3 ± 2.2
	AID-CAP 2.8 mM, 30 min	62.4 ± 2.6	48.1 ± 5.5	30.7 ± 6.0	27.3 ± 1.3
Cav1.2:Cav $\beta_3$	HotA, 5 min	79.2 ± 2.2	79.7 ± 2.3	63.0 ± 2.4	
			61.0 ± 2.4	38.5 ± 1.5	27.9 ± 0.8
	HotA, 30 min	77.0 ± 2.9	78.0 ± 2.7	71.4 ± 4.6	
			56.5 ± 2.0	42.9 ± 4.4	30.0 ± 1.4
	AID-CAP, 5 min	73.2 ± 1.4	75.9 ± 1.2	76.2 ± 4.2	
			57.8 ± 1.2	48.0 ± 3.7	42.0 ± 8.3
	AID-CAP, 30 min	48.3 ± 4.1	66.3 ± 5.0	188.7 ± 30.2	
			ND	ND	ND
Cav1.2:Cav $\beta_3$	AID, 5 min	73.4 ± 2.0	76.9 ± 3.1	62.6 ± 7.6	
			54.0 ± 2.7	40.0 ± 5.2	34.1 ± 1.4
	AID, 30 min	49.8 ± 1.9	65.0 ± 4.0	118.2 ± 11.0	
			ND	ND	ND

**Table 4.3 | Cav1.2 inactivation parameters and GV relationship (ct'd)**

	$\tau_2$ (ms)	$I_{max}$	$V_{1/2}$	N	
Cav1.2:Cav $\beta_{2a}$	159.6 $\pm$ 8.4	-0.411 $\pm$ 0.054	8.1 $\pm$ 1.2	25	
Cav1.2-Y437A:Cav $\beta_{2a}$	177.3 $\pm$ 10.9	-0.816 $\pm$ 0.237	7.5 $\pm$ 1.4	6	
Cav1.2:Cav $\beta_3$	312.0 $\pm$ 47.7	-0.964 $\pm$ 0.008	5.5 $\pm$ 1.4	20	
Cav1.2, no Cav $\beta$	348.3 $\pm$ 41.4	-0.245 $\pm$ 0.028	18.1 $\pm$ 1.0	14	
Cav1.2-Y437A:Cav $\beta_{2a}$	water 5 min	170.5 $\pm$ 6.3	-0.722 $\pm$ 0.092	7.8 $\pm$ 1.3	5
	water 30 min	200.5 $\pm$ 13.8	-0.430 $\pm$ 0.075	11.1 $\pm$ 1.2	5
	HotA, 5 min	212.5 $\pm$ 16.4	-1.001 $\pm$ 0.153	4.7 $\pm$ 1.4	18
	HotA, 30 min	197.9 $\pm$ 10.1	-0.578 $\pm$ 0.064	7.1 $\pm$ 1.1	18
	AID-CAP, 5 min	212.6 $\pm$ 18.6	-1.016 $\pm$ 0.122	5.4 $\pm$ 1.4	16
	AID-CAP, 30 min	469.8 $\pm$ 160.1	-0.156 $\pm$ 0.022	16.9 $\pm$ 1.0	15
	AID, 5 min	251.5 $\pm$ 16.1	-0.883 $\pm$ 0.111	2.9 $\pm$ 1.7	10
	AID, 30 min	304.0 $\pm$ 50.9	-0.242 $\pm$ 0.021	15.1 $\pm$ 2.0	10
Cav1.2:Cav $\beta_{2a}$	water 5 min	222.8 $\pm$ 31.6	-1.344 $\pm$ 0.248	9.1 $\pm$ 1.8	5
	water 30 min	227.3 $\pm$ 12.1	-0.785 $\pm$ 0.074	11.6 $\pm$ 0.7	5
	HotA, 5 min	185.7 $\pm$ 2.1	-0.734 $\pm$ 0.110	10.5 $\pm$ 1.5	3
	HotA, 30 min	209.5 $\pm$ 13.2	-0.531 $\pm$ 0.098	9.0 $\pm$ 0.5	3
	AID-CAP 400 $\mu$ M, 5 min	215.8 $\pm$ 13.2	-0.966 $\pm$ 0.154	9.2 $\pm$ 1.5	8
	AID-CAP 400 $\mu$ M, 30 min	209.7 $\pm$ 9.3	-0.555 $\pm$ 0.132	13.0 $\pm$ 1.7	8
	AID-CAP 2.8 mM, 5 min	172.5 $\pm$ 23.4	-0.984 $\pm$ 0.142	7.2 $\pm$ 0.7	5
	AID-CAP 2.8 mM, 30 min	172.2 $\pm$ 25.9	-0.465 $\pm$ 0.079	10.4 $\pm$ 0.7	5
Cav1.2:Cav $\beta_3$	HotA, 5 min	256.8 $\pm$ 10.8	-0.932 $\pm$ 0.041	6.7 $\pm$ 2.9	5
	HotA, 30 min	241.1 $\pm$ 14.6	-0.577 $\pm$ 0.069	8.6 $\pm$ 3.3	5
	AID-CAP, 5 min	639.1 $\pm$ 238.3	-0.889 $\pm$ 0.135	6.3 $\pm$ 1.6	6
	AID-CAP, 30 min	ND	-0.081 $\pm$ 0.023	20.5 $\pm$ 2.8	6
	AID, 5 min	354.4 $\pm$ 119.2	-0.860 $\pm$ 0.096	10.4 $\pm$ 2.2	7
	AID, 30 min	ND	-0.116 $\pm$ 0.010	21.0 $\pm$ 2.0	7

Data are expressed as mean values  $\pm$  SE.  $\tau$  values were determined at a holding potential of +20 mV (see Materials and methods).  $t_{300}$  denotes percent inactivation at 300 ms.  $I_{max}$  is the maximal current amplitude.  $V_{1/2}$  values for Cav1.2 and mutants were determined with calcium as the charge carrier. Data were fit using the equation  $I = G_{max} * (V_m -$

$I_{rev}/(1 + \exp((V_{1/2} - V_m)/K_a))$ , where  $I$  is the measured peak current at each  $V_m$ ,  $G_{max}$  is the maximal macroscopic conductance,  $V_m$  is the test potential,  $V_{rev}$  is the reversal potential,  $V_{1/2}$  is the midpoint of activation,  $K_a$  is the slope factor<sup>29</sup>, and ND, a value not determined. *Italic lines highlight double exponential fit values for Cav $\beta_3$  experiments.*

**Table 4.4 | Supplementary Table 1 - Crystallographic data collection and refinement statistics**

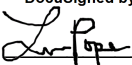
	Ca <sub>v</sub> β <sub>2a</sub> link:AID-CAP	Ca <sub>v</sub> β <sub>2a</sub> link:AID-CEN
<b>Data Collection</b>		
Space group	H3	P2 <sub>1</sub> 2 <sub>1</sub> 2 <sub>1</sub>
Cell dimensions a/b/c (Å)	82 / 82 / 163	55 / 62 / 130
α/β/γ (°)	90 / 90 / 120	90 / 90 / 90
Resolution (Å)	50 – 1.90 (2.00-1.90)	50 – 1.80 (1.89 – 1.80)
R <sub>sym</sub> (%)	13.7 (>100%)	7.9 (>100%)
I / σ I	4.7 (0.4)	8.7 (0.6)
Correlation Coefficient	0.993 (0.152)	0.998 (0.338)
Completeness (%)	96.5 (97.0)	94.7 (77.8)
Redundancy	3.4 (2.6)	3.9 (3.7)
Unique reflections	31133	39617
Wilson B-factor	32.8	20.2
<b>Refinement</b>		
R <sub>work</sub> / R <sub>free</sub> (%)	18.5 / 23.0	15.8 / 19.6
No. of chains in AU	2	2
No. of protein atoms	2367	2531
No. of ligand atoms	41	9
No. of water atoms	374	457
RMSD bond lengths (Å)	0.0073	0.0207
RMSD angles (°)	1.193	1.900
Ramachandran best/disallowed regions (%)	97.6 / 0.0	98.0 / 0.0

**Publishing Agreement**

*It is the policy of the University to encourage the distribution of all theses, dissertations, and manuscripts. Copies of all UCSF theses, dissertations, and manuscripts will be routed to the library via the Graduate Division. The library will make all theses, dissertations, and manuscripts accessible to the public and will preserve these to the best of their abilities, in perpetuity.*

***Please sign the following statement:***

*I hereby grant permission to the Graduate Division of the University of California, San Francisco to release copies of my thesis, dissertation, or manuscript to the Campus Library to provide access and preservation, in whole or in part, in perpetuity.*

DocuSigned by:  
  
E5492FDBBE5C422...

\_\_\_\_\_  
Author Signature

12/16/2019

\_\_\_\_\_  
Date